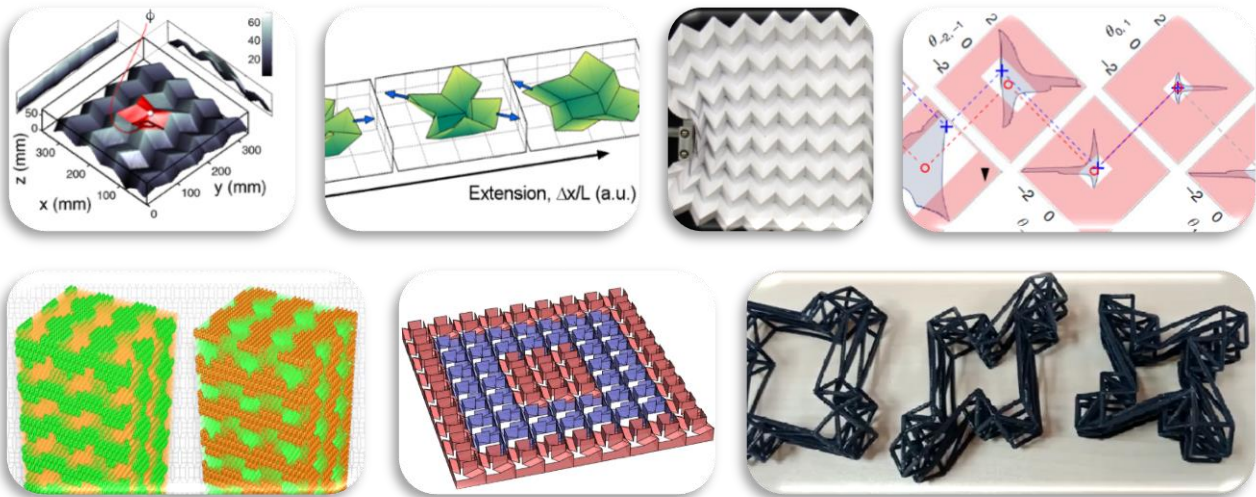


# Origami-Inspired Mechanical Metamaterials

---



*Key Technical Literature, v1.0*



## Table of Contents:

---

- Publication 1

*"Using origami design principles to fold reprogrammable mechanical metamaterials"* by **Silverberg, Evans**, et. al. This paper is quickly becoming the seminal research on origami-inspired metamaterials. It introduces the concept that a folded sheet can have dynamically tuned functionality and exotic mechanical properties.

- Publication 2

*"Origami structures with a critical transition to bistability arising from hidden degrees of freedom"* by **Silverberg, Evans**, et. al. This paper explores and explains how a purely mathematical description of metamaterials breaks-down and how an engineering/physics/materials-based approach is necessary to fully understand these systems.

- Publication 3

*"Lattice mechanics of origami tessellations"* by **Evans, Silverberg**, et. al. This paper provides a detailed systematic computational framework for predicting mechanical properties of origami-inspired metamaterials. The approach described incorporates real-world effects and predicts experimentally-observed phenomenon.

- Publication 4

*"Decoupling local mechanics from large-scale structure in modular metamaterials"* by **Silverberg**, et. al. This paper is the first metamaterial research that asks and answers the question: How does one go from design-specifications to design-patterns (the so-called 'inverse-design' problem). This work is a significant advancement in transforming the exploratory science of metamaterials to a practical engineering tool.

- Publication 5

*"Topological kinematics of origami metamaterials"* by **Silverberg, Evans**, et. al. This paper explains how the mathematics of "topologically protected mechanisms" can be applied to origami-inspired metamaterials. Though conceptually abstract, the application are quite concrete: metamaterial structures can be designed to be failure-resistant and have built-in resilience to engineering design tolerances.

- Publication 6

*"Topological Mechanics of Origami and Kirigami"* co-authored by **Evans**. This paper further explains and generalizes mathematical design principles for resilience to failure modes and flexibility with respect to engineering tolerances.

- Publication 7

*"Reflection and Refraction of Flexural Waves at Geometric Boundaries"* co-authored by **Evans**. This paper shows how to control vibrations using the geometry of non-trivial curved surfaces. It finds specific formulae for how to use discontinuities in surface curvature to tune wave scattering.

- Publication 8 (currently under revision; soon to be published)

*"Emergence and design of extrinsic properties in mechanical metamaterials"* co-authored by **Silverberg**. This paper complements the work described in Publication 4 above. It further investigates the 'inverse-design' problem and addresses how unexpected effects that arise in metamaterial design can be turned from 'bugs' into 'features' through clever computational design schemes.



## APPLIED ORIGAMI

# Using origami design principles to fold reprogrammable mechanical metamaterials

Jesse L. Silverberg,<sup>1\*</sup> Arthur A. Evans,<sup>2</sup> Lauren McLeod,<sup>1</sup> Ryan C. Hayward,<sup>3</sup> Thomas Hull,<sup>4</sup> Christian D. Santangelo,<sup>2</sup> Itai Cohen<sup>1</sup>

Although broadly admired for its aesthetic qualities, the art of origami is now being recognized also as a framework for mechanical metamaterial design. Working with the Miura-ori tessellation, we find that each unit cell of this crease pattern is mechanically bistable, and by switching between states, the compressive modulus of the overall structure can be rationally and reversibly tuned. By virtue of their interactions, these mechanically stable lattice defects also lead to emergent crystallographic structures such as vacancies, dislocations, and grain boundaries. Each of these structures comes from an arrangement of reversible folds, highlighting a connection between mechanical metamaterials and programmable matter. Given origami's scale-free geometric character, this framework for metamaterial design can be directly transferred to milli-, micro-, and nanometer-size systems.

**M**etamaterials are rapidly emerging at the frontier of scientific and technological innovation due to their exotic and tunable material properties, which arise from arrangements of smaller units within the bulk system (1–5). Once fabricated, structural modifications are generally difficult, making it rare to find metamaterials that can be reconfigured beyond their original design. Origami-inspired mechanical metamaterials offer enhanced flexibility in performance because their properties are coupled to a dynamically alterable folding pattern (6–16). Hence, multiple stable configurations can manifest from a single structure yielding programmable metamaterials.

We studied the Miura-ori tessellated folding pattern, which has recently been proposed as an origami metamaterial (Fig. 1, A to C, figs. S1 to S3, and movie S1) (14, 15). Historically, this design was invented to efficiently pack solar panels for space missions (17), but the morphology also naturally occurs in leaves (18) and embryonic intestine (19, 20) and generally arises when thin sheets tethered to a surface undergo biaxial compression. The geometry of a Miura-ori is a herringbone pattern that emerges from a series of convex mountain and concave valley creases (Fig. 1C). Vertices are formed when four creases intersect, and four adjacent vertices bound equal-area facets arranged with inversion symmetry (Fig. 1B). This fold pattern defines a lattice characterized by two static crease lengths  $\ell_1$ ,  $\ell_2$ , and one static plane angle  $\alpha$ . To quantify folding, a vertex angle  $\varepsilon$  is

required (Fig. 1C); when  $\varepsilon = 180^\circ - 2\alpha$ , the structure is maximally contracted into a folded state, and when  $\varepsilon = 180^\circ$ , the structure is an unfolded flat sheet.

If folded from an ideal material with infinite stretching modulus, the Miura-ori would have only one degree of freedom described by  $\varepsilon$  (14). However, generating samples from laser-cut sheets of paper and mylar (Fig. 1C) (see supplementary materials for details), we find additional degrees of freedom, as evidenced by soft bending modes (14, 15). As an extreme example, the Miura-ori supports highly localized heterogeneity introduced after folding by applying force to a vertex in the normal direction and popping it into a categorically different mechanically stable state (Fig. 2A, fig. S4A, and movie S2). This pop-through defect (PTD) changes lattice topology by suppressing one fold and bending adjacent facets through an angle  $\phi$  (Fig. 2, B and C). Quantifying lattice distortion by the surface's Monge patch mean curvature calculated from three-dimensional (3D) digitized scans, we find that displacements of vertices in the  $xy$  plane are negligible within a distance of one unit cell; this compares favorably with theoretical predictions that estimate a distortion decay length  $\approx 1/2$  the unit cell width (Fig. 2D) (see supplementary materials for details) (21, 22). Although highly localized, PTDs are unlike conventional lattice defects because they involve only elastic facet bending and hence are reversibly removable.

To determine the robustness of PTDs to mechanical perturbations, we theoretically model a single unit cell with one mountain and three valley folds in mechanical equilibrium (similar to the paper model in Fig. 2, B and C). To account for experimentally observed facet bending, two additional symmetrically placed creases are included whose folding angles  $\phi$  are equal and have equilibrium values of  $180^\circ$  (14, 15). We assume a

Hookean energy expression for all creases and calculate the dimensionless energy  $u$  as a function of the folding configuration (Fig. 2E and fig. S5) (see supplementary materials for details). We observe that the energy landscape has two distinct regions, each with its own local minimum (Fig. 2E, points I and II), that are connected at a single point corresponding to a fully unfolded unit cell where  $\phi = \varepsilon = 180^\circ$ . For materials with a finite stretching modulus, this connecting point widens along the  $\phi$  axis and allows for otherwise forbidden stretching-enabled transitions. Because the stretching modulus is proportional to sheet thickness (23), the energy required to transition between states is a tunable design feature. Thus, while PTDs are introduced reversibly, their stability to mechanical perturbations is controlled by the competition between the material's bending and stretching energy scales.

The mechanical consequences of a PTD were determined by folding laser-cut structures from 24-lb paper with  $s^2$  unit cells, where  $s$  was varied from 3 to 8 and  $\alpha$  was fixed at  $60^\circ$ . A centrally located defect was introduced by hand, and the compressive modulus  $K_y^{\text{defect}}(\varepsilon)$  was measured as a function of defect density  $n = 1/s^2$  (see supplementary materials for details). Normalizing these data by the modulus of a defect-free lattice,  $K_y^{\text{normal}}(\varepsilon)$ , revealed a divergence in stiffness as a function of compression limited only by tearing of the sheet at the highest strains (Fig. 2F and fig. S4B). This divergence arises from a violation of Maekawa's theorem, which requires the number of mountain folds minus the number of valley folds at every vertex to be  $\pm 2$  for a structure to fold flat (24). By linking enhanced mechanical stiffness to violations of a canonical paper-folding theorem, these data experimentally demonstrate how geometric constraints in origami-based design can dominate bulk material properties.

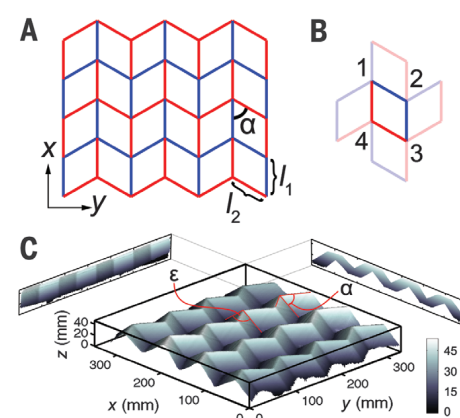


**Fig. 1. Schematic and 3D reconstruction of the Miura-ori with definition of important geometric parameters.** (A) The Miura-ori crease pattern on a flat sheet is depicted with alternating mountain (red) and valley (blue) folds. (B) Each facet is bounded by four vertices labeled 1 through 4. (C) An experimentally recorded 3D image of a 4 by 4 laser-cut Miura-ori with two in-plane projections shows the folded structure at equilibrium. The color bar gives height in mm.

<sup>1</sup>Physics Department, Cornell University, Ithaca, NY 14853, USA. <sup>2</sup>Department of Physics, University of Massachusetts, Amherst, MA 01003, USA. <sup>3</sup>Department of Polymer Science and Engineering, University of Massachusetts, Amherst, MA 01003, USA. <sup>4</sup>Department of Mathematics, Western New England University, Springfield, MA 01119, USA.  
\*Corresponding author. E-mail: JLS533@cornell.edu

Nevertheless, such constraints are still malleable; the value of  $\epsilon$  where  $K_y^{\text{defect}}$  increases is shifted simply by varying  $n$ . Thus, PTDs make attractive elements for metamaterial design because the onset and strength of  $K_y^{\text{defect}}$  are rationally tunable, and moreover, these “mechanical pixels” can be activated on demand to vary the bulk compressive properties. Although PTDs were manually

introduced here, soft robotics-based technology (25), microelectromechanical systems actuator arrays (26), or even thermal fluctuations (27), provide alternative avenues to introduce and remove PTDs.

To understand both the density dependence and compression dependence of the Miura-ori with a PTD, we analytically calculated the in-

trinsic PTD compressive modulus,  $K_y^{\text{PTD}}$  (see supplementary materials for details). This was found by noting that the stress a PTD exerts is proportional to its extension relative to the neighboring undefected unit cells. At low defect densities for a lattice of arbitrary size, the compressive modulus of a lattice with a PTD can be expressed in a dipole expansion,  $K_y^{\text{defect}} = K_y^{\text{normal}} + nK_y^{\text{PTD}}$ , where  $K_y^{\text{PTD}}$

**Fig. 2. Experimental data showing spatial confinement of a PTD and combined experimental/theoretical data for PTD mechanics.**

(A) 3D reconstruction of a Miura-ori with a centrally located PTD (red facets). The color bar is height in mm. (B) Photograph of a single vertex shows that it is mechanically stable in isolation, as is a PTD (C). (D) Mean curvature of 3D scan from (A) shows a modified crease pattern in the presence of a PTD. The color bar is in units of  $\text{mm}^{-1}$ . Overlapping vertex position of same lattice without a PTD (black dots) shows that the PTD is highly localized and causes minimal distortion in finite-sized lattices. (E) Theoretical energy diagram of a single vertex has two energy minima corresponding to a (I) normal and (II) PTD state. Arrows indicate direct pathway to PTD formation. The white background is geometrically forbidden. (F) Experimentally measured modulus as a function of compression  $\epsilon$  and PTD density  $n$ . (Inset) Data follow a theoretically predicted scaling collapse (black line).

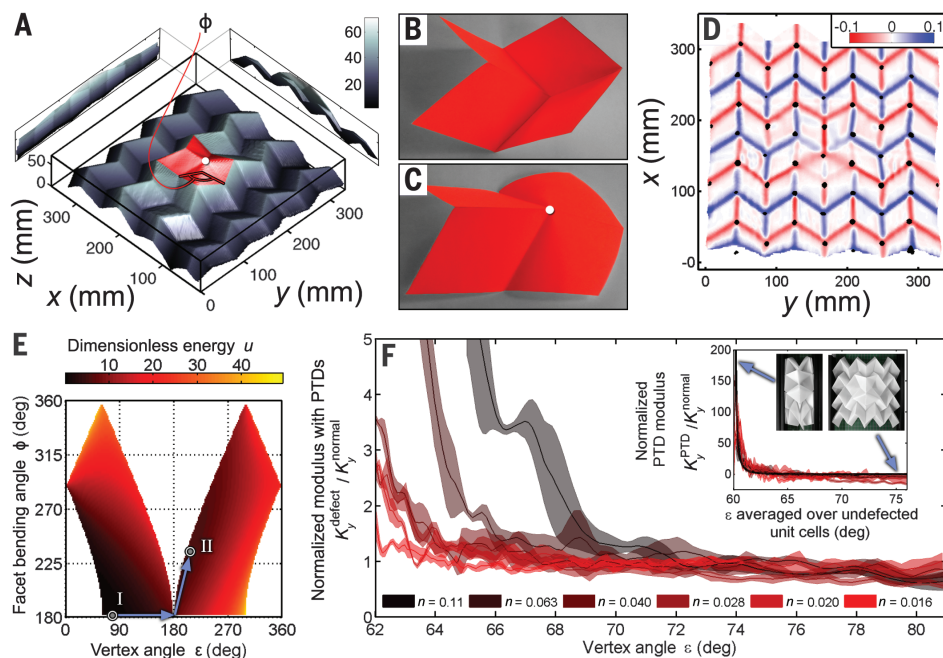
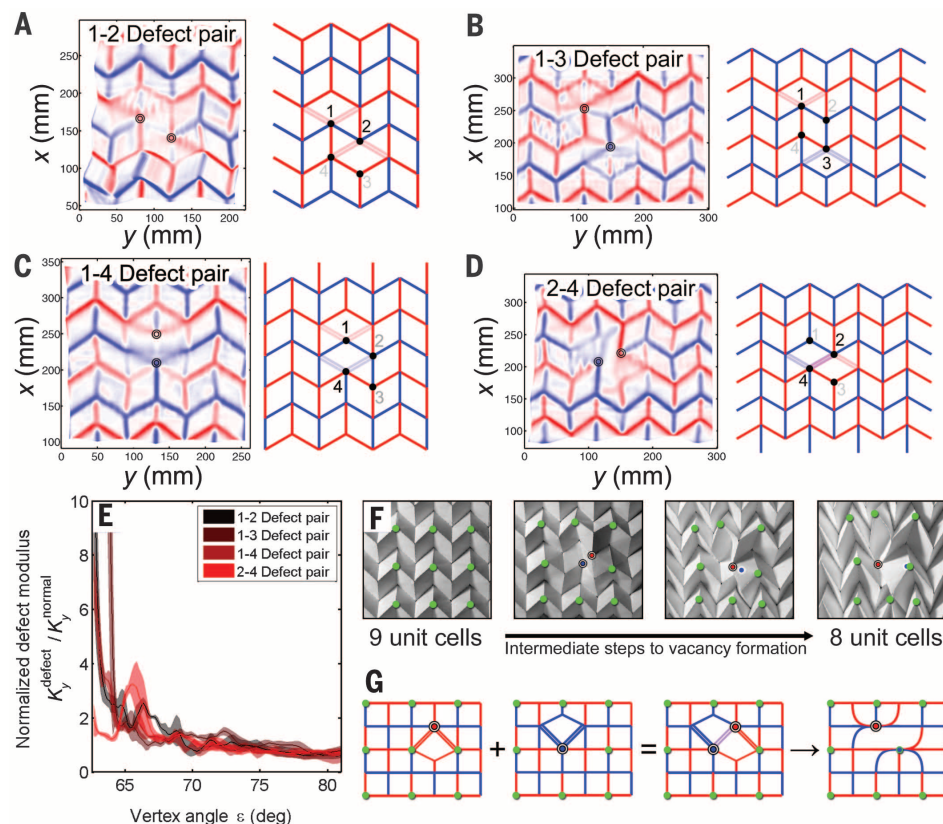


**Fig. 3. Experimental data of two interacting PTDs.**

Mean curvature maps of (A) 1-2, (B) 1-3, (C) 1-4, and (D) 2-4 defect-pair configuration. The color maps saturate at  $\pm 1 \text{ mm}^{-1}$ . Schematic diagrams show defect placement (dots) and facet bending (double lines). (E) Normalized compressive modulus of lattice with each defect-pair configuration shows that three combinations lead to divergent stiffness, whereas the 2-4 configuration does not. (F) Labeling nine unit cells with green dots and examining their location as  $\epsilon$  decreases demonstrates how the 2-4 defect configuration (red and blue dots) leads to a lattice vacancy. (G) Schematic diagrams show where defects interact and the resultant crease pattern.





is a function of  $\epsilon$  averaged over the nondefected unit cells. This expression is valid when  $n \ll 1$  and holds for a lattice with multiple defects as long as defect interactions can be neglected. Moreover, it suggests a data collapse with a one-parameter fit to the theory that sets the scale of  $K_y^{\text{PTD}}$ . Indeed, we find such a collapse (Fig. 2F, inset) and excellent agreement with the analytic expression (Fig. 2F, inset, black line), demonstrating that the contribution of PTDs to the modulus at low densities is linearly additive. This mechanical response is useful for design purposes because it offers great simplicity in predicting the compressive modulus of a Miura-ori with PTDs.

With increasing density, PTD interactions become important, particularly when pairs of defects are on adjacent vertices. There are four unique defect pairs: 1-2, 1-3, 1-4, and 2-4, with the other combinations degenerate by symmetry (Fig. 1B and Fig. 3, A to D). Folding 4 by 4 lattices with  $\alpha = 60^\circ$ , we measured  $K_y^{\text{defect}}(\epsilon)$  in the presence of the four unique defect pair configurations. Normalizing by the defect-free modulus, we found that the 1-2, 1-3, and 1-4 defect pair moduli diverge as the compression increases (Fig. 3E and movie S3).

Surprisingly, the 2-4 configuration has qualitatively different compressive behavior: The modulus first increases during compression similar to other defect-pair configurations, but then decreases, and finally reduces to a near defect-free value at

the highest compressions (Fig. 3E). Effectively, the respective mechanical signatures of the 2-4 defect pair are annihilated during compression. To illustrate the folding sequence, we mark the centers of a 3 by 3 sublattice (Fig. 3F, green dots), as well as the location of each defect (Fig. 3F, red and blue dots). During compression, facets near the defect sites are increasingly bent as  $\epsilon$  decreases, leading to the enhanced stiffness. This enhancement progresses until defect site 4 folds under defect site 2 and all four creases on the facet flip. The defect sites then collapse onto, and overlap with, nearby vertices (Fig. 3F) so that the center lattice site is tucked underneath the adjacent unit cell (movie S4). Visually inspecting the 2-4 defect pair reveals a notable consequence: This defect configuration generates a lattice vacancy analogous to those seen in crystallographic systems (28).

To understand why the 2-4 defect pair is special, we compute the mean curvature from 3D scans of laser-cut sheets (Fig. 3, A to D). Comparing the four cases, we see that the 2-4 pair is distinguished by overlapping bending facets of equal magnitude but opposite sign, as quantified by the zero mean curvature on the central facet. This cancellation is possible due to the symmetry of the 2-4 placement and the reversibility of a PTD's deformation of a Miura-ori lattice. When fully compressed, the defect-modified crease pattern is compatible with Maekawa's theorem for flat-foldability (Fig. 3G and fig. S6), and hence

the compressive modulus is restored to a nearly defect-free value.

Recognizing the 2-4 defect pair as a lattice vacancy immediately suggests that the Miura-ori supports other types of crystallographic defects (23). For example, a column of vacancies forms an edge dislocation (Fig. 4A), and several adjacent edge dislocations form a grain boundary (Fig. 4B). In both cases, these reconfigurations of the lattice are flat-foldable; however, non-flat-foldable configurations are possible as well. For example, a column of PTDs on alternating vertices generates a hinge-like structure that allows the Miura-ori to easily bend out of plane (Fig. 4C). Conversely, a column of PTDs on consecutive vertices forms a corrugated structure that is highly resistive to out-of-plane bending (Fig. 4D). In fact, rationally introducing patterns of defects as design elements swiftly generates a vast library of origami-inspired mechanical metamaterials. To demonstrate in experiments the ability to place these features without permanently altering the crease pattern, we programmed eight configurations into a single sheet with 13 consecutive reprogramming events (Fig. 4E) (29). Measuring  $K_y^{\text{programmed}}$  for a lattice compressed to 68% of its initial width, we found that once calibrated (dashed lines), we are able to predict and realize target modulus values when defect concentration and interactions are altered (solid black lines). This capability to dynamically reprogram elastic properties illustrates the power of our approach.

Extending programmable metamaterial design principles to self-folding robotic (25, 30-33) and polymer (8-10, 13, 16) systems opens the door to engineering devices that can alter their mechanical functionality on demand. Such enhanced capabilities would move these transforming systems whose function depends on configuration from what was merely science fiction in past decades to real-world applications.

## REFERENCES AND NOTES

1. M. Wegener, *Science* **342**, 939-940 (2013).
2. Y. Liu, X. Zhang, *Chem. Soc. Rev.* **40**, 2494-2507 (2011).
3. J.-H. Lee, J. P. Singer, E. L. Thomas, *Adv. Mater.* **24**, 4782-4810 (2012).
4. A. Q. Liu, W. M. Zhu, D. P. Tsai, N. I. Zheludev, *J. Opt.* **14**, 114009 (2012).
5. M. Kadic, T. Bückmann, R. Schittny, M. Wegener, *Rep. Prog. Phys.* **76**, 126501 (2013).
6. C. Py et al., *Phys. Rev. Lett.* **98**, 156103 (2007).
7. A. Papa, S. Pellegrino, *J. Spacecr. Rockets* **45**, 10-18 (2008).
8. N. Bassik, G. M. Stern, D. H. Gracias, *Appl. Phys. Lett.* **95**, 091901 (2009).
9. J. Kim, J. A. Hanna, M. Byun, C. D. Santangelo, R. C. Hayward, *Science* **335**, 1201-1205 (2012).
10. J. Kim, J. A. Hanna, R. C. Hayward, C. D. Santangelo, *Soft Matter* **8**, 2375 (2012).
11. M. A. Dias, L. H. Dudte, L. Mahadevan, C. D. Santangelo, *Phys. Rev. Lett.* **109**, 114301 (2012).
12. M. A. Dias, C. D. Santangelo, *EPL* **100**, 54005 (2012).
13. J. Ryu et al., *Appl. Phys. Lett.* **100**, 161908 (2012).
14. M. Schenk, S. D. Guest, *Proc. Natl. Acad. Sci. U.S.A.* **110**, 3276-3281 (2013).
15. Z. Y. Wei, Z. V. Guo, L. Dudte, H. Y. Liang, L. Mahadevan, *Phys. Rev. Lett.* **110**, 215501 (2013).
16. M. Jamal et al., *Adv. Healthcare Mater.* **2**, 1142-1150 (2013).
17. K. Miura, *Inst. Space Astronaut. Sci. Rep.* **618**, 1-9 (1985).
18. L. Mahadevan, S. Rica, *Science* **307**, 1740 (2005).
19. M. Ben Amar, F. Jia, *Proc. Natl. Acad. Sci. U.S.A.* **110**, 10525-10530 (2013).

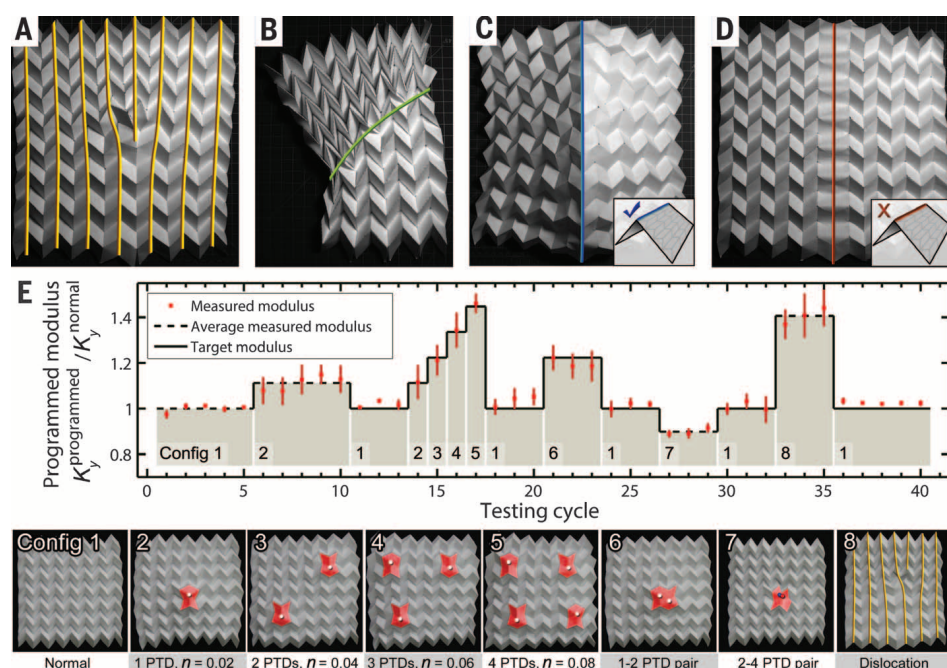


**Fig. 4. Photographs of a Miura-ori with complex defect structures and experimental demonstration of a programmable modulus.** (A) Column of lattice vacancies (2-4 pairs) generate an edge dislocation. (B) Columns of edge dislocations generate a grain boundary. (C) Column of PTDs on alternating vertices generates a hinge-like structure. (D) Column of PTDs on consecutive vertices generates a rigid corrugated structure. (E) Experimentally measured modulus over 40 testing cycles with eight distinct configurations and 13 reprogramming events. Dashed lines are averages of measured values (red dots) and are used to generate predicted target values of the modulus (solid lines). Data demonstrate reversibility and programmability. Photographs below the plot show corresponding structure, with PTDs highlighted as a guide for the eye.

20. A. E. Shyer *et al.*, *Science* **342**, 212–218 (2013).
21. E. Abbena, S. Salamon, A. Gray, *Modern Differential Geometry of Curves and Surfaces with Mathematica* (CRC Press, Boca Raton, FL, 2006).
22. T. D. Gatzke, C. M. Grimm, *Int. J. Shape Model.* **12**, 1–28 (2006).
23. L. D. Landau, E. M. Lifshitz, *Landau and Lifshitz Course of Theoretical Physics, Vol. 7: Theory of Elasticity* (Butterworth Heinemann, New Delhi, ed. 3, 1986).
24. M. Bern, B. Hayes, *Proceedings of the Symposium on Discrete Algorithms* **7**, 175–183 (1996).
25. E. Steltz, A. Mozeika, N. Rodenberg, E. Brown, H. M. Jaeger, IEEE/RSJ International Conference on Intelligent Robots and Systems (IROS), 10 to 15 October 2009, St. Louis, MO (IEEE, 2009), pp. 5672–5677.
26. T. Fukushima, S. Hata, A. Shimokohbe, *J. Microelectromech. Syst.* **14**, 243–253 (2005).
27. T. W. Ebbesen, H. Hiura, *Adv. Mater.* **7**, 582–586 (1995).
28. P. M. Chaikin, T. C. Lubensky, *Principles of Condensed Matter Physics* (Cambridge Univ. Press, Cambridge, ed. 1, 2000).
29. T. Toffoli, N. Margolus, *Physica D* **47**, 263–272 (1991).
30. E. Hawkes *et al.*, *Proc. Natl. Acad. Sci. U.S.A.* **107**, 12441–12445 (2010).
31. S. M. Felton, M. T. Tolley, C. D. Onal, D. Rus, R. J. Wood, 2013 IEEE International Conference on Robotics and Automation (ICRA), 6 to 10 May 2013, Karlsruhe, Germany (IEEE, 2013), pp. 277–282.
32. C. D. Onal, R. J. Wood, D. Rus, 2011 IEEE International Conference on Robotics and Automation (ICRA), 9 to 13 May 2011, Shanghai (IEEE, 2011), pp. 4608–4613.
33. B. An, N. Benbernou, E. D. Demaine, D. Rus, *Robotica* **29**, 87–102 (2011).

## ACKNOWLEDGMENTS

The authors thank R. J. Lang, B. Johnson, B. Parker, and M. Schneider for artistic inspiration, as well as N. Bende, J. Na,

M. Byun, and the Cohen laboratory for useful discussions. We also thank F. Parish for assistance with the laser cutter, as well as X. Cheng, N. Lin, and B. Leahy for their design and construction efforts on the 3D laser scanner hardware. This work was funded by the National Science Foundation through award EFR1 ODISEI-1240441 and the Graduate Research Fellowship Program, which funded J.L.S.

## SUPPLEMENTARY MATERIALS

www.sciencemag.org/content/345/6197/647/suppl/DC1

Materials and Methods

Supplementary Text

Figs. S1 to S6

Movies S1 to S4

Reference (34)

3 March 2014; accepted 19 June 2014

10.1126/science.1252876

## EARLY SOLAR SYSTEM

# Stellar origin of the $^{182}\text{Hf}$ cosmochronometer and the presolar history of solar system matter

Maria Lugaro,<sup>1\*</sup> Alexander Heger,<sup>1,2,3</sup> Dean Osrin,<sup>1</sup> Stephane Goriely,<sup>4</sup> Kai Zuber,<sup>5</sup> Amanda I. Karakas,<sup>6,7</sup> Brad K. Gibson,<sup>8,9,10</sup> Carolyn L. Doherty,<sup>1</sup> John C. Lattanzio,<sup>1</sup> Ulrich Ott<sup>11</sup>

Among the short-lived radioactive nuclei inferred to be present in the early solar system via meteoritic analyses, there are several heavier than iron whose stellar origin has been poorly understood. In particular, the abundances inferred for  $^{182}\text{Hf}$  (half-life = 8.9 million years) and  $^{129}\text{I}$  (half-life = 15.7 million years) are in disagreement with each other if both nuclei are produced by the rapid neutron-capture process. Here, we demonstrate that contrary to previous assumption, the slow neutron-capture process in asymptotic giant branch stars produces  $^{182}\text{Hf}$ . This has allowed us to date the last rapid and slow neutron-capture events that contaminated the solar system material at ~100 million years and ~30 million years, respectively, before the formation of the Sun.

**R**adioactivity is a powerful clock for the measurement of cosmic times. It has provided us the age of Earth (1), the ages of old stars in the halo of our Galaxy (2), the age of the solar system (3, 4), and a detailed chro-

nometry of planetary growth in the early solar system (5). The exploitation of radioactivity to measure time scales related to the presolar history of the solar system material, however, so far has been hindered by our poor knowledge of how radioactive nuclei are produced by stars. Of particular interest are three radioactive isotopes heavier than iron:  $^{107}\text{Pd}$ ,  $^{129}\text{I}$ , and  $^{182}\text{Hf}$ , with half-lives of 6.5 million years (My), 15.7 My, and 8.9 My, respectively, and initial abundances (relative to a stable isotope of the same element) in the early solar system of  $^{107}\text{Pd}/^{108}\text{Pd} = 5.9 \pm 2.2 \times 10^{-5}$  (6),  $^{129}\text{I}/^{127}\text{I} = 1.19 \pm 0.20 \times 10^{-4}$  (7), and  $^{182}\text{Hf}/^{180}\text{Hf} = 9.72 \pm 0.44 \times 10^{-5}$  (8). The current paradigm is that  $^{129}\text{I}$  and  $^{182}\text{Hf}$  are mostly produced by rapid neutron captures (the  $r$  process), in which the neutron density is relatively high ( $>10^{20} \text{ cm}^{-3}$ ), resulting in much shorter time scales for neutron capture than for  $\beta$ -decay (9). The  $r$  process is believed to occur in neutron star mergers or peculiar supernova environments (10, 11). In addition to the  $r$  process,  $^{107}\text{Pd}$  is also produced by slow neutron captures (the  $s$  process), in which the neutron density is relatively low ( $<10^{13} \text{ cm}^{-3}$ ), resulting in shorter time scales for  $\beta$ -decay than

for neutron capture, the details depending on the  $\beta$ -decay rate of each unstable isotope and the local neutron density (9). The main site of production of the  $s$  process elements from Sr to Pb in the Galaxy is in asymptotic giant branch (AGB) stars (12), the final evolutionary phase of stars with initial mass lower than ~10 solar masses ( $M_{\odot}$ ). Models of the  $s$  process in AGB stars have predicted marginal production of  $^{182}\text{Hf}$  (13) because the  $\beta$ -decay rate of the unstable isotope  $^{181}\text{Hf}$  at stellar temperatures was estimated to be much faster (14) than the rate of neutron capture leading to the production of  $^{182}\text{Hf}$  (Fig. 1).

Uniform production of  $^{182}\text{Hf}$  and  $^{129}\text{I}$  by the  $r$  process in the Galaxy, however, cannot self-consistently explain their meteoritic abundances (15–17). The simplest equation for uniform production (UP) of the abundance of a radioactive isotope in the Galaxy, relative to a stable isotope of the same element produced by the same process, is given by

$$\frac{N_{\text{radio}}}{N_{\text{stable}}} = \frac{P_{\text{radio}}}{P_{\text{stable}}} \times \frac{\tau}{T} \quad (1)$$

where  $N_{\text{radio}}$  and  $N_{\text{stable}}$  are the abundances of the radioactive and stable isotopes, respectively;  $P_{\text{radio}}/P_{\text{stable}}$  is the ratio of their stellar production rates;  $\tau$  is the mean lifetime of the radioactive isotope; and  $T \sim 10^{10}$  years is the time scale of the evolution of the Galaxy. Some time during its presolar history, the solar system matter became isolated from the interstellar medium characterized by UP abundance ratios. Assuming that both  $^{129}\text{I}$  and  $^{182}\text{Hf}$  are primarily produced by the  $r$  process, one obtains inconsistent isolation times using  $^{129}\text{I}/^{127}\text{I}$  or  $^{182}\text{Hf}/^{180}\text{Hf}$ : 72 My or 15 My, respectively, before the solar system formation (17). This conundrum led Wasserburg *et al.* (15) to hypothesize the existence of two types of  $r$  process events. Another proposed solution is that the  $^{107}\text{Pd}$ ,  $^{129}\text{I}$ , and  $^{182}\text{Hf}$  present in the early solar system were produced by the neutron burst that occurs during core-collapse supernovae (18–20). This does not result in elemental production, but the relative isotopic abundances of each element are strongly modified because of relatively high neutron densities with values between those of the  $s$  and  $r$  processes.

<sup>1</sup>Monash Centre for Astrophysics (MoCA), Monash University, Clayton VIC 3800, Australia. <sup>2</sup>Joint Institute for Nuclear Astrophysics (JINA), 225 Nieuwland Science Hall, Department of Physics, University of Notre Dame, Notre Dame, IN 46556-5670, USA. <sup>3</sup>School of Physics and Astronomy, University of Minnesota, Minneapolis, MN 55455, USA. <sup>4</sup>Institut d'Astronomie et d'Astrophysique, Université Libre de Bruxelles, CP-226, 1050, Brussels, Belgium. <sup>5</sup>Institut für Kern- und Teilchenphysik, Technische Universität Dresden, 01069 Dresden, Germany. <sup>6</sup>Research School of Astronomy and Astrophysics, Australian National University, Canberra, ACT 2611, Australia. <sup>7</sup>Kavli Institute for the Physics and Mathematics of the Universe (WPI), Todai Institutes for Advanced Study, the University of Tokyo, Japan. <sup>8</sup>Jeremiah Horrocks Institute, University of Central Lancashire, Preston, PR1 2HE, UK. <sup>9</sup>Institute for Computational Astrophysics, Department of Astronomy and Physics, Saint Mary's University, Halifax, NS, B3H 3C3, Canada. <sup>10</sup>UK Network for Bridging Disciplines of Galactic Chemical Evolution (BRIDGCE), www.astro.keele.ac.uk/bridgce, UK. <sup>11</sup>Faculty of Natural Science, University of West Hungary, 9700 Szombathely, Hungary.

\*Corresponding author. E-mail: maria.lugaro@monash.edu



## Supplementary Materials for

### **Using origami design principles to fold reprogrammable mechanical metamaterials**

Jesse L. Silverberg,\* Arthur A. Evans, Lauren McLeod,  
Ryan C. Hayward, Thomas Hull, Christian D. Santangelo, Itai Cohen

\*Corresponding author. E-mail: [JLS533@cornell.edu](mailto:JLS533@cornell.edu)

Published 8 August 2014, *Science* **345**, 647 (2014)  
DOI: 10.1126/science.1252876

#### **This PDF file includes:**

Materials and Methods  
Supplementary Text  
Figs. S1 to S6  
Reference

**Other Supplementary Material for this manuscript includes the following:**  
(available at [www.sciencemag.org/cgi/content/full/345/6197/647/DC1](http://www.sciencemag.org/cgi/content/full/345/6197/647/DC1))

Movies S1 to S4

# Materials and Methods

## Sample fabrication

Origami samples for experimental mechanical testing and 3 dimensional (3D) imaging were first prototyped with hand-folded sheets. While easy to generate, these samples have the disadvantage of including additional “pre-creases” that are not used in the final structure, but nonetheless are necessary to guide crease placement. The presence of pre-creases is problematic as they add additional degrees of freedom. Thus, we employed a laser-cutter to pattern only the essential creases (Fig. 1(A)) into a variety of materials including: 9, 17, 24, 28, 32, 36, 40, 48, 53, and 65 lb paper, 45 and 120 lb cardstock, and 0.001, 0.002, and 0.003 mm thick mylar. Patterns of continuous lines were first designed in Adobe Illustrator with a specified  $\ell_1$ ,  $\ell_2$ , and  $\alpha$ , and then converted to a generic vector format for laser cutting. At the lowest power settings, the laser scored sheets, creating a joint that was easily folded into a crease. However, scores frequently tear and exhibit anisotropic bending properties. Thus, we replaced the continuous line patterns with dash-and-gap perforations. These samples had durable creases that exhibited indistinguishable folding stiffness whether mountain or valley. Geometries were designed with  $\ell_1 = \ell_2 \equiv \ell = 25.4$  mm. The angle  $\alpha$  was varied from  $35^\circ$  to  $65^\circ$  in  $5^\circ$  increments. The number of unit cells was varied according to the experiment. Laser power was set to 45% max output, with a dwell time of 45%.

## Laser scanner

To study the 3D structure of the Miura-ori, we constructed a custom laser scanner. This apparatus consisted of a laser sheet light source and digital camera that were mounted a fixed distance apart, but able to translate vertically along a guided rail track. The laser/camera mount was driven by a digitally controlled electric motor and set to trans-

late at a fixed rate. For each scan, an origami structure was oriented in front of the apparatus to prevent and/or minimize self-shadowing. The laser/camera was then translated vertically, and video was acquired from the camera at 7.5 frames per second in an otherwise unlit room. Experimenting with various materials, we found opaque mylar provided high-quality reconstructions due to the light scattering properties of its surface. Comparing Mylar and paper scan data revealed mutually consistent 3D structure.

Optical aberrations from a camera’s lens produces distortion of 2D images. To correct for this, camera calibration software written for MATLAB (Camera Calibration Toolbox, J.-Y. Bouguet) was used in conjunction with a  $46 \times 61 \text{ cm}^2$  checkerboard pattern to generate a lens-specific correction factor. These correction factors were applied to raw camera data prior to the 3D reconstruction in MATLAB. To generate 3D topographic maps, our custom code tracks the reflected laser sheet light and uses the known apparatus geometry to calculate surface topography in a given plane. Translating the laser/camera plane then provides a 3D map of the origami surface with a voxel resolution of  $0.4 \times 0.4 \times 0.96 \text{ mm}^3$ .

With the surface digitized and reconstructed, we were able to locally measure the curvature (34) using a polynomial approximation method known as a Monge patch (22). In this approach, a local patch of the measured surface approximately  $\ell/10 \times \ell/10$  in size was selected. These dimensions were chosen as they were found to smooth noise associated with the discreteness of the surface, while optimizing spatial resolution. The patch was then fit to a polynomial of the form  $z(x, y) = c_0 + c_x x + c_y y + c_{xx} x^2 + c_{yy} y^2 + c_{xy} xy$ , where the coordinate system for the fit coincides with the center of the patch. From the best-fit values of the polynomial coefficients, the mean curvature was calculated using

$$H = \frac{(1 + c_y^2)c_{xx} - 2c_x c_y c_{xy} + (1 + c_x^2)c_{yy}}{2(1 + c_x^2 + c_y^2)^{3/2}}. \quad (1)$$



This procedure was iterated as the patch center point was rastered over the entire  $xy$  surface at pixel resolution. In a similar fashion, spatial maps of the Gaussian curvature were calculated using

$$K = \frac{c_{xx}c_{yy} - c_{xy}^2}{(1 + c_x^2 + c_y^2)^2}, \quad (2)$$

which while readily able to identify vertex locations, did not identify stretching associated with facet bending.

## Compression stage

A custom built compression stage was developed to measure the mechanical properties of origami structures. This consisted of two smoothly polished aluminum compression plates, one mounted to a Haydon-Kerk linear translation stage (PCM4826X-K IDEA stepper motor), and the other to a Loadstar force measurement sensor (3 kg RSP1 load cell with DI-1000U interface). In a typical experiment, the compression plate separation and load cell force data was simultaneously recorded by a single custom MATLAB program. Smooth lucite panels were mounted underneath the compression plates to provide a low-friction surface for the origami structures to move on during compression. To further reduce friction, one side of the lattice was slightly elevated with a small piece of adhesive tape that simultaneously served to reduce contact area with the lucite panels, while also leaving the folded structure able to freely deform during compression.

To determine the origami lattice compressive modulus, a compression routine was developed that operated in the following manner. Initially, the plate separation was set to a value slightly larger ( $\approx 5\%$ ) than the width of the origami lattice (Fig. S1, point 1). The compression cycle began, and the lattice was compressed 6.35 mm, during which the load and plate separation were recorded. The system paused for two seconds at the maximum compression (Fig. S1, point 2), reversed direction, and returned the plates to

their initial separation. During decompression, the compression plate lost contact with the origami lattice (Fig. S1, point 3). After one compression cycle, we found the origami lattice width was reduced compared to its original state (Fig. S1, compare points 1 and 4), indicating plastic deformation of the mountain and valley creases. The load-unload cycle was repeated 8 times. When the load-displacement curves were superimposed, we found the first cycle was noticeably different from the remaining cycles, while the rest were nearly indistinguishable (Fig. S1, red lines show runs 2 through 8). We then averaged the load-displacement data for runs 3 through 8 producing a single load-displacement curve associated with the compression amplitude (Fig. S1, black lines). The compression amplitude was then increased by 6.35 mm, and the 8 load-unload cycles were repeated, producing an averaged load-displacement curve for the new amplitude (Fig. S1, points 4, 5, 6, 7). This process was iterated until the lattice was compressed to a width of 12.7 mm, yielding load-displacement curves with amplitudes evenly spaced by 6.35 mm.

For mechanical testing, we found 24 lb paper was both representative and easiest to work with. For example, the mechanical behavior reported in the main text concerning PTDs and their interactions was qualitatively consistent across materials, though the compressive moduli magnitude  $K_y$  depended on the material used.

In the main text, it was preferable to express the Miura-ori configuration in terms of the vertex angle  $\varepsilon$  in order to have a single-valued representation of the energy diagram for PTDs. However, pre-existing theory (15), which did not consider the existence of PTDs, has been expressed in terms of a dihedral angles  $\theta$  (Fig. S2(A)). Thus, to make comparisons to existing theory for non-defected lattices we express our results in terms of  $\theta$ , which relates to  $\varepsilon$  by

$$\sin\left(\frac{\varepsilon}{2}\right) = \frac{\cos(\alpha)}{[1 - \sin^2(\alpha) \sin^2(\theta/2)]^{1/2}}. \quad (3)$$

To determine the compressive modulus, we first transformed the plate separation data to the lattice averaged dihedral angle  $\theta$ . For a given instantaneous compression, this was found by dividing the Miura-ori width by the number of unit cells across, and calculating  $\theta$  for the corresponding width of an ideal unit cell (15). Differentiating each curve to find  $K_y(\theta)$ , we found the modulus at a given  $\theta$  was largely insensitive to the equilibrium  $\theta_0$  as well as the maximum compression amplitude. This finding was fortuitous, as it allowed us to simply average the values of  $K_y(\theta)$  across compression amplitudes for a given  $\theta$ . Small-amplitude measurements of the modulus were extracted from data where the Miura-ori's compression was less than 6.35 mm.

## Supplementary Text

### Compressive modulus

To experimentally determine the range of mechanical properties exhibited by the Miura-ori available for metamaterial design, samples were fabricated and tested in our compression apparatus. Under loading, the equilibrium value of the dihedral angle,  $\theta_0$ , varies due to plastic deformation at the crease. Thus, to measure the mechanical properties of the Miura-ori, we systematically vary  $\theta_0$  and make small amplitude measurements of the uniaxial compressive modulus  $K_y(\theta)$  (Fig. S2(B) dots). This measurement was repeated for samples fabricated with each value of  $\alpha$  (Fig. S2(B) different colors). Data sets were then fit to a theoretical model based on the properties of a single Miura-ori unit cell where Hookean elasticity was assumed for each crease (15) (Fig. S2(B) solid lines). We found excellent agreement for  $\alpha \geq 45^\circ$ , and slightly larger deviations in the remaining two samples. From the fits, we extracted the elastic spring constant characterizing a crease in the origami structure  $k_0$ , and compared this value to a measurement made on a sheet with only a single fold (Fig. S2(B) inset; solid line). We found the fitted and measured values

of  $k_0$  agree to better than a factor of 2. Such deviations from the theoretical prediction may arise from heterogeneous deformations that occur in lattices made with more than 1 unit cell, as well as facet bending, which was not accounted for in the single-unit-cell theory. Extending these measurements beyond the validity of the small strain theory, we measured  $K_y(\theta)$  over a larger range of compression (Fig. S2(B) shaded bands). For our samples, these data show a factor of  $\approx 2$  difference between the least and most compliant portions of the modulus for fixed  $\alpha$ , and a factor of  $\approx 3$  between samples with different  $\alpha$ .

## Poisson's ratio

Miura-ori structures with  $\alpha$  varied from  $35^\circ$  to  $65^\circ$  were marked with colored dots on the vertices and compressed using the same set-up as that for the force measurements. 1080p videos of the compression were filmed from overhead using a digital camera at 7.5 fps (Canon Powershot). The colored markings were tracked using custom software written in MATLAB, and the lengths  $L$ , widths  $W$ , and dihedral angle  $\theta$  of all the unit cells except those along the border were calculated by measuring the distances between pairs of valley vertices within a unit cell.  $L$ ,  $W$ , and  $\theta$  were sampled every three frames, and a moving average was computed to produce a smooth measurement of  $L(W)$ .  $dL/dW$  at each frame was defined as the derivative of the quadratic function centered at that frame fit to the values  $L(W)$  for 13 frames. The Poisson's ratio  $\nu$  was then calculated using

$$\nu = -\frac{W}{L} \frac{dL}{dW} \quad (4)$$

and compared to a theoretical prediction (15):

$$\nu = 1 - \left[ \frac{1}{\sin(\alpha) \sin(\theta/2)} \right]. \quad (5)$$

The comparison between experiment and theory (Fig. S3) shows excellent agreement

within measurement errors, and confirmed the wide range of negative Poisson ratio possible within the Miura-ori.

## Lattice size effects and PTD localization

When examining the geometry of samples with a PTD, we found the induced lattice distortions rapidly decayed from the defect center. To study the extent of this distortion, we superimposed mean curvature maps from normal lattices with those taken from a lattice hosting 1 PTD (Fig. S4(A)). Comparing these data sets, we noted vertices immediately adjacent to the PTD were marginally displaced and that the effect rapidly decayed within a distance of one unit cell.

To check for finite-size effects on mechanical measurements, we also studied how the compressive modulus  $K_y$  varied with lattice size for fixed  $\alpha$ . We found  $K_y$  had a 1.2 to 2-fold increase between the  $3 \times 3$  and  $8 \times 8$  lattices (Fig. S4(B)). These differences were most pronounced at the lowest compressions and small compared to the increase in  $K_y$  at high compression when a PTD is introduced. Thus, these mechanical and geometric findings indicate our main results regarding PTD stiffness and interactions are generally insensitive to finite-size effects.

## Details of Theoretical Calculations

**Spherical geometry** Traditional Miura-ori vertices consist of four creases (Fig. S5(A)). To include the experimentally observed facet bending that occurs during formation of a PTD, we require two additional creases whose equilibrium angle is  $\pi$ . In general, equilibrium crease angles are determined by the plastic deformation induced during folding; however, they are also related by geometric constraints. Assuming symmetric deformations of the unit cell, we choose  $\varepsilon$  and  $\phi$  to specify the other fold angles (Fig. S5(B)).

Spherical trigonometry then leads to the following intermediate relationships that determine the angles  $\eta, B_+, B_-, A_+, A_-$ :

$$\cos \eta = \sin^2 \frac{\alpha}{2} + \cos^2 \frac{\alpha}{2} \cos \phi, \quad (6)$$

$$\cos B_+ = \tan \frac{\alpha}{2} \sqrt{\frac{1 - \cos \eta}{1 + \cos \eta}}, \quad (7)$$

$$\cos B_- = \frac{\cos \varepsilon - \cos \alpha \cos \eta}{\sin \alpha \sin \eta}, \quad (8)$$

$$\cos A_+ = \cos B_+, \quad (9)$$

$$\cos A_- = \frac{\cos \alpha - \cos \varepsilon \cos \eta}{\sin \varepsilon \sin \eta}, \quad (10)$$

$$\cos \frac{\theta_-}{2} = \frac{\cos \eta - \cos \varepsilon \cos \alpha}{\sin \varepsilon \sin \alpha}, \quad (11)$$

where all angles are defined on the spherical polygon (Fig. S5(A,B)). With these relations, we find the fold angles obey:

$$\theta_+ = A_+ + A_-, \quad (12)$$

$$\theta_- = 2 \cos^{-1} \left[ \frac{\cos \eta - \cos \varepsilon \cos \alpha}{\sin \varepsilon \sin \alpha} \right], \quad (13)$$

$$\beta = B_+ + B_-. \quad (14)$$

**Energetics** The energy of a Miura-ori vertex can be calculated if we assume that each fold behaves as a linear torsional spring with a preferred rest angle. If all the folds have the same spring constant  $k_0$  then the dimensionless energy is

$$\frac{U}{k_0 \ell} = \frac{1}{2}(\theta_+ - \theta_0)^2 + \frac{1}{2}(\theta_- + \theta_0 - 2\pi)^2 + (\beta - \beta_0)^2 + (\phi - \pi)^2. \quad (15)$$

Here we have assumed that the ground state has  $\theta_0$  and  $\beta_0$  at commensurate values such that there is a non-frustrated state where all the fold angles are at their preferred angle. If we plot the energy as a function of  $\varepsilon$ , and  $\phi$  (Fig. 2(E), main text) we see there is a region of disconnection as  $\varepsilon$  passes through  $\pi$ , and above  $\varepsilon = \pi$  there is a local minimum where  $\phi > \pi$ ; this is the pop-through defect (PTD).

**Scaling collapse of  $K_y^{\text{PTD}}$**  We now derive an expression for the compressive modulus of a pop-through defect (PTD) embedded in a Miura-ori lattice. Our notation follows that of Wei et. al. (15).

A Miura-ori unit cell has dimensions  $L_x$  and  $L_y$  given by

$$\begin{aligned} L_x &= 2\ell\zeta, \\ L_y &= 2\ell\xi, \quad \text{where} \\ \xi &= \sin(\alpha)\sin(\theta/2), \quad \zeta = \cos(\alpha)(1 - \xi^2)^{-1/2}, \end{aligned} \tag{16}$$

$\alpha$  is the folding angle, and all facet edges are of length  $\ell$ . For a wide range of parameters,  $L_y$  of a normal unit cell is approximately equal to that of a PTD. The same however, does not apply in the  $x$  direction where the equilibrium size of a PTD  $L_x^{\text{PTD}}$  is larger than that of a normal unit cell  $L_x^{\text{normal}}$ . This induces a strain on the PTD to accommodate the boundary conditions imposed by the lattice. The mechanical response to external loading is therefore proportional to  $L_x^{\text{PTD}} - L_x^{\text{normal}}$ .

We may write the total response as a linear superposition of the bulk force response and the effect of the PTD, as long as the defect density  $n$  is small enough that the defects do not interact. The inhomogeneous effect of the PTD can be written as a multipole expansion of the point force response, which we approximate using the homogeneous unit cell result. Given a uniform compression along the  $y$  direction on a lattice with PTDs as in our experiments, we can write the total force response in a multipole expansion:

$$f_y^{\text{defect}} = f_y^{\text{normal}} + nP \frac{df_x}{d\zeta}. \tag{17}$$

The zeroth order term is simply the response of a normal lattice  $f_y^{\text{normal}}$  to loading on the  $y$  direction. Because the PTD exerts no net force on the lattice, the first order correction in Eq.(17) is a dipole term  $\sim df_x/d\zeta$  of strength  $P$ , where  $f_x$  is the force response along the  $x$



direction arising from strain of the  $L_x^{\text{PTD}} - L_x^{\text{normal}}$ . With the definition of the compressive modulus  $K_y = df_y/d\varepsilon$ , we differentiate both sides of Eq.(17) to find

$$\begin{aligned}\frac{d}{d\varepsilon} f_y^{\text{defect}} &= \frac{d}{d\varepsilon} f_y^{\text{normal}} + nP \frac{d}{d\varepsilon} \left( \frac{df_x}{d\zeta} \right), \\ K_y^{\text{defect}} &= K_y^{\text{normal}} + nP \frac{d}{d\varepsilon} \left( \frac{df_x/d\varepsilon}{d\zeta/d\varepsilon} \right).\end{aligned}\tag{18}$$

Rearranging this expression to match the scaling collapse form described in the main text, we have

$$\frac{1}{n} \left( \frac{K_y^{\text{defect}}}{K_y^{\text{normal}}} - 1 \right) = \frac{P}{K_y^{\text{normal}}} \frac{d}{d\varepsilon} \left( \frac{df_x/d\varepsilon}{d\zeta/d\varepsilon} \right) = \frac{K_y^{\text{PTD}}}{K_y^{\text{normal}}}.\tag{19}$$

Here,  $P = (3 \pm 1) \times 10^{-3}$  is a fitting parameter for the strength of the dipole and an analytic expression for  $f_x(\varepsilon)$  is available elsewhere (15) assuming Hookean elasticity for each crease in the unit cell. We note that because the force response along the  $x$  direction arises from the strain  $L_x^{\text{PTD}} - L_x^{\text{normal}}$ , the right hand side is evaluated at the dihedral angle  $\varepsilon^*$  of the normal unit cells.

**PTD localization length** To understand how the spatial distortions induced by a PTD on the rest of the Miura-ori are so strongly localized, we must first develop a framework to describe vertex connectivity. We begin by constructing a full Miura-ori tessellation from the angles for a single vertex and place a Cartesian coordinate system on the crease pattern with indices for each vertex using  $(n, m)$  to denote the  $x$  and  $y$  coordinates of the creases. At each vertex there are  $N$  folds, indicating  $N - 3$  degrees of freedom. Modeling a PTD as a vertex with two extra folds to account for facet bending, we have  $N = 6$ , where the three degrees of freedom per vertex are then given by the internal state vector  $\mathbf{s} = \{\epsilon, \phi_+, \phi_-\}$ . Here, we accommodate the most general circumstance where the facet bending angle  $\phi$  is not symmetric on either side of the vertex, but rather, is allowed to take distinct values  $\phi_+$  and  $\phi_-$  on either side. This notation is consistent with that used above and in Fig. S5,

where the angle marked  $\phi$  is now  $\phi_+$ . Specifying  $\mathbf{s}$  yields the solution for the dihedral angles at each vertex, which we collect in the vector  $\mathbf{f}(\mathbf{s}) = \{\theta_+, \phi_+, \beta_+, \theta_-, \beta_-, \phi_-\}$ . To enforce the connectivity of the vertices the following relationships must hold:

$$\begin{aligned}
\theta_+^{n,m} &= \theta_-^{n+1,m}, \\
\beta_-^{n,m} &= \beta_+^{n,m-1}, \\
\beta_+^{n,m} &= \beta_-^{n,m+1}, \\
\phi_+^{n,m} &= \phi_-^{n+1,m+1}, \\
\phi_-^{n,m} &= \phi_+^{n+1,m-1}.
\end{aligned} \tag{20}$$

While the functions  $\mathbf{f}(\mathbf{s})$  are generally nonlinear, we expand about a uniformly folded state  $\mathbf{f} = \mathbf{f}_0 + \mathbf{J}\delta\mathbf{s}$ , where  $\mathbf{J} \equiv \partial\mathbf{f}/\partial\mathbf{s}|_{\mathbf{s}_0}$  is the Jacobian matrix for linearizing about the internal state  $\mathbf{s}_0 \equiv \{\epsilon, \pi, \pi\}$  (i.e., a Miura folded pattern where the extra folds are flat). This relation allows us to solve for the angles in terms of the internal state  $\mathbf{s}$ . The Miura unit cell is composed of four vertices, and thus the matrix  $\mathbf{J}$  is a block diagonal matrix, i.e.,  $\mathbf{J} = \text{diag}\{\mathbf{J}_0, -\mathbf{J}_0, \mathbf{J}_0, -\mathbf{J}_0\}$  is a  $24 \times 12$  rectangular matrix formed from four identical blocks,

$$\mathbf{J}_0 = \begin{pmatrix} A & C & C \\ 0 & 1 & 0 \\ B & C & 0 \\ -A & 0 & 0 \\ B & 0 & C \\ 0 & 0 & 1 \end{pmatrix} \tag{21}$$

where

$$A = \cos \alpha \csc(\epsilon/2) / \sqrt{\sin^2(\epsilon/2) - \cos^2 \alpha}, \tag{22}$$

$$B = \sin^2(\epsilon/2) \sec \alpha A, \tag{23}$$

$$C = \csc(\alpha/2)/2. \tag{24}$$

Finally, since the Miura-ori is periodic in space, in analogy with crystalline materials we decompose the Eq.(20) in a Fourier basis in terms of a wave vector,  $\mathbf{q}$ , lying in the first Brillouin zone of the lattice. This yields

$$\mathbf{Q}(\mathbf{q})\delta\mathbf{s}(\mathbf{q}) = 0, \quad (25)$$

with  $\mathbf{Q}(\mathbf{q}) \equiv \mathbf{D}(\mathbf{q})\mathbf{J}$ .

The matrix  $\mathbf{Q}(\mathbf{q})$  is square such that Eq.(25) has a nontrivial solution whenever  $\det[\mathbf{Q}(\mathbf{q})] = 0$ . This results in the dispersion

$$\frac{\cos^2 \alpha}{\sin^4(\epsilon/2)} \sin^2(q_x/2) + \sin^2(q_y/2) = 0. \quad (26)$$

For an infinite “origami crystal,” the only solution for  $\mathbf{q}$  that is purely real is  $\mathbf{q} \equiv 0$ , indicating that only uniform deformations are allowed. If the tessellation has a boundary, however, imaginary values of the wave vector  $\mathbf{q}$  are allowed, indicating that there are localized states near edges that decay over some natural length scale determined by the crease pattern and fold angles. Assuming  $q_x$  is real, Eq.(26) yields  $q_y = \pm ik(q_x)$ , where  $k(q_x) \equiv 2|\sinh^{-1}[\cos \alpha \sin(q_x/2)/\sin^2(\epsilon/2)]|$ : deformations decay away from the boundaries of constant  $y$  with a length scale  $1/k(q_x)$ .

The effect of a PTD on the distortion of the whole lattice can be quantified in terms of this decay length. The PTD represents a disturbance localized to a single unit cell, and thus  $q_x \sim \pi$ . If we choose a few representative values for  $\epsilon, \alpha$  we can calculate the coherence length  $\ell \equiv 1/k$ . For the reported experiments in Fig. 2 and 3 in the main text,  $\alpha = \pi/3$  and  $\epsilon \approx \pi/2$ , which yields a value for  $\ell \approx 0.56$  measured in unit cells. This indicates that the deformations near a PTD should decay very quickly, as observed experimentally.

## 2-4 defect pairs and Maekawa’s theorem

As described in the main text, we find a Miura-ori with a 2-4 defect pair is flat-foldable, and that this property occurs because the resultant crease pattern is compatible with Maekawa’s theorem, i.e., the number of mountain folds minus the number of valley folds at each vertex is  $\pm 2$ . Because this is a generic theorem about the crease topology, the 2-4 defect pair should be flat-foldable, independent of the lengths  $l_1$ ,  $l_2$  and plane angle  $\alpha$  that define the Miura-ori’s geometry. We experimentally verify this with folded paper models where we sample combinations of  $l_1/l_2 = 1$  or  $1/17$  and  $\alpha = 20^\circ, 45^\circ$ , or  $70^\circ$  (Fig. S6). By the same logic, an isolated PTD will never be flat-foldable as it violates Maekawa’s theorem for any  $l_1$ ,  $l_2$ , and  $\alpha$ . Thus, at sufficiently high compressions, the total modulus will always increase up to the limits set by tearing/crumpling of the underlying material.

## References

34. Eitan Grinspun, Mathieu Desbrun, Konrad Polthier, Peter Schroder, and Ari Stern. Discrete differential geometry: An applied introduction. *ACM SIGGRAPH Course*, 2006.

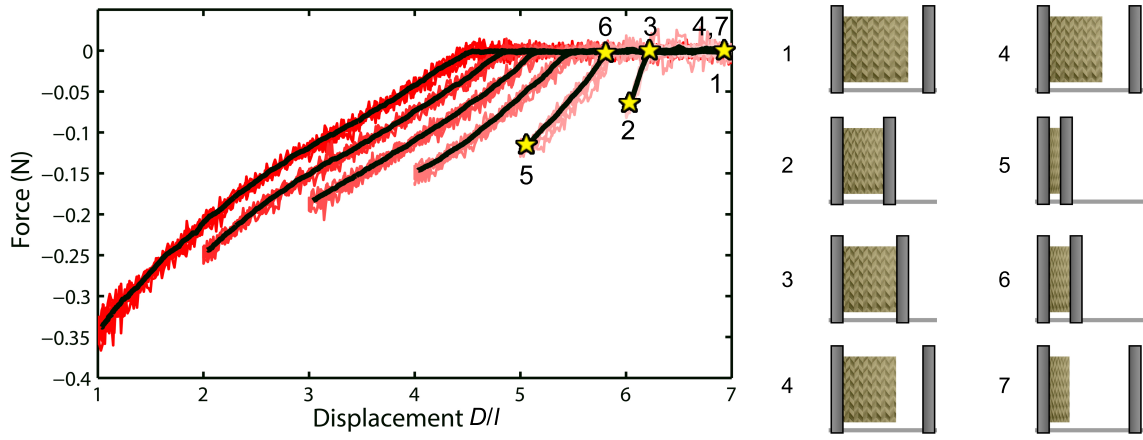


Figure S1: Schematic illustration of the loading protocol used to measure the compressive modulus of origami structures. For clarity, this force-displacement data is a subset of the complete data sets showing only 6 displacement amplitudes from the compression half of the cycle.

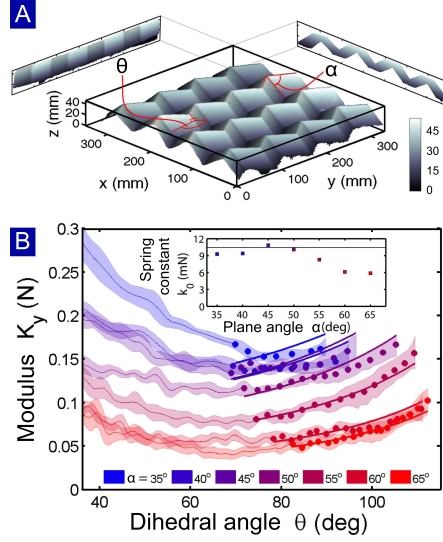


Figure S2: Experimental 3D scan and mechanical data of a normal Miura-ori demonstrating metamaterial properties. (A) A 3D image of a  $4 \times 4$  Miura-ori with two in-plane projections at equilibrium illustrates the folded structure. Color bar gives height in mm. (B) Small strain measurements of the compressive modulus  $K_y(\theta)$  (dots) are compared to theoretical fits (thick lines) for various angles  $\alpha$  (colors). Measurements extend beyond the small strain limit (thin lines), and colored bands indicate error estimates. (Inset) From the theoretical fits, we extract the elastic spring constant of a single crease  $k_0$  for each  $\alpha$  (points) and compare to a measurement made on a single crease (black line).

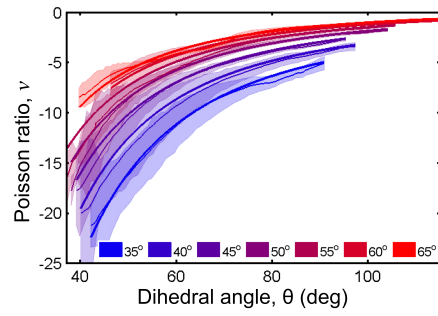


Figure S3: The experimentally measured Poisson ratio  $\nu$  as a function of compression is shown in thin lines with error estimates as shaded bands. Thick lines are parameter-free theoretical predictions, which agree favorably with the data. Colored bands correspond to values of  $\alpha$ .



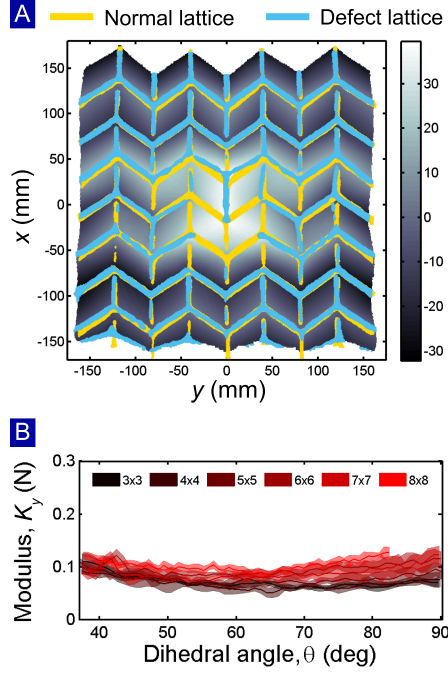


Figure S4: Experimental data showing spatial confinement of a PTD and finite lattice size effects. (A) Data showing crease location for a normal (gold) and defected (cyan) lattice. Crease's locations are determined from mean curvature maps and defined as regions where the absolute value of the mean curvature is greater than  $0.05 \text{ mm}^{-1}$ . The background shading is a surface map of the lattice with a PTD, where the color corresponds to the height in mm. (B) The compressive modulus  $K_y$  as a function of dihedral angle  $\theta$  for lattice sizes ranging from  $3 \times 3$  to  $8 \times 8$  shows a weak variation with lattice size.

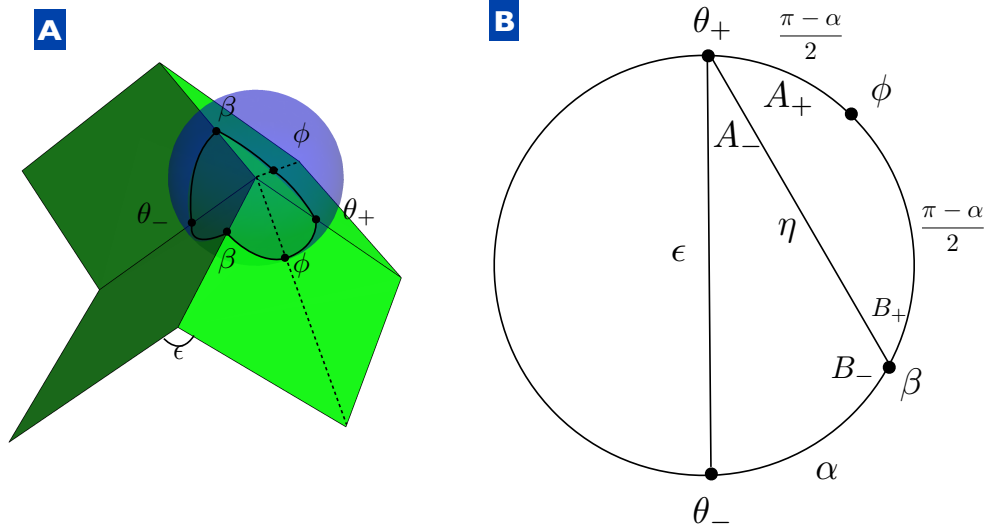


Figure S5: Spherical trigonometric diagrams that illustrate and define angles used in theoretical calculations. (A) A bounding sphere centered on a Miura-ori vertex illustrates the crease and fold angles. (B) The spherical polygon made by unfolding the region bounded by the sphere in (A) schematizes the relationship between the crease and fold angles. In this representation,  $\epsilon$  and  $\eta$  are angles in the folded structure that can be most clearly seen by connecting their end-points in (A). By symmetry only the angles on half of the vertex are shown.

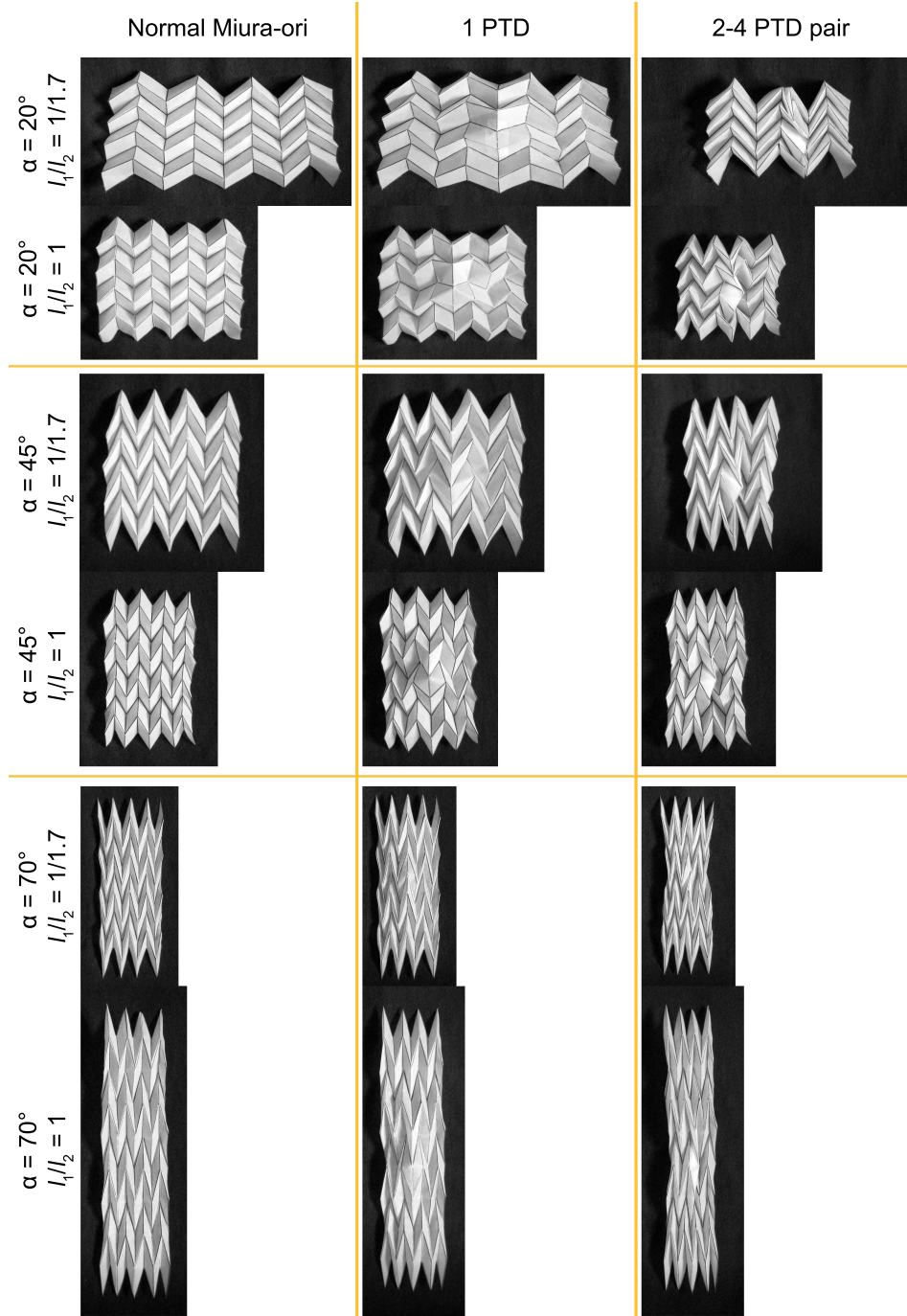


Figure S6: Photographs of hand folded Miura-ori's with various geometric and PTD configurations. In each case, the structures with 1 PTD are non-flat-foldable, while the structures with 2-4 defect pairs are.

**Movie S1:** Introduction of a  $4 \times 4$  Miura-ori demonstrating its structure and compressive behavior.

**Movie S2:** Compression of a  $4 \times 4$  Miura-ori with a PTD showing its formation, mechanical response, and restoration to a normal lattice.

**Movie S3:** Compression of a  $4 \times 4$  Miura-ori with a 1-2 defect pair showing its formation, mechanical response, and restoration to a normal lattice.

**Movie S4:** Compression of a  $4 \times 4$  Miura-ori with a 2-4 defect pair showing the formation, mechanical response, and restoration to a normal lattice.

## References

1. M. Wegener, Metamaterials beyond optics. *Science* **342**, 939–940 (2013). [Medline](#) [doi:10.1126/science.1246545](https://doi.org/10.1126/science.1246545)
2. Y. Liu, X. Zhang, Metamaterials: A new frontier of science and technology. *Chem. Soc. Rev.* **40**, 2494–2507 (2011). [Medline](#) [doi:10.1039/c0cs00184h](https://doi.org/10.1039/c0cs00184h)
3. J.-H. Lee, J. P. Singer, E. L. Thomas, Micro-/nanostructured mechanical metamaterials. *Adv. Mater.* **24**, 4782–4810 (2012). [Medline](#) [doi:10.1002/adma.201201644](https://doi.org/10.1002/adma.201201644)
4. A. Q. Liu, W. M. Zhu, D. P. Tsai, N. I. Zheludev, Micromachined tunable metamaterials: A review. *J. Opt.* **14**, 114009 (2012). [doi:10.1088/2040-8978/14/11/114009](https://doi.org/10.1088/2040-8978/14/11/114009)
5. M. Kadic, T. Bückmann, R. Schittny, M. Wegener, Metamaterials beyond electromagnetism. *Rep. Prog. Phys.* **76**, 126501 (2013). [Medline](#) [doi:10.1088/0034-4885/76/12/126501](https://doi.org/10.1088/0034-4885/76/12/126501)
6. C. Py, P. Reverdy, L. Doppler, J. Bico, B. Roman, C. N. Baroud, Capillary origami: Spontaneous wrapping of a droplet with an elastic sheet. *Phys. Rev. Lett.* **98**, 156103 (2007). [Medline](#) [doi:10.1103/PhysRevLett.98.156103](https://doi.org/10.1103/PhysRevLett.98.156103)
7. A. Papa, S. Pellegrino, Systematically creased thin-film membrane structures. *J. Spacecr. Rockets* **45**, 10–18 (2008). [doi:10.2514/1.18285](https://doi.org/10.2514/1.18285)
8. N. Bassik, G. M. Stern, D. H. Gracias, Microassembly based on hands free origami with bidirectional curvature. *Appl. Phys. Lett.* **95**, 091901 (2009). [doi:10.1063/1.3212896](https://doi.org/10.1063/1.3212896)
9. J. Kim, J. A. Hanna, M. Byun, C. D. Santangelo, R. C. Hayward, Designing responsive buckled surfaces by halftone gel lithography. *Science* **335**, 1201–1205 (2012). [Medline](#) [doi:10.1126/science.1215309](https://doi.org/10.1126/science.1215309)
10. J. Kim, J. A. Hanna, R. C. Hayward, C. D. Santangelo, Thermally responsive rolling of thin gel strips with discrete variations in swelling. *Soft Matter* **8**, 2375 (2012). [doi:10.1039/c2sm06681e](https://doi.org/10.1039/c2sm06681e)
11. M. A. Dias, L. H. Dudte, L. Mahadevan, C. D. Santangelo, Geometric mechanics of curved crease origami. *Phys. Rev. Lett.* **109**, 114301 (2012). [Medline](#) [doi:10.1103/PhysRevLett.109.114301](https://doi.org/10.1103/PhysRevLett.109.114301)
12. M. A. Dias, C. D. Santangelo, The shape and mechanics of curved-fold origami structures. *EPL* **100**, 54005 (2012). [doi:10.1209/0295-5075/100/54005](https://doi.org/10.1209/0295-5075/100/54005)
13. J. Ryu, M. D’Amato, X. Cui, K. N. Long, H. Jerry Qi, M. L. Dunn, Photo-origami: Bending and folding polymers with light. *Appl. Phys. Lett.* **100**, 161908 (2012). [doi:10.1063/1.3700719](https://doi.org/10.1063/1.3700719)
14. M. Schenk, S. D. Guest, Geometry of Miura-folded metamaterials. *Proc. Natl. Acad. Sci. U.S.A.* **110**, 3276–3281 (2013). [Medline](#) [doi:10.1073/pnas.1217998110](https://doi.org/10.1073/pnas.1217998110)
15. Z. Y. Wei, Z. V. Guo, L. Dudte, H. Y. Liang, L. Mahadevan, Geometric mechanics of periodic pleated origami. *Phys. Rev. Lett.* **110**, 215501 (2013). [Medline](#) [doi:10.1103/PhysRevLett.110.215501](https://doi.org/10.1103/PhysRevLett.110.215501)

16. M. Jamal, S. S. Kadam, R. Xiao, F. Jivan, T. M. Onn, R. Fernandes, T. D. Nguyen, D. H. Gracias, Bio-origami hydrogel scaffolds composed of photocrosslinked PEG bilayers. *Advanced Healthcare Materials* **2**, 1142–1150 (2013). [Medline](#)  
[doi:10.1002/adhm.201200458](https://doi.org/10.1002/adhm.201200458)
17. K. Miura, Method of packaging and deployment of large membranes in space. *Inst. Space Astronaut. Sci. Rep.* **618**, 1–9 (1985).
18. L. Mahadevan, S. Rica, Self-organized origami. *Science* **307**, 1740 (2005). [Medline](#)  
[doi:10.1126/science.1105169](https://doi.org/10.1126/science.1105169)
19. M. Ben Amar, F. Jia, Anisotropic growth shapes intestinal tissues during embryogenesis. *Proc. Natl. Acad. Sci. U.S.A.* **110**, 10525–10530 (2013). [Medline](#)  
[doi:10.1073/pnas.1217391110](https://doi.org/10.1073/pnas.1217391110)
20. A. E. Shyer, T. Tallinen, N. L. Nerurkar, Z. Wei, E. S. Gil, D. L. Kaplan, C. J. Tabin, L. Mahadevan, Villification: How the gut gets its villi. *Science* **342**, 212–218 (2013).  
[Medline](#) [doi:10.1126/science.1238842](https://doi.org/10.1126/science.1238842)
21. E. Abbena, S. Salamon, A. Gray, *Modern Differential Geometry of Curves and Surfaces with Mathematica* (CRC Press, Boca Raton, FL, 2006).
22. T. D. Gatzke, C. M. Grimm, Estimating curvature on triangular meshes. *Int. J. Shape Model.* **12**, 1–28 (2006). [doi:10.1142/S0218654306000810](https://doi.org/10.1142/S0218654306000810)
23. L. D. Landau, E. M. Lifshitz, *Landau and Lifshitz Course of Theoretical Physics Volume 7: Theory of Elasticity* (Butterworth Heinemann, New Delhi, 1986), third edn.
24. M. Bern, B. Hayes, *Proceedings of the Symposium on Discrete Algorithms* **7**, 175–183 (1996), 28 to 30 January 1996, Atlanta.
25. E. Steltz, A. Mozeika, N. Rodenberg, E. Brown, H. M. Jaeger, IEEE/RSJ International Conference on Intelligent Robots and Systems (IROS), 10 to 15 October 2009, St. Louis, MO (IEEE, 2009), pp. 5672–5677.
26. T. Fukushige, S. Hata, A. Shimokohbe, A MEMS conical spring actuator array. *J. Microelectromech. Syst.* **14**, 243–253 (2005). [doi:10.1109/JMEMS.2004.839345](https://doi.org/10.1109/JMEMS.2004.839345)
27. T. W. Ebbesen, H. Hiura, Graphene in 3-dimensions: Towards graphite origami. *Adv. Mater.* **7**, 582–586 (1995). [doi:10.1002/adma.19950070618](https://doi.org/10.1002/adma.19950070618)
28. P. M. Chaikin, T. C. Lubensky, *Principles of Condensed Matter Physics* (Cambridge Univ. Press, Cambridge, UK, 2000), first edn.
29. T. Toffoli, N. Margolus, Programmable matter: Concepts and realization. *Physica D* **47**, 263–272 (1991). [doi:10.1016/0167-2789\(91\)90296-L](https://doi.org/10.1016/0167-2789(91)90296-L)
30. E. Hawkes, B. An, N. M. Benbernou, H. Tanaka, S. Kim, E. D. Demaine, D. Rus, R. J. Wood, Programmable matter by folding. *Proc. Natl. Acad. Sci. U.S.A.* **107**, 12441–12445 (2010). [Medline](#) [doi:10.1073/pnas.0914069107](https://doi.org/10.1073/pnas.0914069107)
31. S. M. Felton, M. T. Tolley, C. D. Onal, D. Rus, R. J. Wood, 2013 IEEE International Conference on Robotics and Automation (ICRA), 6 to 10 May 2013, Karlsruhe, Germany (IEEE, 2013), pp. 277–282.

32. C. D. Onal, R. J. Wood, D. Rus, 2011 IEEE International Conference on Robotics and Automation (ICRA), 9 to 13 May 2011, Shanghai (IEEE, 2011), pp. 4608–4613.
33. B. An, N. Benbernou, E. D. Demaine, D. Rus, Planning to fold multiple objects from a single self-folding sheet. *Robotica* **29**, 87–102 (2011). [doi:10.1017/S0263574710000731](https://doi.org/10.1017/S0263574710000731)
34. E. Grinspun, M. Desbrun, K. Polthier, P. Schröder, A. Stern, Discrete differential geometry: An applied introduction. ACM SIGGRAPH Course, 2006.  
<http://mesh.brown.edu/DGP/pdfs/sg06-course01.pdf>



# Origami structures with a critical transition to bistability arising from hidden degrees of freedom

Jesse L. Silverberg<sup>1\*</sup>, Jun-Hee Na<sup>2</sup>, Arthur A. Evans<sup>3</sup>, Bin Liu<sup>1</sup>, Thomas C. Hull<sup>4</sup>,  
Christian D. Santangelo<sup>3</sup>, Robert J. Lang<sup>5</sup>, Ryan C. Hayward<sup>2</sup> and Itai Cohen<sup>1</sup>

**Origami is used beyond purely aesthetic pursuits to design responsive and customizable mechanical metamaterials<sup>1–8</sup>. However, a generalized physical understanding of origami remains elusive, owing to the challenge of determining whether local kinematic constraints are globally compatible and to an incomplete understanding of how the folded sheet's material properties contribute to the overall mechanical response<sup>9–14</sup>. Here, we show that the traditional square twist, whose crease pattern has zero degrees of freedom (DOF) and therefore should not be foldable, can nevertheless be folded by accessing bending deformations that are not explicit in the crease pattern. These hidden bending DOF are separated from the crease DOF by an energy gap that gives rise to a geometrically driven critical bifurcation between mono- and bistability. Noting its potential utility for fabricating mechanical switches, we use a temperature-responsive polymer-gel version of the square twist to demonstrate hysteretic folding dynamics at the sub-millimetre scale.**

A key theme unifying the study of biopolymer gels<sup>15,16</sup>, biological tissues<sup>17</sup>, kinematic mechanisms<sup>18–21</sup>, granular media<sup>22–24</sup>, network glasses<sup>25</sup> and architectural elements<sup>26</sup> is the competition between the number of internal DOF,  $N_f$ , and the number of internal mechanical constraints,  $N_c$ . The macroscopic behaviour of these systems in the absence of self-stresses<sup>27,28</sup> is said to be underconstrained when  $N_f > N_c$ , overconstrained when  $N_f < N_c$ , and isostatic, or marginally stable, when  $N_f = N_c$ . This framework, which was initially laid out by J. C. Maxwell in 1864, has been instrumental in understanding a diverse range of mechanical phenomena in constraint-based materials, including rigidity percolation<sup>16</sup>, topologically protected zero energy modes<sup>19</sup>, nonlinear elasticity<sup>16</sup> and shock waves<sup>24</sup>. A feature intrinsic to real physical materials but often left out of simpler models is the existence of a hierarchy of DOF, each with its own associated energy scale. When the details of these internal features are incorporated, systems can be overconstrained and rigid with respect to low-energy loading, but underconstrained and compliant as higher-energy DOF are accessed. Thus,  $N_f$  should be thought of as a variable quantity that changes with the experimental energy scale.

Although these observations are fairly general, the emergent mechanical phenomena that can be found in materials as the DOF hierarchy is probed has not been well examined. Indeed, this problem plays out in origami mechanics, where crease patterns that are mathematically unfoldable because  $N_f \leq N_c$  nevertheless easily fold when made by hand<sup>10,11,29,30</sup>. In essence, the discrepancy originates when origami structures are modelled as a series of rigid polyhedra connected by freely rotating torsional hinges. Although rigid foldability appears to be a reasonable simplification for the

folding behaviour, the fact that real materials can bend is a critical piece of missing phenomenology. In fact, there is at present no general approach for understanding and predicting the mechanical behaviour of origami structures when their material properties are taken into account. Although numerous examples of unfoldable crease patterns exist, we here investigate the mechanics of a single unit from the square-twist origami tessellation<sup>1</sup> (Fig. 1a,b; see also Supplementary Movies 1 and 2 and Supplementary Fig. 1). Even in this simple test case, we find a rich set of mechanical behaviours that illuminate general principles applicable to any material with measurably different energy scales separating overconstrained and underconstrained states.

The square-twist pattern consists of alternating square and rhombus facets, characterized by the length  $L$  and plane angle  $\phi$ , in which the internal edges are either all mountain or valley creases. An analysis of the geometric constraints reveals the pattern is isostatic. Essentially, this arises from the four-fold rotational symmetry of the structure, which imposes a cyclic set of constraints on the four creases that define the central square facet (Supplementary Information). Although this observation indicates that the crease pattern should not be foldable, a trigonometric analysis of the normalized edge-to-edge distance  $x/L$  shows that the square twist allows two isolated states corresponding to the fully unfolded and folded configurations (Fig. 1c, upper and lower black lines, respectively, and Supplementary Fig. 2).

Experiments measuring  $x/L$  on folded paper sheets without external loading (Methods; Fig. 1c, red data points) indicate qualitatively different behaviour than the crease geometry's naive prediction of rigidity. Instead, below a critical plane angle  $\phi_c = (25 \pm 2.5)^\circ$ , the distinction between folded and unfolded configurations is not observed; the structure is monostable with an intermediate value of  $x/L$  (for example, Fig. 1b, side views). Above  $\phi_c$ , both folded and unfolded configurations are observed; the folded configuration exhibits  $x/L$  values that nearly match the prediction, whereas the unfolded configuration exhibits  $x/L$  values that are smaller than predicted for ideal sheets (Fig. 1b, side view, and Fig. 1c). Although the crease pattern does not admit solutions between folded and unfolded branches for any  $\phi > 0^\circ$ , direct observations during the folding process reveal that the facets bend by a finite amount rather than remaining flat. These deformations are additional DOF hidden from the bare crease pattern, and are essential for foldability as they enable the structure to access otherwise geometrically forbidden configurations. It is the combination of this facet bending and the non-zero rest angles of the creases, which are plastically set when the sheet is fully folded, that gives rise to the observed intermediate configurations.

<sup>1</sup>Physics Department, Cornell University, Ithaca, New York 14853, USA. <sup>2</sup>Department of Polymer Science and Engineering, University of Massachusetts, Amherst, Massachusetts 01003, USA. <sup>3</sup>Department of Physics, University of Massachusetts, Amherst, Massachusetts 01003, USA. <sup>4</sup>Department of Mathematics, Western New England University, Springfield, Massachusetts 01119, USA. <sup>5</sup>Lang Origami, Alamo, California 94507, USA.

\*e-mail: JLS533@cornell.edu

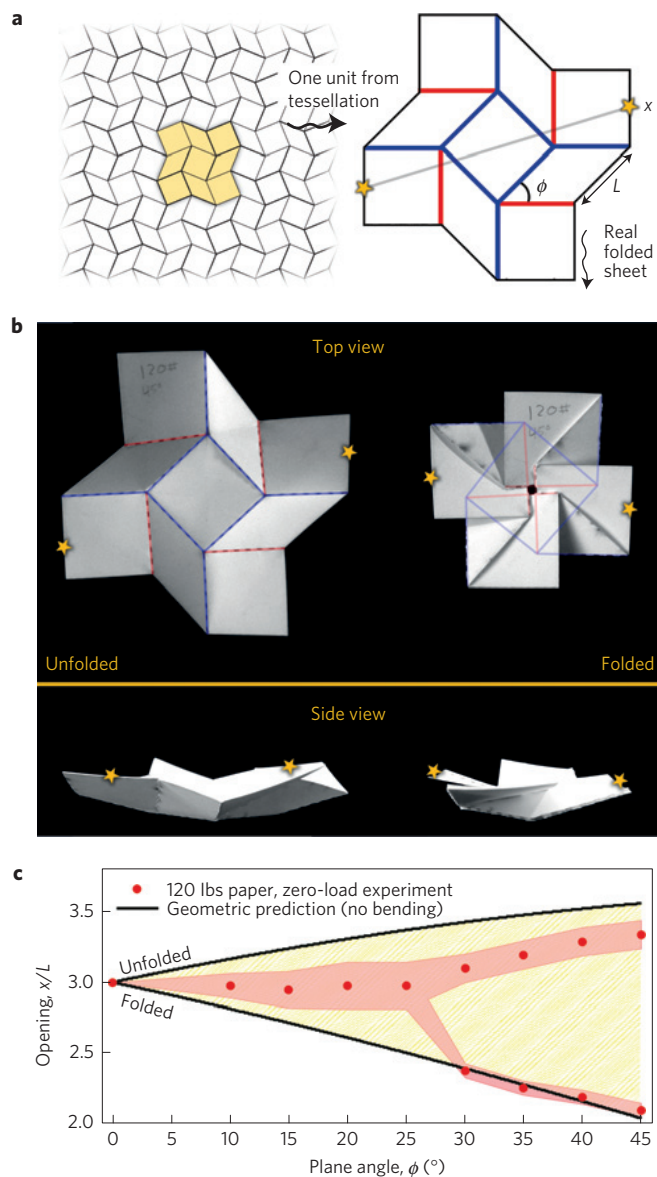


**Figure 1 | Schematics and photographs introducing the square twist's essential geometric properties and mechanical characteristics.** **a**, The square-twist folding pattern is shown with the edges in black, mountain creases in red, and valley creases in blue. The geometry is defined by the length,  $L$ , and the plane angle,  $\phi$ . The Euclidean distance,  $x$ , between the two yellow stars quantifies the macroscopic configuration between folded and unfolded states. **b**, Photographs of a square twist with  $\phi = 45^\circ$  illustrate out-of-plane deformations, and the stars define  $x$  when the square twist is unfolded and folded. **c**, Comparison of geometric predictions to experimental measurements for  $x/L$  as a function of  $\phi$  based purely on the crease pattern reveals qualitative disagreement. The former has bistable solutions for all non-zero  $\phi$  corresponding to folded and unfolded configurations (black lines), and no permissible configurations between these two states (lightly shaded region between lines). Experimental measurements, however, exhibit regions with mono- and bistable solutions depending on  $\phi$  (red points, errors are shaded bands).

To study the unfolding behaviour, we measured the mechanical response of the folded square twist to uniaxial tension. We observe remarkably different behaviours for  $\phi$  above and below the critical plane angle  $\phi_c$ . Below  $\phi_c$ , the structure smoothly opens and closes, as indicated by the folding order parameter  $\delta$  (Fig. 2a inset and blue line; Supplementary Movie 1), whereas above  $\phi_c$  a rapid snapping action between folded and unfolded states is observed, as indicated

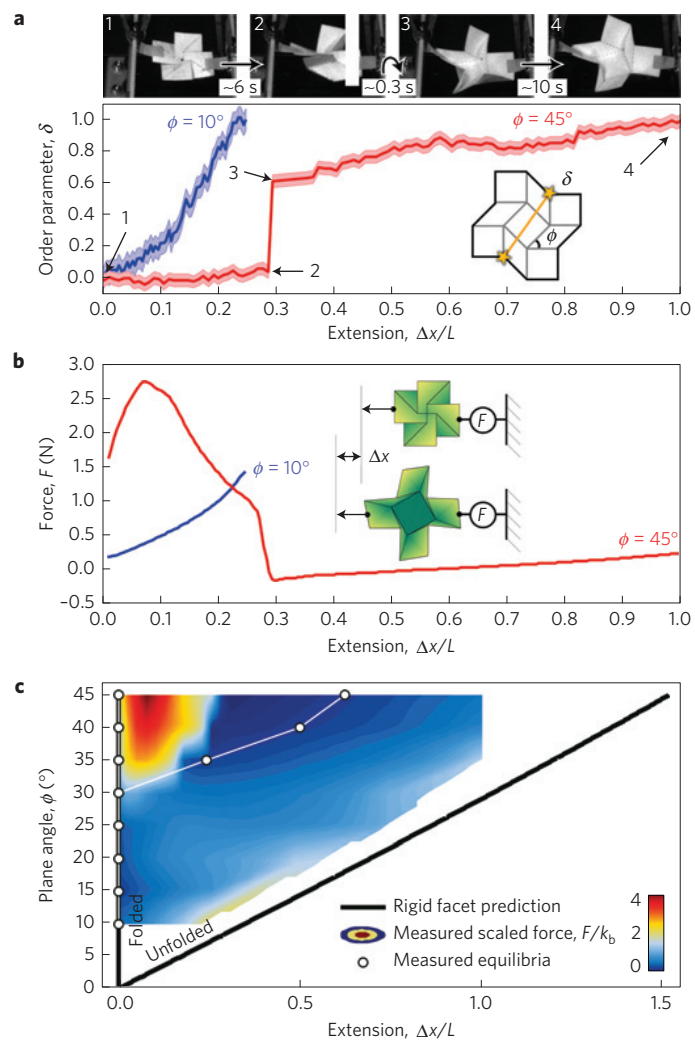


**Figure 2 | Experimental strain-controlled mechanical data studying the transition between mono- and bistability in square twists.**

**a**, Measurements of the folding order parameter,  $\delta$ , show smooth continuous behaviour for  $\phi = 10^\circ$  and an abrupt discontinuous jump for  $\phi = 45^\circ$ . The inset illustrates the definition of  $\delta$ , and photographs show points of interest on the red curve. **b**, Measurements of the tensile force  $F$  as a function of the normalized extension,  $\Delta x/L$ , reveal mechanical bistability between folded and unfolded configurations for  $\phi = 45^\circ$  and monostability for  $\phi = 10^\circ$ . The inset shows schematics of the experiment, definition of  $\Delta x$ , and location of the load cell. **c**, Measurements of the tensile force,  $F(\phi, \Delta x/L)$ , normalized by the sheet's torsional bending stiffness,  $k_b$ , show the transition between mono- and bistability. White circles indicate mechanically stable values of  $\Delta x/L$ , and black lines show predicted solutions based on a crease geometry with rigid facets. Note that these predictions do not permit solutions anywhere off the lines. Furthermore, these data closely correspond to the measurements in Fig. 1c, where load-free stable values of  $x$  were plotted as red dots, and where the predicted solutions based on a rigid-facet geometry were similarly shown as black lines.

by a jump in  $\delta$  (Fig. 2a, red line; Supplementary Movie 2). In the latter case, where  $\phi > \phi_c$ , both folded and unfolded configurations are stable to small external loading, whereas intermediate configurations are unstable and quickly snap to one state or the other. Displacement-controlled measurements of the force  $F$  as a function of  $\phi$  and normalized extension  $\Delta x/L$  also showed qualitatively different behaviour above and below  $\phi_c$  (Fig. 2b and inset). Here, the extension  $\Delta x$  is the change in  $x$  at a given force  $F$  along the direction of loading (Methods). For structures with  $\phi < \phi_c$  the force curves

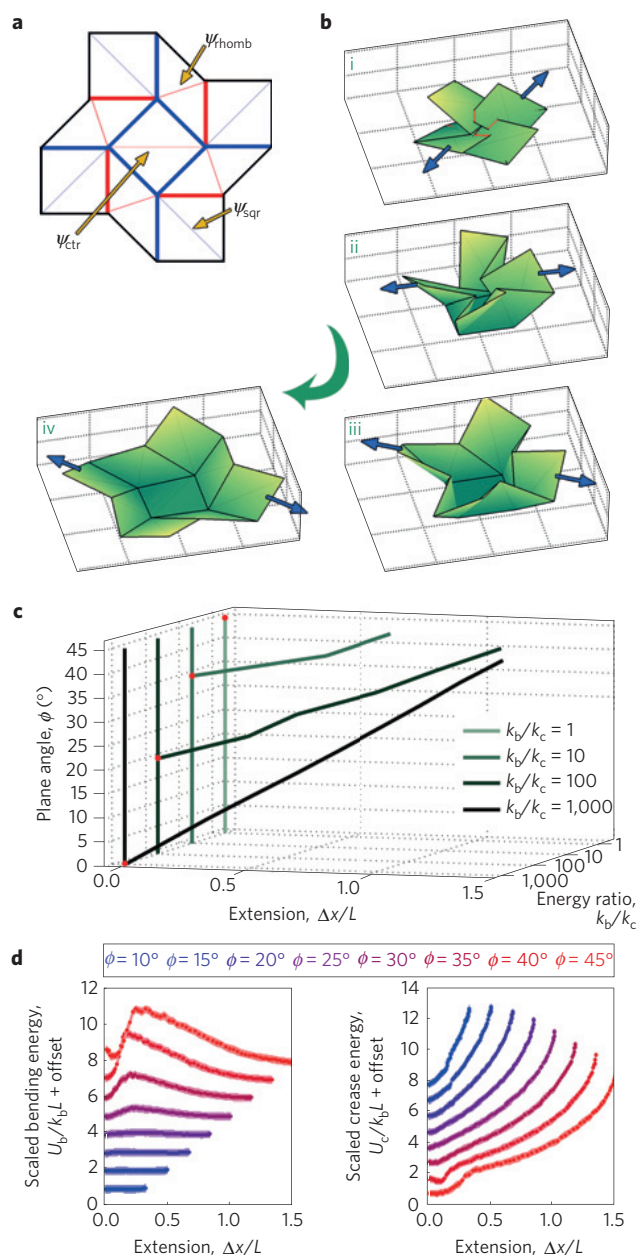


**Figure 3 | Simulation results for the square twist with non-rigid facets.**

**a**, The square-twist crease diagram has been modified with 'virtual creases' that mimic the behaviour of facet bending, as indicated by thin lines. **b**, 3D renderings from the simulation illustrate the unfolding sequence. Blue arrows indicate the external load corresponding to strain-controlled conditions. **c**, Simulation data where each line represents the mechanically stable unfolding sequence as a function of geometry for various material properties. The data reveal a critical angle  $\phi_c$  (red dots) that varies with the bending-to-crease energy ratio  $k_b/k_c$ . For  $k_b/k_c=1$ , monostability is observed for all  $\phi$ , whereas for  $k_b/k_c=10^3$  bistability is found for all  $\phi$ . Between these limits, a bifurcation separating the monostable ( $\phi < \phi_c$ ) and bistable ( $\phi > \phi_c$ ) limits of the phase transition can be found. **d**, Examining the distribution of energy between crease and bending degrees of freedom for  $k_b/k_c=10^2$  as a typical example, we see that the contribution from bending has an energy barrier for intermediate values of  $\Delta x/L$  that increases in magnitude with  $\phi$ . Conversely, the energetic contribution from crease opening essentially increases monotonically with  $\Delta x/L$  for all  $\phi$ . In both energy plots, the band thickness indicates the simulation uncertainty.

increase monotonically, whereas structures with  $\phi > \phi_c$  exhibit force curves with regions of negative slope, indicating mechanical

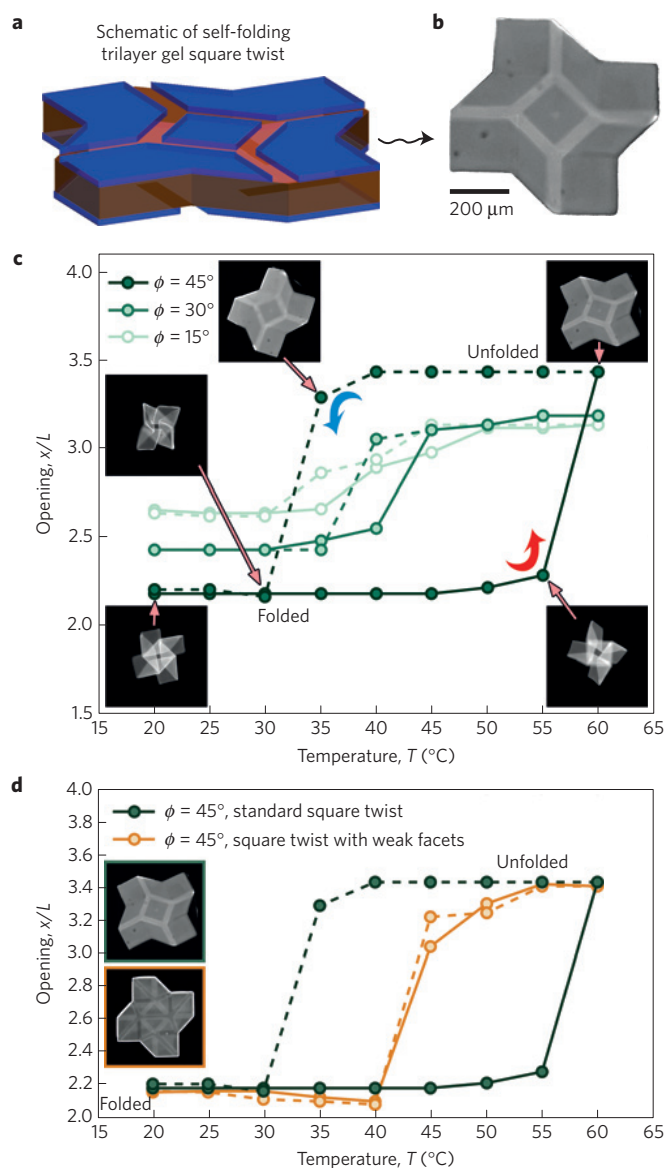


**Figure 4 | A sub-millimetre-scale self-folding polymer-gel version of the square twist is used to verify the geometric nature of bistability in stress-controlled conditions.**

**a**, Schematic of the trilayer structure (dimensions not to scale). Folding is actuated by a temperature-dependent swelling of the middle (pink) layer. Open slits patterned in the top and bottom layers (blue) induce mountain and valley creases, respectively, when viewed from above. **b**, Optical micrograph of a square twist released in an aqueous medium at 60 °C. **c**, Measurements of square-twist opening as a function of temperature demonstrate hysteretic folding/unfolding behaviour for  $\phi > \phi_c$  and non-hysteretic folding/unfolding for  $\phi < \phi_c$ . In this case,  $15^\circ < \phi_c < 30^\circ$ . Solid lines (unfolding) correspond to heating, and dashed lines (folding) to cooling. Inset micrographs show a structure with  $\phi = 45^\circ$  at the indicated measurement points. **d**, Measurements of opening as a function of temperature for the standard square twist compared to a version with creases added where bending would otherwise occur. The additional DOF afforded by setting  $k_b/k_c \lesssim 1$  entirely remove hysteretic folding behaviour.

instability. To determine the force landscape that drives transitions from the folded to the unfolded state, we measured the tensile force normalized by the sheet's torsional bending stiffness,  $k_b$  (Fig. 2c, Supplementary Figs 3 and 4). We find that the force barrier between these states increases in magnitude with  $\phi$ , hinting at an underlying mechanism for bistability. In particular, facet bending is localized to the rhombi short diagonals, forming 'virtual creases' with a deflec-



tion angle  $\psi$  and energy  $\sim Lk_b \sin(\phi/2)\psi^2$ . Because the length of these diagonals increases with  $\phi$ , the force barrier increases as well.

To further investigate this facet-bending mechanism, we developed a numerical simulation of the unfolding behaviour under uniaxial tension that calculates the configuration minimizing the facet-bending and crease-unfolding energies for a given  $\phi$  and  $\Delta x/L$  (Fig. 3a,b, Methods). From these calculations, we determine the energetic minima, which correspond to mechanically stable states, for different ratios of the bending and crease torsional spring constants,  $k_b/k_c$  (Fig. 3c). For  $k_b/k_c \leq 1$ , monostability was observed for all geometries, whereas for  $k_b/k_c \geq 10^3$ , all geometries exhibited bistability. Between these limits, we found a critical plane angle  $\phi_c$  marking a bifurcation between mono- and bistability that varied with  $k_b/k_c$ . When compared with the experimental phase diagram (Fig. 2c), these calculations predict  $10 < k_b/k_c < 100$ , which is consistent with measurements that found  $k_b/k_c \simeq 36$  for the paper used in experiments (Supplementary Information).

Examining the internal distribution of energy by separating the dimensionless bending energy  $U_b/k_b L$  from the dimensionless crease energy  $U_c/k_b L$  sheds light on how different DOF are interacting to tune the bifurcation (Fig. 3d). For example, taking  $k_b/k_c = 10^2$ , where  $\phi_c \approx 20^\circ$ , we see that the system's total bending energy has an energy barrier at intermediate values of  $\Delta x/L$  whose magnitude increases with  $\phi$ . The total crease energy, on the other hand, monotonically increases with  $\Delta x/L$  for all  $\phi$ . Whether this monotonic rise in crease energy is high enough to overcome the energy barrier that arises from hidden bending DOF determines if the system is mono- or bistable (Supplementary Fig. 5).

Collectively, these results provide a geometric understanding for the mechanical bistability of the square twist and, as such, should translate to any thin sheet folded according to this crease pattern. Although our experiments were performed with strain-controlled loading, we predict that the observed bifurcation will give rise to a hysteretic behaviour under stress-controlled loading that can be tuned by both  $\phi$  and  $k_b/k_c$ . To test this prediction, we used a micropatterned gel-trilayer version of the square twist with  $L = 200 \mu\text{m}$  (Fig. 4a,b; Methods). Here, differential swelling between gel layers is used to create internal stresses that fold and unfold the structure as the temperature  $T$  is varied. For this system, we estimate  $k_b/k_c \sim 10^2$  (Supplementary Information), and therefore from simulations we expect  $\phi_c \approx 20^\circ$  (Fig. 3c). Imaging a square twist with  $\phi = 45^\circ$  as the temperature is quasi-statically varied reveals the expected hysteresis (Fig. 4c, dark green line). As predicted, when  $\phi$  is decreased to  $30^\circ$  the hysteresis is reduced (medium green line), and ultimately vanishes for  $\phi = 15^\circ$  (light green line). Our results with paper models and simulations also suggest that hysteretic folding behaviour can be removed if  $k_b/k_c \lesssim 1$ . This scenario can be realized in the gel sheets by modifying and fully triangulating the crease pattern (for example, Fig. 3a), effectively placing creases where bending would otherwise occur. Indeed, we find for  $\phi = 45^\circ$  that the addition of these creases removes the hysteresis (Fig. 4d). These experiments clearly illustrate the first-order properties of the transition between folded and unfolded states that arises from hidden bending DOF in the square twist (Supplementary Fig. 6).

Although this work shows how hidden DOF can be used to create non-trivial features in an origami structure's configuration space, we envisage that the tunable and scale-free nature of the square twist's bistability should make it a useful design for robotic grippers, microfluidic devices and even wearable exoskeletons. Moreover, because the square twist can form 2D tessellations, it should be possible to spatially vary the unit-cell geometry to create origami mechanical metamaterials. For example, in analogy with secondary structures in polymers that provide hidden length<sup>31</sup>, the ability of the pattern to resist deformation up to a predetermined force threshold can be taken advantage of to make materials with extremely high toughness. Such devices would be capable of large bulk strain

without fracture by absorbing energy in a predetermined pattern of sequentially opening square-twist unit cells. More broadly, the possibility of alternative geometries (Supplementary Fig. 7) and additional hidden DOF—such as facet stretching, facet shearing and crease torquing—suggests that an even richer configuration space may be hidden with these more energetically expensive deformation modes. For example, these ideas are found in the mechanics of thin shells, where bending and stretching energy barriers have been shown to be modified by the introduction of creases<sup>32</sup>, leading to a broad range of multistable behaviours. Thus, the geometry of creased sheets offers a simple experimental platform to probe the mechanical behaviour of a wider class of constraint-based materials and the consequences of energy-scale dependent DOF.

## Methods

**Sample fabrication and characterization.** Digital CAD software and a laser cutter were used to fabricate square-twist structures from 120 lb paper (Radianc 120 lb super smooth card stock, Beckett Expressions). Creases were patterned by cutting perforated lines with equal lengths of material and gaps, then folded by hand with a Lineco bone scorer to be mountain or valley according to the crease assignment (Fig. 1a). For these samples, we set  $L = 2.54 \text{ cm}$  and varied  $\phi$  from  $10^\circ$  to  $45^\circ$  in increments of  $5^\circ$ . The lower bound is the limit of what can be reasonably folded from this material, although a theoretical limit of  $0^\circ$  is where the crease pattern is no longer well defined owing to overlapping mountain and valley curves. The upper bound is set by self-intersection, which prevents the structure from folding flat for  $\phi > 45^\circ$ . Samples used throughout this work were folded and unfolded before mechanical testing, thus the unfolded stable configuration retains some folding along the creases owing to plastic deformation and hence responds differently than a 'pristine' sheet that has never been folded.

To quantify a square twist's configuration in the absence of load, each sample was first folded flat, then held to a calliper ruler to measure the Euclidean distance  $x$  (Fig. 1a). Subsequently, each sample was unfolded, flattened on a table under  $2 \text{ s}$  of compression applied by hand, and the distance  $x$  remeasured.

A custom-built mechanical tester previously described<sup>5</sup> was used to measure the mechanical properties of square twists under tension. Samples were fixed to the testing device and suspended in air with small tabs of gaffing tape. Although this pre-loaded the samples with minor tension at zero extension (Fig. 2a), this approach prevented any interactions with the lower surface of the testing apparatus, which would otherwise interfere with the unfolding process. In a typical experiment, the distance between loading plates and load cell force data were simultaneously recorded by a single custom MATLAB program, and the data stored for later analysis. Furthermore, the maximum experimental extension was kept smaller than the theoretical limits (Fig. 2c black lines) to reduce risk of tearing samples apart. Sample testing was video recorded with a Canon Powershot camera filming at 7.5 FPS. Standard image analysis techniques were used to measure the order parameter for folding,  $\delta$ , as a function of the normalized extension  $\Delta x/L$ , which as described in the main text is measured from the mechanically equilibrated folded state (Fig. 1c lower branch of red data).

**Simulated square twists.** To explore how material properties, and in particular finite bending stiffness of the flat facets, influences mechanical behaviour of the system, we developed a numerical simulation of the square twist's folding behaviour. In it, we constrained each of the 16 facet corners to have a fixed distance from their neighbouring corners according to the crease pattern. Crease and facet bending deformations were then assigned an elastic energy given by:

$$U_{\text{total}} = U_{\text{crease}} + U_{\text{bend}} \\ = \frac{L}{2} \left[ k_c \sum_{i=1}^{12} (\theta_i - \theta_0)^2 + k_b \sum_{j=1}^9 \lambda_j \psi_j^2 \right] \quad (1)$$

where

$$\lambda_j = \begin{cases} \sqrt{2} & \text{for square facets,} \\ 2 \sin(\phi/2) & \text{for rhombus facets} \end{cases}$$

In this expression, the first term is the crease energy, which is proportional to the torsional elastic constant  $k_c$  times the crease length  $L$ , and is a sum over the 12 individual creases. It is also a function of the crease angle  $\theta$ , determined from a dot product of two adjacent facet normals, minus an equilibrium value  $\theta_0$ . This represents the fact that, once made, creases no longer lay flat. A value of  $\theta_0 = 10^\circ$  was used here, which is consistent with our experimental samples. The second term is the facet-bending energy, which is proportional to the torsional elastic constant  $k_b$  times the length of the bend  $\lambda_j L$ , and is a sum over the nine indicated facet diagonals (Fig. 3a). It is a function of the bending angle  $\psi_j$ , which, unlike creases, is zero in a stress free state. Like the crease DOF, these bending DOF are also calculated from the dot product of the facet normals.

Specifying  $\phi$  and a target  $\Delta x/L$ , equation (1) was numerically minimized using the Levenberg–Marquardt algorithm in MATLAB, where the target  $\Delta x/L$  was incremented from 0 to its maximum value in 91 steps. This process was repeated 20 times with initial conditions generated from a geometric interpolation between the folded and unfolded states that did not preserve facet areas. In each realization, the facet corners were perturbed along  $x$ ,  $y$  and  $z$  by an amount that was uniformly distributed over the range given by  $\pm L/10$ . In this way, we used semi-random initial conditions to form an ensemble-averaged solution that minimized equation (1) and satisfied the crease pattern's geometric constraints. We then averaged the facet bending angles of the ensemble-averaged solution, producing an overall average rhombus bending angle  $\psi_{\text{rhomb}}$ , an overall average square-facet bending angle  $\psi_{\text{sq}}$ , and a centre square-facet bending angle  $\psi_{\text{ctr}}$  (Supplementary Information).

**Self-folding gel fabrication and imaging.** The self-folding version of the square twist consists of a temperature-responsive hydrogel film capped on both the top and bottom surfaces by rigid patterned layers. Although the method is described elsewhere<sup>33</sup>, we provide a brief summary here. First, we spin-coated a layer of ultraviolet-crosslinkable poly(*p*-methyl styrene) (PpMS) with a thickness of 50 nm. Using a maskless lithographic method, a pattern of stripes corresponding to the valley creases was used to define regions where the PpMS layer was crosslinked. Next, the temperature-responsive poly(*N*-isopropyl acrylamide-*co*-sodium acrylate) (PNIPAM) polymer was deposited and crosslinked on the PpMS layer with a thickness of 1.5  $\mu\text{m}$ . Finally, a second layer of PpMS with a thickness of 50 nm was deposited and crosslinked with a pattern corresponding to the mountain creases. This trilayer structure then consisted of two thin rigid outer layers encompassing a middle layer that swells with temperature. To prevent adhesion between the hydrophobic PpMS panels in the folded state, a 10-nm polyelectrolyte layer was coated on both outer surfaces of PpMS by spin-coating a photo-crosslinkable poly(sulphopropyl methacrylate) copolymer and crosslinking with ultraviolet light. On swelling in an aqueous buffer, stresses are developed within the middle hydrogel layer, causing the bilayer crease-like regions to bend to an angle programmed by the width of the open stripe in the capping PpMS layer. Trilayer regions, on the other hand, remain flat like facets. For the square-twist pattern, each crease segment is programmed to fold to either  $\pm\pi$  at room temperature, corresponding to the flat folded state.

Full triangulation of the fold pattern was accomplished by patterning open stripes in both the top and bottom rigid films where bending was observed in the paper experiments and numerical simulations. Thus, these regions had only a single layer gel film that was not programmed to fold, but instead offered much lower bending resistance than the trilayer facet regions.

To measure the opening  $x$ , each sample was placed in an aqueous medium and observed with epi-fluorescence microscopy through the temperature range 20 to 60 °C. A heat stage was used to control the temperature (Zeiss Tempcontrol 37-2 digital), which was varied in 5 °C increments. At least 30 min at each temperature was allowed for the gel to swell to equilibrium. The folding/unfolding process, therefore, was under quasi-static stress-controlled conditions. 3D images of polymer square twist were reconstructed using ImageJ from image stacks collected using a laser scanning confocal fluorescence microscope (Zeiss LSM 510 META), with the refractive index of the aqueous medium corrected for.

Received 28 November 2014; accepted 30 January 2015;  
published online 9 March 2015

## References

- Greenberg, H., Gong, M., Magleby, S. & Howell, L. Identifying links between origami and compliant mechanisms. *Mech. Sci.* **2**, 217–225 (2011).
- Song, J., Chen, Y. & Lu, G. Axial crushing of thin-walled structures with origami patterns. *Thin. Walled Struct.* **54**, 65–71 (2012).
- Schenk, M. & Guest, S. D. Geometry of miura-folded metamaterials. *Proc. Natl Acad. Sci. USA* **110**, 3276–3281 (2013).
- Wei, Z. Y., Guo, Z. V., Dudte, L., Liang, H. Y. & Mahadevan, L. Geometric mechanics of periodic pleated origami. *Phys. Rev. Lett.* **110**, 215501 (2013).
- Silverberg, J. L. *et al.* Using origami design principles to fold reprogrammable mechanical metamaterials. *Science* **345**, 647–650 (2014).
- Waitukaitis, S., Menaut, R., Chen, B. G.-g. & van Hecke, M. Origami multistability: From single vertices to metasheets. *Phys. Rev. Lett.* **114**, 055503 (2015).
- Lv, C., Krishnaraju, D., Konjevod, G., Yu, H. & Jiang, H. Origami based mechanical metamaterials. *Sci. Rep.* **4**, 5979–5981 (2014).
- Hanna, B. H., Lund, J. M., Lang, R. J., Magleby, S. P. & Howell, L. L. Waterbomb base: A symmetric single-vertex bistable origami mechanism. *Smart Mater. Struct.* **23**, 094009 (2014).
- Huffman, D. A. Curvature and creases: A primer on paper. *IEEE Trans. Comput.* **25**, 1010–1019 (1976).
- Tachi, T. in *Proceedings of the International Association for Shell and Spatial Structures (IASS) Symposium: Evolution and Trends in Design, Analysis and Construction of Shell and Spatial Structures* (eds Domingo, A. & Lazaro, C.) 2287–2294 (Editorial Universitat Politècnica de València, 2009); <http://go.nature.com/HbzSH1>
- Hull, T. *Project Origami: Activities for Exploring Mathematics* (CRC Press, 2012).
- Thiria, B. & Adda-Bedia, M. Relaxation mechanisms in the unfolding of thin sheets. *Phys. Rev. Lett.* **107**, 025506 (2011).
- Dias, M. A., Dudte, L. H., Mahadevan, L. & Santangelo, C. D. Geometric mechanics of curved crease origami. *Phys. Rev. Lett.* **109**, 114301 (2012).
- Lechenault, F., Thiria, B. & Adda-Bedia, M. Mechanical response of a creased sheet. *Phys. Rev. Lett.* **112**, 244301 (2014).
- Feng, S. & Sen, P. N. Percolation on elastic networks: New exponent and threshold. *Phys. Rev. Lett.* **52**, 216–219 (1984).
- Broedersz, C. P., Mao, X., Lubensky, T. C. & MacKintosh, F. C. Criticality and isostaticity in fibre networks. *Nature Phys.* **7**, 983–988 (2011).
- Silverberg, J. L. *et al.* Structure-function relations and rigidity percolation in the shear properties of articular cartilage. *Biophys. J.* **107**, 1–10 (2014).
- Sun, K., Souslov, A., Mao, X. & Lubensky, T. Surface phonons, elastic response, and conformal invariance in twisted kagome lattices. *Proc. Natl Acad. Sci. USA* **109**, 12369–12374 (2012).
- Kane, C. & Lubensky, T. Topological boundary modes in isostatic lattices. *Nature Phys.* **10**, 39–45 (2013).
- Chen, B. G.-g., Upadhyaya, N. & Vitelli, V. Nonlinear conduction via solitons in a topological mechanical insulator. *Proc. Natl Acad. Sci. USA* **111**, 13004–13009 (2014).
- Paulose, J., Chen, B. G.-g. & Vitelli, V. Topological modes bound to dislocations in mechanical metamaterials. *Nature Phys.* **11**, 153–156 (2015).
- Liu, A. J. & Nagel, S. R. Nonlinear dynamics: Jamming is not just cool any more. *Nature* **396**, 21–22 (1998).
- Keys, A. S., Abate, A. R., Glotzer, S. C. & Durian, D. J. Measurement of growing dynamical length scales and prediction of the jamming transition in a granular material. *Nature Phys.* **3**, 260–264 (2007).
- Van den Wildenberg, S., van Loo, R. & van Hecke, M. Shock waves in weakly compressed granular media. *Phys. Rev. Lett.* **111**, 218003 (2013).
- Thorpe, M. Continuous deformations in random networks. *J. Non-Cryst. Solids* **57**, 355–370 (1983).
- Heyman, J. *The Science of Structural Engineering* (World Scientific, 1999).
- Maxwell, J. C. On the calculation of the equilibrium and stiffness of frames. *Lond. Edinb. Dubl. Phil. Mag. J. Sci.* **27**, 294–299 (1864).
- Calladine, C. Buckminster Fuller's "tensegrity" structures and Clerk Maxwell's rules for the construction of stiff frames. *Int. J. Solids Struct.* **14**, 161–172 (1978).
- Demaine, E. D., Demaine, M. L., Hart, V., Price, G. N. & Tachi, T. (Non) existence of pleated folds: How paper folds between creases. *Graphs Combinator.* **27**, 377–397 (2011).
- Hull, T. C. *Origami<sup>3</sup>: Proceedings of the Third International Meeting of Origami Science, Mathematics, and Education* 29–38 (A K Peters, 2002).
- Fantner, G. E. *et al.* Sacrificial bonds and hidden length: Unraveling molecular mesostructures in tough materials. *Biophys. J.* **90**, 1411–1418 (2006).
- Bende, N. P. *et al.* Geometrically controlled snapping transitions in shells with curved creases. Preprint at <http://arxiv.org/abs/1410.7038> (2014).
- Na, J.-H. *et al.* Programming reversibly self-folding origami with micropatterned photo-crosslinkable polymer trilayers. *Adv. Mater.* **27**, 79–85 (2015).

## Acknowledgements

The authors thank J. Mosely, U. Nguyen, B. Johnson, B. Parker and M. Schneider for artistic inspiration, as well as O. Vincent, N. Bende, C.-K. Tung, S. Waitukaitis and the Cohen lab for useful discussions. We also thank F. Parish for assistance with the laser cutter. This work was funded by the National Science Foundation through award EFRI ODISEI-1240441.

## Author contributions

J.L.S., J.-H.N., R.C.H. and I.C. designed the research; J.L.S., J.-H.N. and A.A.E. conducted the research and interpreted the results; B.L., T.C.H., C.D.S., R.J.L., R.C.H. and I.C. supervised the research and interpreted the results; J.L.S., J.-H.N., A.A.E., T.C.H., R.J.L. and I.C. prepared the manuscript.

## Additional information

Supplementary information is available in the online version of the paper. Reprints and permissions information is available online at [www.nature.com/reprints](http://www.nature.com/reprints). Correspondence and requests for materials should be addressed to J.L.S.

## Competing financial interests

The authors declare no competing financial interests.

## Origami structures with a critical transition to bistability arising from hidden degrees of freedom

Jesse L. Silverberg,<sup>1,\*</sup> Jun-Hee Na,<sup>2</sup> Arthur A. Evans,<sup>3</sup> Bin Liu,<sup>1</sup> Thomas C. Hull,<sup>4</sup>  
Christian D. Santangelo,<sup>3</sup> Robert J. Lang,<sup>5</sup> Ryan C. Hayward,<sup>2</sup> and Itai Cohen<sup>1</sup>

<sup>1</sup>Physics Department, Cornell University, Ithaca, NY 14853, USA

<sup>2</sup>Department of Polymer Science and Engineering,

University of Massachusetts, Amherst, MA 01003, USA

<sup>3</sup>Department of Physics, University of Massachusetts, Amherst, MA 01003, USA

<sup>4</sup>Department of Mathematics, Western New England University, Springfield, MA 01119, USA

<sup>5</sup>Lang Origami, Alamo, CA 94507

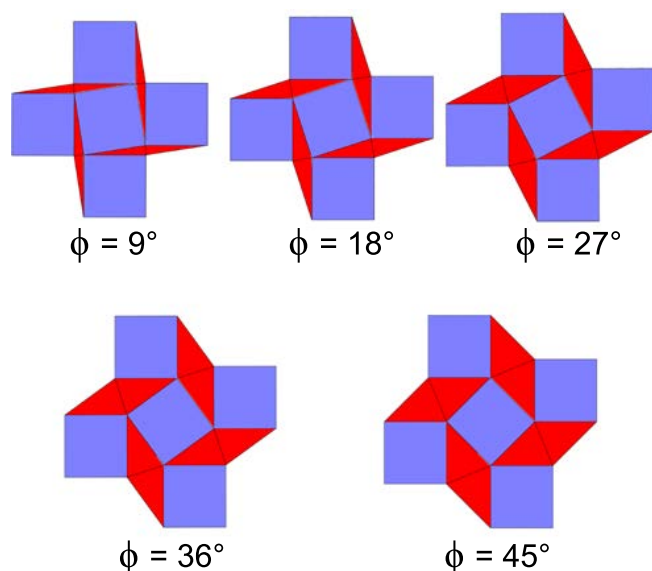


FIG. S1. These schematics show crease patterns for square twists with various plane angles.

### ADDITIONAL SCHEMATICS

To supplement the crease pattern shown in the main text where the plane angle  $\phi = 45^\circ$ , additional fold patterns are shown here with different plane angles  $\phi$  (Fig. S1).

### COUNTING SQUARE TWIST DOF

The number of DOF for a generic polyhedral surface in 3D with no holes can be derived from Euler's polyhedral formula and is expressed as<sup>1,2</sup>

$$\text{DOF} = N_{E,b} - 3 - \sum_{N_{f,i} > 3} (N_{f,i} - 3), \quad (\text{S1})$$

where  $N_{E,b}$  is the number of edges on the boundary and  $N_{f,i}$  is the number of edges of the  $i^{\text{th}}$  facet. For the generic square twist (Fig. 1(a) and S1),  $N_{E,b} = 12$ ,  $N_{f,i} = 4$  for  $i = 1, \dots, 9$ , giving zero DOF. This is consistent with the observation that the *generic* quad mesh

is locked, and thus has no flexibility. As is well-known, there are special non-generic quad meshes such as the Miura-ori<sup>3</sup> for which symmetry makes some constraints redundant. For the Miura-ori this restores one DOF, but in general, more DOF can be restored depending on the specific symmetries. Along these lines, square twists with modified mountain and valley crease assignments are known to be rigidly foldable with one DOF<sup>4</sup>.

### PREDICTED SOLUTIONS FOR RIGID FACETS

Given the crease pattern alone, a trigonometric analysis reveals the square twist should have two configurations corresponding to the folded and unfolded states. Defining the angle  $\Theta$  to be any of the valley creases on the interior square facet, we calculate the distance between the two points that define the folding order parameter  $\delta$  and find the constraint  $\cos^2 \Theta = 1$ . Thus,  $\Theta = 0$  or  $\pi$ , which respectively, is the unfolded and folded configurations. Taking a similar approach and calculating  $\Delta x/L$ , we find

$$\Delta x/L = \left[ (1 + 2 \cos \phi \pm \sin \phi)^2 + (\pm 1 + 2 \sin \phi \mp \cos \phi)^2 \right]^{1/2}, \quad (\text{S2})$$

which was used to plot the two black contours in Fig. 1(c) of the main text.

### MODIFIED SQUARE TWIST WITH 1 DOF

As a simple way to explore the role of bending DOF in the square twist independent of the role played by energetics, we extend the rigid facet geometric model to permit bending along the short diagonals of each rhombus, effectively splitting them into two rigid isosceles triangles. Imposing 4-fold rotational symmetry constrains the crease pattern so that only 1 DOF is added to the system. Using MATLAB, we sweep through  $\phi$  from  $0^\circ$  to  $45^\circ$  in steps of  $2.5^\circ$  and solve for the folding order parameter  $\delta$  as the rhombus facet bending angle  $\psi_{\text{rhomb}}$  is varied. We take a maximum deflection of  $\psi_{\text{rhomb}}$  to



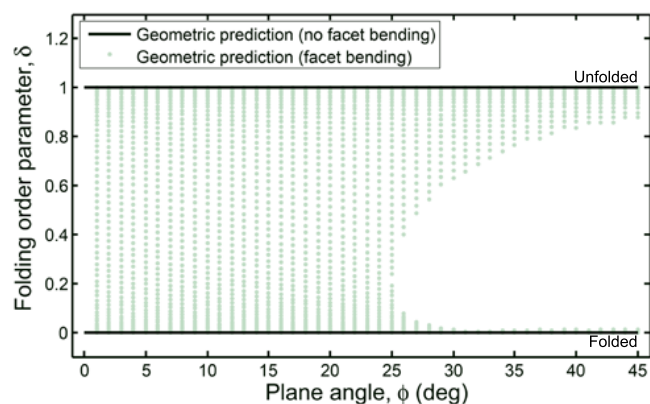


FIG. S2. Bifurcation of the folding order parameter  $\delta$  when 1 DOF is added from facet bending. For a rigid square twist,  $\delta = 0$  when folded, 1 when unfolded, and due to geometric constraints forbidden from taking any intermediate value (black lines). Introducing bending allows  $\delta$  to take intermediate values (green dots) with a critical point at  $\phi_c = (23 \pm 2)^\circ$  that separates a continuously connected region ( $\phi < \phi_c$ ) from a region with disconnected solutions ( $\phi > \phi_c$ ). Green points are uniformly spaced in the bending angle  $\psi_{\text{rhomb}}$ , and the forbidden configurations ( $\phi > \phi_c$ , white space) corresponds to the region with rapid unfolding dynamics (Fig. 2(a), main text).

be  $10^\circ$  and plot the solutions in the  $(\delta, \phi)$  configuration space (Fig. S2). In contrast to the experiments and detailed mechanical simulation described in the main text, each crease DOF here has a bending stiffness  $k_c = 0$ , and each bending DOF has  $k_b = 0$  for  $\psi_{\text{rhomb}} \leq 10^\circ$  and  $k_b = \infty$  for  $\psi_{\text{rhomb}} > 10^\circ$ . Though this constrained bending DOF is a coarse model for how bending works in real materials, it allows us to isolate kinetic properties of the structure and their consequences for configuration space. Indeed, similar to experimental observations, we find a bifurcation at  $\phi_c = (23 \pm 2)^\circ$  with monostability for  $\phi < \phi_c$ , and bistability for  $\phi > \phi_c$ . Evidently, the extra DOF introduced by facet bending is a major factor that enables both the  $\phi$ -dependent bifurcation and foldability of the square twist.

## MEASURING FLEXURAL RIGIDITY

To normalize experimental force and energy data, the flexural rigidity  $D$  was measured from a strip of 120 lb paper whose dimensions were  $L \times 8.5L$ , with  $L = 2.54$  cm. To make this measurement, the strip was clamped horizontally, allowing a controlled length to be suspended under gravity. Digital photographs were taken from a side view so that the strip could be seen edge-on and its deflection determined (Fig. S3(a)). Thus, we captured a series of images where the suspended arc length  $\ell$  varied from  $L$  to  $8L$ , and with standard image tracking techniques, we extracted the vertical deflection  $y$  as a func-

tion of horizontal position  $x$  (Fig. S3(b), red line). This coordinate data was fit to the expression<sup>5</sup>

$$y = \left( \frac{\rho g t}{24D} \right) (x^4 - 4\ell x^3 + 6\ell^2 x^2), \quad (\text{S3})$$

where  $\rho$  is the measured paper density and  $t$  is the measured paper thickness (Fig. S3(c,d)). Eq. (S3) was derived for the small deflection limit and allowed us to perform a one-parameter fit for  $D$  as  $\ell$  was varied from  $L$  to  $8L$ . Generally, measurements for  $\ell < 2L$  were dominated by an intrinsic curvature in the paper. For  $\ell = 8L$  there were also noticeable deviations from the small-deflection approximation used to derive Eq. (S3). For all other values of  $\ell$ , the fits were tightly clustered around the median measured  $D$ . Flipping the strip over and repeating the measurements on the opposite side produced another set of values for  $D$  as a function of  $\ell$  that exhibited the same trends. Averaging the median values from each data set yielded the value used in the main text,  $D = (15.6 \pm 0.7) \times 10^{-3}$  N·m, where  $t = 0.356$  mm and  $\rho = 871$  kg/m<sup>3</sup>.

To convert the flexural rigidity  $D$  to the bending torsional elastic constant  $k_b$ , we note that bending is constrained by the crease pattern to occur over an area of length  $L$  and width  $s$ . Here,  $s$  is the bending arc length and, to a good approximation, is  $s \simeq L/10$  for our experiments. Thus, the bending energy is  $U_b = (D/2) \int R^{-2} dA$ , where the radius of curvature  $R = s/\psi$  and the integral is evaluated over the area where bending occurs. Approximating  $R$  as constant over the bend, we evaluate the integral and find  $U_b = (DL/2s)\psi^2 \equiv (L/2)k_b\psi^2$ . Thus,  $k_b = D/s \simeq 6$  N/rad.

## SQUARE TWISTS WITH DIFFERENT THICKNESS PAPER

In the main text data was presented on 120 lb paper (Fig. 2(b)). Here, we provide measurements of the tensile force  $F$  as a function of plane angle  $\phi$  and normalized extension  $\Delta x/L$  for 53 lb ( $D = 2.1 \times 10^{-3}$  N·m) and 28 lb ( $D = 0.53 \times 10^{-3}$  N·m) paper (Fig S4).

## MEASURING CREASE TORSIONAL STIFFNESS

A single mountain crease 21.6 cm in length was made in a sheet of 120 lb paper and loaded into our custom mechanical testing device<sup>3</sup>. The crease was deflected by 0.94 rad and found to have two linear responses corresponding to small ( $< 0.15$  rad) and large ( $> 0.15$  rad) deflections. For the small deflections characteristic of an elastic response, the torque was linearly proportional to angular deflection by a constant  $k_c = 170 \pm 20$  mN/rad, which we take as the crease torsional stiffness.

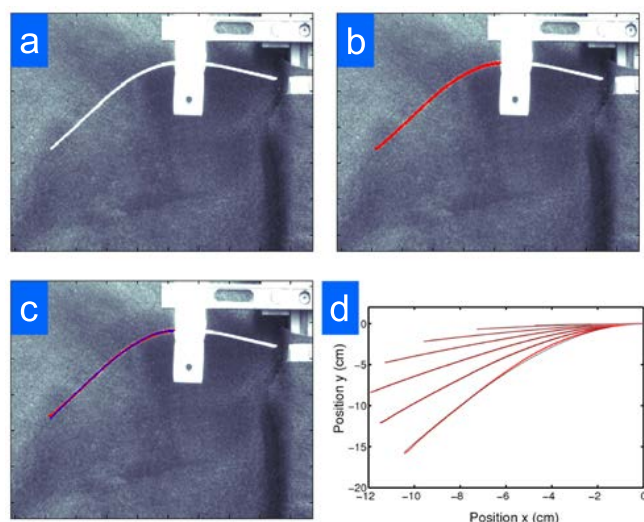


FIG. S3. Steps for measuring the flexural rigidity,  $D$ . (a) A strip of paper is clamped horizontally and allowed to sag under gravity. A photograph of the deflection is taken from the edge view, which extends to the left of the mounting armature. (b) Standard image analysis techniques are used to extract the vertical deflection,  $y$ , as a function of the horizontal position,  $x$ . The red line is the automatically tracked coordinate data superimposed on the corresponding photograph. (c) The measured deflection  $y(x)$  is fit to Eq. (S3) and is shown here in blue for comparison. (d) The process of fitting the deflection to Eq. (S3) is repeated for various lengths  $L$  of paper. This plot superimposes measured deflection for one strip of 7 lengths (red) and best-fits (black). As the fits are nearly indistinguishable from the data, we find this is a highly reliable method to determine  $D$ .

### SIMULATION AND EXPERIMENTAL ENERGY PLOTS

In the main text, we examined the bifurcation between mono- and bistability in terms of mechanically stable equilibrium points. Here, we provide an alternative and equivalent comparison presented in terms of the energy as a function of plane angle  $\phi$  and extension  $\Delta x/L$  (Fig. S5). Specifically, the normalized total energy in simulation and experiments both have a single local energy minimum below the critical plane angle and two energy minima above the critical plane angle. These minima correspond to the mechanically stable equilibrium points described in the main text.

### ESTIMATION OF SELF-FOLDING GEL $k_b$ AND $k_c$

For the self-folding gel sheets, considerations from continuum elasticity show the creases have an energy scale<sup>6</sup>

$$U_{\text{gel crease}} \sim \bar{E}_{\text{gel}} t_{\text{gel}}^3, \quad (\text{S4})$$

while the facets have a bending energy scale

$$U_{\text{gel facet}} \sim \bar{E}_{\text{rigid}} t_{\text{rigid}} t_{\text{gel}}^2. \quad (\text{S5})$$

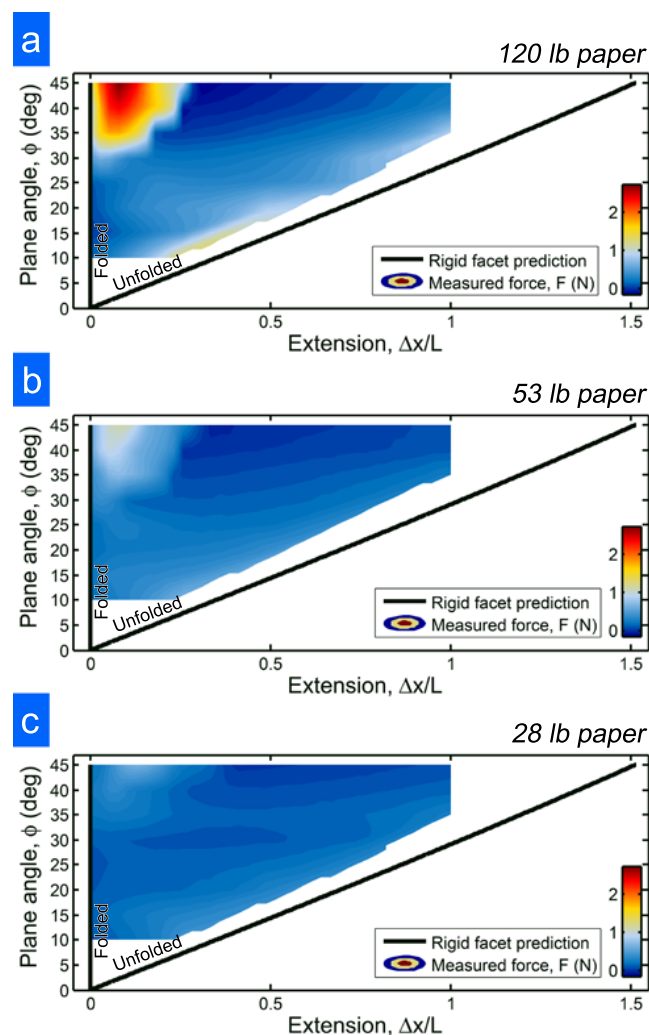


FIG. S4. Experimental strain-controlled mechanical data studying the transition between mono- and bistability in square twists. Measurements of the tensile force  $F(\phi, \Delta x/L)$  for (a) 120 lb paper, (b) 53 lb paper, and (c) 28 lb paper show the transition between mono- and bistability is generic, though the force barrier for  $\phi > \phi_c$  dramatically decreases as the paper becomes thinner.

Taking the PNIPAM gel plane-strain modulus  $\bar{E}_{\text{gel}} \sim 10^6$  Pa, the gel's thickness  $t_{\text{gel}} \sim 10^{-6}$  m, the plane-strain modulus of the rigid PpMS layer  $\bar{E}_{\text{rigid}} \sim 10^9$  Pa, and the PpMS layer thickness  $t_{\text{rigid}} \sim 10^{-7}$  m, we find

$$\frac{U_{\text{gel facet}}}{U_{\text{gel crease}}} \sim \frac{k_b}{k_c} \sim 10^2, \quad (\text{S6})$$

as was used in the main text.

### GLOBAL ENERGY MINIMA FOR STRESS-CONTROLLED LOADING

The custom simulation developed in MATLAB and described in the main text was designed to follow the kine-



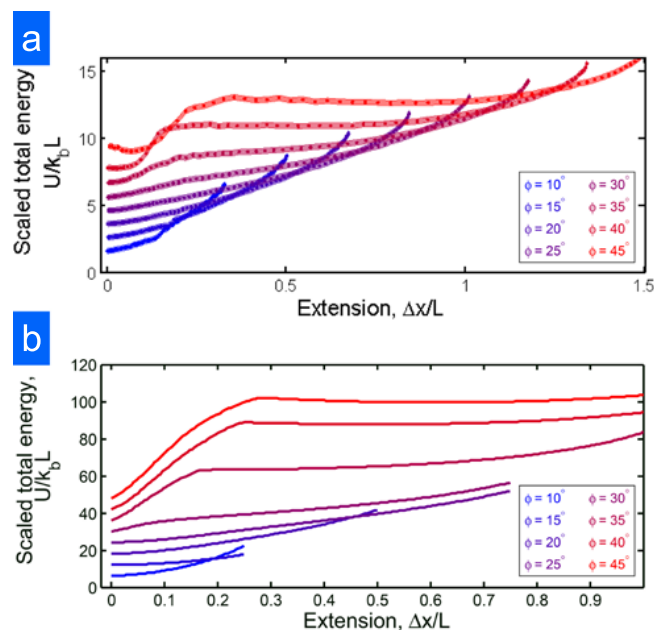


FIG. S5. Dimensionless square twist energy with local minima corresponding to mechanical equilibrium. (a) The sum of crease and bending energy from Fig. 3(d) of the main text shows how the competition between these different deformations gives rise to mono- and bistable regimes. (b) Integrating the experimentally measured force data produces a family of energy curves shown here with an offset, which agrees favorably with simulations.

mathematics of the square twist along a strain-controlled path in phase space. To determine the stress-controlled equivalent and obtain an independent check of our results, we utilized Tessellatica, a freely available Mathematica package. To implement the folding of the square twist in Tessellatica, we define the crease pattern by defining coordinates for 2D vertices, and assign edges to pairs of vertices with an associated mountain, valley, universal, or boundary attribute (Fig. 6(a)).

Valid folding configurations must obey the Kawasaki consistency conditions, which we briefly describe here. We start by drawing a closed curve around any given vertex and define the matrix  $A_i$  that rotates by the sector angle  $\alpha_i$  so that the  $i^{\text{th}}$  crease lies along one of the principal axes. Define the matrix  $C_i$  that rotates about the crease by an angle  $\pi - \gamma_i$ . The entire folded form can then be generated by applying the matrix  $\chi_i = A_i C_i A_i^{-1}$  to the  $i^{\text{th}}$  sector; this matrix rotates the whole sector to the crease, rotates the sector by the fold angle, and then rotates back. The Kawasaki consistency condition states that on a degree  $N$  vertex, the rigidity matrix  $R$  must satisfy the following<sup>7,8</sup>:

$$R = \chi_1 \chi_2 \dots \chi_{N-1} \chi_N = \mathcal{I}, \quad (\text{S7})$$

where  $\mathcal{I}$  is the identity matrix. This gives a system of equations for the fold angles of a vertex satisfying consistency.

To model the self-folding gel experiments, we start with a flat square twist where every crease angle is  $0^\circ$  at equilibrium, and define the 2D graph accordingly in Tessellatica (Fig. 6(a)). We then set a reference angle for each assigned crease, i.e.  $\Theta_0$  for valley creases and  $-\Theta_0$  for mountain creases. Facet bending is implemented by setting the target fold angles to zero for these “creases” in the 2D graph. The energy functional as given in the main manuscript is minimized subject to the Kawasaki vertex consistency constraint. The equilibrium opening distance  $x/L$  is determined for the case where  $k_b/k_c = 50$  as a function of plane angle  $\phi$  and target reference crease angle  $\Theta$  (Fig. 6(b)). This data shows the existence of a critical point  $\phi_c \approx (27.5 \pm 2.5)^\circ$ , below which  $x/L$  smoothly varies with  $\Theta$ , and above which, has a discontinuity. Because Tessellatica analytically solves for globally minimized energy structures, we do not recapitulate the hysteresis curves seen in the experimental measurements of self-folding square twists. The existence of the discontinuity in the global energy minimum, however, is precisely the signature that would be expected in light of this software feature.

## THE TRIANGLE TWIST

While the work presented here focuses on the square twist, it is not the only crease pattern that exhibits a geometrically-driven bifurcation between mono- and bistability. For example, the modified triangle twist<sup>9</sup> (Fig. S7) exhibits similar features. In this origami pattern, the plane angle  $\theta$  (Fig. S7(a)) has a critical point at  $\approx 67^\circ$ . This can be seen by varying  $\theta$  and plotting the folding angle  $a$ , which is  $0^\circ$  when unfolded and  $180^\circ$  when entirely folded. For  $\theta > \theta_c$ , a continuum of values for  $a$  is possible, whereas  $\theta < \theta_c$  has disconnected solutions (Fig. S7(b)).

It's interesting to note that this triangle twist is rigidly foldable while the square twist is not. Thus, the continuum of solutions for folding angle  $a$  does not require bending, whereas solutions in the geometrically forbidden region with do. This highlights an important point: The bifurcation in both square and triangle twists is a geometrically-driven phenomenon *independent* of whether bending occurs or not during the folding process. The path through this configuration space, however, depends sensitively on bending and crease DOF as well as the separation of energy scales  $k_b/k_c$ .

## SUPPLEMENTAL VIDEO CAPTIONS

**SI Video 1:** Demonstration of weak snapping between folded and unfolded states of a square twist with  $\phi \approx \phi_c$ .

**SI Video 2:** Demonstration of pronounced snapping instability between folded and unfolded states of a square

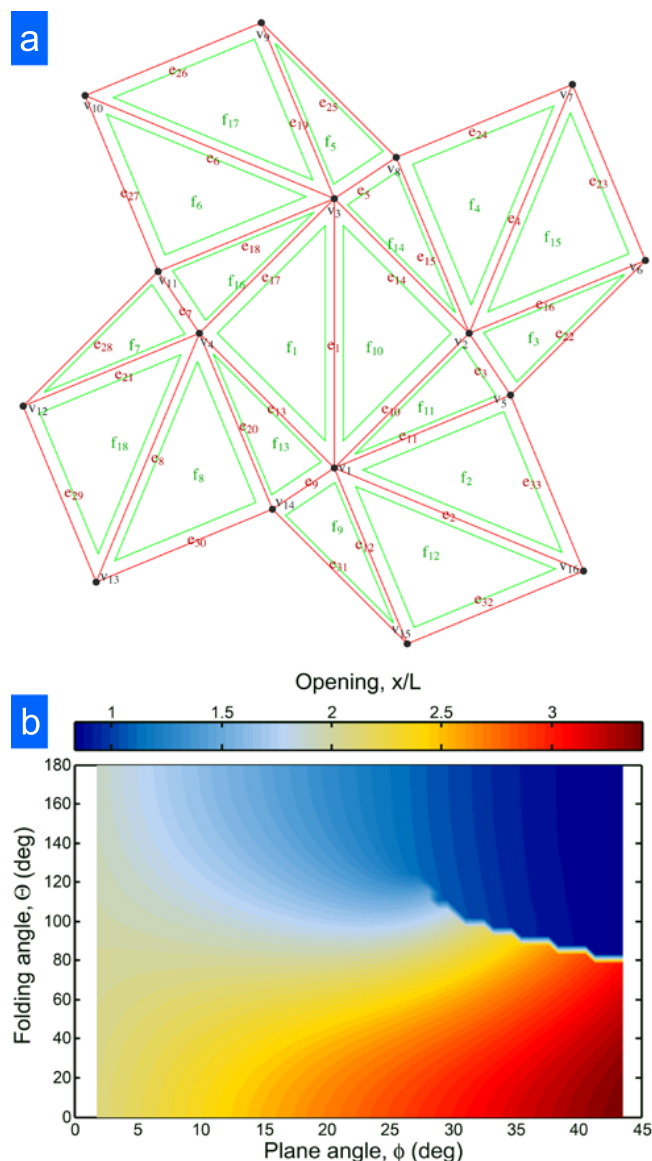


FIG. S6. Input and results from Tessellatica calculations of the stress-controlled square twist. (a) The 2D graph defined in Tessellatica that contains all the information about crease placement and facet bending. (b) Solving for the equilibrium structure as a function of plane angle  $\phi$ , we determine the square twist opening as the equilibrium value of the folding angle  $\Theta$  is varied from  $0^\circ$  to  $180^\circ$ . This simulates stress-controlled conditions and identifies the presence of a discontinuity at a critical plane angle.

twist with  $\phi > \phi_c$ .

\* JLS533@cornell.edu

- [1] Tachi, T. Geometric considerations for the design of rigid origami structures. In *Proceedings of the International Association for Shell and Spatial Structures (IASS) Symposium*, vol. 12, 458–460 (2010).
- [2] Lang, R. J. *Origami Design Secrets: Mathematical Meth-*

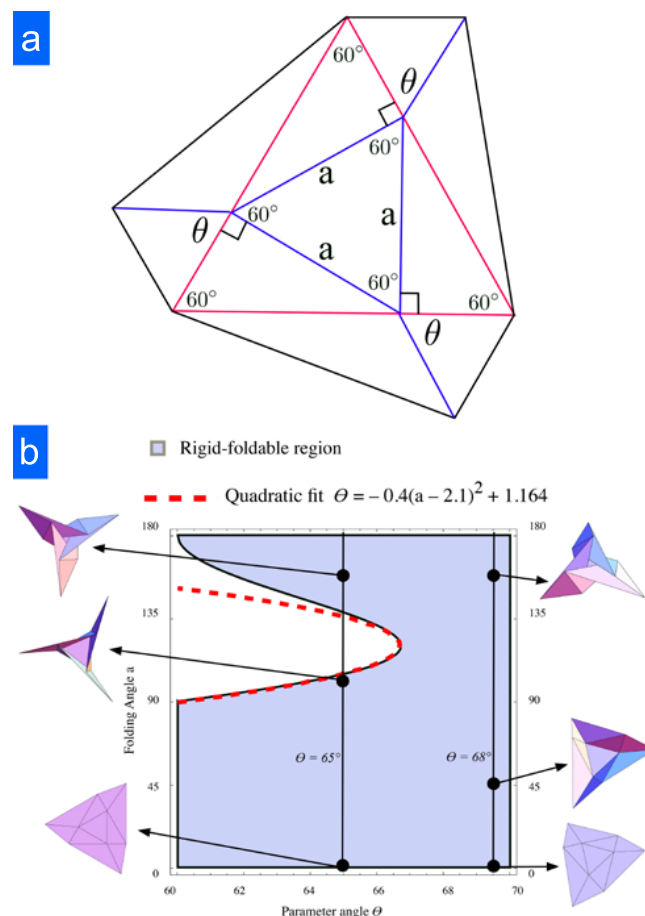


FIG. S7. The triangle twist is another folding pattern that exhibits a geometrically driven bifurcation point. (a) The crease pattern for this triangle twist is parameterized in terms of the plane angle  $\theta$  and the folding angle  $a$ . Red and blue lines are mountain and valley creases, respectively. (b) Solving for the geometrically allowed configuration space reveals a bifurcation in  $a$  as a function of  $\theta$ . Insets show examples of the structure along the indicated folding paths, while the red dashed line highlights the local shape of the bifurcation.

*ods for an Ancient Art* (CRC Press, 2011).

- [3] Silverberg, J. L. *et al.* Using origami design principles to fold reprogrammable mechanical metamaterials. *Science* **345**, 647–650 (2014).
- [4] Evans, T. A., Lang, R. J., Magleby, S. P. & Howell, L. *Rigidly Foldable Origami Twists* (submitted to ORIGAMI6, in review, 2014).
- [5] Landau, L. D. & Lifshitz, E. M. *Landau and Lifshitz Course of Theoretical Physics Volume 7: Theory of Elasticity* (Butterworth Heinemann, New Delhi, 1986), 3 edn.
- [6] Na, J.-H. *et al.* Programming reversibly self-folding origami with micropatterned photo-crosslinkable polymer trilayers. *Adv. Mater.* **27**, 79–85 (2015).
- [7] T, K. & K, M.  $r(\gamma) = i$ . In *Origami Science and Art: Proceedings of the Second International Meeting of Origami Science and Scientific Origami* (OSSO02 31–40, 1997).
- [8] Belcastro, S.-M. & Hull, T. C. Modelling the folding of paper into three dimensions using affine transformations. *Linear Algebra Appl.* **348**, 273–282 (2002).

- [9] Abel, Z., Hull, T. C. & Tachi, T. Locked rigid origami with multiple degrees of freedom. In *Origami<sup>6</sup>: Proceedings of the Sixth International Meeting of Origami Science, Math-*

*ematics, and Education* (submitted to ORIGAMI6, in review, 2014).

# TESSELLATICA CODE

Download and run Tessellatica from:

<http://www.langorigami.com/science/computational/tessellatica/tessellatica.php>

to predefine all the appropriate functions/objects/attributes. Using Mathematica 9, the following code calculates energies of the facets, creases, as well as the value of the order parameter  $x/L$ .

```
TSquareTwistEnergy[phi_, Gamma_, L_] :=
Module[{v1, v2, v1rot, v2rot, verts, edges, faces, types, tobj, tobjff,
faspecs, foldangles, alpha, getverts3d},
v1 = L{1, 1};
v1rot = L{-1, 1};
v2 = L{Sin[phi] + Cos[phi], Cos[phi] - Sin[phi]};
v2rot = L{Sin[phi] - Cos[phi], Cos[phi] + Sin[phi]};
verts = {{0, 0}, v1, v1 + v1rot, v1rot, v2, v2 + v1, v2 + v1 + v2rot,
v1 + v2rot, v1 + v2rot + v1rot, v1 + v2rot + v1rot - v2, v1 + v1rot - v2,
v1rot - v2, v1rot - v2 - v2rot, v1rot - v2rot, -v2rot, v2 - v2rot};
edges = {{1, 3}, {1, 16}, {2, 5}, {2, 7}, {3, 8}, {3, 10}, {4, 11}, {4, 13},
{1, 14}, {1, 2}, {1, 5}, {1, 15}, {1, 4}, {2, 3}, {2, 8}, {2, 6}, {3, 4},
{3, 11}, {3, 9}, {4, 14}, {4, 12}, {5, 6}, {6, 7}, {7, 8}, {8, 9},
{9, 10}, {10, 11}, {11, 12}, {12, 13}, {13, 14}, {14, 15}, {15, 16}, {16, 5}};
(*definedwithfacefoldsfirst, theninternalcreases, thenboundaries*)
faces = {};
types = {U, U, U, U, U, U, U, U, U, M, V, M, M, M, V, M, M, V, M, V, M, B,
B, B, B, B, B, B, B, B, B, B}; (*MMMM central face*)
tobj = MakeTGraph[verts, edges, faces]//AddTAssigned[types]//AddTPlaneGraph;
Do[
alpha = i * .45 * pi/18.1;
faspecs = {{sqrt[2]Gamma, 0}, {sqrt[2]Gamma, 0}, {2GammaSin[phi/2], 0}, {sqrt[2]Gamma, 0},
{2GammaSin[phi/2], 0}, {sqrt[2]Gamma, 0}, {2GammaSin[phi/2], 0}, {sqrt[2]Gamma, 0},
{2GammaSin[phi/2], 0}, {1, -alpha}, {1, alpha}, {1, -alpha}, {1, -alpha}, {1, -alpha},
{1, alpha}, {1, -alpha}, {1, -alpha}, {1, alpha}, {1, -alpha}, {1, alpha}, {1, -alpha}, {infinity, 0},
{infinity, 0}, {infinity, 0}, {infinity, 0}, {infinity, 0}, {infinity, 0}, {infinity, 0}, {infinity, 0},
{infinity, 0}, {infinity, 0}, {infinity, 0}};
foldangles = MakeGraphFoldAngles[tobj, faspecs];
tobjff = FoldGraph3D[tobj, foldangles, StationaryFace -> 1];
getverts3d = GetValues[tobjff, {Vertices3D}];
FaceEnergy[[i]] = Sum [faspecs[[j, 1]] * foldangles[[j]]^2, {j, 1, 9}];
CreaseEnergy[[i]] = Sum [(foldangles[[j]] - faspecs[[j, 2]])^2, {j, 10, 21}];
ShapeList[[i]] = FoldedFormGraphics3D[tobjff]/.OrigamiStyle[];
Folds[[i]] = foldangles;
Deltas[[i]] =
sqrt(((getverts3d[[1, 14]] - getverts3d[[1, 8]])
(getverts3d[[1, 14]] - getverts3d[[1, 8]]));,
{i, 1, 40}]
]
```





# Lattice mechanics of origami tessellations

Arthur A. Evans,<sup>1,\*</sup> Jesse L. Silverberg,<sup>2</sup> and Christian D. Santangelo<sup>1</sup>

<sup>1</sup>*Department of Physics, UMass Amherst, Amherst, Massachusetts 01003, USA*

<sup>2</sup>*Department of Physics, Cornell University, Ithaca, New York 14853, USA*

(Received 18 March 2015; published 27 July 2015)

Origami-based design holds promise for developing materials whose mechanical properties are tuned by crease patterns introduced to thin sheets. Although there have been heuristic developments in constructing patterns with desirable qualities, the bridge between origami and physics has yet to be fully developed. To truly consider origami structures as a class of materials, methods akin to solid mechanics need to be developed to understand their long-wavelength behavior. We introduce here a lattice theory for examining the mechanics of origami tessellations in terms of the topology of their crease pattern and the relationship between the folds at each vertex. This formulation provides a general method for associating mechanical properties with periodic folded structures and allows for a concrete connection between more conventional materials and the mechanical metamaterials constructed using origami-based design.

DOI: [10.1103/PhysRevE.92.013205](https://doi.org/10.1103/PhysRevE.92.013205)

PACS number(s): 46.25.Cc, 05.50.+q, 62.20.-x, 81.05.Zx

## I. INTRODUCTION

While for hundreds of years origami has existed as an artistic endeavor, recent decades have seen the application of folding thin materials to the fields of architecture, engineering, and material science [1–7]. Controlled actuation of thin materials via patterned folds has led to a variety of self-assembly strategies in polymer gels [8] and shape-memory materials [4], as well elastocapillary self-assembly [9], leading to the design of a new category of shape-transformable materials inspired by origami design. The origami repertoire itself, buoyed by advances in the mathematics of folding and the burgeoning field of computational geometry [10], is no longer limited to designs of animals and children's toys that dominate the art in popular consciousness, but now includes tessellations, corrugations, and other nonrepresentational structures whose mechanical properties are of interest from a scientific perspective. These properties originate from the confluence of geometry and mechanical constraints that are an intrinsic part of origami and ultimately allow for the construction of mechanical metamaterials using origami-based design [1–4,6,11–13]. In this paper we formulate a general theory for periodic lattices of folds in thin materials and combine the language of traditional lattice solid mechanics with the geometric theory underlying origami.

A distinct characteristic of all thin materials is that geometric constraints dominate the mechanical response of the structure. Because of this strong coupling between shape and mechanics, it is far more likely for a thin sheet to deform by bending without stretching. Strategically weakening a material with a crease or fold, and thus lowering the energetic cost of stretching, allows complex deformations and reordering of the material for negligible elastic energy cost. This vanishing energy cost, especially combined with increased control over microscopic and nanoscopic material systems, indicates great promise for structures whose characteristics depend primarily on geometry, rather than material composition.

By patterning creases, hinges, or folds into an otherwise flat sheet (be it composed of paper, metal, or polymer gel), the

bulk material is imbued with an effective mechanical response. In contrast to conventional composites engineering, wherein methods generally rely on designing response based on the interaction between the constituent parts that compose the material, origami-based design injects novelty at the atomic level; even single vertices of origami behave as engineering mechanisms [14], providing novel functionality such as complicated bistability [15–17] and auxetic behavior [6,11–13]. This generic property inspires the identification of origami tessellations with mechanical metamaterials or a composite whose effective properties arise from the structure of the unit cell. Although originally introduced to guide electromagnetic waves [18], rationally designed mechanical metamaterials have since been developed that control wave propagation in acoustic media [19,20], thin elastic sheets, and curved shells [21–24] and harness elastic instabilities to generate auxetic behavior [25–29].

Traditional metamaterials invoke the theory of linear response in wave systems, but currently there is no general theory for predicting the properties of origami-inspired designs on the basis of symmetry and structure. In the following we propose a general framework for analyzing the kinematics and mechanics of an origami tessellation as a crystalline material. By treating a periodic crease pattern, we naturally connect the geometric mathematics of origami to the more conventional analysis of elasticity in solid state lattice structures. In Sec. II we outline the general formalism required to find the kinematic solutions for a single origami vertex. In Sec. III we discuss the general formulation for a periodic lattice, including both the kinematics of deformation modes and energetics for a periodic crease pattern. In Sec. IV we examine the well-known case study of the Miura-ori pattern. Our analysis here recovers known aspects of the Miura-ori pattern and identifies key features that have not been quantitatively discussed previously.

## II. SINGLE ORIGAMI VERTEX

Many of the design strategies for self-folding materials involves a single fold, an array of nonintersecting folds, or an array of folds that intersect only at the boundary of the material [9,30–33]. From a formal standpoint, we define a

\*artio.evans@gmail.com



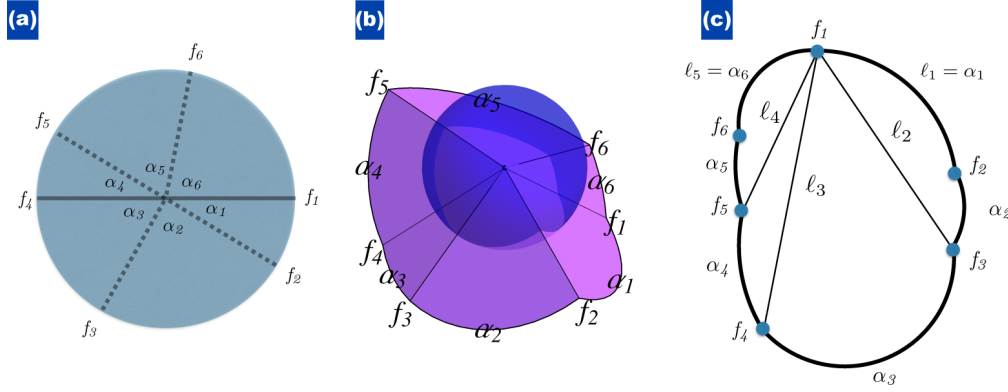


FIG. 1. (Color online) (a) Graph for a single vertex. This degree-6 vertex has its graph determined by the six sector angles  $\alpha_i$ . Each crease has a dihedral angle  $f_i$  associated with it. In the flat case every  $f_i = \pi$  or, equivalently, every fold angle is identically zero, since the fold angle is defined as the supplement of the dihedral angle. (b) By assigning fold angles to each crease, a three-dimensional embedding of the vertex (i.e., the folded form of the origami) is fully determined. Every face must rotate rigidly about the defined creases and the sector angles must remain constant. There is a limited set of fold angles that will solve these conditions. (c) Schematic projection of the curve of intersection between the unit sphere and the folded form origami. For an  $N$ -degree vertex this projection generates a spherical  $N$ -gon. To proceed, the  $N$ -gon is divided into  $N - 2$  spherical triangles and the interior angles (i.e., the  $f_i$ ) follow as a result of applying the rules of spherical trigonometry. All three-dimensional origami structures are visualized using *Tessellatica*, a freely available online package for *Mathematica* [34].

fold as a straight line demarcating the boundary between two flat sheets of unbendable, unstretchable material. These sheets, in isolation, are allowed to rotate around the fold so that the structure behaves mechanically like a simple hinge. If the fold is produced by plastically deforming a piece of material, rather than functioning as a hinge the fold has a preferred angle and is more precisely called a crease. Herein we shall use the terms interchangeably, since the kinematic motions of a fold and the energetics involved for a crease can be described separately. An important, and arguably defining, characteristic of an origami structure is that it requires that more than one fold meet at a vertex. While each fold individually allows for unrestricted rigid body rotation of a sheet, geometrical constraints arise when several folds coincide at a vertex. These constraints are what provide origami structures with their mechanical novelty and ultimately are why deployable structures and mechanical metamaterials display exotic and tunable properties.

A vertex of degree  $N$  is defined as a point where  $N$  straight creases meet. Figure 1(a) shows the crease pattern for a schematic six-degree vertex, with sectors defined by planar angles  $\alpha_i$ . The three-dimensional folded form of this vertex is found by supplying fold angles to each of the creases, subject to the constraints mentioned previously [35,36]. This procedure is an exercise in spherical trigonometry.

One way to visualize the constraints is to surround each vertex with a sphere and consider the intersection between it and the surface [Fig. 1(b)]. In this construction, the side lengths of the spherical polygon are the angles between adjacent folds, which must remain fixed, and the dihedral fold angles are the internal angles of the polygon on the sphere. Since an  $N$ -sided polygon has  $N - 3$  continuous degrees of freedom, each vertex does as well. These  $N - 3$  degrees of freedom can be thought of, for example, as the angles between a fixed fold and the remaining nonadjacent folds.

Starting with a general vertex containing dihedral angles  $f_i$ , we use spherical trigonometry to calculate these angles in terms of the  $N - 3$  degrees of freedom. To calculate  $f_1$  we

partition the angle into sectors by subdividing the spherical  $N$ -gon into  $N - 2$  triangles [Fig. 1(c)]. We label the angles that lead from  $f_1$  to  $f_i$  as  $\ell_i$ , where  $\ell_1 = \alpha_1$  and  $\ell_{N-1} = \alpha_N$  are sector angles. All the angles  $\alpha_i$  are spherical polygon edges and since origami structures allow only isometric deformations, these angles are constant. The  $\ell_i$  are the angles subtended by drawing a geodesic on the encapsulating sphere from  $f_1$  to  $f_{i+1}$ ; expressions for relating the  $\ell_i$  to the fold angles  $f_i$  are found by using the spherical law of cosines around the vertex [35]:

$$f_1 = \sum_{i=1}^{N-2} \cos^{-1} \left[ \frac{\cos \alpha_{i+1} - \cos \ell_{i+1} \cos \ell_i}{\sin \ell_{i+1} \sin \ell_i} \right], \quad (1)$$

$$f_2 = \cos^{-1} \left[ \frac{\cos \ell_2 - \cos \alpha_1 \cos \alpha_2}{\sin \alpha_1 \sin \alpha_2} \right], \quad (2)$$

$$f_N = \cos^{-1} \left[ \frac{\cos \ell_{N-2} - \cos \alpha_{N-1} \cos \alpha_N}{\sin \alpha_{N-1} \sin \alpha_N} \right], \quad (3)$$

$$f_i = \cos^{-1} \left[ \frac{\cos \ell_{i-2} - \cos \alpha_{i-1} \cos \ell_{i-1}}{\sin \ell_{i-1} \sin \alpha_{i-1}} \right] + \cos^{-1} \left[ \frac{\cos \ell_i - \cos \alpha_i \cos \ell_{i-1}}{\sin \ell_{i-1} \sin \alpha_i} \right]. \quad (4)$$

These expressions are essentially all that is required to determine the folding of a single vertex, although the associated solutions are generically multivalued. These results imply that there are multiple branches of configuration space for any given spherical polygon.

To specify the internal state of each vertex we define an  $N - 3$  component vector  $\mathbf{s}$ . Given the internal state of a vertex, all  $N$  of the dihedral fold angles are determined, which we collect in the vector  $\mathbf{f}(\mathbf{s})$ . In practice, computations are vastly simplified by choosing the appropriate degrees of freedom; for example, for a degree-6 vertex of the type displayed in Fig. 1, we choose  $\mathbf{s} = \{\ell_3, f_2, f_6\}$  and the fold vector is given by  $\mathbf{f} = \{f_1, f_2, f_3, f_4, f_5, f_6\}$ .

### III. GENERAL LATTICE THEORY

To determine the mechanical properties of an origami tessellation we begin by examining how many vertices are connected together in a crease pattern. When constructing a real piece of origami, artists and designers specify “mountain” and “valley” creases in the pattern to encode instructions for how the structure will fold. In our formulation we will treat the crease pattern as a simple connected graph, where each unique crease is an edge that connects two vertices to one another.

#### A. Kinematically allowed deformations

In addition to the origami constraints discussed above for a single vertex, joining multiple vertices together generates further constraints on the folds. Consider a crease pattern that consists of  $P$  vertices. Each vertex  $v_p$ , with  $p \in \{1, \dots, P\}$ , has  $N_p$  folds, collected in the vector  $\mathbf{f}^p = (f_1^p f_2^p \dots f_{N_p}^p)^T$ . If we collect all the folds into the vector  $\mathcal{F}$ , given by

$$\mathcal{F} = \begin{pmatrix} f_1^1 \\ f_2^1 \\ \vdots \\ f_{N_1}^1 \\ f_1^2 \\ f_2^2 \\ \vdots \\ f_{N_2}^2 \\ \vdots \\ f_1^P \\ f_2^P \\ \vdots \\ f_{N_P}^P \end{pmatrix}, \quad (5)$$

then we have the following constraint equation for the folds:

$$\mathbf{D}\mathcal{F} = \mathbf{0}, \quad (6)$$

where  $\mathbf{D}$  is a sparse rectangular matrix that enforces the condition that if two vertices  $v_q, v_p$  are adjacent and two folds  $\mathcal{F}_i, \mathcal{F}_j$  connect  $v_q, v_p$ , then  $\mathcal{F}_i = \mathcal{F}_j$  (see Fig. 2 for an example). This constraint enforces the connectivity of the graph, since each unique crease clearly must have a compatible fold angle associated with the vertices that connect it. Each

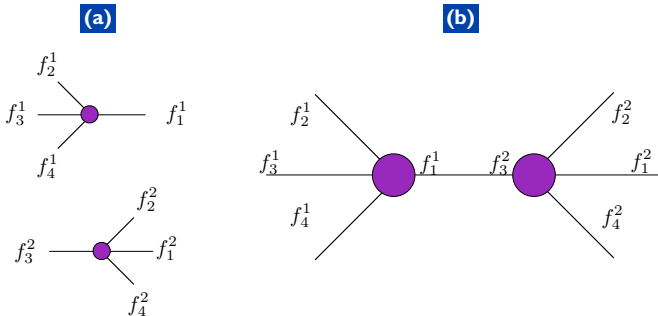


FIG. 2. (Color online) (a) Two degree-4 vertices with labeled folds. (b) Graph for the crease pattern consisting of these two vertices contains a single crease that is shared by both vertices. In this case the constraint equation  $\mathbf{D}\mathcal{F} = \mathbf{0}$  simply becomes the scalar relationship  $f_1^1 = f_3^2$ .

row of  $\mathbf{D}$  corresponds to a fold connecting a pair of vertices in the origami tessellation while each column corresponds to a component of  $\mathcal{F}$ . Analysis of this construction is the essence of origami mechanics and lies at the heart of the difficulty in determining general properties of tessellations and corrugations. Finding the null vectors of  $\mathbf{D}$  amounts to finding all of the possible solutions for the fold angles and thus all of the kinematically allowed motions of the rigid origami. While computational methods have been developed for simulating the kinematics of origami and linkage structures [2,6,11,12], there has been no general analytical study that seeks to identify mechanical properties based solely on the crease pattern.

The functions  $\mathcal{F}(\mathbf{s})$  are, in general, nonlinear. To proceed analytically, we expand  $\mathbf{s}$  about a state  $\mathbf{s}_0$  that solves the constraint equations. That is, if  $\mathcal{F}(\mathbf{s}_0) = \mathcal{F}_0$  then  $\mathbf{D}\mathcal{F}_0 \equiv \mathbf{0}$ . A trivial choice for  $\mathbf{s}_0$  has every entry identically equal to  $\pi$ , indicating that the piece of origami is unfolded. The more common, and more interesting, scenario involves a folded state where the values of the internal vector  $\mathbf{s}_0$  are known. Assuming that such a state exists, we write  $\mathbf{s} = \mathbf{s}_0 + \delta\mathbf{s}$ , with  $\delta\mathbf{s}$  a small perturbation, and then have

$$\mathbf{D}\mathbf{J}\delta\mathbf{s} \equiv \mathbf{R}\delta\mathbf{s} = \mathbf{0}, \quad (7)$$

where the Jacobian of the fold angles for each vertex  $\mathbf{J} \equiv \partial\mathcal{F}/\partial\mathbf{s}|_{\mathbf{s}_0}$  is a block diagonal matrix defining the small deviations from the ground state  $\mathbf{s}_0$  and  $\mathbf{R}$  is a rigidity matrix that informs on the infinitesimal isometric deformations of the origami structure [37,38]. This formulation is convenient since it separates the effects of the crease pattern topology (contained entirely in  $\mathbf{D}$ ) from the constrained motion of a single vertex (contained entirely in  $\mathbf{J}$ ). We can thus solve for each of these matrices individually.

To find  $\mathbf{D}$ , we first exploit the periodicity of the lattice to decompose the vector  $\mathcal{F}$  and matrix  $\mathbf{D}$  in a Fourier basis such that  $\mathcal{F} = \sum_{n,m} e^{i\mathbf{q}\cdot\mathbf{x}} \mathcal{F}_q + \text{c.c.}$  Here  $\mathbf{q}$  is a two-dimensional wave vector and  $\mathbf{x} = n\mathbf{a}_1 + m\mathbf{a}_2$  is the two-dimensional position vector of the fundamental unit cell on the crease pattern lattice, where  $(n,m)$  indexes this position in terms of the lattice vectors  $\mathbf{a}_{1,2}$ . Since  $\mathcal{F} \approx \mathbf{J}\delta\mathbf{s}$  and  $\mathbf{J}$  is independent of the lattice position, we also have  $\delta\mathbf{s} = \sum_{n,m} e^{i\mathbf{q}\cdot\mathbf{x}} \delta\mathbf{s}_q + \text{c.c.}$ , where  $\mathcal{F}_q = \mathbf{J}\delta\mathbf{s}_q$ . In this representation the constraints given in Eq. (6) are

$$\mathbf{D}(\mathbf{q})\mathcal{F}_q = \mathbf{D}(\mathbf{q})\mathbf{J}\delta\mathbf{s}_q = \mathbf{0}. \quad (8)$$

Now, instead of a matrix operation over all the vertices, the size of  $\mathbf{D}(\mathbf{q})$  is vastly simplified. For a pattern with  $p$  distinct vertices per unit cell, each of degree  $N_p$ ,  $\mathbf{D}(\mathbf{q})$  is a  $\sum_{i=1}^p (N_i/2) \times \sum_{i=1}^p N_i$  matrix. In Fourier space,  $\mathbf{D}(\mathbf{q})$  is the complex-valued constraint matrix for the graph of the unit cell vertices and folds. Specifically, each fold of the unit cell is represented by a row in  $\mathbf{D}(\mathbf{q})$  having only two nonzero entries. Those entries all have the form  $\pm e^{i\mathbf{q}\cdot\mathbf{a}_1}$ ,  $\pm e^{i\mathbf{q}\cdot\mathbf{a}_2}$ ,  $\pm 1$ , depending on whether the fold connects to an adjacent unit cell along  $\mathbf{a}_{1,2}$  or is internal to the unit cell.

The formulation in terms of the matrix  $\mathbf{R}(\mathbf{q})$  is completely general for any origami tessellation. The rectangular matrix  $\mathbf{D}(\mathbf{q})$  carries all of the topological information regarding the fold network, while the Jacobian  $\mathbf{J}$  carries the information about the type of vertex that has been specified;  $\mathbf{J}$  will be



block diagonal with one block for each vertex of a unit cell, but does not depend on  $\mathbf{q}$  for a regular tessellation.

### B. Origami energetics

While the  $\mathbf{R}$  matrix determines the kinematically isometric deformation to leading order, these constraints are generally not the end of the story for real materials. Creases in folded paper, thermoresponsive gels with programmed folding angles, and elastocapillary hinges all balance energetic considerations with geometric constraints. In many cases these creases and hinges act as torsional springs, while the bending of faces have additional elastic energy content [7,39,40].

The energy associated with the entire structure may be written, to quadratic order in the dihedral vectors, as

$$\mathcal{E} = \frac{1}{2}(\mathcal{F} - \mathcal{F}_0)^T \mathcal{A}(\mathcal{F} - \mathcal{F}_0), \quad (9)$$

where  $\mathcal{A}$  is a general stiffness matrix and  $\mathcal{F}_0$  is a reference fold angle. For linear response this is the most generic form for the energy. In the simplest of cases  $\mathcal{A}$  is constant over the lattice and diagonal with respect to  $\mathcal{F}$ ; this models each crease as a torsional spring with uniform spring constant [7,13,40]. A small amplitude response is found by examining the origami structure near the ground state, that is, when  $\mathcal{F} = \mathcal{F}_0$ . When the energy is expanded about the ground state  $\mathcal{E}_0$  we find

$$\mathcal{E} = \mathcal{E}_0 + \frac{1}{2} \delta \mathbf{s}^T \mathbf{J}^T \mathbf{A} \mathbf{J} \delta \mathbf{s}, \quad (10)$$

or in the Fourier decomposition

$$\mathcal{E} = \frac{LW}{2} \sum_{\mathbf{q}} \delta \mathbf{s}_{\mathbf{q}}^\dagger \mathcal{M} \delta \mathbf{s}_{\mathbf{q}}, \quad (11)$$

where  $L$  is the length of the tessellation in the  $\mathbf{a}_1$  direction,  $W$  is the width in the  $\mathbf{a}_2$  direction, and  $\mathcal{M} = \mathbf{J}^T \mathbf{A} \mathbf{J}$  is a matrix operator that is independent of wave number. Since the null space of  $\mathbf{R}(\mathbf{q})$  will determine the modes of deformation, the solution to this problem lies in finding the kinematically allowed deformations and then any energetic description will simply involve a change of basis to a system of deformations that diagonalize the operator  $\mathcal{M}$ .

### IV. MIURA-ORI

As an example of this formulation, we consider inhomogeneous deformations of a particular origami metamaterial, the Miura-ori. First introduced as a framework for a deployable surface, the design appears often in nature, from plant leaves [41] to animal viscera [42]. Additionally, theoretical calculations and experiments have suggested the Miura-ori as a canonical, origami-based, auxetic metamaterial [6,7,11–13]. Its ubiquity may be related to its simplicity: The Miura-ori is determined from a single crease angle  $\alpha$  and the mountain and valley assignments of the pattern shown in Fig. 3. Conventional origami mathematics considers that each Miura-ori vertex is degree 4 and thus there is only one degree of freedom. However, casual experimentation with a real Miura-ori quickly demonstrates that it has far more than one degree of freedom, indicating an array of soft modes enabled by the bending of the individual faces. This breakdown of the assumptions of mathematical origami is well known and there are many crease patterns that are mathematically impossible to fold that can in

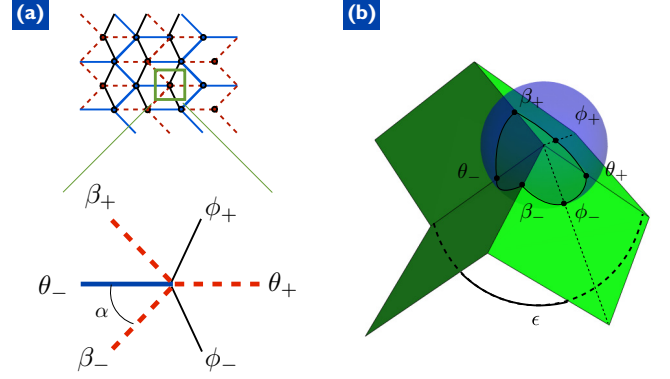


FIG. 3. (Color online) (a) While the crease pattern of a Miura-ori generally introduces only four folds per vertex, the bending of faces acts to allow two extra folds per vertex, so the crease pattern we consider is a triangulated lattice. At each vertex the dihedral angles contained in  $\mathbf{f}$  are determined by specifying the state vector  $\mathbf{s}$  and satisfying the geometric constraints. (b) Single-vertex origami with enclosing sphere to visualize the constraints between  $\mathbf{f}$  and  $\mathbf{s}$ .

fact be done with little effort [43]. To incorporate these extra degrees of freedom into Miura-ori, we assume that there are two extra folds per vertex to account for face bending. While in the extreme case of the creases being perfectly rigid these extra folds would actually take the form of stretching ridges [44], many real applications involve fabrication processes that will allow the face to be well approximated as perfect bending. Each unit cell in the tessellation has four six-valent vertices (Fig. 3) so there are 12 degrees of freedom per unit cell. In this example the fold vector for the  $i$ th vertex is given by  $\mathbf{f}^i = (\theta_+^i, \phi_+^i, \beta_+^i, \theta_-^i, \beta_-^i, \phi_-^i)^T$  and the vector  $\mathcal{F} = (\mathbf{f}^1 \mathbf{f}^2 \mathbf{f}^3 \mathbf{f}^4)^T$ . There are three degrees of freedom per vertex that define the internal state  $\mathbf{s}$ , which we parametrize using three angles:  $\epsilon$ , the angle between folds labeled  $\theta_{\pm}$  in Fig. 3, and the angles  $\phi_{\pm}$  representing the bending of the faces. Using the geometric relationships between the angles [35], we find the general nonlinear relationship for a single vertex and then expand about the ground state  $\mathbf{s}_0 = \{\epsilon + \delta\epsilon, \pi + \delta\phi_+, \pi + \delta\phi_-\}$  to find the matrix  $\mathbf{J}$ ; here  $\epsilon \in [\pi - 2\alpha, \pi + 2\alpha]$ . This expansion naturally follows from assuming that the faces are nearly flat and that the Miura-ori has been folded into the standard configuration. The Jacobian  $\mathbf{J} = \text{diag}(\mathbf{J}_0 \quad -\mathbf{J}_0 \quad \mathbf{J}_0 \quad -\mathbf{J}_0)$  is a  $24 \times 12$  diagonal block matrix formed from four identical blocks

$$\mathbf{J}_0 = \begin{pmatrix} A & C & C \\ 0 & 1 & 0 \\ B & C & 0 \\ -A & 0 & 0 \\ B & 0 & C \\ 0 & 0 & 1 \end{pmatrix}, \quad (12)$$

where

$$A = \cos \alpha \csc(\epsilon/2) / \sqrt{\sin^2(\epsilon/2) - \cos^2 \alpha}, \quad (13)$$

$$B = \sin(\epsilon/2) / \sqrt{\sin^2(\epsilon/2) - \cos^2 \alpha}, \quad (14)$$

$$C = \csc(\alpha/2) / 2. \quad (15)$$

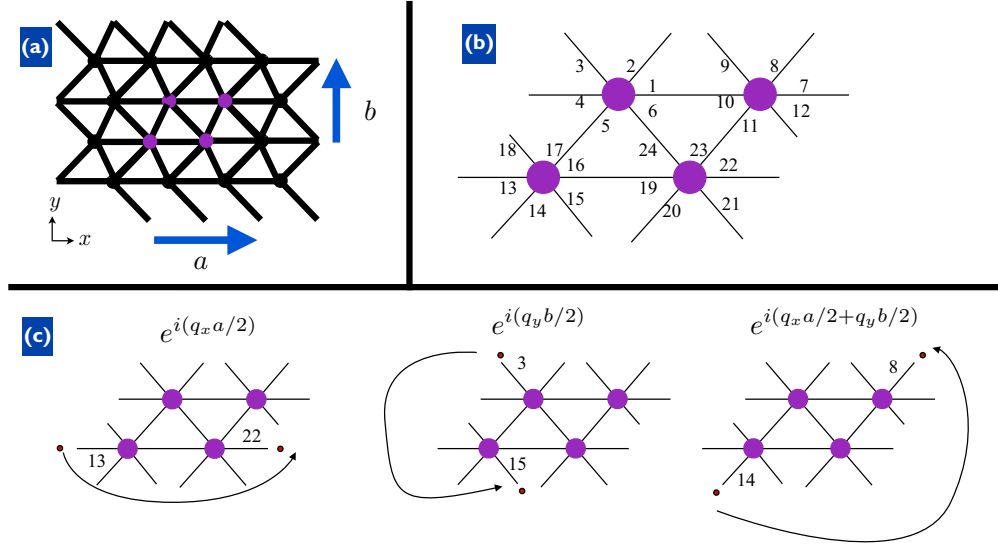


FIG. 4. (Color online) (a) Miura-ori, without the assignment of mountain and valley folds, has a simple directed graph structure with a unit cell composed of four vertices. By tessellating these four vertices, the entire pattern emerges. Note that the tessellation is rectangular, with lattice vectors  $\mathbf{a}_1 = a\hat{\mathbf{x}}$  and  $\mathbf{a}_2 = b\hat{\mathbf{y}}$ . (b) Each vertex has six folds, labeled in the fashion shown here. (c) In Fourier space, translations associated with connecting these folds together throughout the tessellation merely amounts to a phase factor associated with the appropriate wave number and lattice vector. Shown on the left is translating in the  $x$  direction. The middle shows translating in the  $y$  direction. The right shows that connecting the extra folds involves a diagonal translation across the unit cell. Note that the five internal folds have a phase factor identically equal to one.

To calculate the constraint matrix, we note that there are 12 unique folds per unit cell, so  $\mathbf{D}(\mathbf{q})$  is a  $12 \times 24$  rectangular matrix. It has a row for each bond in Fig. 4 with two nonzero columns indicating which folds of each vertex

are interconnected. For internal folds the constraint matrix has a value of  $\pm 1$ , while folds that leave the unit cell have a phase factor associated with it. For convenience of computation we have symmetrized these phase factors, and the full matrix is given by

$$\mathbf{D}^T(\mathbf{q}) = \begin{pmatrix} 1 & 0 & 0 & 0 & 0 & 0 & 0 & 0 & 0 & 0 & 0 & 0 \\ 0 & e^{iq_y/2} & 0 & 0 & 0 & 0 & 0 & 0 & 0 & 0 & 0 & 0 \\ 0 & 0 & e^{iq_y/2} & 0 & 0 & 0 & 0 & 0 & 0 & 0 & 0 & 0 \\ 0 & 0 & 0 & -e^{-iq_x/2} & 0 & 0 & 0 & 0 & 0 & 0 & 0 & 0 \\ 0 & 0 & 0 & 0 & -1 & 0 & 0 & 0 & 0 & 0 & 0 & 0 \\ 0 & 0 & 0 & 0 & 0 & -1 & 0 & 0 & 0 & 0 & 0 & 0 \\ 0 & 0 & 0 & e^{iq_x/2} & 0 & 0 & 0 & 0 & 0 & 0 & 0 & 0 \\ 0 & 0 & 0 & 0 & 0 & 0 & e^{iq_x/2+iq_y/2} & 0 & 0 & 0 & 0 & 0 \\ 0 & 0 & 0 & 0 & 0 & 0 & 0 & e^{iq_y/2} & 0 & 0 & 0 & 0 \\ -1 & 0 & 0 & 0 & 0 & 0 & 0 & 0 & 0 & 0 & 0 & 0 \\ 0 & 0 & 0 & 0 & 0 & 0 & 0 & 0 & -1 & 0 & 0 & 0 \\ 0 & 0 & 0 & 0 & 0 & 0 & 0 & 0 & 0 & e^{iq/2} & 0 & 0 \\ 0 & 0 & 0 & 0 & 0 & 0 & -e^{-iq_x/2-iq_y/2} & 0 & 0 & 0 & -e^{-iq/2} & 0 \\ 0 & 0 & -e^{-iq_y/2} & 0 & 0 & 0 & 0 & 0 & 0 & 0 & 0 & 0 \\ 0 & 0 & 0 & 0 & 0 & 0 & 0 & 0 & 0 & 0 & 0 & 1 \\ 0 & 0 & 0 & 0 & 1 & 0 & 0 & 0 & 0 & 0 & 0 & 0 \\ 0 & 0 & 0 & 0 & 0 & 0 & 0 & 0 & 0 & -e^{-iq_x/2} & 0 & 0 \\ 0 & 0 & 0 & 0 & 0 & 0 & 0 & 0 & 0 & 0 & 0 & -1 \\ 0 & -e^{-iq_y/2} & 0 & 0 & 0 & 0 & 0 & 0 & 0 & 0 & 0 & 0 \\ 0 & 0 & 0 & 0 & 0 & 0 & 0 & -e^{-iq_y/2} & 0 & 0 & 0 & 0 \\ 0 & 0 & 0 & 0 & 0 & 0 & 0 & 0 & 0 & 0 & e^{iq_x/2} & 0 \\ 0 & 0 & 0 & 0 & 0 & 0 & 0 & 0 & 1 & 0 & 0 & 0 \\ 0 & 0 & 0 & 0 & 0 & 1 & 0 & 0 & 0 & 0 & 0 & 0 \end{pmatrix}. \quad (16)$$

### A. Bulk deformation

The combination  $\mathbf{D}(\mathbf{q})\mathbf{J}$  is square such that Eq. (7) has a nontrivial solution whenever  $\det[\mathbf{D}(\mathbf{q})\mathbf{J}] = 0$ . We nondimensionalize the wave number by the physical lengths of the lattice vectors such that  $q_x a \rightarrow q_x$  and  $q_y b \rightarrow q_y$  and the resulting dispersion relation is

$$\frac{\cos^2 \alpha}{\sin^4(\epsilon_0/2)} \sin^2(q_x/2) + \sin^2(q_y/2) = 0. \quad (17)$$

The only real solution to this equation is  $\mathbf{q} = 0$ , indicating that an infinite origami tessellation does not admit spatially inhomogeneous solutions; only uniform deformations are allowed. The null space of  $\mathbf{R}$  is three dimensional here, corresponding to three uniform deformation modes of the Miura-ori. These zero modes are given by the vectors  $\Psi_i$ :

$$\Psi_I = \begin{pmatrix} 1 \\ 0 \\ 0 \\ 1 \\ 0 \\ 0 \\ 1 \\ 0 \\ 0 \\ 0 \end{pmatrix}, \quad \Psi_{II} = \begin{pmatrix} 0 \\ -1 \\ 1 \\ 0 \\ -1 \\ 1 \\ 0 \\ -1 \\ 1 \\ 1 \end{pmatrix}, \quad \Psi_{III} = \begin{pmatrix} -2\frac{C}{A} \\ 1 \\ 1 \\ 0 \\ 1 \\ 1 \\ -2\frac{C}{A} \\ 1 \\ 1 \\ 1 \end{pmatrix}. \quad (18)$$

These infinitesimal deformations of the unit cell correspond to a uniform contraction, a twisting mode, and a saddlelike deformation, respectively (see Fig. 5). To describe the kinematics of deformation, all we require are the null vectors of the constraint equations, but for examining energy associated with the creases we need to calculate the eigenvalues of the matrix  $\mathcal{M} = \mathbf{J}^T \mathcal{A} \mathbf{J}$ . In general, it is not unreasonable to assume that a creased and folded Miura-ori will have a crease stiffness  $k$  that is approximately equal for all patterned

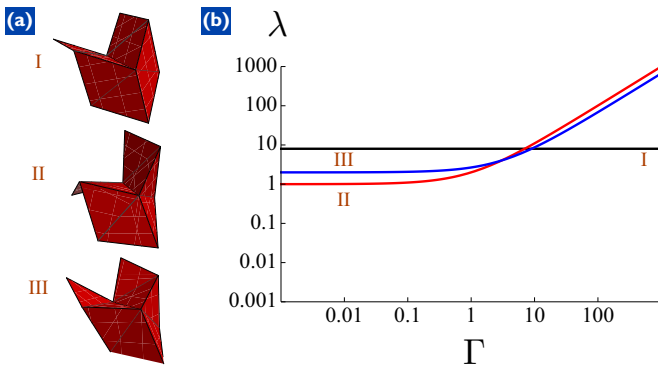


FIG. 5. (Color online) Shapes and energy eigenvalues for the three uniform modes for  $\epsilon = \pi/2$  and  $\alpha = \pi/3$ . (a) The three uniform null vectors correspond to a uniform mode (I), a twisting mode (II), and a saddle mode (III). These are identical to the modes determined numerically in previous studies [6,12]. (b) Eigenvalues associated with each of the three bulk modes as a function of face stiffness  $\Gamma$ . Note that over a wide range the softest mode is the twisting mode (II), since it involves purely face bending.

creases, but the energy scale for bending of the faces will depend on the material properties of the structure [7]. The energy for bending can be treated as an effective torsional spring constant  $k_b$  and thus the energy can be written in terms of the ratio  $k_b/k \equiv \Gamma$ . Nondimensionalizing the energy by  $kL_x L_y$ , we find the energy eigenvalues  $\lambda$  in terms of the null vectors. Decomposing the internal variable deformation  $\delta \mathbf{s} = \sum_i a_i \psi_i$ , where  $\psi_i = \Psi_i / |\Psi_i|$  is the normalized null vector with  $i \in \{I, II, III\}$ , we write Eq. (11) as

$$E = \frac{L_x L_y}{2} \mathbf{a}^T \mathbf{M} \mathbf{a}, \quad (19)$$

$$\mathbf{a} = \begin{pmatrix} a_I \\ a_{II} \\ a_{III} \end{pmatrix}, \quad (20)$$

$$\mathbf{M} = \begin{pmatrix} \psi_I^T \mathcal{M} \psi_I & \psi_I^T \mathcal{M} \psi_{II} & \psi_I^T \mathcal{M} \psi_{III} \\ \psi_{II}^T \mathcal{M} \psi_I & \psi_{II}^T \mathcal{M} \psi_{II} & \psi_{II}^T \mathcal{M} \psi_{III} \\ \psi_{III}^T \mathcal{M} \psi_I & \psi_{III}^T \mathcal{M} \psi_{II} & \psi_{III}^T \mathcal{M} \psi_{III} \end{pmatrix}. \quad (21)$$

Each matrix element of  $\mathbf{M}$  represents overlaps between the null vectors  $\psi_i$  and the energy matrix  $\mathcal{M}$ ; only in exceptional circumstances will  $\mathbf{M}$  be diagonal in the null basis. In general it is given by

$$\mathbf{M} = \begin{pmatrix} 2(A^2 + B^2) & 0 & \frac{\sqrt{2}(A-B)BC}{\sqrt{C^2+A^2}} \\ 0 & C^2 + \Gamma & 0 \\ \frac{\sqrt{2}(A-B)BC}{\sqrt{C^2+A^2}} & 0 & \frac{\Gamma A^2 + (3A^2 - 2BA + 2B^2)C^2}{A^2 + C^2} \end{pmatrix}. \quad (22)$$

An example for when  $\mathbf{M}$  is diagonal is given by  $\alpha = \pi/3, \epsilon = \pi/2$  (see Fig. 5), for which  $\mathbf{M}$  becomes

$$\mathbf{M} = \begin{pmatrix} 8 & 0 & 0 \\ 0 & 1 + \Gamma & 0 \\ 0 & 0 & \frac{2}{3}(3 + \Gamma) \end{pmatrix}. \quad (23)$$

Note that for this particular combination of parameters the uniform expansion mode has a flat stiffness over all ranges of  $\Gamma$  since there is no face bending for this deformation. In the regime where face bending is relatively inexpensive ( $\Gamma \ll 1$ ), the out-of-plane deformation modes are correspondingly softer than the uniform deformation. These results are in agreement with previous numerical research done on the structural mechanics of Miura-ori [6,11,12]. Should other values of  $(\alpha, \epsilon)$  be chosen, the energy matrix is not necessarily diagonal and thus eigensolutions mix the null vectors.

### B. Inhomogeneous deformation

For a finite tessellation, the deformation is fundamentally different, since some folds reach the boundary and, consequently, do not yield constraints. Since the tessellation mechanics are determined by the allowable deformations, which are determined by the constraint equations, the presence of free boundaries allows much more flexibility and the Miura-ori develops additional degrees of freedom. These localized edge states are reminiscent of evanescent waves in electromagnetism, boundary layers in elastic lattices [45], and Rayleigh surface waves [46]. Letting  $q_x \equiv q$  (where  $q$  is

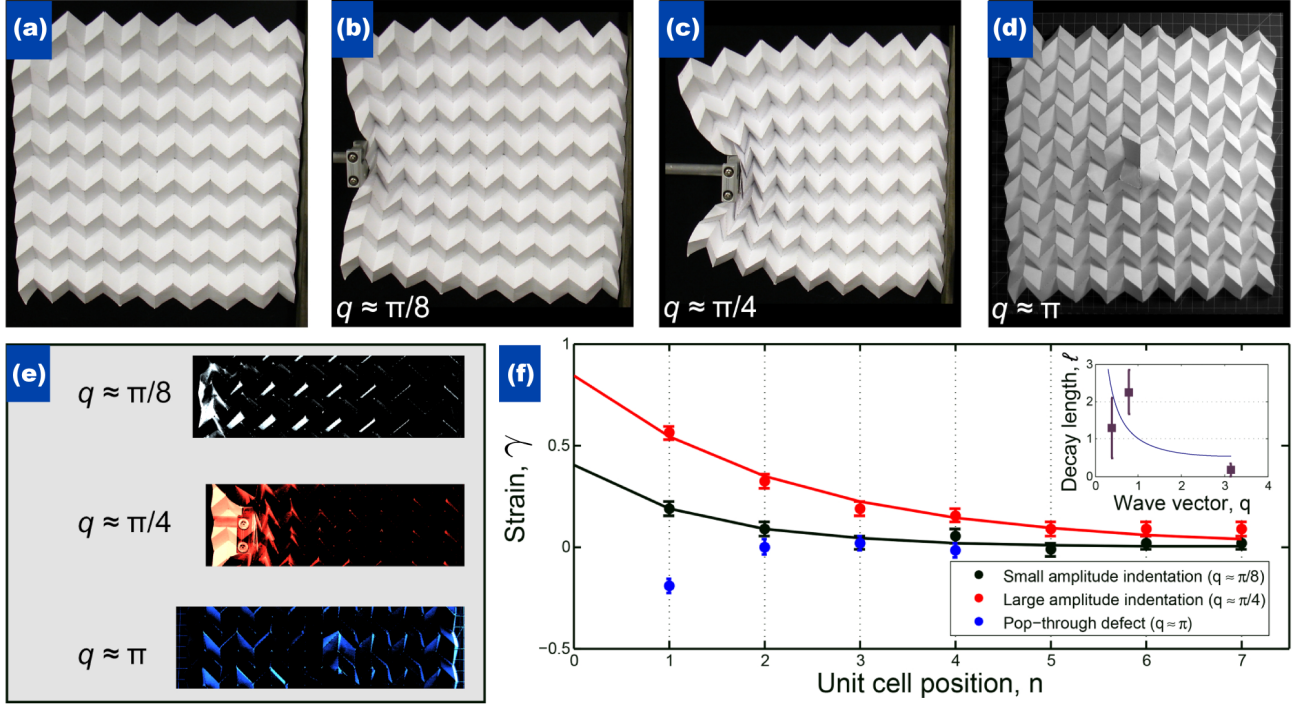


FIG. 6. (Color online) Experimental observations of deformation localization in an  $8 \times 8$  Miura-ori tessellation. (a) An undeformed Miura-ori shows a regular periodic pattern. Under (b) small deformations, (c) large deformations, and (d) in the presence of a pop-through defect (PTD) [7], the lattice distorts to accommodate the induced strain. (e) Qualitatively, the amount of deformation localization can be easily seen by a simple image subtraction between the deformed and undeformed state. (f) Measuring strain along the horizontal axis as a function of unit cell position  $n$  relative to the location of the disturbance shows a rapid decay for all three scenarios (points). For small and large amplitudes, the decays can be readily fit to an exponential function with decay length  $\ell$  [upper (red) and lower (black) lines], whereas for a PTD, the decay length can be estimated to within 100%. Because the PTD induces an extensional distortion rather than a compression, the strain is oppositely signed. The inset is a plot of the decay length against an approximate measure of the distortion wave vector  $q$  showing that the larger wave vector decays much more rapidly than the shorter wave vectors. Within error bars, this measurement is consistent with an inverse relationship between decay length and wave vector. The solid line is the theoretical prediction from Eq. (24) for  $\epsilon = \pi/2$  and  $\alpha = \pi/3$ .

real), Eq. (17) yields  $q_y = \pm i\kappa(q)$ , where deformations decay away from the boundaries of constant  $y$  with a length scale  $\ell \equiv 1/\kappa(q)$ , with

$$\ell(q) = \frac{1}{2|\sinh^{-1}[\cos \alpha \sin(q/2)/(\sin^2 \epsilon/2)]|}. \quad (24)$$

This localization length is readily observed in deformation experiments on Miura-ori sheets (see Fig. 6). Using laser-cut sheets of paper, an  $8 \times 8$  Miura-ori is constructed by folding the whole sheet using a planar angle of  $\alpha = \pi/3$  into the ground state given by  $\epsilon = \pi/2$  [Fig. 6(a)]. Inhomogeneous deformations are created using both an external indenter to apply a displacement [Figs. 6(b) and 6(c)] and by placing reversible pop-through defects [Fig. 6(d)] [7]. The strain  $\gamma_n$  at each unit cell  $n$  is measured such that  $\gamma_n = \Delta w_n / \bar{w}$ , where  $\Delta w_n$  is the change in width of the  $n$ th cell and  $\bar{w}$  is the average width for an undisturbed cell. As shown in Fig. 6, the strain decays exponentially away from the indenter with a decay length that is consistent (within error) with our theoretical predictions.

To examine these deformation modes more quantitatively, we return to the dispersion relation given by Eq. (17). There are two possible solutions to Eq. (17), corresponding to different decay directions, and thus the null space of  $\mathbf{R}$  corresponding to each of these branches is two dimensional. We decompose

$\delta \mathbf{s}(\mathbf{x})$  into a sum of upward (in  $y$ ) decaying and downward decaying modes

$$\delta \mathbf{s} = e^{iqx} [(u_1 \chi_1 e^{-k(q)y} + u_2 \chi_2 e^{-k(q)y}) + (d_1 \eta_1 e^{k(q)y} + d_2 \eta_2 e^{k(q)y})] + \text{c.c.} \quad (25)$$

The vectors  $\chi_{1,2}$  correspond to the upward decaying modes and  $\eta_{1,2}$  the downward decaying modes. Note that, since the values of the angles must be real,  $\eta_{1,2}(q) = \bar{\chi}_{1,2}(-q)$ . In the long-wavelength limit, i.e.,  $q \ll 1$ , we have

$$\chi_1 = \begin{pmatrix} \frac{-CAq + CB(q-2i)}{AB} \\ 0 \\ 2q \\ \frac{-CAq + CB(q+2i)}{AB} \\ 0 \\ 0 \\ \frac{CAq - CB(q-2i)}{AB} \\ 0 \\ 0 \\ \frac{CAq + CB(q+2i)}{AB} \\ 0 \\ 2q \end{pmatrix}, \quad \chi_2 = \begin{pmatrix} \frac{-2C}{A} \\ 0 \\ 0 \\ \frac{-2C}{A} \\ -2iq \\ 0 \\ \frac{-2C}{A} \\ -2iq \\ 0 \\ \frac{-2C}{A} \\ 0 \\ 0 \end{pmatrix}. \quad (26)$$



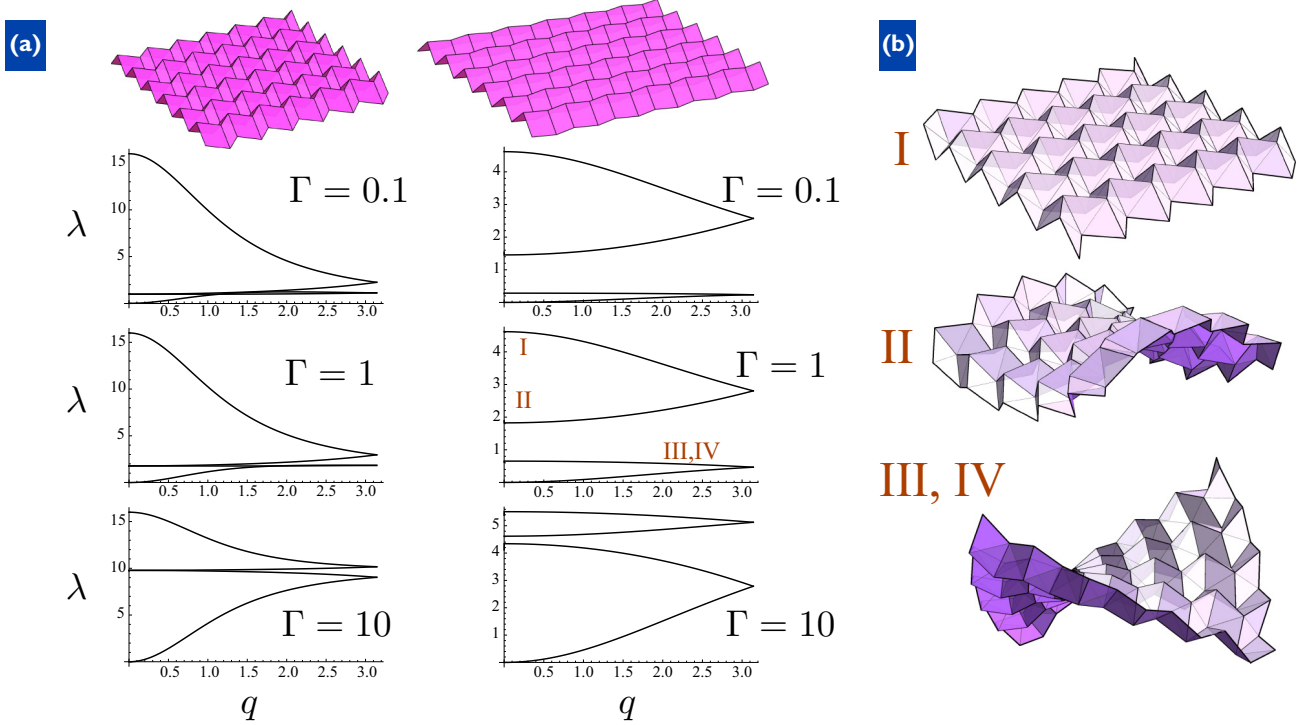


FIG. 7. (Color online) Eigenvalues and mode shapes as a function of wave number for a given  $\Gamma$ . (a) Shown on the left is the mode structure for  $\Gamma = 0.1, 1$ , and  $10$ , with  $\epsilon = \pi/2$  and  $\alpha = \pi/3$ . At long wavelengths the saddle mode  $\mathcal{I}$  is the stiffest for a wide range of  $q$ , since it involves both bending of the faces and deformation of the angles away from the reference state. Shown on the right is the mode structure for  $\Gamma = 0.1, 1$ , and  $10$ , with  $\epsilon = \pi/2$  and  $\alpha = 9\pi/20$ . The labeled modes are in ascending order from largest eigenvalue (mode I) to lowest eigenvalue (mode IV). (b) Visualization of the basic modes for  $q = \pi/6$ .

The null space, and thus the number of elementary excitations, for a finite-size Miura-ori is actually different than for the limit  $q \rightarrow 0$ . While this may seem counterintuitive, the nature of the null vectors is inherently chiral, as indicated by the decomposition into upward and downward decaying solutions. At  $q = 0$ , the dimensionality of the null space is smaller because there is no distinction between handedness for uniform deformation.

### C. Miura-ori's soft modes

The vectors  $\chi_{1,2}$  govern the kinematic deformations of Miura-ori, giving the possible solutions to the constraint equations. For a tessellation with an associated torsional spring energy at each crease, the energy density per mode may be written in Fourier space as

$$\mathcal{E} = \frac{L_x L_y}{2} \mathbf{c}^\dagger(q) \mathbf{H}(q) \mathbf{c}(q), \quad (27)$$

where

$$\mathbf{c}(q) = \begin{pmatrix} u_1(q) \\ u_2(q) \\ d_1(q) \\ d_2(q) \end{pmatrix} \quad (28)$$

and  $\mathbf{H}$  is the  $2 \times 2$  Hermitian block matrix

$$\mathbf{H} = \begin{pmatrix} \mathbf{H}_0 & \mathbf{H}_1 \\ \mathbf{H}_1^\dagger & \mathbf{H}_0^\dagger \end{pmatrix}. \quad (29)$$

The two independent blocks of  $\mathbf{H}$  are given by

$$\mathbf{H}_0 = \begin{pmatrix} \chi_1^\dagger \mathcal{M} \chi_1 & \chi_1^\dagger \mathcal{M} \chi_2 \\ \chi_2^\dagger \mathcal{M} \chi_1 & \chi_2^\dagger \mathcal{M} \chi_2 \end{pmatrix} \quad (30)$$

and

$$\mathbf{H}_1 = \begin{pmatrix} \chi_1^\dagger \mathcal{M} \eta_1 & \chi_1^\dagger \mathcal{M} \eta_2 \\ \chi_2^\dagger \mathcal{M} \eta_1 & \chi_2^\dagger \mathcal{M} \eta_2 \end{pmatrix}. \quad (31)$$

For finite wave number there are four modes of deformation. Typical eigenvalues of  $\mathbf{H}(q)$  are shown in Fig. 7. The largest two eigenvalues are typically associated with changing  $\epsilon$ , since there is an energetic cost even for very small  $\Gamma$ . The typically smallest two eigenvalues correspond to twisting mode and a fourth mode that has no analog in the zero wave number case. This mode has a qualitative shape that is similar to the twisting mode and an energy that vanishes as  $q \rightarrow 0$ , much like an acoustic mode in a crystal. Previous analyses of inhomogeneous deformations have not found this mode, which we identify here as arising from the breaking of continuous symmetry when a boundary is added to one side of the tessellation. The acoustic mode corresponds to an antisymmetric combination of upward and downward decaying modes; consequently, as  $q$  becomes smaller, the change in fold angles associated with the combination cancels and only three modes appear at  $q = 0$ .

The modes that are softest depend not only on the stiffness of face bending, but on the ground state defined by  $\epsilon_0$  (see Fig. 7). This stiffness dependence is in accord

with the previously predicted anisotropic in-plane stiffness response [6,13]. Additionally, since our analysis allows for arbitrary size and wave number, we are able to capture the response of the previously unidentified acoustic mode.

## V. DISCUSSION

While there has been numerical analysis of tessellations in the past, our theoretical formulation provides several key insights into the design and understanding of origami mechanics. We not only analytically calculated expressions for first-order inhomogeneous deformations, but we found an additional acoustic mode of deformation that has not been identified using numerics. Moreover, we have found an analytical expression for a decay length that arises in Miura-ori and identified that these soft modes are edge states that cannot occur in an infinite tessellation. Indeed, the appearance of a single decay length and the ability to fully quantify the deformation modes using a single wave number indicates that the boundaries of Miura-ori fully define the deformation state. We can directly conclude from this that, unlike normal solids, the number of degrees of freedom scales with the perimeter of a finite tessellation, rather than the area. This result suggests that there are surface boundary states that can be used to probe the full deformation of the material and hints at the connection between our work and recent studies on topological mechanics [38]. In fact, our mathematical formalism shares many parallels with the topological mechanics of linkages [47–49], as well as the more conventional literature concerning topological insulators and semimetals [50–52]. It remains to be seen exactly how the symmetry and topology of the crease pattern affect the nature of chiral modes in origami, but there is evidence to suggest that even slight modifications of the

crease pattern symmetry may lead to preferentially directed chiral states.

A great deal of this analysis can be carried through to other origami fold patterns. What is less clear, however, is how the number of degrees of freedom, the null space of  $\mathbf{R}(\mathbf{q})$ , changes for different fold patterns. At the outset it may seem coincidental that the matrix  $\mathbf{R}(\mathbf{q})$  is square. In fact, this behavior is likely more generic. In particular, the Miura-ori, with additional folds across the faces, is composed of triangular subunits. In any triangulated origami fold pattern, vertices will tend to have, on average, six folds. Hence, for  $V$  vertices (with  $V$  very large), we have  $3V$  unique folds and  $3V$  degrees of freedom per vertex. Consequently,  $\mathbf{R}(\mathbf{q})$  will be a  $3V \times 3V$  square matrix for sufficiently large  $V$ .

Finally, a great advantage to this approach is the ability to separate the topological nature of the crease pattern from the geometry of the vertex. The ability to isolate mechanical deformations or elementary excitations in exotic materials is of great interest in quantum condensed matter [38], amorphous solids [53–55], and complex fluids [56]. Our theoretical framework for origami tessellations bridges the gap between the origami mechanics literature and a theory of origami metamaterials by identifying the constraint-based nature of the folding mechanisms and applying well-known methods of analysis from solid state physics and lattice mechanics.

## ACKNOWLEDGMENTS

The authors acknowledge interesting and helpful discussions with Tom Hull, Robert Lang, Tomohiro Tachi, Scott Waitukaitis, Martin van Hecke, and Michael Assis. We also thank F. Parish for help with the laser cutter. This work was funded by the National Science Foundation through Grant No. EFRI ODISSEI-1240441.

- 
- [1] T. Tachi, *Symposium of the International Association for Shell and Spatial Structures (50th. 2009. Valencia). Evolution and Trends in Design, Analysis and Construction of Shell and Spatial Structures: Proceedings* (Editorial de la Universitat Politècnica de Valencia, Valencia, 2009).
  - [2] T. Tachi, in *Proceedings of the International Association for Shell and Spatial Structures (IASS) Symposium*, edited by A. Domingo and C. Lazaro (Editorial de la Universitat Politècnica de Valencia, Valencia, 2010), Vol. 12, pp. 458–460.
  - [3] T. Tachi, in *Symposium of the International Association for Shell and Spatial Structures (50th. 2009. Valencia). Evolution and Trends in Design, Analysis and Construction of Shell and Spatial Structures: Proceedings* (Editorial de la Universitat Politècnica de Valencia, Valencia, 2010).
  - [4] E. Hawkes, B. An, N. Benbernou, H. Tanaka, S. Kim, E. Demaine, D. Rus, and R. Wood, *Proc. Natl. Acad. Sci. USA* **107**, 12441 (2010).
  - [5] M. A. Dias, L. H. Dudte, L. Mahadevan, and C. D. Santangelo, *Phys. Rev. Lett.* **109**, 114301 (2012).
  - [6] M. Schenk and S. D. Guest, *Proc. Natl. Acad. Sci. USA* **110**, 3276 (2013).
  - [7] J. L. Silverberg, A. A. Evans, L. McLeod, R. C. Hayward, T. Hull, C. D. Santangelo, and I. Cohen, *Science* **345**, 647 (2014).
  - [8] J.-H. Na, A. A. Evans, J. Bae, M. C. Chiappelli, C. D. Santangelo, R. J. Lang, T. C. Hull, and R. C. Hayward, *Adv. Mater.* **27**, 79 (2015).
  - [9] C. Py, P. Reverdy, L. Doppler, J. Bico, B. Roman, and C. N. Baroud, *Phys. Rev. Lett.* **98**, 156103 (2007).
  - [10] J. Solomon, E. Vouga, M. Wardetzky, and E. Grinspun, *Computer Graphics Forum* (Wiley, New York, 2012), Vol. 31, pp. 1567–1576.
  - [11] M. Schenk and S. Guest, *Folded shell structures*, Ph.D. thesis, University of Cambridge, 2011.
  - [12] M. Schenk and S. D. Guest, *Origami* **5**, 291 (2011).
  - [13] Z. Y. Wei, Z. V. Guo, L. Dudte, H. Y. Liang, and L. Mahadevan, *Phys. Rev. Lett.* **110**, 215501 (2013).
  - [14] K. Abdul-Sater, F. Irlinger, and T. C. Lueth, *J. Mech. Robot.* **5**, 031005 (2013).
  - [15] S. Waitukaitis, R. Menaut, B. G.-g. Chen, and M. van Hecke, *Phys. Rev. Lett.* **114**, 055503 (2015).
  - [16] B. H. Hanna, J. M. Lund, R. J. Lang, S. P. Magleby, and L. L. Howell, *Smart Mater. Struct.* **23**, 094009 (2014).
  - [17] N. P. Bende, A. A. Evans, S. Innes-Gold, L. A. Marin, I. Cohen, R. C. Hayward, and C. D. Santangelo, *arXiv:1410.7038*.
  - [18] J. B. Pendry, D. Schurig, and D. R. Smith, *Science* **312**, 1780 (2006).

- [19] M. Kadic, T. Bückmann, N. Stenger, M. Thiel, and M. Wegener, *Appl. Phys. Lett.* **100**, 191901 (2012).
- [20] S. Brûlé, E. H. Javelaud, S. Enoch, and S. Guenneau, *Phys. Rev. Lett.* **112**, 133901 (2014).
- [21] M. Farhat, S. Guenneau, and S. Enoch, *Phys. Rev. Lett.* **103**, 024301 (2009).
- [22] N. Stenger, M. Wilhelm, and M. Wegener, *Phys. Rev. Lett.* **108**, 014301 (2012).
- [23] J. Shim, S. Shan, A. Košmrlj, S. H. Kang, E. R. Chen, J. C. Weaver, and K. Bertoldi, *Soft Matter* **9**, 8198 (2013).
- [24] A. A. Evans and A. J. Levine, *Phys. Rev. Lett.* **111**, 038101 (2013).
- [25] Y. Zhang, E. A. Matsumoto, A. Peter, P.-C. Lin, R. D. Kamien, and S. Yang, *Nano Lett.* **8**, 1192 (2008).
- [26] E. A. Matsumoto and R. D. Kamien, *Phys. Rev. E* **80**, 021604 (2009).
- [27] K. Bertoldi, P. M. Reis, S. Willshaw, and T. Mullin, *Adv. Mater.* **22**, 361 (2010).
- [28] E. A. Matsumoto and R. D. Kamien, *Soft Matter* **8**, 11038 (2012).
- [29] J. T. B. Overvelde, S. Shan, and K. Bertoldi, *Adv. Mater.* **24**, 2337 (2012).
- [30] C. Yoon, R. Xiao, J. Park, J. Cha, T. D. Nguyen, and D. H. Gracias, *Smart Mater. Struct.* **23**, 094008 (2014).
- [31] Y. Liu, J. K. Boyles, J. Genzer, and M. D. Dickey, *Soft Matter* **8**, 1764 (2012).
- [32] L. Ionov, *Soft Matter* **7**, 6786 (2011).
- [33] G. Stoychev, N. Pureskiy, and L. Ionov, *Soft Matter* **7**, 3277 (2011).
- [34] *Tessellatica*, <http://www.langorigami.com/science/computational/tessellatica/tessellatica.php>
- [35] D. A. Huffman, *IEEE Trans. Comput.* **25**, 1010 (1976).
- [36] s.-m. belcastro and T. C. Hull, *Linear Algebra Appl.* **348**, 273 (2002).
- [37] R. Hutchinson and N. Fleck, *J. Mech. Phys. Solids* **54**, 756 (2006).
- [38] C. Kane and T. Lubensky, *Nat. Phys.* **10**, 39 (2014).
- [39] F. Lechenault, B. Thiria, and M. Adda-Bedia, *Phys. Rev. Lett.* **112**, 244301 (2014).
- [40] J. L. Silverberg, J.-H. Na, A. A. Evans, B. Liu, T. C. Hull, C. D. Santangelo, R. J. Lang, R. C. Hayward, and I. Cohen, *Nat. Mater.* **14**, 389 (2015).
- [41] L. Mahadevan and S. Rica, *Science* **307**, 1740 (2005).
- [42] A. E. Shyer, T. Tallinen, N. L. Nerurkar, Z. Wei, E. S. Gil, D. L. Kaplan, C. J. Tabin, and L. Mahadevan, *Science* **342**, 212 (2013).
- [43] E. D. Demaine, M. L. Demaine, V. Hart, G. N. Price, and T. Tachi, *Graphs Combinator.* **27**, 377 (2011).
- [44] T. Witten, *Rev. Mod. Phys.* **79**, 643 (2007).
- [45] A. S. Phani and N. A. Fleck, *J. Appl. Mech.* **75**, 021020 (2008).
- [46] J. W. Strutt and L. Rayleigh, *Proc. London Math. Soc.* **17**, 4 (1885).
- [47] B. G.-g. Chen, N. Upadhyaya, and V. Vitelli, *Proc. Natl. Acad. Sci. USA* **111**, 13004 (2014).
- [48] J. Paulose, B. G.-g. Chen, and V. Vitelli, *Nat. Phys.* **11**, 153 (2015).
- [49] J. Paulose, A. S. Meeussen, and V. Vitelli, [arXiv:1502.03396](https://arxiv.org/abs/1502.03396).
- [50] M. Z. Hasan and C. L. Kane, *Rev. Mod. Phys.* **82**, 3045 (2010).
- [51] X.-L. Qi and S.-C. Zhang, *Rev. Mod. Phys.* **83**, 1057 (2011).
- [52] H. C. Po, Y. Bahri, and A. Vishwanath, [arXiv:1410.1320](https://arxiv.org/abs/1410.1320).
- [53] K. Sun, A. Souslov, X. Mao, and T. Lubensky, *Proc. Natl. Acad. Sci. USA* **109**, 12369 (2012).
- [54] X. Mao, N. Xu, and T. C. Lubensky, *Phys. Rev. Lett.* **104**, 085504 (2010).
- [55] M. Wyart, S. Nagel, and T. Witten, *Europhys. Lett.* **72**, 486 (2005).
- [56] E. Lerner, G. Düring, and M. Wyart, *Proc. Natl. Acad. Sci. USA* **109**, 4798 (2012).



# Decoupling local mechanics from large-scale structure in modular metamaterials

Nan Yang<sup>a,1,2</sup> and Jesse L. Silverberg<sup>b,1,2</sup>

<sup>a</sup>Tianjin Key Laboratory of the Design and Intelligent Control of Advanced Mechatronical Systems, Tianjin University of Technology, Xiqing District, Tianjin 300384, China; and <sup>b</sup>Wyss Institute for Biologically Inspired Engineering, Harvard University, Boston, MA 02115

Edited by David A. Weitz, Harvard University, Cambridge, MA, and approved February 21, 2017 (received for review December 16, 2016)

**A defining feature of mechanical metamaterials is that their properties are determined by the organization of internal structure instead of the raw fabrication materials. This shift of attention to engineering internal degrees of freedom has coaxed relatively simple materials into exhibiting a wide range of remarkable mechanical properties. For practical applications to be realized, however, this nascent understanding of metamaterial design must be translated into a capacity for engineering large-scale structures with prescribed mechanical functionality. Thus, the challenge is to systematically map desired functionality of large-scale structures backward into a design scheme while using finite parameter domains. Such “inverse design” is often complicated by the deep coupling between large-scale structure and local mechanical function, which limits the available design space. Here, we introduce a design strategy for constructing 1D, 2D, and 3D mechanical metamaterials inspired by modular origami and kirigami. Our approach is to assemble a number of modules into a voxelized large-scale structure, where the module’s design has a greater number of mechanical design parameters than the number of constraints imposed by bulk assembly. This inequality allows each voxel in the bulk structure to be uniquely assigned mechanical properties independent from its ability to connect and deform with its neighbors. In studying specific examples of large-scale metamaterial structures we show that a decoupling of global structure from local mechanical function allows for a variety of mechanically and topologically complex designs.**

mechanical metamaterials | modular origami | kirigami | forward design | inverse design

**R**ecent experiments with mechanical metamaterials (1–3) have demonstrated constitutive relations including pentamode behavior (4), negative effective bulk modulus (5), and negative Poisson ratio (6). As a design motif, origami, the art of paper folding, offers interesting possibilities to realize these properties in a wide range of contexts. Because origami is grounded in a centuries-old art form, this approach to creating complex 3D structures benefits from a large body of established techniques. Indeed, from simple flat sheets, studies have documented structures with negative Poisson ratio (7–10), reprogrammable stiffness (11), multistability (12–14), curved metasurfaces (15–17), topologically protected modes (18), tunable low-energy deformations (19), and multiple degrees of freedom (DOF) (20). These examples generally involve relatively simple repeated folding patterns where creasing DOF compete with local and global geometric constraints. As such, collective interactions lead to the observed macroscopic constitutive relations. However, to apply origami design motifs to next-generation devices we must address the challenge of creating folding diagrams for an arbitrarily prescribed large-scale structure, independently from the structure’s desired metamaterial properties.

In most quantitative studies of tessellated origami metamaterials the folding pattern is deeply coupled to the structure’s mechanics. Consequently, the design space for large-scale bulk structure is tightly constrained by the selection of metamaterial properties. Here, we overcome this difficulty with inspiration

from two distinct branches of origami. One of these branches specifically explores structures constructed with two or more pieces of folded paper. These modular origami structures can incorporate hundreds of folded sheets connected together by inserting flaps from one module, which are created during the folding process, into pockets of adjacent modules. The bulk structure is then held together through a tensegrity-like pattern of stresses and friction (21). Our second source of inspiration is the branch of origami that intersects with paper cutting known as kirigami. In this art form, elaborate structures are designed by combining folding and cutting. Mechanically speaking, the removal of material by cutting provides opportunities to introduce additional design parameters and DOF. Combining modular origami with kirigami leads to a metamaterial design strategy that takes mechanically distinct kirigami modules and treats them as voxels in a larger structure. When the kirigami module has more design parameters  $N_p$  than constraints imposed by bulk assembly of multiple units  $N_c$ , each voxel can have its mechanical properties independently prescribed from their adjacent neighbors. In essence, this approach where  $N_p - N_c > 0$  solves the inverse-design problem (22) and enables a decoupling of large-scale structure from local mechanical function.

## Results and Discussion

It is possible to conceive innumerable structures for metamaterial assembly that illustrate the general  $N_p - N_c > 0$  design strategy. To focus our efforts on a specific example, we designed a

### Significance

**The forward-design approach to mechanical metamaterials determines a structure’s properties after it is designed. In contrast, the inverse-design approach specifies parameter domains then optimizes a cost function to achieve a desired property. The former approach guarantees a structure will exist but lacks the ability to prescribe function. The latter approach has prescribed function, but existence is not guaranteed. Here, we trivialize these design challenges for metamaterials by decoupling local mechanical properties from the bulk structure, allowing both to be specified independently. This work introduces a design strategy that substantially advances the capacity to engineer mechanical metamaterials by specifically using modular units with more free design parameters than constraints. The fundamental strategy is explicitly demonstrated with an origami- and kirigami-inspired structure.**

Author contributions: N.Y. and J.L.S. designed research; N.Y. performed research; N.Y. and J.L.S. analyzed data; N.Y. and J.L.S. wrote the paper; and J.L.S. supervised the research.

The authors declare no conflict of interest.

This article is a PNAS Direct Submission.

<sup>1</sup>N.Y. and J.L.S. contributed equally to this work.

<sup>2</sup>To whom correspondence may be addressed. Email: yn@tjut.edu.cn or Jesse.Silverberg@wyss.harvard.edu.

This article contains supporting information online at [www.pnas.org/lookup/suppl/doi:10.1073/pnas.1620714114/-DCSupplemental](http://www.pnas.org/lookup/suppl/doi:10.1073/pnas.1620714114/-DCSupplemental).

kirigami-inspired lantern-like pattern formed by cutting a thin sheet (Fig. 1A, black outline), folding along the prescribed lines to form hinge-like creases (Fig. 1A, pink dashed and solid lines), and bonding adjacent edges to form crease-like hinges (Fig. 1A, e.g.,  $BCD$  bonds  $BC'D'$ ; 3D rendering shows the module's assembled form, *SI Appendix*, Fig. S1). The cutting and folding geometry is determined by angles  $\alpha$ ,  $\gamma$ , and lengths  $m$ ,  $n$ , and  $q$  so that  $N_p = 5$ . Each assembled module has only a single kinematic DOF represented here by the dihedral angle  $\theta$  measured between planes  $BCFG$  and  $BCF'G'$ . Although this choice for the DOF is not unique,  $\theta$  conveniently varies from  $0^\circ$  to  $360^\circ$  when the module is designed with parameters that avoid self-intersection during folding (Fig. 1B and *Materials and Methods*).

When constructed from rigid sheets that neither bend nor stretch the kirigami module's kinematics are fully determined by geometry. As  $\theta$  varies the structure simultaneously undergoes longitudinal and transverse deformations in its dimensions  $X(\theta)$ ,  $Y(\theta)$ , and  $Z(\theta)$  (Fig. 1A and B). From these quantities we can calculate the Poisson ratios  $\nu_{ZX}$  and  $\nu_{ZY}$ , which are essentially the ratios of strain (*Materials and Methods*). In addition to taking values well beyond the 0 to 0.5 range found in most common materials, we found wide regions of parameter space for  $\alpha$  and  $\gamma$  as well as wide regions in configuration space  $\theta$  that supports two simultaneously negative Poisson ratios (Fig. 1C–F and *SI Appendix*, Figs. S2 and S3). Combining the kinematic equations with a linear elastic energy expression reveals further useful properties for bulk metamaterial design (*Materials and Methods*). Specifically, we find the kirigami module can exhibit monostability or bistability depending on the parameter values for  $\alpha$  and  $\gamma$  (Fig. 1G and H and *SI Appendix*, Fig. S4), which were experimentally confirmed in hand-folded models (*SI Appendix*, Figs. S4–S6). Having shown the basic lantern-like kirigami module has a wide range of mechanical features, we shift to the more acute challenge of designing large-scale metamaterials with prescribed mechanical properties.

Insights from modular origami art suggest large-scale metamaterials can be assembled by voxelizing the desired large-scale shape into cuboids and assembling the voxelized geometry from a collection of kirigami-inspired modules. As mechanical building blocks, we require each module to be geometrically compatible with its neighbors within design tolerances. In the general case, this condition means voxels are able to freely deform without (i) colliding into their neighbors, (ii) separating from their neighbors, or (iii) experiencing geometric frustration. In the specific example of the lantern-like kirigami module studied here, these conditions impose  $N_c = 4$  constraints for all  $\theta$  in the prescribed folding domain  $[\theta_a, \theta_b]$ : The dimensions  $X(\theta)$ ,  $Y(\theta)$ ,  $Z(\theta)$ , and the angle  $\angle EDE'$  must match for all voxels. The first three constraints ensure voxels do not intersect during folding, and the fourth constraint ensures structures can be rigidly connected along the  $\hat{z}$ -axis. Because the basic module has five independent design parameters, these four constraints imposed by bulk assembly leave  $N_p - N_c = 5 - 4 = 1$  free parameter to choose mechanical properties of each voxel. As an example, we picked a set of parameters for a target module (Fig. 2A–C, gray module) and constructed two additional geometrically compatible modules with independently prescribed  $\alpha$  (Fig. 2A–C, orange and red modules). The remaining parameter values for these additional modules were found by calculating an error function  $\epsilon(\theta)$  between the target and candidate geometries (*Materials and Methods*) and searching for optimal parameter values that minimize the integrated error  $s = \int_{\theta_a}^{\theta_b} \epsilon d\theta$  over the design interval, which in this case was chosen to be  $[300^\circ, 360^\circ]$ . A subspace projection of the parameter landscape helps visualize the optimization and shows a local minimum representing optimal values for the dimensionless lengths  $m/q$  and  $n/q$  (Fig. 2D, red

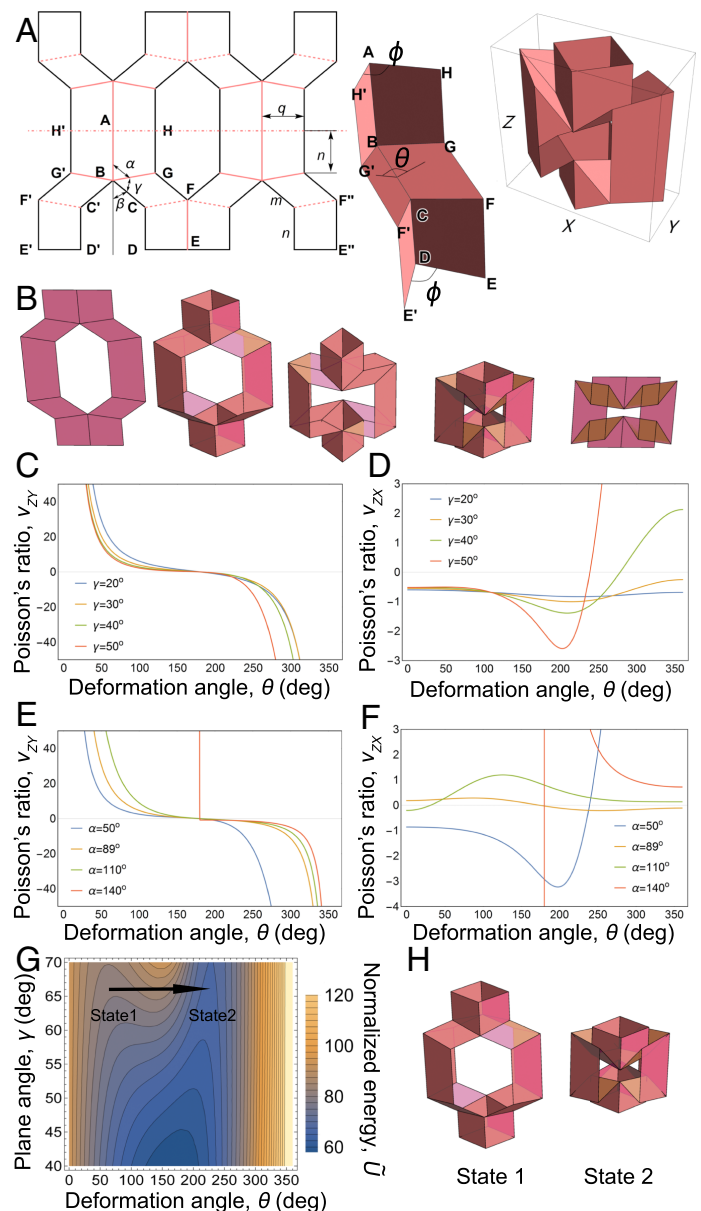


**Fig. 1.** Geometry-driven metamaterial properties of a kirigami lantern-like module. (A) The design pattern of one module (Left) involves cutting a thin sheet along the thick black lines, then folding along the mountain (dashed) and valley (solid) creases. Edges  $BCD$  and  $BC'D'$  are bonded to create crease-like hinges in each of the four symmetric quadrants. Similarly,  $F'E'$  is bonded to  $F''E''$ , along with the symmetric edges in the module's upper half. The plane angle parameters  $\alpha$  and  $\gamma$  and lengths  $m$ ,  $n$ ,  $q$  determine the 3D structure shown in the 1/4 (Middle) and full (Right) unit module. The dihedral angle  $\theta$  is chosen to quantify the module's configuration. Parameters  $\phi$  and  $\beta$  are useful for the mathematical description of the geometry (*Materials and Methods*). (B) The module takes various forms determined by the configuration angle  $\theta = 0^\circ, 90^\circ, 180^\circ, 270^\circ$ , and  $360^\circ$ . Poisson ratios (C)  $\nu_{ZY}$  and (D)  $\nu_{ZX}$  as functions of folding configuration for  $\alpha = 60^\circ$  and  $\gamma = 20^\circ, 30^\circ, 40^\circ$ , and  $50^\circ$ . Poisson ratios (E)  $\nu_{ZY}$  and (F)  $\nu_{ZX}$  as functions of folding configuration for  $\gamma = 40^\circ$  and  $\alpha = 50^\circ, 89^\circ, 110^\circ$ , and  $140^\circ$ . Calculations in C–F use  $m/q = n/q = 1.5$ . (G) The normalized elastic energy  $\bar{U}$  as a function of  $\gamma$  and  $\theta$  for parameter values  $\alpha = 100^\circ$ ,  $m/q = n/q = 1$ ,  $k_2/k_1 = 1.5$ , and  $\theta_0 = 10^\circ$ . Arrow indicates the module undergoes a bistable transition between two energetic minima during folding. (H) The module's configuration for the two mechanically stable states in G. Reading left to right in B and H corresponds to compression along  $\hat{z}$ , whereas right to left corresponds to tension along  $\hat{z}$ .

star). Varying  $\alpha$  to other prescribed values shifts this local minimum within the subspace, leading to different values for the

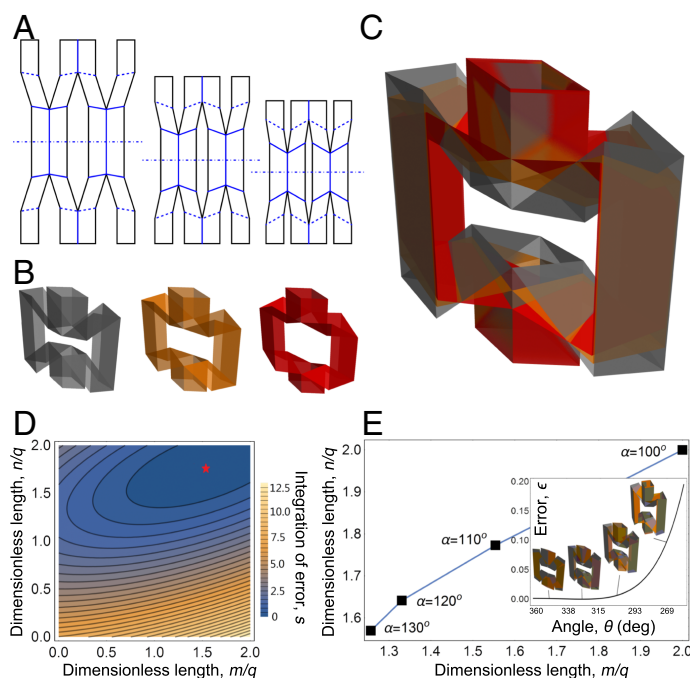


**Fig. 2.** Geometric compatibility of modular kirigami voxels. (A) Design patterns and (B) structure for three geometrically compatible voxels where the first structure (gray:  $\alpha = 100^\circ$ ,  $\gamma = 62.4^\circ$  and  $m/q = n/q = 2$ ) is the target, and the second (orange:  $\alpha = 110^\circ$ ,  $\gamma = 57.7^\circ$ ,  $m/q = 1.55$ , and  $n/q = 1.77$ ) and third (red:  $\alpha = 120^\circ$ ,  $\gamma = 51.2^\circ$ ,  $m/q = 1.33$ , and  $n/q = 1.64$ ) are determined by parameter optimization over a prescribed folding domain. (C) Overlapping the three voxels shows how different design patterns can simultaneously satisfy the  $N_c = 4$  conditions for geometric compatibility in  $X$ ,  $Y$ ,  $Z$ , and  $\angle EDE'$  (e.g.,  $X_{\text{gray}} = X_{\text{orange}} = X_{\text{red}}$  and  $Y_{\text{gray}} = Y_{\text{orange}} = Y_{\text{red}}$ , etc.). This mutual consistency allows geometrically compatible voxels to be interchangeable within a large-scale structure assembled from a mechanically heterogeneous collection of modules. (D) Identifying geometric compatibility requires minimizing the integrated error  $s$  over the design parameters. This projection of parameter space shows the local minimum of  $s$  (red star) as a function of dimensionless lengths  $n/q$  and  $m/q$ . (E) Varying folding angle  $\alpha$  changes the optimal values of  $n/q$  and  $m/q$  that minimize error between the target structure and the structure being optimized for geometric compatibility. (Inset) The error function from which we calculate and minimize the integrated error  $s$ .

optimized parameters (Fig. 2E, points). Generally, we found our method reliably produced geometric compatibility satisfying tight error tolerances within the prescribed folding domain (Fig. 2E, Inset,  $\epsilon$  for  $300 \leq \theta \leq 360^\circ$ ) but that these same designs become incompatible outside the prescribed bounds (Fig. 2E, Inset,  $\epsilon$  for  $\theta < 300^\circ$ ). With this approach for designing geometrically compatible and mechanically distinct building blocks we now focus on voxelizing and assembling 1D, 2D, and 3D large-scale metamaterials.

A simple metamaterial for experimentally validating geometric and mechanical predictions is a 1D chain of voxels aligned on the  $\hat{z}$ -axis (SI Appendix, Figs. S5 and S6). We fabricated these structures with one, two, and three voxels from thin sheets and measured their force–displacement relation. These data compared favorably with the simple energetic model predictions (Materials and Methods), and we generally found the results to be reproducible up to material-specific plastic deformations arising from multiple cycles of testing. A notable exception between the model and data was observed when one voxel with large  $m$ , which was predicted to undergo a bistable transition, instead underwent two bistable transitions (SI Appendix, Figs. S5 and S6). In these data, we found the lower portion of the voxel hopped between bistable states as the strain increased, while the upper portion hopped between bistable states as further strain was applied.

Because the energetic model is symmetric with respect to inversion along  $\hat{z}$ , the transitions of a voxel's upper and lower sections between states 1 and 2 are predicted to occur simultaneously (Fig. 1G and H). Real materials and practical fabrication methods, however, introduce heterogeneities that break this symmetry. As a whole, these experiments generally show mechanical properties in voxelized 1D metamaterials can be predicted, prescribed, and designed, but nevertheless, experimental validation is still important.

Next, we use the  $N_p - N_c > 0$  design strategy to construct 2D bulk metamaterials, which by scaling up in dimension allows for greater mechanical and topological complexity. The two examples we study mask bulk deformations of a large-scale structure using a target module with prescribed properties (Fig. 3A) and geometrically compatible modules optimized to (i) neutralize bulk strain in the  $\hat{x}$  direction (Fig. 3B) and (ii) “cloak” a structural hole (Fig. 3C). In our first example, the 2D structure is voxelized into a series of 1D stripes alternating target and geometrically compatible modules (Fig. 3D). When compressed along the  $\hat{z}$ -axis, the target module's  $\theta$ -dependent Poisson ratio  $\nu_{ZX}$  is compensated for by the compatible module, whose Poisson ratio is optimized to be equal and opposite (Fig. 3E, pink and gray lines). The collective effect is to allow for deformations along the  $\hat{z}$ -axis while neutralizing bulk strain along the  $\hat{x}$ -axis (Fig. 3E, Inset). Interestingly, the zero bulk Poisson ratio engineered into this structure is what makes cork useful as a bottle stopper; cork stoppers provide a tight transverse seal while still allowing for longitudinal motion in or out of the bottle's opening (23). In our second example, a homogeneous 2D structure composed from the target module (Fig. 3F) is structurally weakened with a hole (Fig. 3G) and then reinforced with geometrically compatible modules (Fig. 3H). In terms of the bulk properties, the original and reinforced structures have Young's moduli of 8.1 kPa, whereas the weakened structure has a Young's modulus  $\approx 53\%$  lower at 3.8 kPa. In this example, we optimized the free parameter of the reinforcing module to restore the initially prescribed bulk force–displacement relation to its original form (Fig. 3I and Materials and Methods). When probed with external loads, this new heterogeneous structure can function as a mechanical cloak by obscuring any contents placed in the hole.

Topological complexity can be greatly increased in large-scale 3D metamaterials. To construct such structures, we voxelize the  $\hat{x}\hat{y}$ -plane (Fig. 4A) and stack along the  $\hat{z}$ -axis to create a cuboidal structure with all modules in the same orientation (Fig. 4B). As with the 1D and 2D structures, this 3D voxelization of space is independent from the prescribed mechanical properties of the modules as long as geometric compatibility and  $N_p - N_c > 0$  are satisfied. For a demonstrative example of what can be achieved with the same  $4 \times 7 \times 4$  cuboidal volume (Fig. 4B), we chose three sets of parameters and calculated the respective Poisson ratios (Fig. 4C and D). These data illustrate how the same large-scale structure can have distinct mechanical properties. For practical purposes, it is important to note the accuracy between a target 3D structure and a structure fabricated from finite-size voxels will be tunable. These differences, quantified by an error metric such as  $\epsilon_{3D}$  (Methods and Materials), can be reduced by scaling down the voxel size relative to the target structure (Fig. 4D, Inset), which produces a practical trade-off between structural accuracy and the total number of voxels needed for an application. To fully demonstrate the potential of the  $N_p - N_c > 0$  design strategy, we chose five large-scale 3D target structures including a sphere, three triply periodic minimal surfaces, and a micro-CT volumetric scan of mouse femur bone (Fig. 4E, first row). We voxelized these structures, arbitrarily prescribed one set of mechanical properties on all modules involved, and calculated the various configurations as a function of  $\theta$  (Fig. 4E, second and third rows). Although all of these 3D structures





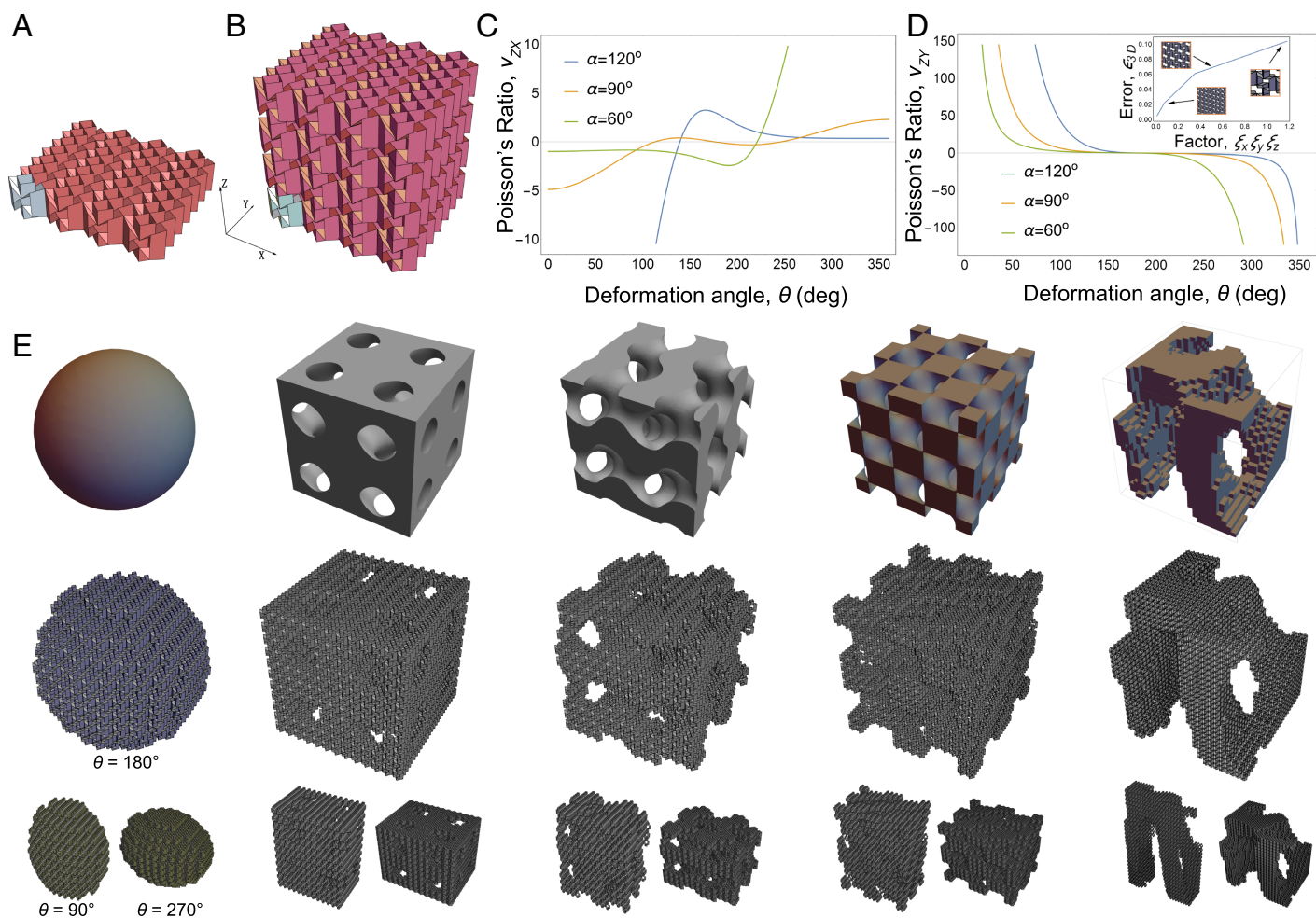


**Fig. 4.** Assembly of kirigami modules into voxelized 3D mechanical metamaterials. (A) Tesselating voxels in the  $\hat{x}\hat{y}$ -plane leads to metamaterials that are (B) stackable along the  $\hat{z}$ -axis. These structures have mechanical properties independent of their ability to tessellate 3D space. Plots of the Poisson ratios (C)  $\nu_{ZX}$  and (D)  $\nu_{ZY}$  as a function of deformation angle  $\theta$  show a wide range of allowable behaviors for the same  $4 \times 7 \times 4$  cuboid bulk structure in B, but with variable parameters for  $\alpha$  and  $\gamma$ . For the plots shown here, we chose  $\gamma = \arcsin[(9/10) \sin(\alpha)]$  to obtain a wide variety of behavior in  $\nu_{ZX}$ . D, Inset shows the error  $\epsilon_{3D}$  between target 3D structure and voxelized 3D structure as a function of the product of scaling factors  $\xi_x$ ,  $\xi_y$ , and  $\xi_z$  (Materials and Methods). Larger values of  $\xi$  lead to larger voxels with a coarser approximation of the target structure, whereas lower values of  $\xi$  have smaller voxels and a more fine approximation. (E) The top row shows five target 3D structures representing a sphere, three triply-periodic minimal surfaces, and a digitized micro-CT scan of a mouse femur bone. The second and third rows are renderings of the different voxelized 3D metamaterials with folding configurations given by  $\theta = 90^\circ$ ,  $180^\circ$ , and  $270^\circ$ . Increasing  $\theta$  corresponds to compression along  $\hat{z}$ , whereas decreasing  $\theta$  corresponds to tension along  $\hat{z}$ . Although all structures have identical compressive properties ( $\alpha = 60^\circ$ ,  $\gamma = 51^\circ$ , and  $m/q = n/q = 1$ ), the scaling factor triplets  $\langle \xi_x, \xi_y, \xi_z \rangle$  are  $\langle 0.37, 0.21, 0.26 \rangle$  for the sphere and triply-periodic minimal surfaces, whereas the micro-CT scan has  $\langle \xi_x, \xi_y, \xi_z \rangle = \langle 8, 9, 5 \rangle \times 10^{-3}$ . These large-scale metamaterials highlight the complex topology that can be achieved independent from the prescribed mechanical properties using the  $N_p - N_c > 0$  design strategy.

deformations under tension along  $\hat{z}$ . Mechanical properties of the kirigami module were calculated by modeling creases as torsional springs with spring constant  $k_1$  that rest at a preferred angle  $\theta_0$ . Joined edges, such as  $BCD$  and  $BC'D'$ , are similarly treated as torsional springs with the same rest angle but with a different spring constant  $k_2$ . Using a common rest angle for creases and crease-like joined edges while assigning two different spring constants reflects the details of how experimental samples were fabricated (SI Appendix). These choices can be easily modified according to the context of how modules are assembled. For the case considered here, the energy function takes the form  $U = \frac{1}{2} [4k_1 \cdot \overline{AB} \cdot (\phi - \theta_0)^2 + 2k_1 \cdot \overline{EF} \cdot (\pi - \phi - \theta_0)^2 + 16k_1 \cdot \overline{BG} \cdot (\theta_{ABGH,CBGF} - \theta_0)^2 + 2k_2 \cdot \overline{E'F'} \cdot (\pi - \phi - \theta_0)^2 + 4k_2 \cdot \overline{CD} \cdot (\phi - \theta_0)^2 + 4k_2 \cdot \overline{BC} \cdot (\theta - \theta_0)^2]$ . Here, we use overlines to denote length between two points. Specifically,  $\overline{AB} = \overline{EF} = \overline{E'F'} = n + q \cdot \cot(\alpha)$ ,  $\overline{BG} = q / \sin(\alpha)$ ,  $\overline{CD} = n$ , and  $\overline{BC} = m$ . Dividing  $U$  by  $qk_1$  leads to the normalized energy  $\tilde{U} = U/qk_1$  (Fig. 1G), which we find exhibits parameter domains with monostability and bistability (SI Appendix, Fig. S4). Note that this stability landscape is not driven by the competition between creasing and bending DOF, as has been shown with other origami structures (11), nor is it driven by a topological discontinuity in configuration space. Instead, the stability landscape found here arises strictly from geometry, which forces some creases to move away from their rest angle (e.g.,  $\overline{BG}$ ,  $\overline{BC}$ , and  $\overline{CF}$ ) while allowing others to

return to their rest angle (e.g.,  $\overline{AB}$ ,  $\overline{CD}$ , and  $\overline{EF}$ ). In this idealized model, the transition between bistable states is a symmetric process where the top and bottom portions of the kirigami module simultaneously hop between stable configurations. In real materials, small heterogeneities can lead to sequential hopping (SI Appendix, Figs. S5 and S6). As a consequence, a 1D structure with  $N$  voxels is capable of supporting up to  $4^N$  distinct stable configurations (SI Appendix, Fig. S4).

**Optimizing Voxels for Geometric Compatibility.** As described in the text, geometrically compatible metamaterials are constructed in a two-step process. Step one is to analyze the number of available design parameters  $N_p$  and pick a set of values that produces the desired properties. For the specific example of the lantern-like module, these chosen parameters are denoted  $\alpha_0$ ,  $\gamma_0$ ,  $m_0$ ,  $n_0$ , and  $q_0$ . Step two is to assemble the bulk metamaterial either from (i) identical voxels, which are by definition geometrically compatible for all folding configurations, or from (ii) dissimilar voxels, which are designed to be geometrically compatible by optimizing parameters to satisfy the design tolerances over the folding interval  $[\theta_a, \theta_b]$ .

For geometric compatibility, there are  $N_c$  constraints imposed on each voxel in the bulk structure. In the specific example discussed in the text of the lantern-like module,  $N_c = 4$ . The constraint on  $\angle EDE'$ , which is the



angle  $\phi(\theta; \alpha, \gamma)$  (Fig. 1A), ensures voxels have matching  $\phi(\theta)$  over  $[\theta_a, \theta_b]$  and  $\sin(\gamma) \propto \sin(\alpha)$ . In light of these observations, the constraint that  $Y(\theta)$  also match between voxels implies  $q \equiv q_0$  for every voxel. Our error function used to match a candidate voxel to a target voxel is then simply defined as  $\epsilon(\theta) = \left[ \frac{X(\theta; \alpha, \gamma, m, n, \phi) - X(\theta; \alpha_0, \gamma_0, m_0, n_0, \phi_0)}{q_0} \right]^2 + \left[ \frac{Z(\theta; \alpha, \gamma, m, n, \phi) - Z(\theta; \alpha_0, \gamma_0, m_0, n_0, \phi_0)}{q_0} \right]^2$ , where  $\phi$  is a function of  $\theta$  parametrized by  $\alpha$  and  $\gamma$ . The parameters  $\alpha, \gamma, m$ , and  $n$ , along with the already set value of  $q = q_0$ , define the geometry of the voxel being optimized for compatibility. To find the optimal set of parameters, we calculate the integrated error  $s = \int_{\theta_a}^{\theta_b} \epsilon(\theta) d\theta$  and seek a set of parameters that satisfy  $[\epsilon(\theta_a), \epsilon(\theta_b)] < \delta$ , where  $\delta$  is our design tolerance. Typically, the solution that minimizes  $s$  satisfies this condition, but pathological situations can be constructed where near-minimum values of  $s$  can satisfy the overall design tolerances with more desirable results.

When constructing the large-scale 2D metamaterial with zero Poisson ratio (Fig. 3D and E) our error function used for calculating geometrically compatible design patterns was adapted to penalize nonzero  $\nu_{ZX}$ . Specifically, we used  $\epsilon_{2D}(\theta) = \left[ \frac{Z_0(2\pi - \theta; \alpha, \gamma, m, n, \phi) - Z_T(\theta; \alpha_0, \gamma_0, m_0, n_0, \phi_0)}{q_0} \right]^2 + \left[ \frac{X_0(2\pi - \theta; \alpha, \gamma, m, n, \phi) + X_T(\theta; \alpha_0, \gamma_0, m_0, n_0, \phi_0)}{\partial Z_T(\theta; \alpha_0, \gamma_0, m_0, n_0, \phi_0) / \partial \theta} \right]^2$ . The first term penalizes differences between the target module's height  $Z_T$  and the optimized module's height  $Z_0$ . The second term penalizes Poisson effects, which are calculated using the sum of target and optimized module widths. To more easily find a set of parameters that satisfy the zero bulk Poisson ratio along the  $\hat{x}$ -direction, we set the optimized functions to depend on  $2\pi - \theta$  whereas the target function depends on  $\theta$ . This ensures solutions are symmetric about  $\theta = \pi$  and is similar in principle to an expression of the form  $\sin(\theta) + \sin(2\pi - \theta) = 0$ . In calculating the bulk strain (Fig. 3E, Inset) we defined  $X_0 = X(\theta = 0)$  and  $\Delta X = X(\theta) - X_0$ .

For the mechanical cloak (Fig. 3F–I) we performed a similar optimization with structures that consist of a  $15 \times 15$  lattice. The original structure contains 225 voxels (Fig. 3F), the structure with the hole contains 104 voxels (Fig. 3G), and the cloaking structure contains 60 gray voxels and 44 orange voxels (Fig. 3H). Force-extension relations were calculated with  $F_{\text{original}}(\theta) = \frac{\partial [225 \cdot U(\theta; \alpha_0, \gamma_0, m_0, n_0)] / \partial \theta}{\partial [15 \cdot Z(\theta; \alpha_0, \gamma_0, m_0, n_0, \phi_0)] / \partial \theta}$ ,  $F_{\text{hole}}(\theta) = \frac{\partial [104 \cdot U(\theta; \alpha_0, \gamma_0, m_0, n_0)] / \partial \theta}{\partial [15 \cdot Z(\theta; \alpha_0, \gamma_0, m_0, n_0, \phi_0)] / \partial \theta}$ ,  $F_{\text{cloak}}(\theta; \alpha, \gamma, m, n) = \frac{\partial [60 \cdot U(\theta; \alpha, \gamma, m, n, \phi) + 44 \cdot U(\theta; \alpha_0, \gamma_0, m_0, n_0, \phi_0)] / \partial \theta}{\partial [4 \cdot Z(\theta; \alpha, \gamma, m, n, \phi) + 11 \cdot Z(\theta; \alpha_0, \gamma_0, m_0, n_0, \phi_0)] / \partial \theta}$ , where  $U$  and  $Z$  denote the energy and height of a voxel,  $\alpha_0, \gamma_0, m_0, n_0$ , and  $q_0$  are the geometric parameters of the gray target voxel. Parameters for the orange reinforcing voxels were obtained by minimizing the integrated error  $s$  over the design interval with the error function  $\epsilon_{\text{cloak}}(\theta) =$

$\left[ \frac{F_{\text{cloak}}(\theta; \alpha, \gamma, m, n) - F_{\text{original}}(\theta)}{F_{\text{original}}(\theta = \pi)} \right]^2 + \left[ \frac{Z(\theta; \alpha, \gamma, m, n) - Z(\theta; \alpha_0, \gamma_0, m_0, n_0, \phi_0)}{q_0} \right]^2$ , where we set  $\sin(\gamma) \propto \sin(\alpha)$  to ensure the constraints imposed on  $\phi(\theta; \alpha, \gamma)$  were obeyed throughout the structure's heterogeneous columns. Thus, we obtain values for  $\alpha, \gamma, m$ , and  $n$  for the orange voxels that allow us to reconstitute the mechanical properties of the original structure. For the force-extension calculations, we chose  $\theta_0 = 10^\circ$ ,  $k_1 = 0.02$  N/mm,  $k_2 = 0$ , and  $q = 1$  cm, then calculated  $\bar{F}(\theta) = d\bar{U}/d(Z/q)$ . These values were chosen to approximate our experimental materials (SI Appendix). We note that for this structure the error function being optimized only generates geometric compatibility along  $Z$  and allows for gaps along  $X$ . For this particular application, the extra constraint on  $X$  is unnecessary.

To quantify differences between large-scale target 3D metamaterial structures, and approximate voxelized structures, we define  $\epsilon_{3D} = 1 - V_{\text{voxel}}/V_{\text{target}}$ . Here,  $V_{\text{target}}$  is the volume of the desired 3D shape and  $V_{\text{voxel}} = N \cdot (\xi_x X) \cdot (\xi_y Y) \cdot (\xi_z Z)$  is the volume of the structure assembled from metamaterial voxels. In this expression,  $N$  is the total number of voxels,  $X, Y, Z$  are dimensions of a single module, and the scaling factors  $\xi_x, \xi_y, \xi_z$  control how small the voxels are in the structure. That is,  $\xi_x X = X_{\text{voxel}}$ ,  $\xi_y Y = Y_{\text{voxel}}$ , and  $\xi_z Z = Z_{\text{voxel}}$ . As such, smaller values for  $\xi_x, \xi_y$ , and  $\xi_z$  lead to a greater number  $N$  of smaller voxels, which, in turn, better approximates the target structure. In the limit where the  $\xi_x, \xi_y, \xi_z \rightarrow 0$ , we have  $N \rightarrow \infty$  in such a way that  $V_{\text{voxel}} \rightarrow V_{\text{target}}$  and  $\epsilon_{3D}$  vanishes.

**Design Patterns.** Design patterns for 1D and 2D metamaterials are typically straightforward to generate from a voxelized structure. For example, folding diagrams for the 1D and both 2D metamaterials are essentially the structure split into a “front” and “back” connected along one edge (SI Appendix, Fig. S7). Folding patterns for 3D metamaterials, however, can be substantially more difficult to generate. Fortunately, methods for continuously transforming 3D objects is an active field of research in computational geometry, and the existing body of work offers potential solutions (28, 29). Alternatively, multisheet assembly methods are also possible and have been described in detail elsewhere (30, 31).

**ACKNOWLEDGMENTS.** We thank Q. B. Deng and C. Q. Zhang for assistance with force experiments, W. Zhang for assistance with preparing photographs, and X. R. Ma, S. J. Wang, J. Mosely, R. J. Lang, U. Nguyen, B. Johnson, B. Parker, and M. Schneider for artistic and intellectual inspiration. This work was supported by Tianjin Natural Science Foundation Grants 14JCZDJC39500 and 16JCYBJC28400 and National Natural Science Foundation of China Grants 11432016, 11672208 and 11402171 (to N.Y.). J.L.S. was independently funded.

- Liu A, Zhu W, Tsai D, Zheludev N (2012) Micromachined tunable metamaterials: A review. *J Opt* 14(11):114009.
- Wegener M (2013) Metamaterials beyond optics. *Science* 342(6161):939–940.
- Christensen J, Kadic M, Kraft O, Wegener M (2015) Vibrant times for mechanical metamaterials. *MRS Commun* 5(03):453–462.
- Kadic M, Bückmann T, Stenger N, Thiel M, Wegener M (2012) On the practicability of pentamode mechanical metamaterials. *Appl Phys Lett* 100(19):191901.
- Lee SH, Park CM, Seo YM, Wang ZG, Kim CK (2009) Acoustic metamaterial with negative modulus. *J Phys Condens Matter* 21(17):175704.
- Bückmann T, et al. (2012) Tailored 3D mechanical metamaterials made by dip-in direct-laser-writing optical lithography. *Adv Mater* 24(20):2710–2714.
- Wei ZY, Guo ZV, Dudt L, Liang HY, Mahadevan L (2013) Geometric mechanics of periodic pleated origami. *Phys Rev Lett* 110(21):215501.
- Schenk M, Guest SD (2013) Geometry of Miura-folded metamaterials. *Proc Natl Acad Sci USA* 110(9):3276–3281.
- Eidini M, Paulino GH (2015) Unraveling metamaterial properties in zigzag-base folded sheets. *Sci Adv* 1(8):e1500224.
- Yasuda H, Yang J (2015) Reentrant origami-based metamaterials with negative Poisson's ratio and bistability. *Phys Rev Lett* 114(18):185502.
- Silverberg JL, et al. (2014) Using origami design principles to fold reprogrammable mechanical metamaterials. *Science* 345(6197):647–650.
- Hanna BH, Lund JM, Lang RJ, Magleby SP, Howell LL (2014) Waterbomb base: A symmetric single-vertex bistable origami mechanism. *Smart Mater Struct* 23(9):094009.
- Silverberg JL, et al. (2015) Origami structures with a critical transition to bistability arising from hidden degrees of freedom. *Nat Mater* 14(4):389–393.
- Waitukaitis S, Menaut R, Chen BG, van Hecke M (2015) Origami multistability: From single vertices to metasheets. *Phys Rev Lett* 114(5):055503.
- Evans TA, Lang RJ, Magleby SP, Howell LL (2015) Rigidly foldable origami gadgets and tessellations. *R Soc Open Sci* 2(9):150067.
- Dudt LH, Vouga E, Tachi T, Mahadevan L (2016) Programming curvature using origami tessellations. *Nat Mater* 15(5):583–588.
- Filipov E, Paulino G, Tachi T (2016) Origami tubes with reconfigurable polygonal cross-sections. *Proc Math Phys Eng Sci* 472(2185):20150607.
- Chen BG, et al. (2016) Topological mechanics of origami and kirigami. *Phys Rev Lett* 116:135501.
- Evans AA, Silverberg JL, Santangelo CD (2015) Lattice mechanics of origami tessellations. *Phys Rev E Stat Nonlin Soft Matter Phys* 92(1):013205.
- Overvelde JT, et al. (2016) A three-dimensional actuated origami-inspired transformable metamaterial with multiple degrees of freedom. *Nat Commun* 7:10929.
- Inger DE, Wang N, Stamenović D (2014) Tensegrity, cellular biophysics, and the mechanics of living systems. *Rep Prog Phys* 77(4):046603.
- Xu S, et al. (2012) Experimental demonstration of a free-space cylindrical cloak without superluminal propagation. *Phys Rev Lett* 109(22):223903.
- Silva S, et al. (2005) Cork: Properties, capabilities and applications. *Int Mater Rev* 50(6):345–365.
- Gladman AS, Matsumoto EA, Nuzzo RG, Mahadevan L, Lewis JA (2016) Biomimetic 4D printing. *Nat Mater* 15(4):413–418.
- Andersen ES, et al. (2009) Self-assembly of a nanoscale DNA box with a controllable lid. *Nature* 459(7243):73–76.
- Gerling T, Wagenbauer KF, Neuner AM, Dietz H (2015) Dynamic DNA devices and assemblies formed by shape-complementary, non-base pairing 3D components. *Science* 347(6229):1446–1452.
- Ke Y, Ong LL, Shih WM, Yin P (2012) Three-dimensional structures self-assembled from DNA bricks. *Science* 338(6111):1177–1183.
- Tachi T (2010) Origamizing polyhedral surfaces. *IEEE Trans Vis Comput Graph* 16(2):298–311.
- Zhou Y, Sueda S, Matusik W, Shamir A (2014) Boxelization: Folding 3D objects into boxes. *ACM Trans Graph* 33(4):71.
- Babae S, Overvelde JT, Chen ER, Tournat V, Bertoldi K (2016) Reconfigurable origami-inspired acoustic waveguides. *Sci Adv* 2(11):e1601019.
- Overvelde JT, Weaver JC, Hoberman C, Bertoldi K (2017) Rational design of reconfigurable prismatic architected materials. *Nature* 541(7637):347–352.

# SUPPLEMENTAL INFORMATION:

## Decoupling local mechanics from large-scale structure in modular metamaterials

Nan Yang<sup>1,\*</sup> and Jesse L. Silverberg<sup>2,†</sup>

<sup>1</sup>*Tianjin Key Laboratory of the Design and Intelligent Control of Advanced Mechatronical Systems, Tianjin University of Technology, Binshuixi Road No. 391, Xiqing District, Tianjin 300384, China*

<sup>2</sup>*Wyss Institute for Biologically Inspired Engineering, Harvard University, Boston, MA 02115*

### RENDERINGS OF EXAMPLE STRUCTURES

In the main text, we showed snap-shots of a lantern-like kirigami module at various folding configurations as a function of  $\theta$  for a single set of parameters (Fig. 1B). To the best of our knowledge, this structure has not been previously described elsewhere. Therefore, to expand on these illustrations, we calculated and rendered three more examples with different parameters, which provides a broader grasp of how these modules change with  $\theta$  (Fig. S1).

### ADDITIONAL POISSON RATIO DATA

In the main text, we provided data on the Poisson ratios  $\nu_{ZY}$  and  $\nu_{ZX}$  for a variety of geometries (Fig. 1C-F). While these data illustrated mechanical properties potentially useful for constructing various bulk metamaterials, we include here  $\nu_{YX}$  for completeness (Fig. S2).

As discussed in the main text, the kirigami module supports two simultaneously negative Poisson ratios (Fig. 1C-F). To further show how the geometric design parameters influence the Poisson ratios, we calculated domains where  $\nu_{ZX}$  and  $\nu_{ZY}$  were less than zero and plotted them in the  $(\theta, \gamma)$  plane for various  $\alpha$  (Fig. S3). We find the design space exhibits non-trivial complexity and offers a wide range of options for specific metamaterial properties. In particular,  $\nu_{ZY} < 0$  for all  $\theta > 180^\circ$  and any  $\gamma$ . Conversely, the sign of  $\nu_{ZX}$  is sensitive to  $\theta$ ,  $\alpha$ , and  $\gamma$ .

### STABILITY OF THE LANTERN-LIKE KIRIGAMI MODULE

In the main text we provided data on the energetic landscape of a single lantern-like kirigami module. Here, we show additional energy plots as a function of  $\theta$  as the parameters  $\alpha$ ,  $\gamma$ ,  $\theta_0$ , and  $k_2/k_1$  are varied (Fig. S4A-D). While these data are for idealized models with fully symmetric structure, we note that real materials can be subject to symmetry-breaking heterogeneities. For example, we show with a half-module that 4 distinct stable states are possible (Fig. S4E). This finding also ap-

plies to the full module, which in turn implies a chain of  $N$  voxels in a 1D metamaterial supports up to  $4^N$  stable configurations. This high degree of multistability presents an opportunity for engineering non-trivial force-extension relationships with piece-wise smooth behavior, as well as other features not readily achievable with a single module.

### MECHANICAL EXPERIMENTS

Kinematic and mechanical designs were prototyped using Mathematica 10.2. This software was used to produce 2D design patterns that were printed and cut from paper sheets (70 g/m<sup>2</sup>). Structures were then hand-folded and edges were bonded using cellophane tape. Each structure was then placed inside a closed book and subject to  $\approx 10$  kg of weight overnight. This process produced structures with an equilibrium configuration angle of  $\theta_0 \approx 0^\circ$ , and with creased hinges that were generally stiffer than the cellophane-bonded edges. Modules were assembled with  $q = 10$  mm, while  $m$  and  $n$  were chosen as described in the figure captions.

Force-extension measurements on individual voxels and 1D chains (Fig. S5A-C) were conducted with a loading speed set to 2 mm/min while the boundaries were mounted with long cellophane strips (Fig. S5B and C). These loading conditions allowed for  $\phi$ , which quantifies the configuration of the module in the regions closest to the testing apparatus, to smoothly vary during the experiments while still maintaining tension. In our idealized mathematical model, we find the upper and lower portions of the lantern-like module always undergo simultaneous bistability transitions. However, the experiments did not undergo the anticipated *simultaneous* transitions (Fig. S5B and C, insets). Instead, upper and lower portions of the structure underwent *sequential* bistability transitions. For the simplest case of one voxel (Fig. S5C, insets), the two photographs illustrate a typical example taken after the lower portion had transitioned between bistable states, but show the upper portion before-and-after bistable transitions. As can be seen, deformations are almost entirely localized to the upper region of bistability while the lower region maintains its configuration. To facilitate comparison with theory, we converted the

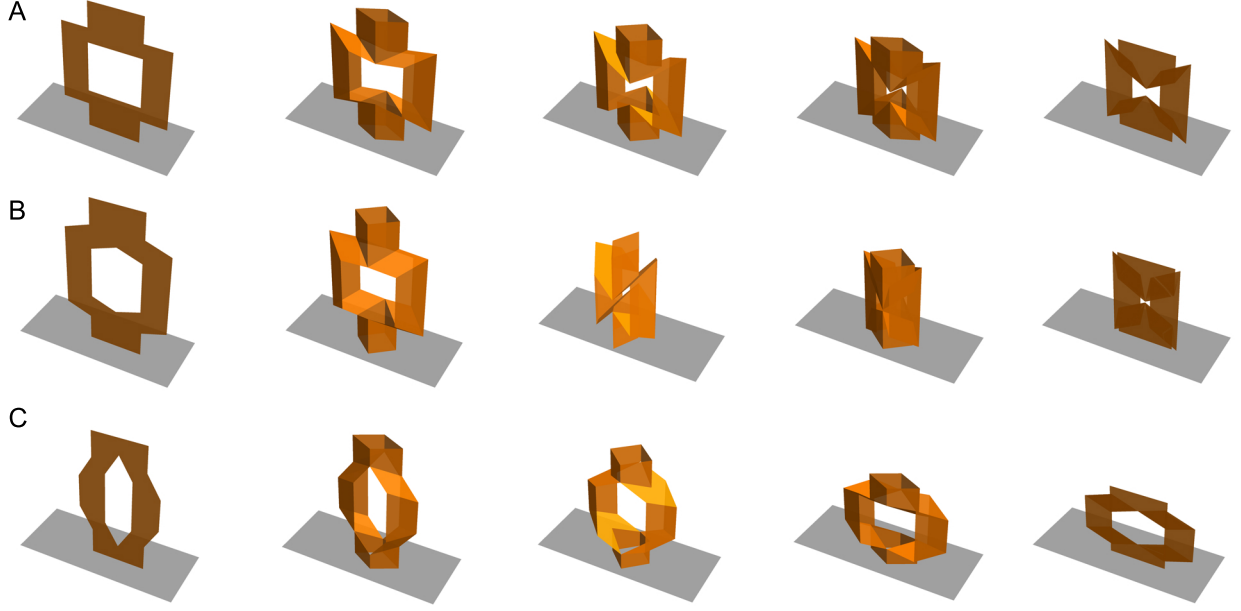


Fig. S1. Example illustrations of lantern-like kirigami module's folding behavior. To elaborate on the main text (Fig. 1B) we show additional example modules at various points in the folding sequence. Geometric parameters are (A)  $\alpha = 60^\circ, \gamma = 30^\circ, m/q = n/q = 1$ , (B)  $\alpha = 60^\circ, \gamma = 50^\circ, m/q = n/q = 1$ , and (C)  $\alpha = 110^\circ, \gamma = 40^\circ, m/q = n/q = 1$ . The columns correspond to  $\theta = 0^\circ, 90^\circ, 180^\circ, 270^\circ$ , and  $360^\circ$ . Reading left-to-right corresponds to compression along  $\hat{z}$ , while reading right-to-left corresponds to tension along  $\hat{z}$ .

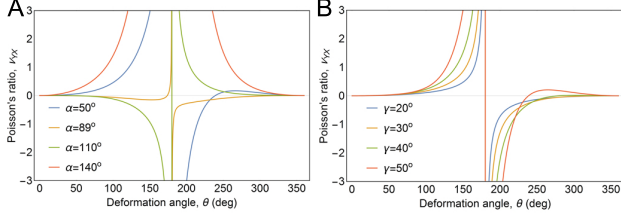


Fig. S2. Poisson ratio  $\nu_{YX}$ . (A) Poisson ratio for  $\gamma = 40^\circ$  and  $\alpha = 50^\circ, 89^\circ, 110^\circ$ , and  $140^\circ$ . (B) Poisson ratio for  $\alpha = 60^\circ$  and  $\gamma = 20^\circ, 30^\circ, 40^\circ$ , and  $50^\circ$ . Calculations use  $m/q = n/q = 1.5$ .

measured height  $Z(\theta)$  at each moment during testing to the corresponding value of  $\theta$  that would be anticipated in an idealized case (see equation for  $Z(\theta)$  in *Materials and Methods*). This value  $\bar{\theta}$  is the *expected deformation angle* in an idealized model, and corresponds to a structure-wide average in the experimental measurements.

To validate the mechanical model for various designs, we fit force-extension measurements to the calculated force-extension relationship  $\tilde{F}(\theta) = d\tilde{U}/d(Z/q)$ . To obtain robust results, we performed a simultaneous fit to three consecutive force-displacement measurements of each design, minimizing the difference between computed and experimental data. The fits have three free parameters corresponding to the rest angle  $\theta_0$  and the

two torsional spring constants  $k_1$  and  $k_2$ . We found for the  $\alpha = 120^\circ$  module (Fig. S5B, red dashed line)  $\theta_0 = (9 \pm 2)^\circ, k_1 = (14.7 \pm 0.2) \times 10^{-3}$  N/mm, and  $k_2$  was bounded to the interval  $[10^{-8}, 10^{-4}]$  N/mm. Because the 2-voxel (Fig. S5B, blue dashed line) and 3-voxel (Fig. S5B, black dashed line) structures are assembled from modules that have the same geometry as the 1-voxel module, we expect the fits to identify commensurate parameter values. We found for the 2-voxel structure  $\theta_0 = (9 \pm 2)^\circ, k_1 = (6.3 \pm 0.1) \times 10^{-3}$  N/mm, and  $k_2$  was bounded to the interval  $[10^{-8}, 10^{-4}]$  N/mm. For the 3-voxel structure,  $\theta_0 = (9 \pm 2)^\circ, k_1 = (3.5 \pm 0.1) \times 10^{-3}$  N/mm, and  $k_2$  was bounded to the interval  $[10^{-8}, 10^{-4}]$  N/mm. Taken together, we see the fits consistently agree on the value for  $\theta_0$  and that it is reasonably close to the estimated value of  $0^\circ$ . Moreover, we see  $k_2/k_1 \ll 1$ , suggesting  $k_1$  dominates the mechanical properties. If the system were a series of Hookean springs in series, we would expect  $k^{2\text{-voxel}} = k^{1\text{-voxel}}/2$  and  $k^{3\text{-voxel}} = k^{1\text{-voxel}}/3$ . Interestingly, we see the 2-voxel value is slightly less than half the 1-voxel case, while the 3-voxel value is about 1/5 the 1-voxel case. Finally, we note that  $k_2$  was not precisely fit, but the bounded values for  $k_2$  compared to the fitted values for  $k_1$  are consistent with expectation that  $k_2 \ll k_1$ , which was qualitatively observed during sample fabrication.

Our second batch of mechanical experiments com-



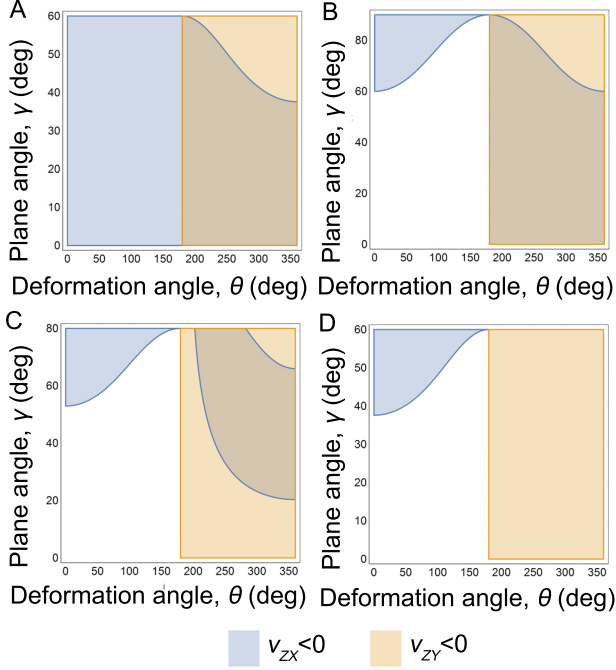


Fig. S3. Regions of negative Poisson ratio. Here, we show domains where  $\nu_{ZX} < 0$  (light blue) and  $\nu_{ZY} < 0$  (light orange) in the  $(\theta, \gamma)$  plane for various values of  $\alpha$ . Specifically, (A)  $\alpha = 60^\circ$ , (B)  $\alpha = 90^\circ$ , (C)  $\alpha = 100^\circ$ , and (D)  $\alpha = 120^\circ$ . Regions of overlapping blue and orange correspond to both Poisson ratios being simultaneously negative, while non-shaded regions correspond to positive Poisson ratios. In all plots,  $m/q = n/q = 2$ .

pared the predicted force-displacement relationships for the three geometries. The first sample (Fig. S5C, red data) is the same as the 1-voxel sample from the previous measurements (Fig. S5B, red data). For the  $\alpha = 110^\circ$  module (Fig. S5C, orange dashed line),  $\theta_0$  was bounded to the interval  $[0.01^\circ, 3^\circ]$ ,  $k_1 = (18.4 \pm 0.4) \times 10^{-3}$  N/mm, and  $k_2$  was bounded to the interval  $[10^{-7}, 10^{-4}]$  N/mm. For the  $\alpha = 100^\circ$  module (Fig. S5C, gray dashed line),  $\theta_0$  was bounded to the interval  $[(10^{-3})^\circ, 11^\circ]$ ,  $k_1 = (19 \pm 2) \times 10^{-3}$  N/mm, and  $k_2$  was bounded to the interval  $[10^{-7}, 10^{-4}]$  N/mm. Broadly, we find the fits are again consistent with qualitative expectations. In all cases,  $\theta_0$  is close to the expected value of  $0^\circ$ , and the values for  $k_1$  are self-consistent across all measurements as well as with previous work[1]. While some parameters are poorly bounded by the fits, the “non-stiff” nature of these variables serves to indicate their weakness in determining the overall fit quality relative to the tightly bounded, or “stiff,” parameters.

We also note that all experiments were conducted under tension in order to avoid the complex non-linear buckling instabilities often found in compression. For example, a failure mode leading to out-of-plane deformations is analogous to Euler buckling found in compressed

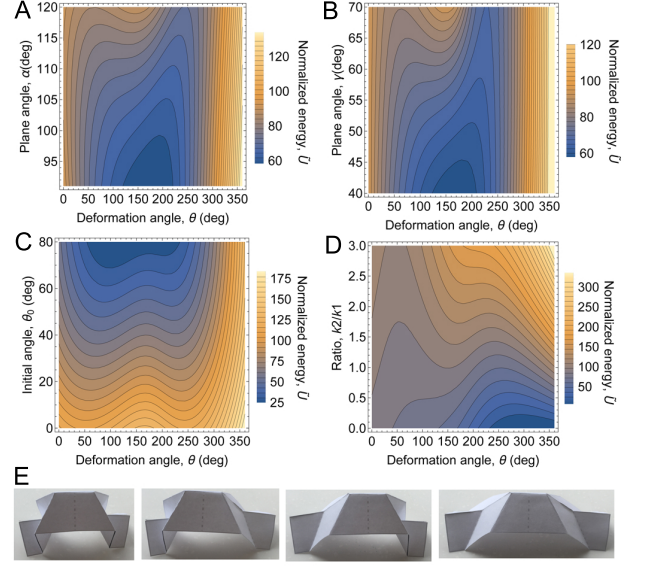


Fig. S4. Stability of the kirigami module. Normalized energy landscapes as a function of  $\theta$  and various parameters. Specifically, (A) varying  $\alpha$  with  $\gamma = 60^\circ, m/q = n/q = 1, k_2/k_1 = 1.5$  and  $\theta_0 = 10^\circ$ . (B) Varying  $\gamma$  with  $\alpha = 100^\circ, m/q = n/q = 1, k_2/k_1 = 1.5$ , and  $\theta_0 = 10^\circ$ . (C) Varying  $\theta_0$  with  $\alpha = 120^\circ, \gamma = 51.2^\circ, m/q = 1.33, n/q = 1.64$ , and  $k_2/k_1 = 1.5$ . (D) Varying  $k_2/k_1$  with  $\alpha = 120^\circ, \gamma = 51.2^\circ, m/q = 1.33, n/q = 1.64$ , and  $\theta_0 = 10^\circ$ . (E) A half-module is used to show four distinct stable states accessible under no external loads.

rods[2]. Additionally, localized bistability transitions or “collapses” can also lead to broken symmetry, as has been observed in origami-inspired bellows[3].

To supplement the experimental force measurements described above (Fig. S5 B and C), we also show the same data presented as a function of displacement along the  $\hat{z}$ -axis (Fig. S6), which may be a more intuitive functional form for certain applications. Notably, this presentation of the measurements does not utilize a back-calculated value for  $\theta$  corresponding to a given height  $Z$ . As can be seen, the theoretical model still fits the measured data quite well.

## 1D AND 2D DESIGN PATTERNS

We show here design patterns for the 1D and 2D metamaterials (Fig. S7). Essentially, the structures are split along the  $\hat{x}\hat{z}$  mid-plane and “opened” so that their edges are connected. This connected edge becomes the vertical line of left-right symmetry in the middle of the folding diagram.

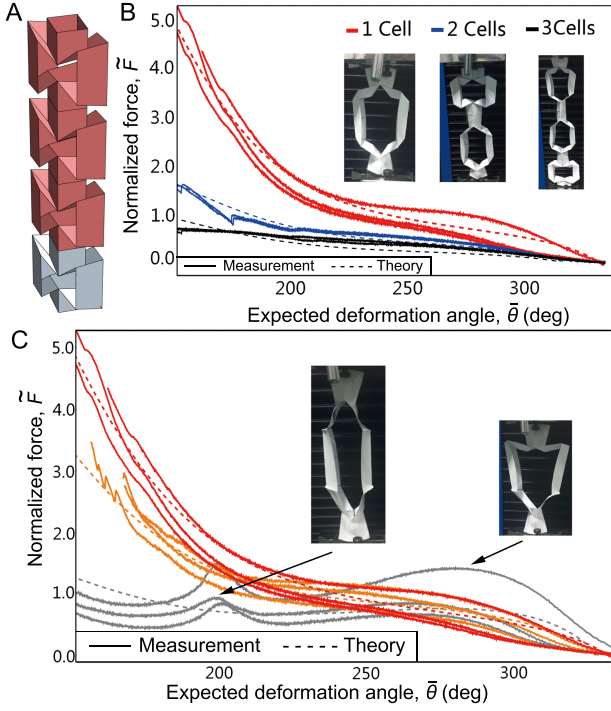


Fig. S5. Assembly of kirigami modules into voxelized 1D mechanical metamaterials. (A) A repeated pattern along the  $\hat{z}$ -axis of a single voxel (gray) leads to a 1D chain of voxels (gray and pink). (B) Mechanical tests of experimentally fabricated structures (solid lines; geometry based on red voxel in Fig. 2 A-C,  $\alpha = 120^\circ$ ,  $\gamma = 51.2^\circ$ ,  $m/q = 1.33$ , and  $n/q = 1.64$ ) show good agreement with theoretical predictions (dashed lines) for 1, 2, and 3 connected voxels. We show three consecutive force-displacement measurements for each structure indicating reproducibility with physical engineering materials. (C) We fabricated and mechanically tested the three gray, orange, and red voxels (Fig. 2 A-C) demonstrating each unit has unique mechanical properties. This ability to have geometrically compatible voxels with independently assigned mechanical properties is a key advantage of the  $N_p - N_c > 0$  design strategy. Each sample was measured three consecutive times (solid lines) and compared to theory (dashed lines). An empirical phenomenon not predicted by our idealized model are the double-peaks in the  $\alpha = 100^\circ$  (gray curves) data. These arise from an asymmetric transition between stable points (Fig. 1 G-H) associated with the upper and lower halves of each voxel (inset). In (B) and (C), the expected deformation angle  $\bar{\theta}$  is the value of  $\theta$  calculated from the total measured length of the structure along  $\hat{z}$ .

### LATTICE KIRIGAMI, AUXETIC HONEYCOMBS AND RIGID ROD NETWORK DESIGNS

While various auxetic structures have long been studied for their geometrically-driven properties, lattice based kirigami and honeycomb-like patterns are two areas of contemporary interest for their applications in biomedical devices, graphene-based materials, and as a general mechanical design motif[4–12]. In these designs, a family of mechanical properties including negative Poisson

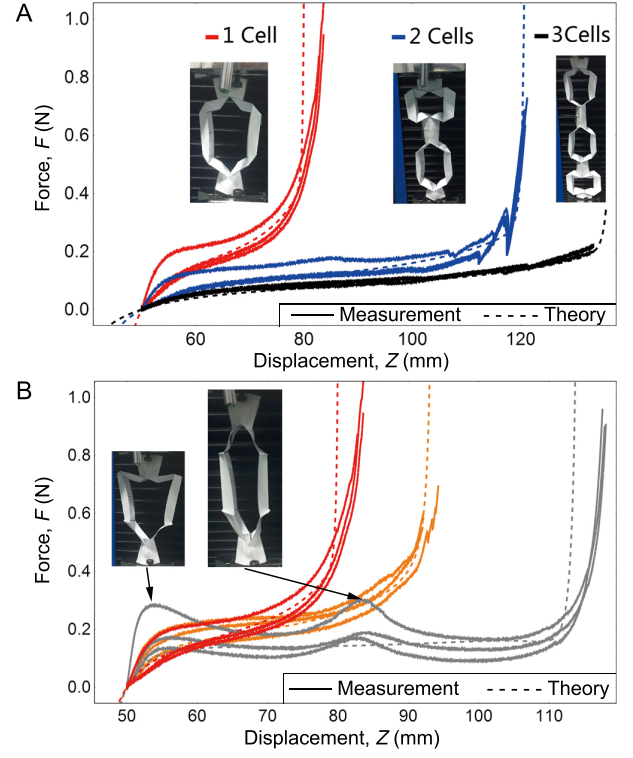


Fig. S6. Experimental measurements presented as a function of voxel height  $Z$ . (A) Force-displacement curves for 1, 2, and 3 voxels strung together in a 1D metamaterial. (B) Force-displacement curves for a single voxel with various parameter values. In all plots, solid lines are experimental measurements, dashed lines are fits to theoretical calculations.

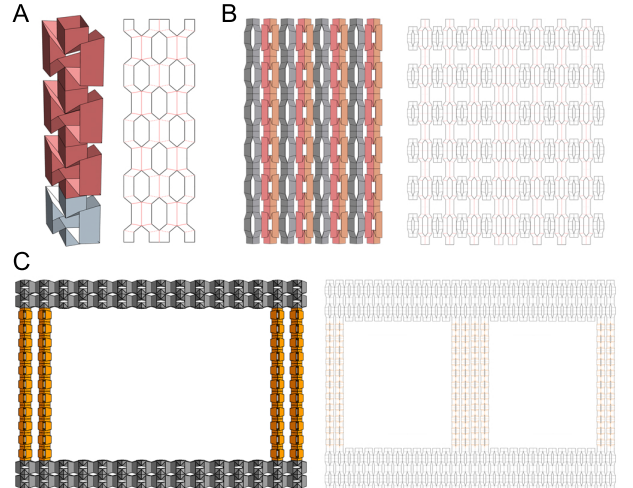


Fig. S7. Metamaterial design patterns. (A) 1D metamaterial design pattern. 2D metamaterial design pattern for the (B) zero bulk Poisson ratio and (C) mechanical cloak structure.

ratio and tunable stiffness has emerged as a generic set of qualities that can be expected from these structures. Nevertheless, when these structures are fabricated, there is a deep coupling of mechanical response between neighboring unit cells that limits the available design space and potential for modularity, especially for 3D structures. A potentially impactful area of research, therefore, would be in developing a modular design strategy similar to the one proposed in the main text specifically for these lattice kirigami and honeycomb-like structures. The benefits over the lantern-like kirigami structure proposed in the main text could include an easier 1-step manufacturing processes as well as rapid deployment in commercially useful materials such as graphene.

Continuing to think about how the ideas proposed in the main text could be realized in practical situations, we turn our attention to network based structures formed from rigid rods (Fig. S8). These lattices have a one-to-one mapping where creases become rods and vertices become joints. Structures similar to the example renderings shown here have been engineered and found to possess a variety of interesting metamaterial properties such as pentamode structure[13, 14] and topologically protected deformations[15, 16]. While such rod-and-stick like structures may be easier to fabricate in practical contexts, it remains unknown whether metamaterial properties can be translated between these two design motifs. In particular, the origami facets typically provide a bending rigidity that resists deformation. For these rod-and-stick structures, the equivalent bending stiffness goes to zero, leading to a different constraint network. Nevertheless, the similarities may still be worth exploring given the opportunities to employ alternative fabrication technologies. A potentially useful analogy from crystallography is the notion of a real space lattice and the corresponding reciprocal lattice in dual space. In the same way solid state physics has established techniques to map frequency-domain phenomena in the dual space to physical properties in real space, there may be a similar connection between the origami-inspired mechanisms and rod-lattice mechanisms. Whether this metaphor offers practical insights would be a subject worth further investigation, since it may lead to a generic method for mapping between two different metamaterial structures with related properties.

## POROUS AND BIPHASIC METAMATERIALS

In terms of applications, porous mechanical metamaterials present interesting opportunities for the framework proposed in the main text. For example, many mechanically-responsive biological materials such as cartilage, muscle, lung tissue, and skin are biphasic. That is, they consist of water-saturated solid structures. Along these lines, we can conceive of a biologically-inspired class

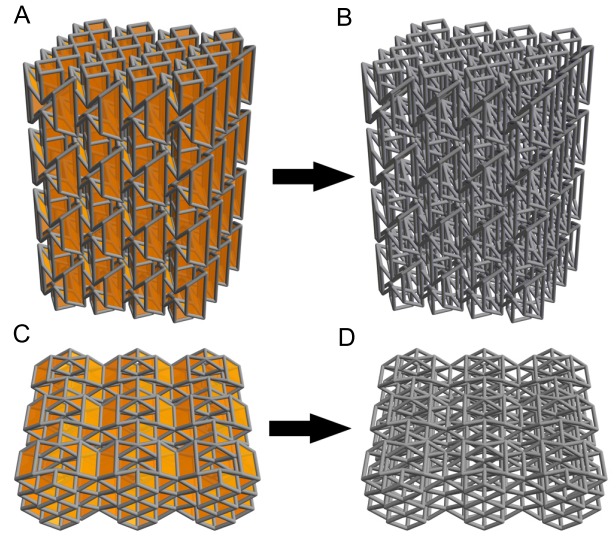


Fig. S8. Rigid rod network materials. Here, we show that a rigid-rod material can be generated by taking (A) the crease pattern of a voxelized kirigami metamaterial, and (B) converting the creases to rods and vertices to joints. A similar mapping (C,D) shows another example structure.

of biphasic mechanical metamaterials. As an example, we propose that voxelized 3D structures assembled from kirigami modules would form the solid phase, while fluid saturating the structure would form the liquid phase. The structures discussed in the main text are particularly well-suited for these applications since they are highly porous, which would allow fluids to rapidly equilibrate.

\* yn@tjut.edu.cn

† jesse.silverberg@wyss.harvard.edu

- [1] Jesse L Silverberg, Arthur A Evans, Lauren McLeod, Ryan C Hayward, Thomas Hull, Christian D Santangelo, and Itai Cohen. Using origami design principles to fold reprogrammable mechanical metamaterials. *Science*, 345(6197):647–650, 2014.
- [2] Lev Davidovich Landau, Evgenij M Lifshic, LP Pitaevskii, and AM Kosevich. *Course of Theoretical Physics: Volume 7, Theory of Elasticity*. Pergamon Press, 1986.
- [3] Austin Reid, Frederic Lechenault, Sergio Rica, and Mokhtar Adda-Bedia. Geometry and design of origami bellows with tunable response. *Physical Review E*, 95(1):013002, 2017.
- [4] Nicholas Karnesis and Gaetano Burriesci. Uniaxial and buckling mechanical response of auxetic cellular tubes. *Smart Materials and Structures*, 22(8):084008, 2013.
- [5] Kun Cai, Jing Luo, Yiru Ling, Jing Wan, and Qing-hua Qin. Effects of size and surface on the auxetic behaviour of monolayer graphene kirigami. *Scientific Reports*, 6, 2016.
- [6] Robin M Neville, Fabrizio Scarpa, and Alberto Pirrera. Shape morphing kirigami mechanical metamaterials. *Sci-*

- entific Reports*, 6:31067, 2016.
- [7] Terry C Shyu, Pablo F Damasceno, Paul M Dodd, Aaron Lamoureux, Lizhi Xu, Matthew Shlian, Max Shtein, Sharon C Glotzer, and Nicholas A Kotov. A kirigami approach to engineering elasticity in nanocomposites through patterned defects. *Nature Materials*, 14(8):785–789, 2015.
  - [8] Yigil Cho, Joong-Ho Shin, Avelino Costa, Tae Ann Kim, Valentin Kunin, Ju Li, Su Yeon Lee, Shu Yang, Heung Nam Han, In-Suk Choi, et al. Engineering the shape and structure of materials by fractal cut. *Proceedings of the National Academy of Sciences*, 111(49):17390–17395, 2014.
  - [9] Ruben Gatt, Luke Mizzi, Joseph I Azzopardi, Keith M Azzopardi, Daphne Attard, Aaron Casha, Joseph Briffa, and Joseph N Grima. Hierarchical auxetic mechanical metamaterials. *Scientific Reports*, 5:8395, 2015.
  - [10] Toen Castle, Yigil Cho, Xingting Gong, Euiyeon Jung, Daniel M Sussman, Shu Yang, and Randall D Kamien. Making the cut: Lattice kirigami rules. *Physical Review Letters*, 113(24):245502, 2014.
  - [11] Daniel M Sussman, Yigil Cho, Toen Castle, Xingting Gong, Euiyeon Jung, Shu Yang, and Randall D Kamien. Algorithmic lattice kirigami: A route to pluripotent materials. *Proceedings of the National Academy of Sciences*, 112(24):7449–7453, 2015.
  - [12] Melina K Blees, Arthur W Barnard, Peter A Rose, Samantha P Roberts, Kathryn L McGill, Pinshane Y Huang, Alexander R Ruyack, Joshua W Kevek, Bryce Kobrin, David A Muller, et al. Graphene kirigami. *Nature*, 524(7564):204–207, 2015.
  - [13] Muamer Kadic, Tiemo Bückmann, Nicolas Stenger, Michael Thiel, and Martin Wegener. On the practicality of pentamode mechanical metamaterials. *Applied Physics Letters*, 100(19):191901, 2012.
  - [14] Tiemo Bückmann, Nicolas Stenger, Muamer Kadic, Johannes Kaschke, Andreas Frölich, Tobias Kennerknecht, Christoph Eberl, Michael Thiel, and Martin Wegener. Tailored 3d mechanical metamaterials made by dip-in direct-laser-writing optical lithography. *Advanced Materials*, 24(20):2710–2714, 2012.
  - [15] Bryan Gin-ge Chen, Bin Liu, Arthur A. Evans, Jayson Paulose, Itai Cohen, Vincenzo Vitelli, and C. D. Santangelo. Topological mechanics of origami and kirigami. *Physical Review Letters*, 116:135501, Mar 2016.
  - [16] CL Kane and TC Lubensky. Topological boundary modes in isostatic lattices. *Nature Physics*, 10(1):39–45, 2014.



# Topological kinematics of origami metamaterials

Bin Liu<sup>1,2,8\*</sup>, Jesse L. Silverberg<sup>1,3,4,8</sup>, Arthur A. Evans<sup>5</sup>, Christian D. Santangelo<sup>5</sup>, Robert J. Lang<sup>6</sup>, Thomas C. Hull<sup>7</sup> and Itai Cohen<sup>1</sup>

**A variety of electronic phases in solid-state systems can be understood by abstracting away microscopic details and refocusing on how Fermi surface topology interacts with band structure to define available electron states<sup>1</sup>. In fact, topological concepts are broadly applicable to non-electronic materials and can be used to understand a variety of seemingly unrelated phenomena<sup>2–6</sup>. Here, we apply topological principles to origami-inspired mechanical metamaterials<sup>7–12</sup>, and demonstrate how to guide bulk kinematics by tailoring the crease configuration-space topology. Specifically, we show that by simply changing the crease angles, we modify the configuration-space topology, and drive origami structures to dramatically change their kinematics from being smoothly and continuously deformable to mechanically bistable and rigid. In addition, we examine how a topologically disjointed configuration space can be used to constrain the locally accessible deformations of a single folded sheet. While analyses of origami structures are typically dependent on the energetics of constitutive relations<sup>11–14</sup>, the topological abstractions introduced here are a separate and independent consideration that we use to analyse, understand and design these metamaterials.**

For our purposes, we define origami-inspired mechanical metamaterials as materials constructed from a series of torsional creases embedded within a thin sheet<sup>15</sup>. Each crease adds a degree of freedom (DOF) and increases the dimensionality of the configuration space. Each crease intersection, or vertex, generates geometric constraints and limits the available portion of configuration space<sup>16,17</sup>. A folded structure then occupies a single point in this configuration space, and in the same way the Fermi surface topology defines nearby accessible electron states, the configuration space's topology defines nearby accessible folding configurations. By introducing constraints on folding angles, the connectivity of the configuration-space topology can be substantially altered. As such, this coupling between folding angles and configuration-space topology allows for unusual kinematic phenomena to emerge.

To understand the significance of this point, we should clearly distinguish the roles played by energetics and configuration-space topology in the context of origami-inspired metamaterials. We examine these differences through the lens of bistability, which is a common phenomenon to many origami structures<sup>16,18–21</sup> (Fig. 1a). On the one hand, a purely energetic bistability appears when the configuration space is simply connected and there are two distinct local energy minima (Fig. 1a, left). Origami-inspired structures assembled from rigid panels and torsional springs can exhibit this type of energetic bistability (Fig. 1b)<sup>19,22</sup>. On the other hand,

a purely topological bistability appears when the configuration space is no longer simply connected, and there exist distinct configurations that are inaccessible from one another (Fig. 1a, right). Both energetic and topological bistabilities allow for multiple configurations. However, the origins of these bistabilities are quite

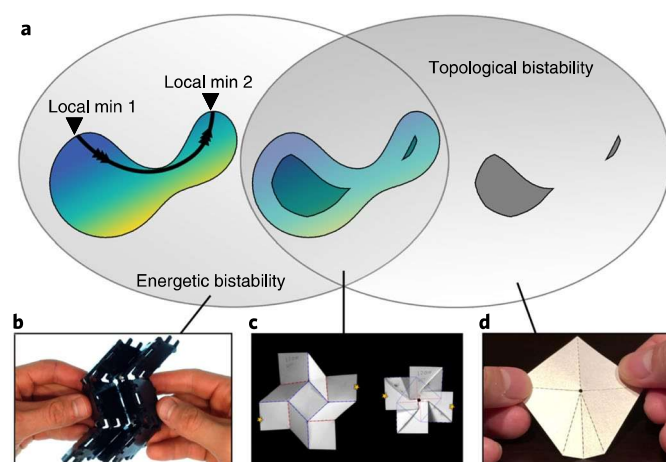


**Fig. 1 | Distinguishing the roles of topological and energetic considerations in origami mechanics.** **a**, Venn diagram illustrating the differences and relationship between energetic and topological bistability. An energetic bistability (left) arises when a simply connected configuration space (coloured region; energetic landscape indicated by colouring, with yellow being high-energy and blue being low-energy) contains two energetic minima (blue areas indicated by arrows). A topological bistability (right) arises when the configuration space is disconnected and no path exists that connects these two regions (isolated grey shapes). Many origami structures have their mechanics arising from both topological and energetic considerations (middle). In particular, a topological bistability defined by the crease geometry can be bridged by bending deformations that cost energy (blue-to-yellow coloured region connecting topologically isolated regions). **b**, An example of an origami-inspired pure-energetic bistability with multiple stable states accessible through changes to the folding angles in a simply connected configuration space. **c**, A common example of an origami structure whose unfolded and folded configurations are topologically disconnected when only considering crease DOFs<sup>16</sup>. The introduction of mechanical bending adds additional DOFs at an energetic cost that bridges the two configurations. **d**, An example structure considered here with a tuneable topological bistability. Credit: courtesy of S. Waitukaitis, P. Dieleman and M. van Hecke (**b**).

<sup>1</sup>Department of Physics, Cornell University, Ithaca, NY, USA. <sup>2</sup>School of Natural Sciences, University of California, Merced, Merced, CA, USA. <sup>3</sup>Wyss Institute for Biologically Inspired Engineering, Harvard University, Boston, MA, USA. <sup>4</sup>Department of Systems Biology, Harvard Medical School, Boston, MA, USA. <sup>5</sup>Department of Physics, University of Massachusetts Amherst, Amherst, MA, USA. <sup>6</sup>Lang Origami, Alamo, CA, USA. <sup>7</sup>Department of Mathematics, Western New England University, Springfield, MA, USA. <sup>8</sup>These authors contributed equally: Bin Liu, Jesse L. Silverberg.

\*e-mail: [blu27@ucmerced.edu](mailto:blu27@ucmerced.edu)

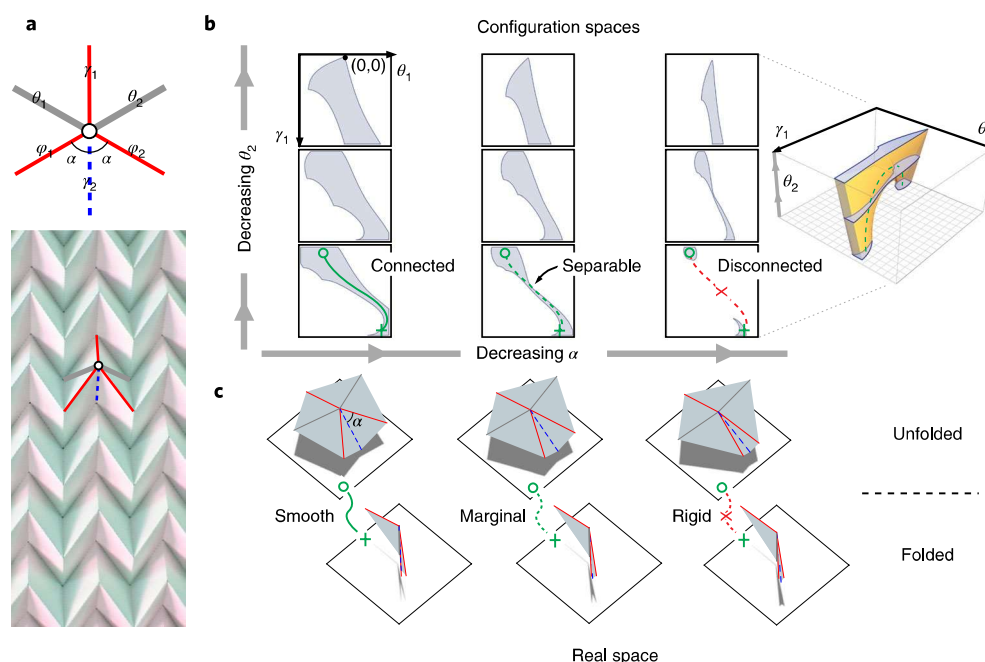


**Fig. 2 | Configuration-space topology of origami-inspired mechanical metamaterials is determined by the underlying crease pattern.** **a**, A triangulated Miura-ori vertex has four creases (three mountain folds in solid red and one valley fold in dashed blue) and two additional crease-like hinges that come from the thin sheet's flexibility (grey lines). In this symmetric Miura-ori vertex, the plane angle  $\alpha$  parameterizes the folding pattern. The photograph below shows the folded structure colour-coded by the above crease pattern. **b**, Configuration spaces for varying plane angle  $\alpha$  and fold angle  $\theta_2$ . In each  $(\theta_2, \gamma_1)$  configuration space, the allowed configurations are grey and the forbidden configurations are white, similar to Fig. 1. As  $\alpha$  and  $\theta_2$  vary, the configuration-space topology can change from one continuously connected region to two disconnected regions. The 3D diagram shows the configuration space of the right-most column and indicates the three cuts with monostable, separable and disconnected domains. **c**, The real-space 3D structures for the bottom row of the configuration spaces in **b**. The folding actuation varies from smooth (monostable) to rigid (bistable) as the configuration space goes from connected to disconnected (Supplementary Movie 1).

different: an energetic bistability is rooted in the material properties that determine the cost of moving through configuration space, while a topological bistability is rooted in the connectivity between available configurations with no regard for material properties. While this theoretical abstraction is quite precise, many experimental origami structures convolve these effects. As a result, we often find topological bistabilities in crease patterns that are connected by hidden DOFs such as facet bending (Fig. 1c). In these cases, energetics bridge a topological bistability through the interplay between crease geometry and the mechanics of bending (Fig. 1a, middle). Here, we broadly disregard energetic considerations relating to hidden DOFs, and instead focus strictly on the phenomena that emerge from the dynamics of configuration space topology. While physical materials will always have some amount of hidden DOFs that play into the bulk mechanical properties, the study of configuration space itself uncovers a variety of new insights regarding vertex-vertex coupling and its ability to mediate non-local influence through dynamic constraints on the global configuration space.

Origami metamaterials are typically designed by tessellating individual units<sup>19,23,24</sup>. Before we address these more complex systems, we first analyse the configuration-space topology of a single vertex (Fig. 1d). For example, we extract a single vertex from a triangulated Miura-ori pattern<sup>25</sup> parametrized by folding angle  $\alpha$  and analyse its configuration space. The vertex has four prescribed creases with non-zero preferred rest angles (three mountain folds  $\phi_1, \phi_2, \gamma_1 < 0$  rad, and one valley fold  $\gamma_2 > 0$  rad) and two virtual creases ( $\theta_1, \theta_2$ ) with zero preferred rest angle (Fig. 2a). A Miura-ori vertex without virtual creases has only one DOF, which we choose here to be  $\gamma_1$ . Triangulating the folding pattern introduces two extra DOFs to the configuration space. For a range of  $\alpha$ , we find the three-dimensional (3D) configuration space of the vertex is simply

connected (Fig. 2b, left column), and the resulting kinematics demonstrate smooth actuation (Fig. 2c, left column). As we decrease  $\alpha$ , the configuration-space topography narrows, with all pathways between the initial and final configurations passing through a single point in configuration space. This marginal actuation (Fig. 2b, middle column) is smooth but tightly constrained (Fig. 2c, middle column). As we continue to decrease  $\alpha$ , the configuration topology becomes disconnected for  $\theta_2$  larger than a critical value (Fig. 2b, right column; see Supplementary Information). For fixed  $\theta_2$ , we find that varying  $\alpha$  breaks configuration-space homotopy<sup>26</sup> (Fig. 2b, bottom row), and the disconnection results in bistable systems (Fig. 2c, right). As demonstrated by the isolated vertex, configuration-space topology has both qualitative and quantitative effects for the real-space kinematics (Supplementary Movie 1).

In a multi-vertex folding pattern, the configuration-space dimensionality is larger than the isolated vertex just considered. As a result, the folding of a crease in one region of the structure can change the global configuration-space topology, affecting the folding behaviour in another region of the structure. This interplay allows for the potential to design multiple distinct mechanical functionalities into the global behaviour of a single folding sheet. To illustrate this principle, we connected vertices in a series of concentric Miura-ori-like rings (Fig. 3a), which bears similarities to artistic origami structures<sup>27,28</sup>. Here, we consider only the vertices along the radial direction due to the azimuthal symmetry, and we permit creases to fold only in the prescribed directions. When the structure begins to fold from a flat sheet, each vertex initially has a continuously connected configuration space. As long as the innermost vertex remains unfolded, the entire structure remains only moderately constrained and flexible. However, as the innermost ring folds, it constrains the neighboring ring to a configuration space



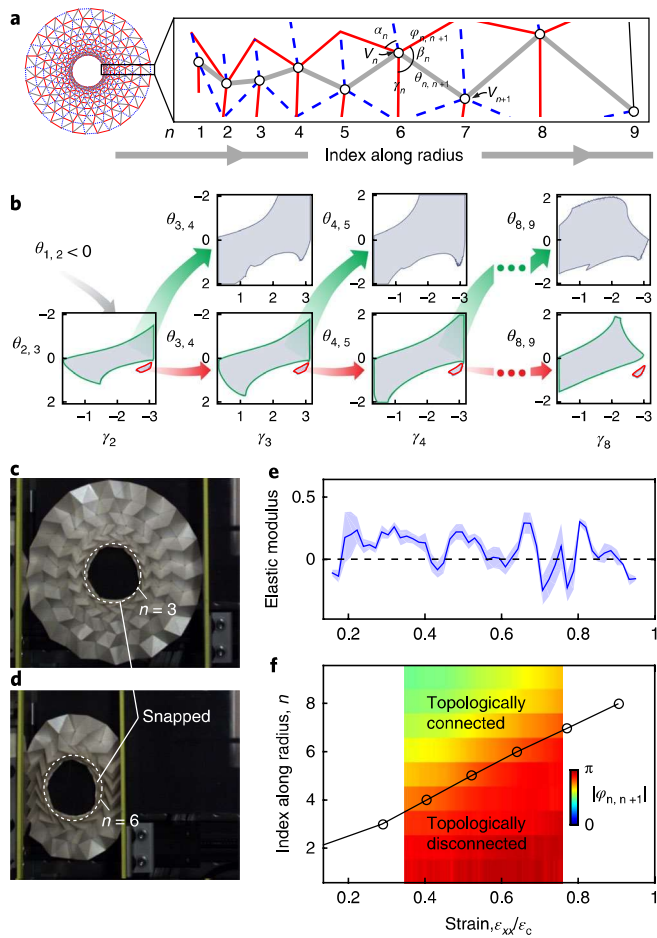


**Fig. 3 | Coupling configuration-space topology with vertex-vertex**

**interactions.** **a**, Folding diagram for a Miura-ori ring and definition of the fold angles  $\theta_{n,n+1}$  and  $\gamma_n$ . The geometry consists of triangulated Miura-ori vertices (Fig. 2a) connected such that  $\alpha_n$  and  $\beta_n = \pi - \alpha_n$  vary as a function of indexed position along the ring radius. The resulting configuration space includes pure-crease DOFs (red, blue lines) as well as facet-bending DOFs (grey lines) all operating at the same energy scale. **b**, For all  $\theta_{1,2} < 0$ , the configuration space  $\langle \gamma_2, \theta_{2,3} \rangle$  is topologically disconnected. Configurations in the larger region (outlined green) lead to configurations at the next vertex ( $\langle \gamma_3, \theta_{3,4} \rangle$ ) that are topologically connected. Configurations in the smaller region (outlined red) lead to configurations at the next vertex ( $\langle \gamma_3, \theta_{3,4} \rangle$ ) that are topologically disconnected. This pattern of coupling configuration-space topology continues along the radial index  $n$  due to vertex-vertex interactions. **c, d**, An experimentally fabricated Miura-ori ring (**c**) is compressed using a controlled strain measurement device (**d**). The mechanical actuation drives the structure through series of topologically disconnected configurations depicted in the lower row of **b**. **e**, The compressive elastic modulus of the Miura-ori ring as a function of normalized strain  $\epsilon_{xx}/\epsilon_c$ , where the critical strain  $\epsilon_c = 0.75$  and corresponds to the strain at which the entire sheet snaps into a cylindrical wall, is obtained from the force-strain measurement (see Supplementary Information). The modulus shows a sequence of drops in its value, each of which corresponds to a bistability snap. The blue line is a ten-point boxcar average of the measured modulus value and the shaded band is the ten-point boxcar standard deviation. **f**, Quantitative image analysis measures the folding angle  $\phi_{n,n+1}$ , which correlates with the configuration-space topology of each vertex. At the lowest measured strain, vertices with  $n \leq 4$  have been driven into the topologically disconnected configuration spaces, whereas vertices with  $n > 4$  still have topologically connected configuration spaces. The solid line shows the boundary between the vertices with topologically connected configuration spaces and the vertices with topologically disconnected configuration spaces (see Supplementary Information).

with a topological bistability (Fig. 3b,  $\langle \gamma_2, \theta_{2,3} \rangle$ , disconnected green and red regions). As the structure is further folded, each vertex in the second ring moves through configuration space, and ultimately transitions across the topological bistability (Fig. 3b, moving from the green region to red region). In the mathematical abstraction of configuration space (Fig. 1a, right-most motif), this transition is strictly forbidden. However, in experimental systems, the transition becomes possible when hidden DOFs are invoked to bridge the topological gap (Fig. 1a, centre motif). When the second ring crosses the bistability transition, this newly occupied region of configuration space constrains the third ring so that its previously connected configuration space (Fig. 3b, upper  $\langle \gamma_3, \theta_{3,4} \rangle$  configuration space) now exhibits a topological bistability (Fig. 3b, lower  $\langle \gamma_3, \theta_{3,4} \rangle$  configuration space). This process repeats across the entire structure; as each ring crosses a topological bistability, it generates constraints that introduce topological bistability in the next ring of the sequence (Fig. 3b, configuration-space diagrams read left-to-right). In practice, we therefore expect that a physical Miura-ori ring that contains hidden DOFs will undergo a sequential series of snaps as the structure is folded and each ring transitions through its respective topological bistability via energetic deformations not described by the configuration-space topology. We experimentally fabricated this structure (Fig. 3c,d), measured its force-displacement relation as the structure was folded (Methods), and confirmed the expected bulk phenomenology (Fig. 3e). Coexistence of the topologically connected and disconnected configuration spaces can be predicted and quantitatively compared with the measurements, which are most conveniently expressed by the crease angle  $\phi_{n,n+1}$  (Fig. 3f). While the crease pattern of this structure has apparent similarities with other cyclic origami designs<sup>29–32</sup>, the sequence of transitions through topological bistabilities shown here is a significant difference that distinguishes the kinematic behaviour from related flat-foldable and nearly single-DOF structures. As such, these seemingly small differences in folding pattern demonstrate that vertex-vertex coupling has consequential significance by propagating topologically prescribed mechanical effects across the entire structure during folding actuation.

In the Miura-ori ring structure, we showed how folding on one crease can alter the configuration-space topology elsewhere in the structure. Next, we consider the opposite scenario where the global configuration space is disjointed and actuation of a family of creases in one region has no effect in another. For this two-DOF actuation to occur, the configuration-space topology will be separated into two domains that touch only at a single point. One domain in configuration space corresponds to half of the physical structure, while the other domain in configuration space corresponds to the other half of the physical structure. Thus, an actuation in one half of the structure is dimensionally reduced at the interface between the two structures; as the topology of configuration space involves two domains that touch at a single point, the beginning and end points of the path are collapsed onto this point in configuration space. This collapse of the path to a point creates a degeneracy that places no constraints on the allowed configurations within the other half of the structure. As such, any other simply connected path in the other domain is freely realizable, since it too will be dimensionally reduced to the same point in configuration space.

To illustrate this principle in a non-trivial tessellation, we connect a series of vertices such that the parameter  $\alpha$  varies in a prescribed fashion for each column (Fig. 4a). If each vertex were isolated from the overall structure, there would be a set of independent configuration spaces (Fig. 4b, grey region in each configuration space diagram). However, vertex-vertex coupling imposes topological constraints (Fig. 4b, shaded pink region) on the accessible configuration space. If we actuate folding at the vertex described by the  $\langle \theta_{-5,-4}, \theta_{-4,-3} \rangle$  configuration space (Fig. 4b, arbitrary trace within the topologically allowed region from the red circle to the

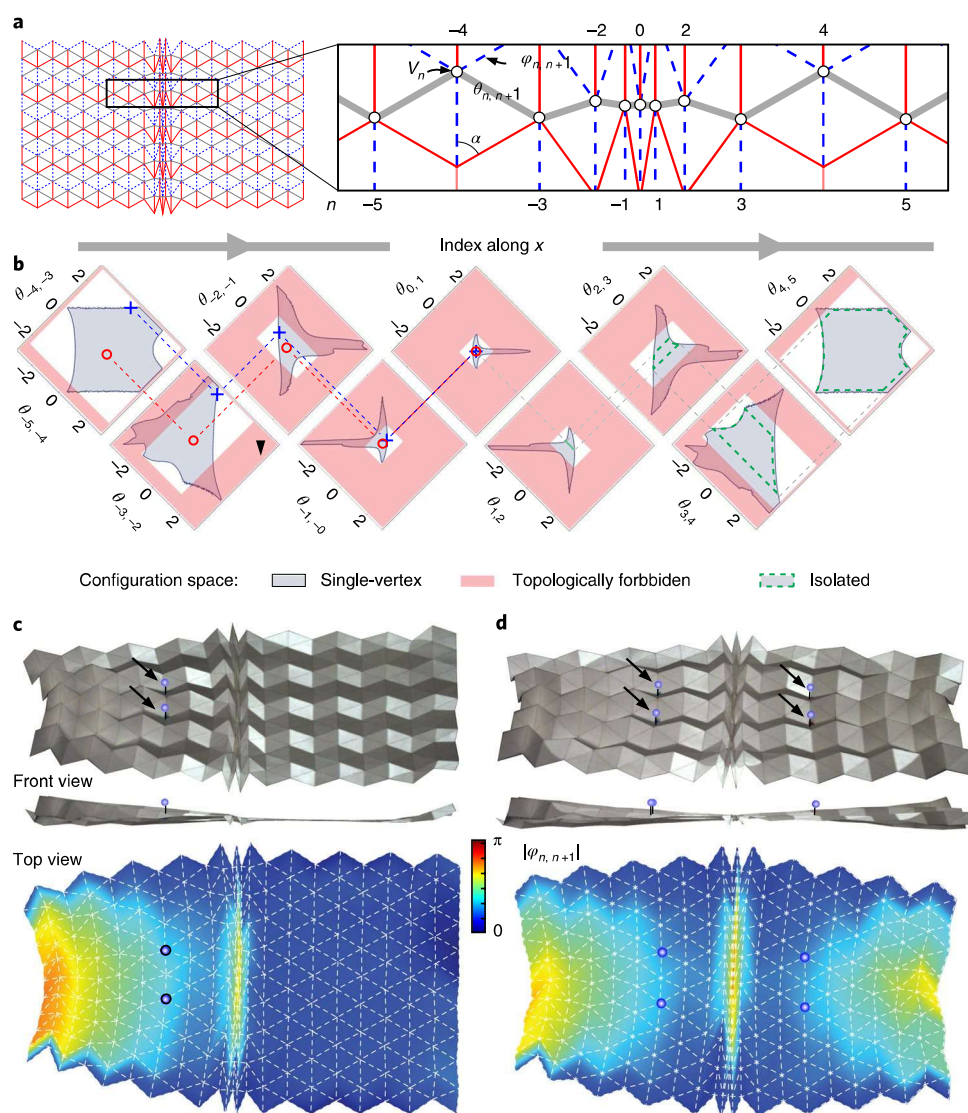


**Fig. 4 | Decoupling configuration-space topology with vertex-vertex interactions.** **a**, Folding diagram for a two-DOF Miura-ori-like structure and definition of the fold angles  $\theta_{n,n+1}$ . The geometry consists of triangulated Miura-ori vertices (Fig. 2a) connected such that  $\alpha_n$  vary as a function of indexed position along the  $x$  axis. The resulting configuration space includes pure-crease DOFs (red, blue lines) as well as facet-bending DOFs (grey lines) all operating at the same energy scale. **b**, Isolated vertices have allowed configuration spaces  $\langle \theta_{n-1,n}, \theta_{n,n+1} \rangle$  (grey shaded regions); however, when connected, regions of configuration space become topologically forbidden (red shaded regions). Nevertheless, deformations between  $n < 0$  and  $n > 0$  are decoupled. For example, a path between two points in the  $\langle \theta_{-5,-4}, \theta_{-4,-3} \rangle$  configuration space has a corresponding path in the configuration spaces  $\langle \theta_{-4,-3}, \theta_{-3,-2} \rangle$ ,  $\langle \theta_{-3,-2}, \theta_{-2,-1} \rangle$  and  $\langle \theta_{-2,-1}, \theta_{-1,0} \rangle$ . This path collapses to a single point in the  $\langle \theta_{-1,0}, \theta_{0,1} \rangle$  configuration space, which permits a variety of configurations for the vertices with increasing index (green isolated regions). As  $n$  increases, the constraints on configuration space rapidly vanish, decoupling deformations between  $n < 0$  and  $n > 0$ . **c,d**, The experimentally fabricated structure is pinched at two points (**c**) and four points (**d**) on either side of  $n=0$  (top), leading to strain fields (bottom) that are decoupled by the crease pattern at  $n=0$ .

blue cross), then the neighbouring vertices to the right will undergo an actuation within their own topologically allowed configuration space. In the configuration space  $\langle \theta_{-1,0}, \theta_{0,1} \rangle$ , the end points of these paths collapse onto a single point that allows for a range of configurations for the vertices further to the right (Fig. 4b), regions of configuration spaces within the green dashed lines). In fact, the configuration space  $\langle \theta_{3,4}, \theta_{4,5} \rangle$  is essentially unconstrained by the path in the  $\langle \theta_{-1,0}, \theta_{0,1} \rangle$  configuration space, and any effects from actuation in the left half of the tessellation are suppressed in the right half of the tessellation. In essence, the configuration spaces on the left and right portions of this structure are disconnected. We experimentally fabricated this tessellation and found that we could independently actuate the left and right halves as expected

(Fig. 4c,d). Hence, vertex-vertex coupling in this structure allows us to decouple the configuration-space topology in a manner that allows for localization of real-space kinematics. Importantly, this design can be treated as a modular structure and combined with the Miura-ori ring to create larger composite structures where the configuration-space constraints act locally on each module.

Origami-inspired metamaterials have a number of desirable features including single-sheet fabrication, compatibility with well-established self-assembly methods, and an essentially infinite design space associated with the rich variety of folding patterns. Here, we have added to this list the capacity to design kinematic properties from the configuration-space topology that can be modularly assembled as constituents of a larger structure. This approach to

metamaterial design produces structures with regions that are physically attached to one another but kinematically isolated through constraints on their configuration space. In applications, the benefits of our findings allow for the design of structures insensitive to real-world manufacturing defects and tolerances<sup>23,33,34</sup>. This flexibility can be potentially achieved by incorporating known imperfections as added volume into the analysis of configuration-space topology, ensuring the folding actuations are as intended. From this perspective, monostability and bistability can be robustly designed even in the presence of parasitic compliance. With the results presented here, it becomes possible to design topologically constrained metamaterials with well-defined properties even in the presence of irregular or unpredictable forces. Such devices are particularly exciting at the meso- and microscale for applications in biological fluid flow and tissue engineering.

## Methods

Methods, including statements of data availability and any associated accession codes and references, are available at <https://doi.org/10.1038/s41567-018-0150-8>.

Received: 15 October 2017; Accepted: 19 April 2018;

Published online: 28 May 2018

## References

- Qi, X.-L. & Zhang, S.-C. Topological insulators and superconductors. *Rev. Mod. Phys.* **83**, 1057–1110 (2011).
- Bader, R. & Nguyen-Dang, T. T. A topological theory of molecular structure. *Rep. Prog. Phys.* **44**, 893–948 (1981).
- Avron, J. E., Osadchy, D. & Seiler, R. A topological look at the quantum Hall effect. *Phys. Today* **56**, 38–42 (2003).
- Lu, L., Joannopoulos, J. D. & Soljačić, M. Topological photonics. *Nat. Photon.* **8**, 821–829 (2014).
- Kane, C. L. & Lubensky, T. C. Topological boundary modes in isostatic lattices. *Nat. Phys.* **10**, 39–45 (2013).
- Paulose, J., Chen, B. G.-g & Vitelli, V. Topological modes bound to dislocations in mechanical metamaterials. *Nat. Phys.* **11**, 153–156 (2015).
- Mahadevan, L. & Rica, S. Self-organized origami. *Science* **307**, 1740–1740 (2005).
- Schenk, M. & Guest, S. D. Geometry of Miura-folded metamaterials. *Proc. Natl Acad. Sci. USA* **110**, 3276–3281 (2013).
- Wei, Z. Y., Guo, Z. V., Dudge, L., Liang, H. Y. & Mahadevan, L. Geometric mechanics of periodic pleated origami. *Phys. Rev. Lett.* **110** (2013).
- Silverberg, J. L. et al. Using origami design principles to fold reprogrammable mechanical metamaterials. *Science* **345**, 647–650 (2014).
- Yasuda, H. & Yang, J. Reentrant origami-based metamaterials with negative Poisson's ratio and bistability. *Phys. Rev. Lett.* **114**, 185502 (2015).
- Filipov, E. T., Tachi, T. & Paulino, G. H. Origami tubes assembled into stiff, yet reconfigurable structures and metamaterials. *Proc. Natl Acad. Sci. USA* **112**, 12321–12326 (2015).
- Giamperio, A., Perego, U. & Borsari, R. A constitutive model for the mechanical response of the folding of creased paperboard. *Int. J. Solids Struct.* **48**, 2275–2287 (2011).
- Lechenault, F., Thiria, B. & Adda-Bedia, M. Mechanical response of a creased sheet. *Phys. Rev. Lett.* **112**, 244301 (2014).
- Hull, T. *Project Origami: Activities for Exploring Mathematics*. (CRC Press: Boca Raton, FL, 2006).
- Silverberg, J. L. et al. Origami structures with a critical transition to bistability arising from hidden degrees of freedom. *Nat. Mater.* **14**, 389–393 (2015).
- Chen, B. G.-g et al. Topological mechanics of origami and kirigami. *Phys. Rev. Lett.* **116**, 135501 (2016).
- Hanna, B. H., Lund, J. M., Lang, R. J., Magleby, S. P. & Howell, L. L. Waterbomb base: a symmetric single-vertex bistable origami mechanism. *Smart Mater. Struct.* **23**, 094009 (2014).
- Waitukaitis, S., Menaut, R., Chen, B. G.-g & van Hecke, M. Origami multistability: from single vertices to metasheets. *Phys. Rev. Lett.* **114**, 055503 (2015).
- Yang, N. & Silverberg, J. L. Decoupling local mechanics from large-scale structure in modular metamaterials. *Proc. Natl Acad. Sci. USA* **114**, 3590–3595 (2017).
- Brunck, V., Lechenault, F., Reid, A. & Adda-Bedia, M. Elastic theory of origami-based metamaterials. *Phys. Rev. E* **93**, 033005 (2016).
- Waitukaitis, S. & van Hecke, M. Origami building blocks: Generic and special four-vertices. *Phys. Rev. E* **93**, 023003 (2016).
- Tachi, T. Rigid-foldable thick origami. In *Origami 5: The 5th International Conference on Origami in Science Mathematics and Education* (eds Wang-Iverson, P. et al.) 253–264 (Taylor & Francis, New York, NY, 2011).
- Evans, A. A., Silverberg, J. L. & Santangelo, C. D. Lattice mechanics of origami tessellations. *Phys. Rev. E* **92**, 013205 (2015).
- Miura, K. Method of packaging and deployment of large membranes in space. *Inst. Space Astronaut. Sci. Rep.* **618**, 1–9 (1985).
- Nakahara, M. *Geometry, Topology and Physics* 2nd edn (Taylor & Francis, Boca Raton, FL, 2003).
- Nojima, T. *Origami Modeling of Functional Structures Based on Organic Patterns*. MSc thesis, Kyoto Univ. (2002).
- Tachi, T. Designing freeform origami tessellations by generalizing Resch's patterns. *J. Mech. Des.* **135**, 111006 (2013).
- Barreto, P. T. Lines meeting on a surface: the “Mars” paperfolding. In *Proc. 2nd International Meeting of Origami Science and Scientific Origami* 323–331 (ed. Miura, K.) (Sein Univ. Art and Design, Otsu, 1997).
- Nojima, T. Modelling of folding patterns in flat membranes and cylinders by origami. *JSME Int. J. Ser. C* **45**, 364–370 (2002).
- Lang, R. J. The science of origami. *Phys. World* **20**, 30 (2007).
- Kovac, M. & Sareh, P. Aerial devices capable of controlled flight. WO patent application PCT/GB2016/051,567 (2016); <https://www.google.com/patents/WO2016193690A1?cl=en>
- Francis, K. C. et al. From crease pattern to product: considerations to engineering origami-adapted designs. In *Proc. ASME 2014 IEDTC & CIEC, Buffalo, NY, 17–20 August 2014*, V05BT08A030 (ASME, New York, NY, 2014).
- Chen, Y., Peng, R. & You, Z. Origami of thick panels. *Science* **349**, 396–400 (2015).

## Acknowledgements

The authors thank A. Ruina, T. Healy, J. Jenkins, U. Nguyen, L. Freni and the Cohen laboratory for useful discussions. We also thank F. Parish for assistance with the laser cutter, and S. Waitukaitis, P. Dieleman and M. van Hecke for providing the photo in Fig. 1b. This work was supported by the National Science Foundation grant no. EFRI ODISSEI-1240441. I.C. received continuing support from DMREF-1435829. B.L. acknowledges the support of the National Science Foundation grant no. NSF CBET-1706511. C.D.S. acknowledges the kind hospitality of the Kavli Institute of Theoretical Physics in Santa Barbara, CA, funded by the National Science Foundation under grant no. NSF PHY-1125915.

## Author contributions

B.L. and J.L.S. designed the research; B.L. conducted the research; B.L., J.L.S., A.A.E., R.J.L., T.C.H. and I.C. interpreted the results; C.D.S., R.J.L., T.C.H. and I.C. supervised the research; B.L., J.L.S., C.D.S., R.J.L., T.C.H. and I.C. prepared the manuscript.

## Competing interests

The authors declare no competing interests.

## Additional information

**Supplementary information** is available for this paper at <https://doi.org/10.1038/s41567-018-0150-8>.

**Reprints and permissions information** is available at [www.nature.com/reprints](http://www.nature.com/reprints).

**Correspondence and requests for materials** should be addressed to B.L.

**Publisher's note:** Springer Nature remains neutral with regard to jurisdictional claims in published maps and institutional affiliations.



## Methods

**3D model of origami structures.** A mathematical model of each experimentally generated origami structure is formulated for numerical simulation and 3D reconstruction. The model is composed of the vertex coordinates and the constraints imposed by the crease length between neighbouring vertices. Given a 2D projection of all the vertex positions  $(x_i, y_i)$ , the  $z_i$  coordinates in the third dimension are obtained by minimizing a penalty function<sup>28</sup>

$$V(z) = \frac{k}{2} \sum_{i,j} [\sqrt{(x_i - x_j)^2 + (y_i - y_j)^2 + (z_i - z_j)^2} - l_{ij}]^2, \text{ where } l_{ij} \text{ is the length of the}$$

crease between two connected vertices of indices  $i$  and  $j$  on the triangular crease lattice. The  $z$  coordinates can thus be obtained by solving the associated ordinary differential equation array as  $\dot{z}_i = -k \sum_j [\sqrt{(x_i - x_j)^2 + (y_i - y_j)^2 + (z_i - z_j)^2} - l_{ij}]$

$$\hat{r}_{ij} \cdot \hat{z}, \text{ where the unit vector } \hat{r}_{ij} = ((x_i - x_j)\hat{x} + (y_i - y_j)\hat{y} + (z_i - z_j)\hat{z})$$

$/\sqrt{(x_i - x_j)^2 + (y_i - y_j)^2 + (z_i - z_j)^2}$  and  $k$  is the virtual spring constant for perturbing the crease lengths. The ambiguity due to mountain–valley crease alignments is avoided by shifting the vertices up or down by a small amount in the  $z$  direction as the initial condition.

**Configuration-space analysis.** The configuration space of each vertex is described by the accessible folding angles of the connected creases. In the case of a degree-6 vertex, the configuration space is 3D. Any potentially foldable structure is

realized by rotating the creases through those three independent folding angles. The foldability is validated by the criterion that the distance between any pair of transformed vertices cannot be greater than that in the flat unfolded state for any inextensible sheet. Self-intersections of the structures are also identified and excluded from the configuration space (see Supplementary Information). The numeric code for the configuration-space analysis is made available for sharing through Mathematica (<https://www.wolframcloud.com/objects/6a35243a-e7ba-479f-af5d-0d77e13f467b>).

**Experiments.** The origami structures described in the main text were made from a flat paper sheet (Stardream Metallics 811b) with measured thickness  $\tau = 0.16$  mm and flexural rigidity  $D = 4.0 \times 10^{-4}$  N m (ref. 16). The crease lines were perforated by a laser cutter and weakened manually by flat-folding along the perforation lines in both directions. Folding kinematics and vertex locations were recorded by a USB digital camera (Imaging Source DFK), which was calibrated to remove perspective and lens distortions. The  $(x, y)$  coordinates of the vertices were fed into the aforementioned mathematical model to extract the  $z$  positions of the vertices. 3D configurations of the folded origami sheets were then reconstructed and plotted using MATLAB.

**Data availability.** The data that support the plots within this paper and other findings of this study are available from the corresponding author upon request.

In the format provided by the authors and unedited.

# Topological kinematics of origami metamaterials

Bin Liu <sup>1,2,8\*</sup>, Jesse L. Silverberg <sup>1,3,4,8</sup>, Arthur A. Evans<sup>5</sup>, Christian D. Santangelo<sup>5</sup>, Robert J. Lang<sup>6</sup>, Thomas C. Hull<sup>7</sup> and Itai Cohen<sup>1</sup>

<sup>1</sup>Department of Physics, Cornell University, Ithaca, NY, USA. <sup>2</sup>School of Natural Sciences, University of California, Merced, Merced, CA, USA. <sup>3</sup>Wyss Institute for Biologically Inspired Engineering, Harvard University, Boston, MA, USA. <sup>4</sup>Department of Systems Biology, Harvard Medical School, Boston, MA, USA. <sup>5</sup>Department of Physics, University of Massachusetts Amherst, Amherst, MA, USA. <sup>6</sup>Lang Origami, Alamo, CA, USA. <sup>7</sup>Department of Mathematics, Western New England University, Springfield, MA, USA. <sup>8</sup>These authors contributed equally: Bin Liu, Jesse L. Silverberg.

\*e-mail: [bliu27@ucmerced.edu](mailto:bliu27@ucmerced.edu)

## SYMBOLIC MODEL OF A DEGREE-6 VERTEX

We model the degree-6 Miura-ori vertex as in Figure S1(a). The crease pattern is determined by 6 neighboring vertices on a circle, here  $\mathbf{v}_1, \mathbf{v}_2, \dots, \mathbf{v}_6$ , and the radius has 1 unit length. We denote by  $t_1, t_2$ , and  $t_3$  the *folding angles* (i.e.,  $\pi -$  the dihedral angle) of the creases  $\mathbf{v}_1, \mathbf{v}_2$ , and  $\mathbf{v}_3$  respectively. Here  $t_2$  is assigned to be a mountain fold, i.e.  $t_2 < 0$ , while  $t_1$  and  $t_3$  are virtual folds, corresponding to facet bending for a degree-4 vertex [S1]. If we fix the location of the sector between creases  $\mathbf{v}_1$  and  $\mathbf{v}_6$ , we can determine  $\mathbf{v}'_4$ , the final position of the crease  $\mathbf{v}_4$  after sequentially folding along  $\mathbf{v}_3, \mathbf{v}_2$  and  $\mathbf{v}_1$ , using standard kinematics:

$$\mathbf{v}'_4 = R_z\left(-\frac{3(\pi-\alpha)}{2}\right) R_x(-t_1) R_z\left(\frac{3(\pi-\alpha)}{2}\right) R_z(-(\pi-\alpha)) R_x(-t_2) R_z(\pi-\alpha) R_z\left(-\frac{\pi-\alpha}{2}\right) R_x(-t_3) R_z\left(\frac{\pi-\alpha}{2}\right) \cdot \mathbf{v}_4$$

where  $R_x(\theta)$  and  $R_z(\theta)$  denote the  $3 \times 3$  rotation matrices about the  $x$ - and  $z$ -axes, respectively, with  $\theta$  the angle of rotation.

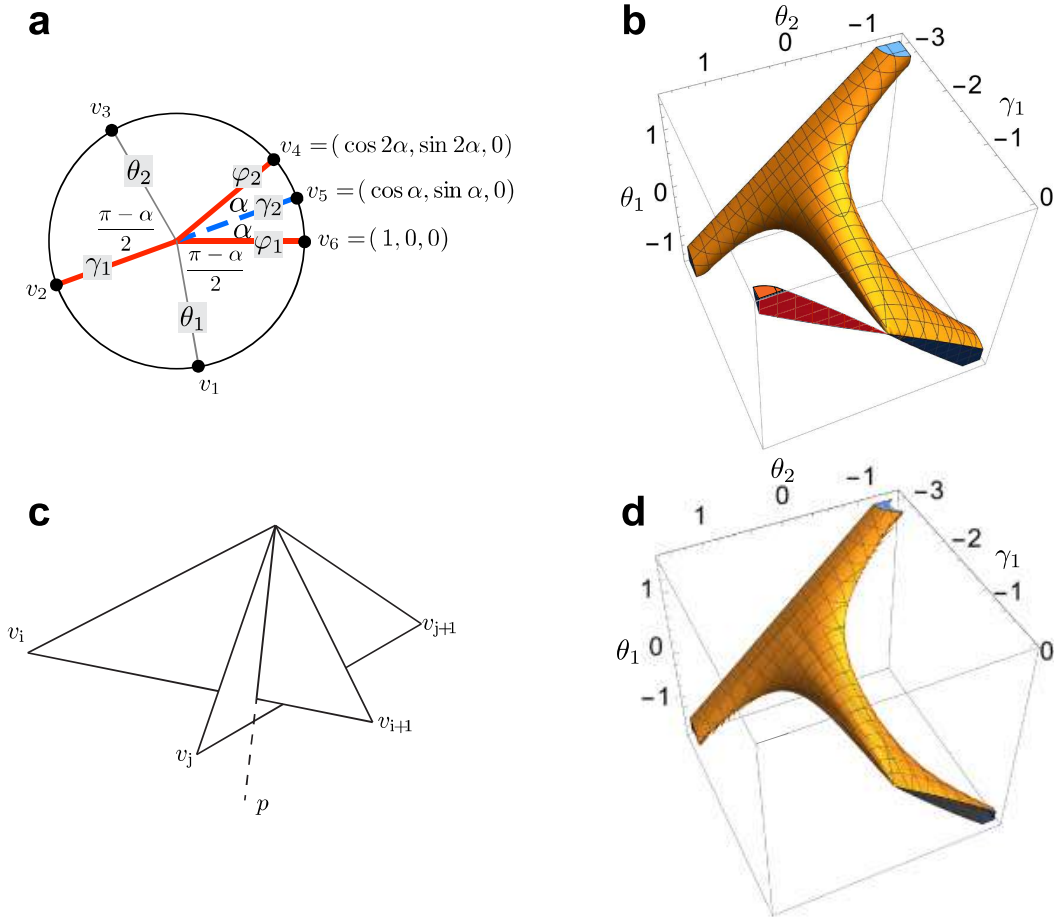


FIG. S1. A symbolic model of the degree-6 Miura-ori vertex is constructed. (a) The vertex coordinates are given. The rigid folding process is then modeled using standard kinematic techniques. The mountain and valley folds are shown in solid and dashed thick lines, and thin gray lines denote the virtual creases, which correspond to facet bending in a degree-4 vertex [S1]. (b) The configuration space when  $\alpha = 0.16$  rad. We let the  $\theta_1, \gamma_1$ , and  $\theta_2$  be the *folding angles* of the creases  $\mathbf{v}_1, \mathbf{v}_2$ , and  $\mathbf{v}_3$  respectively. The topological separable region in red corresponds to pop-through defects. (c) An example of intersection between two facets. (d) A modified configuration space that eliminates self-intersections, pop-through defects, incorrect assignment of mountain or valley configurations for  $\mathbf{v}_2, \mathbf{v}_4, \mathbf{v}_5$ , and  $\mathbf{v}_6$ .



## CONFIGURATION SPACE

The greatest distance the points  $\mathbf{v}_4$  and  $\mathbf{v}_6$  can be from each other is in the unfolded state, where  $\|\mathbf{v}_4 - \mathbf{v}_6\| = 2|\sin \alpha|$ . We then obtain the configuration space for the folded vertex by plotting all points  $(t_1, t_2, t_3)$  that satisfy the inequality

$$\|\mathbf{v}'_4 - \mathbf{v}_6\| \leq 2|\sin \alpha|.$$

This configuration space when  $\alpha = 0.16$  is shown in Figure S1(b). The singular point  $(0,0,0)$  in the configuration space corresponds to the unfolded state.

Potential self-intersection of the single vertex can be further excluded from the accessible configuration space by satisfying the following criteria. For any pair of facets  $i$  and  $j$ , comprising  $\mathbf{v}_i$ ,  $\mathbf{v}_{i+1}$ ,  $\mathbf{v}_j$ , and  $\mathbf{v}_{j+1}$ , the intersection-free condition requires (see Fig. S1(c))

$$(\mathbf{v}_i \times \mathbf{p}) \cdot (\mathbf{v}_{i+1} \times \mathbf{p}) > 0, \text{ or } (\mathbf{v}_j \times \mathbf{p}) \cdot (\mathbf{v}_{j+1} \times \mathbf{p}) > 0,$$

where  $\mathbf{p}$  is the intersection line between two infinite planes containing this pair of facets.

$$\mathbf{p} = (\mathbf{v}_i \times \mathbf{v}_{i+1}) \times (\mathbf{v}_j \times \mathbf{v}_{j+1}).$$

To ensure that  $\mathbf{v}_4$  and  $\mathbf{v}_6$  correspond to two mountain folds, we have the two following equalities

$$[(\mathbf{v}_5 \times \mathbf{v}_4) \times (\mathbf{v}_4 \times \mathbf{v}_3)] \cdot \mathbf{v}_4 \leq 0 \text{ and } [(\mathbf{v}_1 \times \mathbf{v}_6) \times (\mathbf{v}_6 \times \mathbf{v}_5)] \cdot \mathbf{v}_1 \leq 0.$$

Misfolds associated with a swap between mountain and valley vertices (and vice versa) can be excluded explicitly by the following criterion,

$$[(\mathbf{v}_4 \times \mathbf{v}_2) \times (\mathbf{v}_2 \times \mathbf{v}_6)] \cdot \mathbf{v}_5 \geq 0.$$

The resulting configuration space satisfying all above criteria are shown in Fig. S1(d).

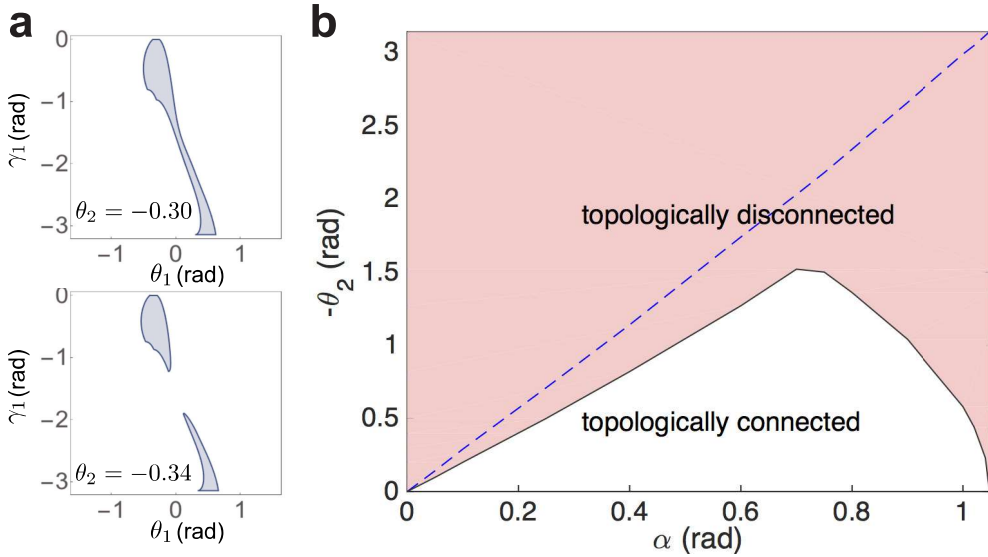


FIG. S2. Restricted configuration spaces due to fold angle  $\theta_2$ . (a) For plane angle  $\alpha = 0.16$  rad (Fig. S1), given fold angles  $\theta_2$  lead to either simply connected ( $\theta_2 = -0.3$  rad) or disconnected ( $\theta_2 = -0.34$  rad) configuration subspaces. (b) The critical  $\theta_2$ , above which the configuration subspaces is disconnected (shaded) is shown as a function of the plane angle  $\alpha$ . The dashed line shows the critical  $\theta_2$  without considering self-intersections.

Given a fold angle along one crease will restrict the 3-D configuration space into a 2-D subspace. An example of such subspaces (for plane angle  $\alpha = 0.16$  rad) is shown in Fig. S2(a). By increasing the magnitude of fold angle  $\theta_2$  above a critical value  $\theta_{2,c} \approx -0.32$  rad, the configuration space topology varies from one simply connected region to two disconnected regions. Such critical fold angles  $\theta_{2,c}$  as a function of  $\alpha$  are shown in Fig. S2(b).

## RECONSTRUCTION OF THE ORIGAMI MORPHOLOGY

3D reconstructions of the origami structure are obtained by matching the 2D coordinates of all its vertices with a projection of an idealized origami model. The crease length of the origami model is determined by the crease pattern. For any two vertices  $\mathbf{r}_i$  and  $\mathbf{r}_j$  that are connected by a single crease of length  $l_{ij}$ , they must satisfy the following condition

$$r_{ij} = |\mathbf{r}_{ij}| = |\mathbf{r}_i - \mathbf{r}_j| = l_{ij}. \quad (\text{S1})$$

The corresponding vertex coordinates  $(X_i, Y_i)$  in the real origami structure are obtained from its top-view images, using MATLAB's camera calibration toolbox to correct for distortions. The location of the vertices are initially identified by manually tracking the vertex positions. Using MATLAB's feature tracking algorithm in conjunction with particle image velocimetry [S2] we automatically track the vertex locations in successive images. To calculate the out-of-plane coordinates of these vertices along  $z$ , we draw inspiration from previous work [S3] and minimize the penalty function:

$$V(\{\mathbf{r}_i\}) = \frac{k_1}{2} \sum_i [(x_i - g(z_i)X_i)^2 + (y_i - g(z_i)Y_i)^2] + \frac{k_2}{2} \sum'_{i>j} (r_{ij} - l_{ij})^2, \quad (\text{S2})$$

where  $k_1 \ll k_2$  are the effective spring constants that constrain these vertices,  $g(z) = 1 - z/H$  is the first-order perspective correction for a camera placed at  $(0, 0, H)$ , and  $|z/H| \ll 1$  [S4]. Here,  $\sum'$  denotes the summation over directly connected vertices. The minimal value  $\min V(\{\mathbf{r}_i\})$  can be achieved iteratively using a conjugate gradient method. At the  $(k+1)$ th iteration with a step size  $\Delta$ , we have

$$\frac{\mathbf{r}_i^{(k+1)} - \mathbf{r}_i^{(k)}}{\Delta} = k_1 \left[ \left( g(z_i^{(k)}) X_i - x_i^{(k)} \right) \hat{x} + \left( g(z_i^{(k)}) Y_i - y_i^{(k)} \right) \hat{y} \right] + k_2 \sum'_j (l_{ij} - r_{ij}^{(k)}) \hat{\mathbf{r}}_{ij}^{(k)}. \quad (\text{S3})$$

The initial coordinates are set as  $x_i^{(0)} = X_i$ ,  $y_i^{(0)} = Y_i$ , and  $z_i^{(0)}$  slightly off from 0 with its sign determined by the mountain-valley assignments. The convergence is achieved at a tolerance level  $\delta$  so that  $\sqrt{\sum'_{i>j} (r_{ij} - l_{ij})^2} < \delta$ . The value of  $\delta$  is typically set at  $10^{-10}$  for relatively low computational time. In addition to the 3D morphology, the obtained coordinates also allow us to compute the folding angles for each vertex.

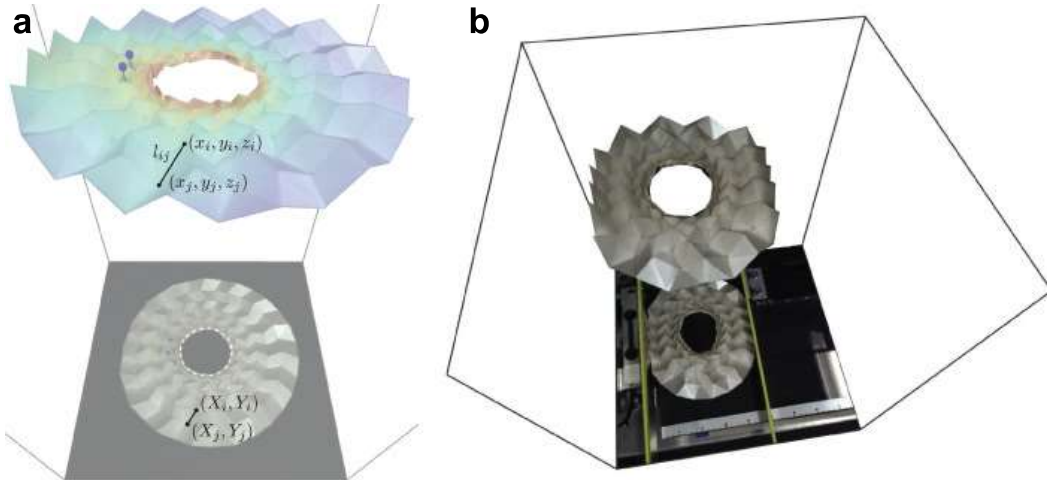


FIG. S3. 3D reconstruction of the origami structure. (a) Schematics of the reconstruction, where  $(X, Y)$  are the 2D coordinates from the raw image and  $(x, y, z)$  are the 3D coordinates reconstructed by constraining these vertices with a given crease length  $l$ . (b) An example of this 3D reconstruction showing the deformation of the origami structure under compression, achieved by tracing the 2D coordinates  $(X, Y)$  of all the vertices.

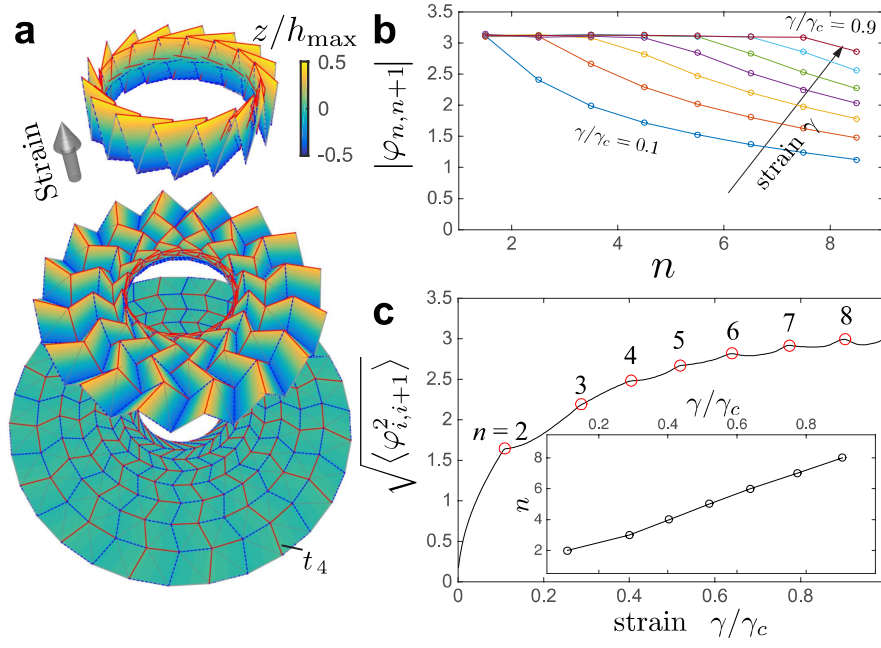


FIG. S4. Simulation of the folding kinematics of a Miura-ori ring structure. (a) Under isotropic strain, the origami structure deforms from a plane sheet (bottom) and collapses onto a cylindrical shape (top). (b) Folding angle  $\varphi_{i,i+1}$  for creases shared by adjacent vertices versus vertex layer number  $n$  at different values of compressive strain  $\gamma/\gamma_c$ . Here,  $\gamma_c$  is the maximum strain that can be applied without buckling the inner boundary. Generally, we observe the outer creases to have a lower value of  $\varphi_{i,i+1}$ . As strain increases this value rapidly approaches the saturation angle of  $\pi$ . (c) The root mean square of  $\varphi_{i,i+1}$  for all vertices versus strain  $\gamma/\gamma_c$ . The abrupt changes in the slope are associated with the snapping behavior of the folded sheet. We identify these locations by taking the second-order derivative, identifying the local minima, and labeling them with the number of collapsed layers of vertices. The number of collapsed layers  $n$  versus the strain  $\gamma/\gamma_c$  is shown in the inset.

## NUMERICAL SIMULATION OF THE FOLDED STRUCTURE

The folded origami structure can be simulated numerically with a similar scheme for the penalty function. Instead of matching the 2D projection of the position of every vertex, we restricted the coordinates of a subset of all  $N$  vertices on the outer boundary and obtain the optimized origami structure. The penalty function thus becomes

$$V(\{\mathbf{r}_i\}) = \frac{k_1}{2} \sum_i'' [(x_i - X_i)^2 + (y_i - Y_i)^2] + \frac{k_2}{2} \sum_{i>j}' (r_{ij} - l_{ij})^2 + \frac{k_3 L^2}{2} \sum_{\sigma} t_{\sigma}^2, \quad (\text{S4})$$

where  $\sum_i''$  is performed over the restricted vertices,  $t_{\sigma}$ 's are the folding angle along the virtual creases,  $k_3$  is the bending stiffness of the virtual creases, and  $L$  is the size of the unfolded sheet. The non-vanishing bending stiffness  $k_3$  leads to a unique folded structure associated with the lowest bending energy for all virtual creases. It should be noted that the penalty function here does not forbid any self-intersections.

In case of isotropic compression of the Miura-ori ring, the radius of the vertices on the outer boundaries are prescribed as  $\sqrt{X^2 + Y^2} = (1 - \gamma)R_0$ , where  $\gamma$  is the compressive strain, and  $R_0$  is the radius of the unfolded origami sheet. The penalty function can be rewritten as

$$V(\{\mathbf{r}_i\}) = \frac{k_1}{2} \sum_i'' \left( \sqrt{x_i^2 + y_i^2} - (1 - \gamma)R_0 \right)^2 + \frac{k_2}{2} \sum_{i>j}' (r_{ij} - l_{ij})^2 + 2k_3 R_0^2 \sum_{\sigma} t_{\sigma}^2, \quad (\text{S5})$$

The folding kinematics can be solved as

$$\frac{\mathbf{x}_i^{(k+1)} - \mathbf{x}_i^{(k)}}{\Delta} = \quad (S6)$$

$$\begin{cases} -k_1 \left( x_i^{(k)} \hat{x} + y_i^{(k)} \hat{y} \right) \left( 1 - \frac{(1-\gamma)R_0}{\sqrt{x_i^{(k)2} + y_i^{(k)2}}} \right) - k_2 \sum_j' \left( r_{ij}^{(k)} - l_{ij} \right) \hat{\mathbf{r}}_{ij}^{(k)} - 4k_3 R_0^2 \sum_{\sigma} \hat{\theta}_{i\sigma}^{(k)} t_{\sigma}^{(k)}, \\ \text{for } i \in \text{outer boundary,} \\ -k_2 \sum_j' \left( r_{ij}^{(k)} - l_{ij} \right) \hat{\mathbf{r}}_{ij}^{(k)} - 4k_3 R_0^2 \sum_{\sigma} \hat{\theta}_{i\sigma}^{(k)} t_{\sigma}^{(k)}, \text{ otherwise.} \end{cases} \quad (S7)$$

Here,  $\hat{\theta}_{i\sigma} = \hat{d}_{\sigma} \times (\mathbf{r}_i - \mathbf{v}_{\sigma}) / |\hat{d}_{\sigma} \times (\mathbf{r}_i - \mathbf{v}_{\sigma})|$  with  $\hat{d}_{\sigma}$  and  $\mathbf{v}_{\sigma}$  are the orientation and center of the virtual crease  $\sigma$ . In practice, we let  $k_1 \Delta = 0.1$ , and  $k_2 \Delta = k_3 \Delta = 0.005$ . Using the Runge-Kutta method, the differential equation leads to convergent coordinates of all vertices. An example of such simulated folding is shown and described in Fig. S4.

## EXPERIMENTAL CHARACTERIZATION OF THE SEQUENTIAL BISTABILITY

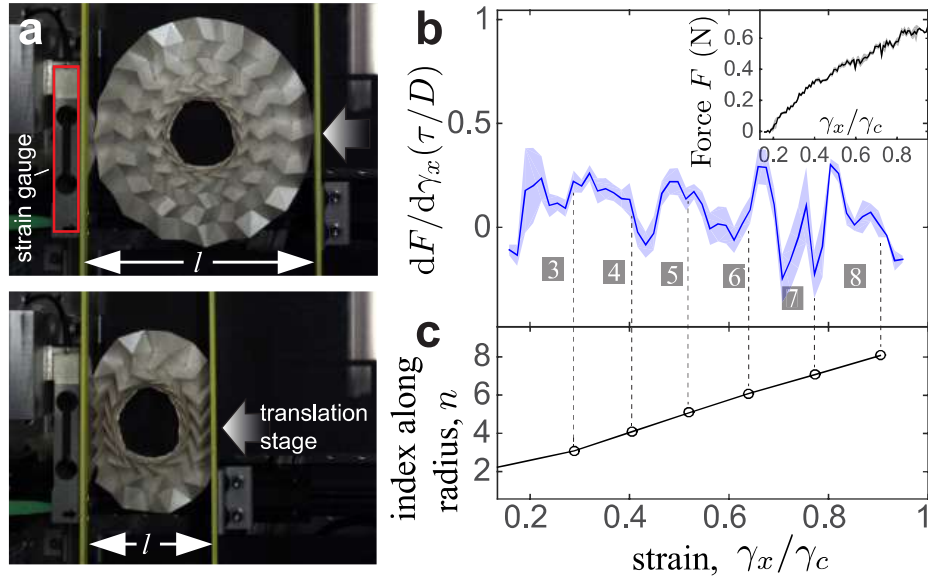


FIG. S5. Realization of sequential bistability through vertex-vertex coupling. (a) The Miura-ori ring is deformed uni-axially between two parallel plates. (b) The compressive modulus of the Miura-ori ring  $K \propto \frac{dF}{d\gamma_x}$  is obtained from the force-strain relationship  $F$  vs.  $\gamma_x/\gamma_c$ . Here  $\gamma_c = 0.75$  and corresponds to the strain at which the entire sheet snaps into a cylindrical wall. The modulus  $K = \frac{dF}{d\gamma_x} \cdot (\tau/D)$ , normalized by flexural rigidity  $D$  and thickness of the sheet  $\tau$ , shows a sequence of drops in its value each of which corresponds to a snap. For both the force and the modulus curves, the solid line is a 10-point boxcar average of the measured value and the shaded band is the 10-point boxcar standard deviation. (c) We simulated uniform compression of this structure and overlay the normalized strain values at which each layer undergoes a snapping transition (circles). The dashed lines are guides to the eye.

To characterize the topologically disconnected configurations in a Miura-ori ring, we laterally compressed the fabricated structure between two plates (Fig. S5(a)). We find that the structure is able to accommodate a large degree of compressive strain  $\gamma_x = (l_0 - l)/l_0$ , where  $l_0$  and  $l$  correspond to the lateral size of the unfolded and folded sheet respectively. During compression, the innermost layer is the first to collapse. Upon further compression, successive layers collapse onto the inner layer (Supplementary Movie 2). At the same time the remaining uncollapsed layers retain their flexibility. Importantly, throughout the entire folding process up to where the strain reaches  $\gamma_c$  indicating full collapse, the inner boundary maintains its shape indicating effective strain isolation.

The snapping behavior of successive layers can be quantified by the compressive modulus, which is the derivative of the applied compressive force  $F$  with respect to the strain  $\gamma_x$  (Fig. S5(b)). We find that each snap, indicated by the number of collapsed layers  $n$ , corresponds to a rapid decrease of  $dF/d\gamma_x$  as the normalized strain  $\gamma_x/\gamma_c$  is increased

(Fig. S5(b)). This decrease arises from the extra space that is released when a layer snaps into place, which relaxes the folds in the remaining layers and reduces their resistance to compression.

To determine the theoretical strain value associated with successive snapping of layers onto the inner cylinder, we simulate an isotropic deformation of the same origami geometry (Fig. S4(c)). We plot the number of collapsed layers as a function of the applied normalized strain (black line and open circles in Fig. S5(c)). We find that comparison with  $dF/d\gamma_x$  (vertical dashed lines) identifies where the structure undergoes an abrupt drop in compressive modulus due to each sequential snap (labeled by  $n$ ).

- 
- [S1] Z. Y. Wei, Z. V. Guo, L. Dudte, H. Y. Liang, and L. Mahadevan, *Phys. Rev. Lett.* **110** (2013).
  - [S2] J. Westerweel, “Digital particle image velocimetry: theory and application,” Delft University Press (1993).
  - [S3] A. Smith, A. E. Smith, D. W. Coit, T. Baeck, and D. Fogel, in *Handbook of Evolutionary Computation*, edited by T. Baeck, D. Fogel, and Z. Michalewicz (Institute of Physics Publishing and Oxford University Press, 1997).
  - [S4] I. Carlbom and J. Paciorek, *ACM Computing Surveys (CSUR)* **10**, 465 (1978).





## Topological Mechanics of Origami and Kirigami

Bryan Gin-gē Chen,<sup>1,\*</sup> Bin Liu,<sup>2,†</sup> Arthur A. Evans,<sup>3,‡</sup> Jayson Paulose,<sup>1</sup>  
Itai Cohen,<sup>2</sup> Vincenzo Vitelli,<sup>1</sup> and C. D. Santangelo<sup>3</sup>

<sup>1</sup>*Instituut-Lorentz, Universiteit Leiden, 2300 RA Leiden, The Netherlands*

<sup>2</sup>*Department of Physics, Cornell University, New York 14853, USA*

<sup>3</sup>*Department of Physics, University of Massachusetts, Amherst, Massachusetts 01002, USA*

(Received 5 August 2015; published 30 March 2016)

Origami and kirigami have emerged as potential tools for the design of mechanical metamaterials whose properties such as curvature, Poisson ratio, and existence of metastable states can be tuned using purely geometric criteria. A major obstacle to exploiting this property is the scarcity of tools to identify and program the flexibility of fold patterns. We exploit a recent connection between spring networks and quantum topological states to design origami with localized folding motions at boundaries and study them both experimentally and theoretically. These folding motions exist due to an underlying topological invariant rather than a local imbalance between constraints and degrees of freedom. We give a simple example of a quasi-1D folding pattern that realizes such topological states. We also demonstrate how to generalize these topological design principles to two dimensions. A striking consequence is that a domain wall between two topologically distinct, mechanically rigid structures is deformable even when constraints locally match the degrees of freedom.

DOI: 10.1103/PhysRevLett.116.135501

Recent interest in origami mechanisms has been spurred by advances in fabrication and manufacturing [1–3], as well as a realization that folded structures can form the basis of mechanical metamaterials [4–8]. The ability to identify kinematic mechanisms—allowable folding motions of a crease pattern—is critical to the use of origami to design new deployable structures and mechanical metamaterials. For example, the mechanism in the celebrated Miura ori that allows it to furl and unfurl in a single motion [9,10] is also the primary determinant of the fold pattern’s negative Poisson ratio [4,5]. Identifying these mechanisms becomes more challenging when the number of apparent constraints matches the number of degrees of freedom (DOF).

When there is an exact balance between DOF and constraints in a periodic structure, the structure is marginally rigid [11,12]. In such a case, new mechanical properties such as nonlinear response to small perturbations emerge [13–16]. A recent realization is that the flexibility of such solids may be influenced by nontrivial topology in the phonon band structure [17,18]. Here, we show how to extend these topological ideas to origami and kirigami. We show that periodically folded sheets may exhibit distinct mechanical “phases” characterized by a topological invariant called the *topological polarization*, recently introduced by Kane and Lubensky [17] using a mapping of mechanically marginal structures to topological insulators [19]. The importance of this invariant has emerged in the study of the soft modes of spring networks [18], and the nonlinear mechanics of linkages [20] and buckling [21]. As in these examples, the phases in our origami and kirigami structures exhibit localized vibrational modes on certain boundaries,

and transitions from between topological phases are characterized by the appearance of bulk modes that cost zero energy. These are the hallmarks of topologically protected behavior in classical mechanical systems [22–29]. Topology provides a new knob to tune how materials and, as we show here, origami and kirigami structures, respond to external perturbations.

We denote by *origami*, mechanical structures consisting of rigid flat polygonal plates joined by hinges. We will first discuss origami with no missing plates or “holes,” and then generalize to *kirigami*, defined to be origami where such holes are allowed. We will consider the mechanics of origami in the geometrical limit—folds will cost zero energy and faces do not stretch or bend.

To demonstrate the power of our approach, we introduce an example of a 1D strip of origami analogous to the Su-Schrieffer-Heeger polyacetylene model [17,30]. It admits localized modes and stresses determined and protected by topology, which we realize and characterize in experiments. Additionally, we show how to generalize this to 2D periodic origami sheets, where we have observed a striking property that causes origami without holes to have zero topological polarization. We give examples of hinged structures with holes (kirigami) that do admit distinct polarizations and thus can be used as building blocks for metasheets with programmable local flexibility.

*Quasi-1D origami strip.*—We start with a simple quasi-1D origami structure. Consider an origami strip of zig-zagging rigid quadrilateral plates, depicted in Fig. 1, consisting of a periodically repeating unit cell of two fourfold vertices. Each vertex in a cell (labeled by

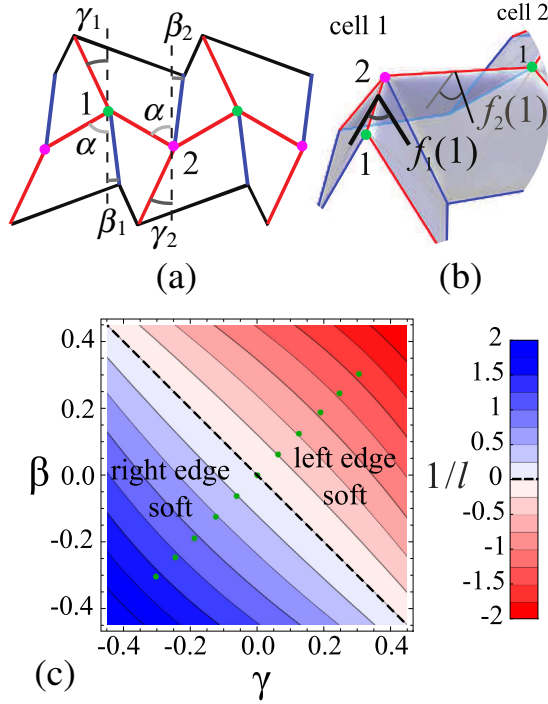


FIG. 1. A quasi-1D origami strip. (a) A unit cell of the fold pattern corresponding to the origami mechanism with planar angles labeled. Red (blue) creases are mountain (valley) folds, respectively. (b) A 3D depiction of a part of the strip with folding angles  $f_i(n)$  labeled. (c) The phase diagram where  $\alpha = \pi/3$ ,  $\beta \equiv \beta_1 = \beta_2$ , and  $\gamma \equiv \gamma_1 = \gamma_2$ . The colors indicate the phase (blue for right-localized, red for left-localized); the contours and intensity of color follow the inverse decay length  $1/l$  (see legend). Configurations where folds at a vertex become collinear lie on  $\gamma = \beta$ , and the green points along that line were constructed in experiment [along this line,  $(\gamma, \beta)$  and  $(-\gamma, -\beta)$  are related by a rotation in three dimensions].

$n = 1, 2$ ) has four creases [Fig. 1(a)], and one DOF [31] that we track with the dihedral angles of the bolded crease,  $f_n(j)$ , where  $j$  indexes the unit cell [Fig. 1(b)]. Each adjacent pair of dihedral angles is coupled by the kinematics of the intervening vertex. As each vertex contributes a DOF and a constraint, this origami structure has marginal rigidity.

We analyze the mechanical response of the origami strip by determining its configurations analytically as functions of the fold pattern angles  $\beta_1, \beta_2, \gamma_1$ , and  $\gamma_2$  [defined in Fig. 1(a)]. We define a generalized displacement  $u(j) = \cos f_2(j) + 1$ . The function  $u(j)$  encodes the dihedral angle  $f_2$  of the rightmost fold of unit cell  $j$ , and satisfies

$$u(j+1) = \kappa(\alpha, \beta_1, \beta_2, \gamma_1, \gamma_2)u(j), \quad (1)$$

where

$$\kappa = \left[ \frac{\sin(\alpha - \beta_1) \sin(\alpha - \gamma_1)}{\sin(\alpha + \beta_1) \sin(\alpha + \gamma_1)} \right] \left[ \frac{\sin(\alpha - \beta_2) \sin(\alpha - \gamma_2)}{\sin(\alpha + \beta_2) \sin(\alpha + \gamma_2)} \right]. \quad (2)$$

The derivation is an application of the spherical law of cosines and is given in the Supplemental Material [32]. The fact that  $u(j)$  determines  $u(j+1)$  implies that the strip has 1 degree of freedom, globally. Equation (1) is solved by an exponential  $u(j) = u(0) \exp[j \ln(\kappa)]$  with deformation localized to one side or the other, following the sign of the inverse decay length  $l^{-1} = \ln \kappa$ .

The mechanical “phase diagram” in Fig. 1(c) shows the values of  $l^{-1}$  for patterns with  $\gamma_1 = \gamma_2 \equiv \gamma$ ,  $\beta_1 = \beta_2 \equiv \beta$ . There are two phases distinguished by the sign of  $\ln \kappa$ , which is determined here by the sign of  $\gamma + \beta$ , a quantity not obviously related to any symmetry breaking. When  $\gamma + \beta > (<) 0$ ,  $\kappa < (>) 1$ , and by Eq. (1), the mechanical response is localized to the left (right) of the origami strip. A special role is played by fold patterns with  $\kappa = 1$ , where the decay length diverges and  $u(j)$  neither grows nor shrinks (denoted by the dashed line). This is precisely the condition for which a global kinematic mechanism exists and the fold pattern is *deployable* [33]. As an example, when  $\gamma = \beta = 0$ , the strip realizes a row of the Miura ori fold pattern, which has a single collapse motion. More generically, however, as long as  $\ln \kappa$  never changes sign, the deformation in a strip,  $u(j)$ , is localized even if the values of  $\alpha, \beta_j, \gamma_j$  vary due to disorder or imperfections, i.e., as long as the material remains within the same phase. The existence of phases of robust, boundary-localized zero-energy deformations separated by critical configurations with bulk zero modes suggests that the origami strip has topologically protected properties.

To make the topology explicit, we calculate a topological invariant of the above phases. Unlike in periodic spring networks with marginal rigidity [17,34,35], a linear analysis is inadequate to capture the topology of the origami strip. Coplanar hinges in the flat state are redundant constraints, and this results in extra zero modes at linear order which do not extend to higher order. In the Supplemental Material [32], we derive a rigidity matrix capturing the *second-order* deformations of this structure and show that it has the same pattern of entries as the Hamiltonian of the Su-Schrieffer-Heeger chain of Refs. [17,30]. Therefore, phases of the origami strip are characterized by their topological polarization  $\bar{P}_T$  [17,18], defined as a winding number of the determinant of the rigidity matrix [36]. Indeed, the sign of  $\ln \kappa$  is precisely correlated with the topological polarization, and thus the fact that different edges are soft or stiff in different phases is a manifestation of the bulk-boundary correspondence [19] in this system. While topological modes in 1D linkages have been found to lead to propagating domain walls [20,37], this is not possible for our 1D strip. In Eq. (2),  $\kappa$  depends only on the fold pattern angles  $\alpha, \beta_j, \gamma_j$ , not the dihedral angles  $f_j$ —this means that the topological polarization of the unit cell cannot change via the zero-energy deformations, which would be necessary for propagation.

To test the consequences of Eq. (1) away from the ideal limit, in a structure where faces can bend and hinges can

twist, a mylar sheet (200  $\mu\text{m}$  thick) is perforated by a laser cutter into the desired crease pattern, rendering it foldable along lines of perforations. We strengthen the facets by sandwiching the mylar sheet between pairs of 1 mm thick, plastic plates made of polylactic acid (PLA) on a 3D printer. To mount the plastic plates onto the mylar sheet, we use a pushed-in clip design: one facet has clips and the corresponding facet has holes. Equivalent holes are cut on the mylar sheet so that the clips can be pushed through to meet the holes on the plate on the other side of the mylar. An example of the assembled origami structure is shown in Fig. 2(a). Here, we fixed the angle  $\alpha = \pi/3$  and varied  $\gamma \equiv \beta_1 = \gamma_1 = \beta_2 = \gamma_2$  to explore the localization of the deformation within one phase (with  $\kappa < 1$ ) [38]. A video camera captured the deformation of the strip from above as it was symmetrically compressed. The position of each vertex was obtained via image analysis, and fit with a 3D model to reconstruct the complete morphology of the origami strip, as shown in Fig. 2(b). Finally, the folding angles along the interior creases were extracted from the 3D shape and were used to compute the generalized strain  $u$ . Figure 2(c) shows the strain as a function of distance along

the strip for samples with different values of the pattern parameter  $\gamma$ . Observe that there is a “soft” edge (cell index 0), where the deformation is high, and on the other end a “stiff” edge, with low deformation.

As shown by a semilog fit [dashed lines in Fig. 2(c)], the strains decay exponentially at small distances from the soft edge. For small  $\gamma$ , the folding angles level off to a roughly constant value at larger distances, which violates Eq. (1). The constant folding angle background corresponds to the activation of a mode with uniform deformation. This mode is easy to excite as it is the zero energy mode at  $\gamma = 0$  and thus remains very low energy for small  $\gamma$ . A deviation from the ideal geometrical limit is possible due to the finite flexibility of the facets and the finite crease thicknesses. Despite the nonideality of the experimental origami strip, the decay lengths extracted from the fit are in good agreement with  $1/l = \ln \kappa$  [Fig. 2(d)], confirming the robustness of our topological design principle.

*Two-dimensional origami.*—Having established that marginally rigid 1D periodic origami can exhibit topological phases, we now ask whether marginality also leads to similar phases in 2D origami. We first characterize the class of *marginally rigid* 2D periodic origami and show that they must have a triangulated crease pattern. To avoid trigonometric complexity inherent to a folding angle representation, we model the kinematics of triangulated origami as a central-force spring network with vertices as joints and hinges as springs. Triangles in such a network automatically enforce the no-bending constraint on the facets. Arbitrary origami can be modeled with spring networks, but nontriangular faces require additional internal springs to remain rigid.

In this framework, each joint has 3 degrees of freedom and each spring adds one constraint, so marginal structures satisfy  $E = 3V$  where  $E$  is the number of bonds and  $V$  is the number of joints. In a triangulated surface without a boundary, each of the  $F$  faces is a triangle, so  $3F = 2E$ . The Euler characteristic  $\chi$  is defined as  $\chi = V - E + F$ ; thus we obtain  $E = 3(V - \chi)$ .

Periodic origami structures in two dimensions have the topology of the torus and thus  $\chi = 0$ , which shows that triangulations are marginally rigid. While achieving marginality in granular packings and glassy networks requires some fine-tuning in pressure or coordination, the analogous origami triangulations arise naturally. Any nontriangular plate in an origami pattern can be triangulated by adding diagonals, and the bending of nontriangular plates in real origami can be modeled as the addition of new creases [4,6].

One might now expect a variety of topological phases upon changing the angles and lengths of a triangulated crease pattern, by analogy with the 1D strip. Surprisingly, our calculations indicate otherwise. As discussed above, an analysis of the rigidity of *flat* origami must go beyond linear order. To bypass this complication, we consider periodic triangulated origami where we break the flat-state

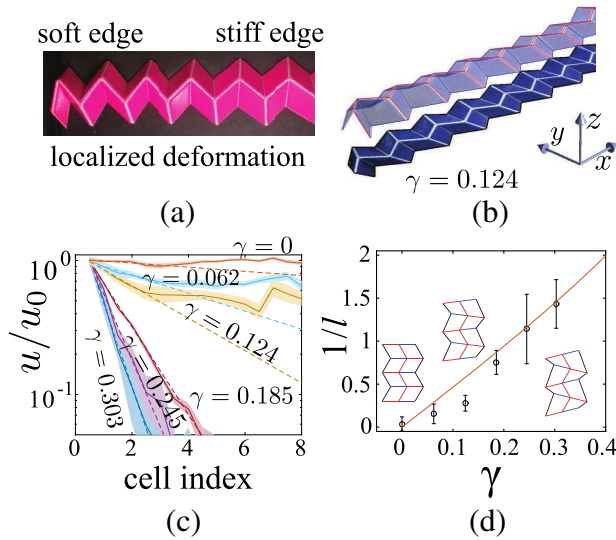


FIG. 2. (a) Localized deformations in an experimental realization of the origami strip ( $\alpha = \pi/3$ ,  $\gamma_1 = \gamma_2 = \beta_1 = \beta_2 = 0.062$ ). (b) 3D reconstruction of the configuration of the strip from a flat image ( $\gamma = 0.124$ ). (c) Normalized generalized strain  $u/u_0$  as a function of distance from the deformable boundary (measured in number of unit cells) from experiments (shaded curves) with fits to an exponential decay (dashed lines). Each curve shows the average of data from 6 to 30 experimental images and has a width equal to the standard error. Folding angles  $f_2(1)$  [related to  $u_0$  via  $u_0 = 1 + \cos f_2(1)$ ] at cell 1 varied from 1.06 to 1.45. (d) Inverse decay lengths ( $1/l$ ) versus  $\gamma$ , where data points are averages over the fitting coefficients of all images for each  $\gamma$  and error bars show 95% confidence bounds. The analytical result for  $l^{-1} = \ln \kappa$  [Eq. (2)] is plotted as a solid red line. The deviations for small  $\gamma$  arise from a “uniform bending mode” (see text).



degeneracy by introducing small vertical displacements to the vertices. The linear rigidity and topological properties of such a structure can then be expressed in terms of the (Fourier-transformed) rigidity matrix  $\mathbf{R}$  for its associated spring network [17,18]. However, for all triangulated periodic fold patterns we have considered, the function  $\det \mathbf{R}(\mathbf{q})$ , *a priori* a complex-valued function, is in fact real valued for all  $\mathbf{q}$  in the Brillouin zone [39]. Though a proof of this statement for all triangulated origami eludes us, extensive numerical tests on a large number of distinct fold patterns bear out this conjecture. We give details and partial results in the Supplemental Material [32].

A consequence of the “reality” property is that the winding numbers of  $\text{Arg } \det \mathbf{R}(\mathbf{q})$  along any closed curves in the Brillouin zone must be zero (when defined), and, hence, the topological polarization  $\vec{P}_T$  must vanish. Localized boundary modes for such origami still exist, but must be isotropically distributed. Even if the hinges in a unit cell break left-right symmetry, the number of boundary modes per unit cell on each edge of a finite patch is left-right and up-down symmetric. If in fact all triangulated periodic origami structures have this property, the only way to get an imbalance in the number of zero modes at the boundary of origami is by locally adding or removing constraints. This behavior contrasts with that of the 1D strip of origami studied above as well as 3D periodic networks and marginal spring networks confined to 2D.

*Topological kirigami.*—Thus the question remains: do there even exist 2D periodic hinged structures with a nonzero topological polarization? The answer is yes, but we must go beyond origami to *kirigami*, folded structures with holes. There is a simple way to generate marginal kirigami from triangulated origami. Cutting out an adjacent pair of triangles removes one bond from the associated spring network, eliminating a constraint. Likewise, merging two triangles into a rigid quadrilateral plate adds a constraint. We therefore modify a triangular lattice by cutting and merging twice, resulting in a structure with two quadrilateral plates and two quadrilateral holes per unit cell (top center of Fig. 3). Now  $\det \mathbf{R}(\mathbf{q})$  is complex-valued, and by randomly perturbing a flat realization, we find the “green” (left) and “blue” (right) structures depicted in Fig. 3, which have  $\vec{P}_T = (1, 0)$  and  $(0, 0)$ , respectively (see Supplemental Material [32] for more details). With free boundary conditions, the boundary soft modes in the green kirigami are polarized to the  $+x$  edge (analogous to the 1D strip and in contrast to the blue kirigami and all triangulated origami structures we tested).

Finding the green kirigami answers the question above positively, and we leave a determination of the possible phases that can occur in the modified triangular lattice to future work. A full characterization will likely be difficult due to the high dimensionality of the realization space (cf. Ref. [40], which shows the complexity of the phase diagram in a simpler mechanical system). We thus switch

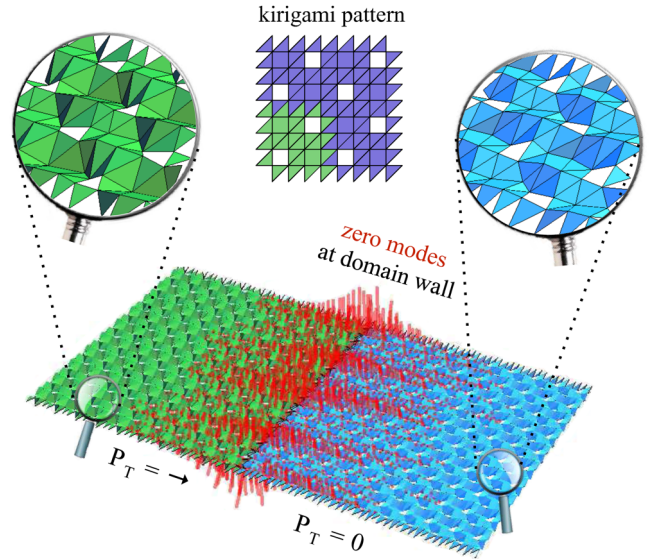


FIG. 3. Topologically protected zero mode (red) in a kirigami heterostructure [left green with topological polarization  $\vec{P}_T = (1, 0)$  / right blue with  $\vec{P}_T = (0, 0)$ ]. Numerically the mode depicted has energy nearly indistinguishable from the translation modes. This is a close-up of a larger periodic  $50 \times 5$  system, divided into two  $25 \times 5$  domains (two copies in the shorter direction are shown). The magnifying glass insets show the fine structure of four unit cells of each type, and between them is a schematic showing how the quadrilateral plates, strips of triangles, and quadrilateral holes are joined by hinges. The schematic shows four unit cells, with the lower left cell highlighted in green.

gears and present an example of localized modes designed into a kirigami “heterostructure” to illustrate the power of our techniques. In Fig. 3, we show a kirigami structure that exhibits zero modes localized at a domain wall (one per unit cell) between the two kirigami structures described above. The zero modes render the heterostructure flexible in the vicinity of the domain wall (the mode depicted leads to out-of-plane wrinkling), while keeping it rigid further away. By contrast, a domain wall between distinct patterns with equal polarization has no such localized modes (see Supplemental Material [32]). In general, domain walls between structures with different polarizations create either soft lines along which the system easily deforms, or “stressed” lines which first bear the loads under applied strains [21]. Similar effects may arise at point defects in otherwise uniform polarized structures [41].

*Outlook.*—We have demonstrated that origami and kirigami structures are characterized by a topological polarization that classifies the ways that a marginally rigid fold pattern can be floppy close to its boundaries. Our results give strong constraints on the types of boundary modes that can be created in origami and will guide the design of fold patterns that achieve a targeted mechanical response. In the design space of geometric realizations, two

structures with different polarizations must be separated by globally flexible, i.e., deployable, realizations. Thus not only can structures with distinct phases be combined in real space to form domain walls with useful functionality, but also they can be used to find deployable patterns in design space. These realization spaces are high dimensional in general, so the problem of determining simple rules to create a given polarization remains open.

We acknowledge conversations with T. C. Lubensky and R. D. Kamien. We are grateful for funding from the NSF through EFRI ODISSEI-1240441 (A. A. E., B. L., J. C., C. S.), as well as financial support from FOM (B. G. C., J. P.), from the D-ITP consortium (J. P.) and a VIDI grant (V. V.) funded by NWO.

\*Current Address: Department of Physics, University of Massachusetts, Amherst, MA 01002, USA.

†Current Address: School of Natural Sciences, University of California, Merced, CA 95343, USA.

‡Current Address: Department of Mathematics, University of Wisconsin, Madison, WI 53706, USA.

- [1] J. Ryu, M. D'Amato, X. Cui, K. N. Long, H. J. Qi, and M. L. Dunn, *Appl. Phys. Lett.* **100**, 161908 (2012).
- [2] M. T. Tolley, S. M. Felton, S. Miyashita, D. Aukes, D. Rus, and R. J. Wood, *Smart Mater. Struct.* **23**, 094006 (2014).
- [3] Y. Liu, M. Miskiewicz, M. J. Escuti, J. Genzer, and M. D. Dickey, *J. Appl. Phys.* **115**, 204911 (2014).
- [4] Z. Y. Wei, Z. V. Guo, L. Dudte, H. Y. Liang, and L. Mahadevan, *Phys. Rev. Lett.* **110**, 215501 (2013).
- [5] M. Schenk and S. D. Guest, *Proc. Natl. Acad. Sci. U.S.A.* **110**, 3276 (2013).
- [6] J. L. Silverberg, A. A. Evans, L. McLeod, R. C. Hayward, T. Hull, C. D. Santangelo, and I. Cohen, *Science* **345**, 647 (2014).
- [7] C. Lv, D. Krishnaraju, G. Konjevod, H. Yu, and H. Jiang, *Sci. Rep.* **4**, 5979 (2014).
- [8] S. Waitukaitis, R. Menaut, B. G. Chen, and M. van Hecke, *Phys. Rev. Lett.* **114**, 055503 (2015).
- [9] K. Miura, Proc. 31st Congr. Int. Astronaut. Federation **IAF-8 0-A 31**, 1 (1980).
- [10] A. A. Evans, J. L. Silverberg, and C. D. Santangelo, *Phys. Rev. E* **92**, 013205 (2015).
- [11] C. S. O'Hern, L. E. Silbert, A. J. Liu, and S. R. Nagel, *Phys. Rev. E* **68**, 011306 (2003).
- [12] S. Alexander, *Phys. Rep.* **296**, 65 (1998).
- [13] M. Wyart, S. Nagel, and T. Witten, *Europhys. Lett.* **72**, 486 (2005).
- [14] M. Wyart, H. Liang, A. Kabla, and L. Mahadevan, *Phys. Rev. Lett.* **101**, 215501 (2008).
- [15] L. R. Gómez, A. M. Turner, M. van Hecke, and V. Vitelli, *Phys. Rev. Lett.* **108**, 058001 (2012).
- [16] S. Ulrich, N. Upadhyaya, B. van Opheusden, and V. Vitelli, *Proc. Natl. Acad. Sci. U.S.A.* **110**, 20929 (2013).
- [17] C. Kane and T. Lubensky, *Nat. Phys.* **10**, 39 (2014).
- [18] T. Lubensky, C. Kane, X. Mao, A. Souslov, and K. Sun, *Rep. Prog. Phys.* **78**, 073901 (2015).
- [19] M. Z. Hasan and C. L. Kane, *Rev. Mod. Phys.* **82**, 3045 (2010).
- [20] B. G. Chen, N. Upadhyaya, and V. Vitelli, *Proc. Natl. Acad. Sci. U.S.A.* **111**, 13004 (2014).
- [21] J. Paulose, A. S. Meussen, and V. Vitelli, *Proc. Natl. Acad. Sci. U.S.A.* **112**, 7639 (2015).
- [22] E. Prodan and C. Prodan, *Phys. Rev. Lett.* **103**, 248101 (2009).
- [23] H. C. Po, Y. Bahri, and A. Vishwanath, *arXiv:1410.1320*.
- [24] M. Xiao, G. Ma, Z. Yang, P. Sheng, Z. Q. Zhang, and C. T. Chan, *Nat. Phys.* **11**, 240 (2015).
- [25] Z. Yang, F. Gao, X. Shi, X. Lin, Z. Gao, Y. Chong, and B. Zhang, *Phys. Rev. Lett.* **114**, 114301 (2015).
- [26] L. M. Nash, D. Kleckner, V. Vitelli, A. M. Turner, and W. T. M. Irvine, *Proc. Natl. Acad. Sci. U.S.A.* **112**, 14495 (2015).
- [27] P. Wang, L. Lu, and K. Bertoldi, *Phys. Rev. Lett.* **115**, 104302 (2015).
- [28] Y.-T. Wang, P.-G. Luan, and S. Zhang, *New J. Phys.* **17**, 073031 (2015).
- [29] R. Susstrunk and S. D. Huber, *Science* **349**, 47 (2015).
- [30] W. P. Su, J. R. Schrieffer, and A. J. Heeger, *Phys. Rev. Lett.* **42**, 1698 (1979).
- [31] T. Hull, *Project Origami: Activities for Exploring Mathematics* (CRC Press, Boca Raton, 2012).
- [32] See Supplemental Material at <http://link.aps.org/supplemental/10.1103/PhysRevLett.116.135501> for additional technical details and derivations.
- [33] S. Pellegrino, *Deployable Structures* (Springer-Verlag, Wien, 2001).
- [34] L. Asimow and B. Roth, *Trans. Am. Math. Soc.* **245**, 279 (1978).
- [35] C. Calladine, *Int. J. Solids Struct.* **14**, 161 (1978).
- [36] For structures with  $\kappa = 1$ , that lie on the transition between the two distinct topological phases, the winding number and, hence, polarization is not defined.
- [37] V. Vitelli, B. G. Chen, and N. Upadhyaya, *arXiv:1407.2890*.
- [38] Note that by rotating the structure by  $180^\circ$  one ends up with a “new” unit cell with  $\gamma \rightarrow -\gamma$  and  $\beta \rightarrow -\beta$ , which is in the opposite topological phase.
- [39] More precisely, since the function  $\det \mathbf{R}(\mathbf{q})$  is gauge dependent, the claim is that this is true in the gauge arising from a “balanced” unit cell as defined in Refs. [17,18].
- [40] D. Z. Rocklin, B. G. Chen, M. Falk, V. Vitelli, and T. Lubensky, *arXiv:1510.04970*.
- [41] J. Paulose, B. G. Chen, and V. Vitelli, *Nat. Phys.* **11**, 153 (2015).



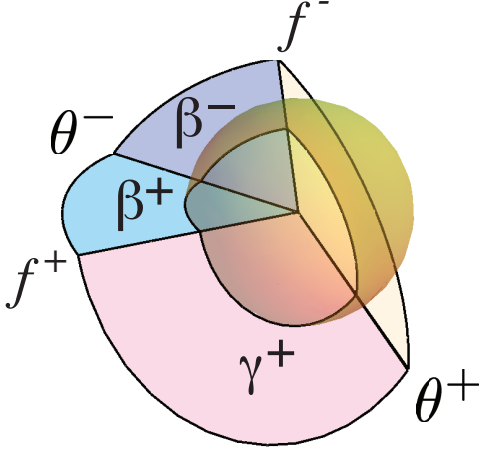


FIG. SI-1: Spherical polygons for a four-fold vertex. Angle variables are different from those used in the main text.

## Supplementary Information

### Appendix A: Vertex kinematics and spherical polygons

The intersection between an origami vertex and a sphere traces out a spherical polygon on the sphere surface [1] (Fig. SI-1). For a four-fold vertex, this polygon is a quadrilateral whose side lengths are inherited from the angles between adjacent folds in the fold pattern (the unlabeled fourth angle in Fig. SI-1 is  $\gamma^- = 2\pi - \beta^+ - \beta^- - \gamma^+$ ). The relationship between dihedral angles  $f^\pm$  is

$$\begin{aligned} \cos \beta^+ \cos \gamma^+ + \sin \beta^+ \sin \gamma^+ \cos f^+ &= \\ \cos \beta^- \cos \gamma^- + \sin \beta^- \sin \gamma^- \cos f^- &. \end{aligned} \quad (\text{S1})$$

Since  $\beta^+ + \gamma^+ = 2\pi - \beta^- - \gamma^-$ , Eq. (S1) becomes

$$\sin \beta^+ \sin \gamma^+ (\cos f^+ + 1) = \sin \beta^- \sin \gamma^- (\cos f^- + 1) \quad (\text{S2})$$

A similar relationship between  $\theta^+$  and  $\theta^-$  can be derived as

$$\sin \gamma^+ \sin \gamma^- (\cos \theta^+ + 1) = \sin \beta^+ \sin \beta^- (\cos \theta^- + 1) \quad (\text{S3})$$

The relationship between  $f^+$  and  $\theta^+$ , however, is more complex (Fig. SI-2). Define  $\epsilon$  to be the angle between  $\theta^+$  and  $\theta^-$  given by

$$\cos \epsilon = \cos \beta^+ \cos \theta^+ + \sin \beta^+ \sin \theta^+ \cos f^+. \quad (\text{S4})$$

and such that  $\epsilon = \beta^+ + \gamma^+$  when the vertex is flat. Then

$$\begin{aligned} \theta^+ &= \cos^{-1} \left( \frac{\cos \beta^+ - \cos \epsilon \cos \gamma^+}{\sin \epsilon \sin \gamma^+} \right) \\ &\pm \cos^{-1} \left( \frac{\cos \beta^- - \cos \epsilon \cos \gamma^-}{\sin \epsilon \sin \gamma^-} \right). \end{aligned} \quad (\text{S5})$$

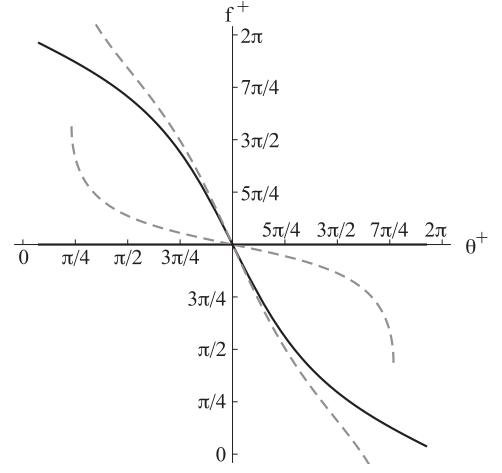


FIG. SI-2: The angle  $\theta^+$  versus  $f^+$  for two cases: (solid)  $\beta^+ = \beta^- = \pi/3$ ,  $\gamma^+ = \gamma^- = 2\pi/3$  and (dashed)  $\beta^+ = \pi/3 - \pi/10$ ,  $\beta^- = \pi/3 + \pi/10$ ,  $\gamma^+ = \gamma^- = 2\pi/3$ . In each case, there are two distinct branches joined only at the flat state. Note that one of the branches for the solid curves lies along  $f^+ = 0$ .

Either sign in Eq. (S5) satisfies the geometric constraint equations; this ambiguity arises from the different branches of  $\cos^{-1}$ . Yet, the branches are physical, and correspond to different ways of choosing which folds are “mountain” and which folds are “valley” folds. In particular, there is a branch in which  $f^+$  and  $f^-$  are both either mountain or valley folds and one in which they have the opposite sense [2]. In either case, however,  $\cos f^\pm$  remains the same and the exponential solution for  $u = 1 + \cos f$  in Eqs. 1 and 2 of the main text is valid.

One special case bears additional analysis. When the vertex has  $\gamma^\pm + \beta^\pm = \pi$ , the folds  $\theta^+$  and  $\theta^-$  are collinear. In that case, one branch of the vertex has both  $f^+$  and  $f^-$  as mountain (valley) folds. For the other branch, however,  $f^+ = f^- = \pi$  is strictly satisfied and  $\theta^+ = \theta^-$ . That is simply the case that a vertex is folded along the line shared by  $\theta^+$  and  $\theta^-$ , and this prevents the two adjacent folds  $f^\pm$  from folding at all. This motivates the choice of variables discussed in the main text, for which  $\beta^\pm = \alpha \mp \beta$  and  $\gamma^\pm = 2\pi - \alpha \mp \gamma$ . Then  $\beta = \gamma$  precisely when  $\theta^\pm$  are collinear.

### Appendix B: Second-order rigidity matrix for 1D strip

We label each unit cell with an index  $j$  and the two vertices within a unit cell with  $n = 1, 2$ . For convenience, we also express the dihedral angles in terms of their difference from  $\pi$ ,  $\delta f_n^\pm(j) = f_n^\pm(j) - \pi$  for the folds  $f^\pm$  of vertex  $n$  within unit cell  $j$ . Each vertex has one DOF, which we will parameterize with  $\delta\theta_n^+(j)$ . Since there is a two vertex unit cell, we combine these parameters into

two vectors,

$$\mathbf{f}(j) = \begin{pmatrix} f_1^-(j) \\ f_1^+(j) \\ f_2^-(j) \\ f_2^+(j) \end{pmatrix}, \quad (\text{S6})$$

and

$$\mathbf{s}(j) = \begin{pmatrix} \theta_1^+(j) \\ \theta_2^+(j) \end{pmatrix}. \quad (\text{S7})$$

Using spherical trigonometry, we compute  $\mathbf{f}(j) = \mathbf{J}\mathbf{s}(j)$ , where

$$\mathbf{J} = \begin{pmatrix} A_1^- + \sigma_1 B_1^- & 0 \\ A_1^+ + \sigma_1 B_1^+ & 0 \\ 0 & A_2^- + \sigma_2 B_2^- \\ 0 & A_2^+ + \sigma_2 B_2^+ \end{pmatrix}, \quad (\text{S8})$$

$\sigma_n = \pm 1$  is an arbitrary choice of branch in configuration space the vertex should be folded,

$$A_n^\pm = \frac{\sin(\alpha \mp \gamma_n)}{\sin(2\alpha)}, \quad (\text{S9})$$

and

$$B_n^\pm = \frac{1}{\sin(2\alpha)} \sqrt{\frac{\sin(\alpha - \gamma_n) \sin(\alpha + \gamma_n) \sin(\alpha \mp \beta_n)}{\sin(\alpha \pm \beta_n)}}. \quad (\text{S10})$$

For this paper, we have always assumed that  $\sigma_n = 1$ .

To complete our description, we must enforce the linear constraints  $\delta f_1^-(j+1) - \delta f_2^+(j) = 0$  and  $\delta f_2^-(j) - \delta f_1^+(j) = 0$ . In Fourier space, these constraints lead to an equation of the form

$$\mathbf{R}(q)\mathbf{s}(q) = \mathbf{0}. \quad (\text{S11})$$

for the infinitesimal deformations of the origami strip, where

$$\mathbf{R}(q) = \begin{pmatrix} (A_1^- + B_1^-)e^{iq} & -(A_2^+ + B_2^+) \\ A_2^- + B_2^- & (A_1^+ + B_1^+) \end{pmatrix}. \quad (\text{S12})$$

### Appendix C: Real-valuedness of the determinant: a hidden symmetry

We will restate the observed “reality” property here more formally. For all periodic triangulations we have checked, there exists a choice of unit cell so that the determinant of the rigidity matrix  $\det \mathbf{R}(\vec{q})$  is real valued for all  $\vec{q}$  in the Brillouin zone. The consequence of this is that with such a choice of unit cell, the phase of  $\det \mathbf{R}(\vec{q})$  cannot wind and so the topological polarization must vanish. There are also obvious consequences for the set of bulk zero modes which we will not discuss here. In Fig. SI-3 we display a sample calculation and visualization of this property for a small periodic triangulated origami, represented by a spring network.

This real-valuedness can be expressed in the following equivalent way. First, define  $z_1 = e^{iq_1 a_1}$  and  $z_2 = e^{iq_2 a_2}$ ,

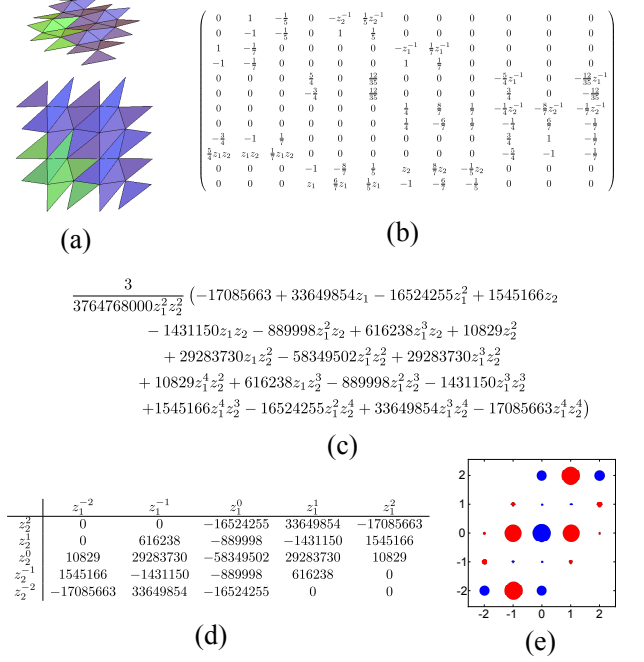


FIG. SI-3: Illustration of the reality property for triangulated origami. (a) A periodic triangulation based on the triangular lattice with four vertices, 12 edges and 8 triangles. The vertex coordinates are  $(0, 0, 0)$ ,  $(0, 1, 1/5)$ ,  $(1, 1/7, 0)$ ,  $(3/4, 1, -1/7)$  and the lattice primitive vectors are  $(2, 0, 0)$  and  $(0, 2, 0)$ . Above is a side view and below is a top view. Four unit cells are shown, with one highlighted in green. (b) The Fourier transformed rigidity matrix  $\mathbf{R}(z_1, z_2)$ , where  $z_1 = e^{iq_1 a_1}$  and  $z_2 = e^{iq_2 a_2}$ . Every row corresponds to an edge in the triangulation. (c) The Laurent polynomial  $\det \mathbf{R}(z_1, z_2)$ . (d) The table of coefficients of  $\det \mathbf{R}(z_1, z_2)$ , organized by powers of  $z_1$  and  $z_2$ . The number  $3/3764768000$  has been factored out of all entries. (e) A graphical representation of the coefficients of  $\det \mathbf{R}(z_1, z_2)$ . Red dots are positive coefficients, blue dots are negative, and the area of the disks is proportional to the absolute value of the coefficients (with a minimum disk size imposed for visibility).

and observe that  $\det \mathbf{R}(z_1, z_2)$  is a Laurent polynomial in those variables. Next, note that  $\det \mathbf{R}(\vec{q})$  is real if and only if:

$$\begin{aligned} \det \mathbf{R}(\vec{q}) &= \overline{\det \mathbf{R}(\vec{q})} \\ \det \mathbf{R}(z_1, z_2) &= \overline{\det \mathbf{R}(z_1, z_2)} \\ &= \det \mathbf{R}(\bar{z}_1, \bar{z}_2) \\ &= \det \mathbf{R}(z_1^{-1}, \bar{z}_2^{-1}). \end{aligned}$$

In the third line, we use the fact that the coefficients of this polynomial are real, and in the final line, we use the fact that all  $\vec{q}$  in the Brillouin zone,  $z_1$  and  $z_2$  lie on the unit circle and so  $\bar{z}_i = z_i^{-1}$ . This shows that for all  $p, q$ , the coefficients of the  $z_1^p z_2^q$  and  $z_1^{-p} z_2^{-q}$  terms must be equal in order for this polynomial to be real-valued on the unit circle.

A change of unit cell merely changes  $\det \mathbf{R}$  by a factor  $z_1^m z_2^n$  where  $m$  and  $n$  are integers related to the change in the number of bonds crossing unit cell boundaries [3]. If one imagines the coefficients of  $\det \mathbf{R}$  as a table (Fig. SI-3(d)), then such a factor does not change the values in the table, but merely shifts the positions of the entries in the table by a vector  $(m, n)$ . Therefore, the “reality property” is equivalent to the polynomial  $\det \mathbf{R}(z_1, z_2)$  being “2D palindromic”, i.e.

$$\det \mathbf{R}(z_1^{-1}, z_2^{-1}) = z_1^k z_2^l \det \mathbf{R}(z_1^{-1}, z_2^{-1}), \quad (\text{S13})$$

for some integers  $k, l$ . Equivalently, the table of coefficients of  $\det \mathbf{R}(z_1, z_2)$  is symmetric under inversion through some point  $(k/2, l/2)$ .

*Examples and tests performed:* We generated small triangulations of a torus via flipping edges from the triangular lattice and in all cases checked found that the the polynomial  $\det \mathbf{R}(z_1, z_2)$  was a palindrome. To ensure that the loss of precision from floating-point operations did not become an issue, we did these computations in rational arithmetic in the Mathematica computer algebra system.

Specifically, we began with periodic triangulation “seeds” displayed in Fig. SI-4 and performed random edge flips (transforming two adjacent triangles into two different triangles on the same four vertices) repeatedly onto randomly chosen edges. This procedure is illustrated in Fig. SI-4(a).

For every such crease pattern generated, we used vertex coordinates made by randomly perturbing a flat embedding of the seed triangulation. These were rounded to the nearest rational number with denominator lower than 10. The Laurent polynomial  $\det \mathbf{R}(z_1, z_2)$  was then calculated exactly and the coefficients of different terms were compared to check whether the polynomial was indeed palindromic as in Eq. (S13). In some cases, a flip would cause this polynomial to vanish (due e.g. to a degenerate edge connecting a vertex to itself). Afterwards, it is quite likely that further flips would produce triangulations with zero determinant. While the zero polynomial is of course real-valued, if this occurred, in order to get more substantive tests, we rejected this triangulation and flipped another edge instead. Regardless, for all triangulated origami checked we found that Eq. (S13) was always satisfied. In Table I we show a summary of the tests performed.

*Partial result:* We can show that subdividing a triangle in triangulated origami preserves the property that  $\det \mathbf{R}(\vec{q})$  remains real. To see this, note that such a subdivision creates one new vertex and three edges. With an appropriate choice of unit cell we can ensure that this vertex is not on the boundary and thus does not pick up factors of  $e^{iq_1 a_1}$  or  $e^{iq_2 a_2}$ .

The new vertex introduces three columns into  $\mathbf{R}(\vec{q})$  whose only nonzero entries can be in the rows corresponding to the three new edges. By reordering the vertices and columns, one finds that the determinant takes a block upper-triangular form with a  $3 \times 3$  block on the diagonal from the new additions (which we call  $\mathbf{R}_n(\vec{q})$ )

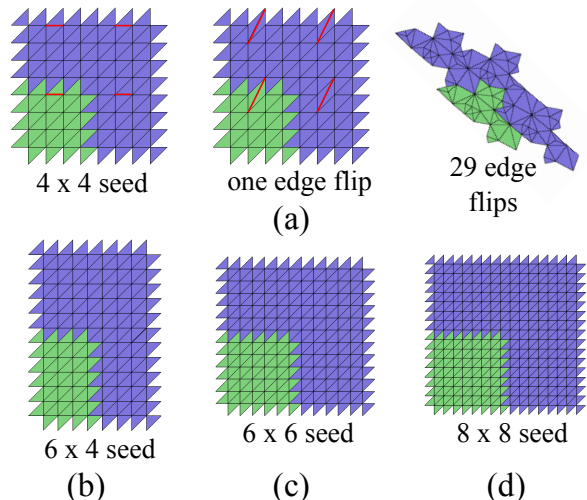


FIG. SI-4: Seed triangulations and edge flips. In each image, four unit cells are shown, with one highlighted in green. The triangulations are only shown with planar embeddings for clarity, the actual tested triangulations were deformed into 3D with random perturbations. (a) left: The 4 by 4 seed triangulation with one highlighted edge, center: the triangulation resulting from the edge flip of the red edge, right: a triangulation resulting from 29 random edge flips on the seed. (b) The 6 by 4 seed triangulation. (c) The 6 by 6 seed triangulation. (d) The 8 by 8 seed triangulation.

seed	$ V $	$ E $	$ T $	(runs, flips)
4 by 4	16	48	32	(100, 1000)
6 by 4	24	72	48	(50, 500)
6 by 6	36	108	72	(20, 200)
8 by 8	64	192	128	(10, 100)

TABLE I: Summary of tests performed of the “reality” property on different families of periodic triangulated origami. Each line of the table corresponds to a different seed (depicted in Fig. SI-4), and displays the number of vertices  $|V|$ , edges  $|E|$  and triangles  $|T|$  in the seed and shows the number of runs started as well as the number of random flip operations performed. Note that a flip preserves  $|V|$ ,  $|E|$  and  $|T|$ , and that the computations require computing determinants of symbolic  $|E| \times 3|V|$  matrices. In all runs, every single triangulation generated had the reality property, as described in the text.

as well as  $\mathbf{R}_0(\vec{q})$  as another block on the diagonal. By a well-known property of the determinant, this implies that  $\det \mathbf{R}(\vec{q}) = \det \mathbf{R}_n(\vec{q}) \det \mathbf{R}_0(\vec{q})$ .

If we were able to prove an analogous result for edge flips, then we would have shown that the palindromic property holds for all triangulations.

#### Appendix D: On the design of topological kirigami

We found topologically polarized kirigami via the following steps. We first constructed the pattern of plates and hinges as follows. As in Appendix C, we began with

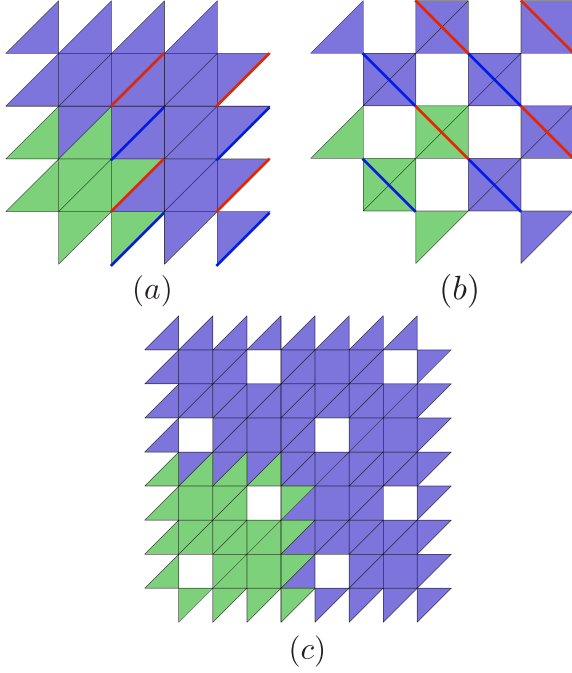


FIG. SI-5: Schematics of some structures created while designing the kirigami. In each image, four unit cells are shown, with one highlighted in green. These images only show the pattern of hinges and plates, and do not represent 3D embeddings. (a) A triangulated origami based on the triangular lattice. Two families of creases are highlighted in red and blue which are moved to create the next structure. (b) The checkerboard lattice of tetrahedra. This structure consists of tetrahedra joined by universal joints at their vertices. (c) The final kirigami structure. Created by placing rows and columns of additional triangles between tetrahedra, and then replacing the tetrahedra with flat quadrilateral plates.

a periodic spring network with the combinatorics of the standard triangular lattice (drawn in Fig. SI-5(a) as a square lattice with all NE diagonals added). This pattern models a triangulated origami structure, which seems to have a real determinant. To try to break this symmetry we attempted to add holes in the unit cell.

To add holes without changing the marginal rigidity property, we removed one NE diagonal bond from a square  $A$  and placed it in an adjacent (already occupied) square  $B$  as a NW diagonal bond. This yields a hole in  $A$  and a new tetrahedron in  $B$ . If one does this for all squares in a checkerboard pattern, one ends up with the so-called checkerboard lattice of tetrahedra (Fig. SI-5(b)). This is the simplest 2D periodic structure in 3D which admits geometric realizations with distinct topological polarizations. However, the tetrahedra are joined at vertices, not along hinges, so it is neither origami nor kirigami.

To remedy this, we may add rows and columns of triangulated strips between the holes and the tetrahedra. Now we do have a structure made of solid bodies joined along

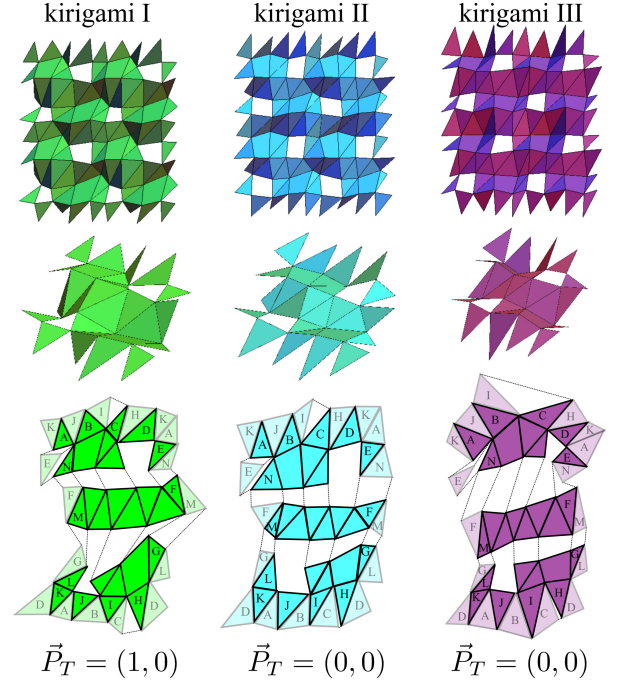


FIG. SI-6: Three kirigami unit cells with different topological polarizations. A top view and side view of the 3D unit cells are shown above exploded versions that have been cut into strips and then flattened into the plane. The dashed lines indicate how the strips are to be joined to create the 3D structure shown above and the faces labeled by letters indicate the periodicity of the structure.

hinges, but the bodies are tetrahedra and not yet flat plates. Flat plates can be modeled by a marginal spring network with pyramids over two coplanar triangles. By adding an additional vertex above the two triangles and attaching it to the four vertices of the plate, we create a minimally rigid body which is attached to the rest of the structure by four coplanar hinges. The final pattern of hinges and plates is shown in Fig. SI-5(c) (pyramids not shown for clarity).

Given this design, we still have to find a suitable realization of this structure as a 3D object. We did this by beginning with a flat embedding of a unit cell and perturbing the vertices randomly, subject to the condition that the quadrilateral plates remain planar. These randomly generated unit cells were then checked to determine if they had a topological polarization by (1) examining the contours where  $\text{Re } \det \mathbf{R}$  and  $\text{Im } \det \mathbf{R}$  vanish to ensure that they did not cross and create a “Weyl point” [4] and (2) computing the winding numbers of  $\text{Arg } \det \mathbf{R}$  to find the polarization vector. We found in general that Weyl points did occur frequently. However we also found many “gapped” examples as well. Fig. SI-6 shows the unit cells of three kirigami structures with this crease pattern but with differing topological polarizations: kirigami I has polarization  $(1, 0)$ , and kirigami II and III have polarization  $(0, 0)$ . Their 3D structures

are also displayed in an “exploded” view, where they have been cut apart into flattened strips which must be bent in space and then glued together to form the kirigami structures. Unit cells I and II were used to construct the domain wall in Fig. 3 in the main text.

In Fig. SI-7 we show kirigami structures consisting of pairs of unit cells from Fig. SI-6. The domain walls do not contain any extra or missing bonds, so there are no differences in the local counting of degrees of freedom. These kirigami structures are rectangular sheets with periodic boundary conditions in both directions, so one might expect the lowest energy vibrational modes to

be bulk bending modes. This is indeed the case when the two unit cells used have the same polarization vector (Fig. SI-7(a)). However, when a structure is made of unit cells with two distinct polarizations, one of the domain walls carries localized very low-energy modes (Fig. SI-7(b) and Fig. 3 in the main text). The eigenvalue corresponding to the energy of the topological mode is  $\omega^2 = 1.42 \times 10^{-16}$  (comparable to the eigenvalues corresponding to the translational zero modes), whereas the eigenvalue corresponding to the bending mode is much larger,  $\omega^2 = 1.82 \times 10^{-9}$ .

- 
- [1] T. Hull, *Project origami: activities for exploring mathematics* (CRC Press, 2012).
  - [2] S. Waitukaitis, R. Menaut, B. G. Chen, and M. van Hecke, Phys. Rev. Lett. **114**, 055503 (2015).

- [3] C. Kane and T. Lubensky, Nature Physics **10**, 39 (2014).
- [4] D. Z. Rocklin, B. G. Chen, M. Falk, V. Vitelli, and T. Lubensky, arXiv preprint (2015), 1510.04970.



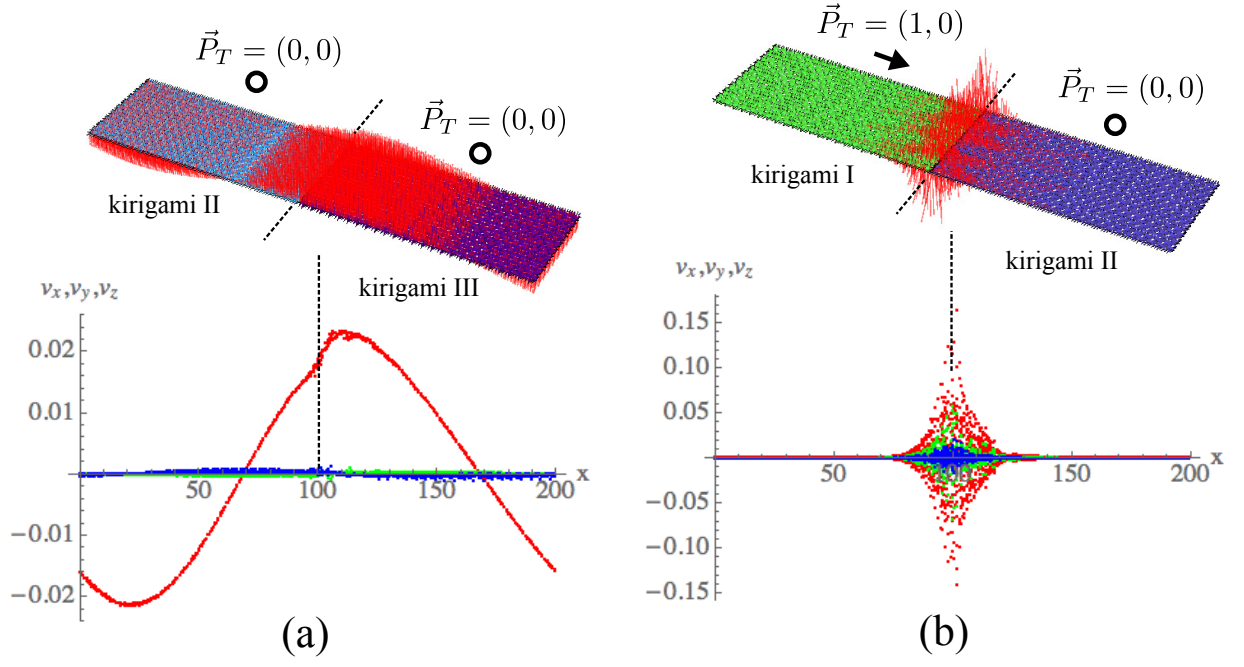


FIG. SI-7: Composite kirigami systems constructed from unit cells I, II and III from Fig. SI-6 and their lowest energy eigenmodes. Both structures depicted consist of 50 unit cells (along the  $x$ -direction) by 5 unit cells (along the  $y$ -direction), which are divided into two domains each of size 25 by 5. Two copies in the shorter direction are shown in the upper figures, and the displacements in the mode are overlaid as red lines. The structures are periodic in both directions, so there are domain walls at  $x = 0 = 200$  and  $x = 100$ . The domain wall at  $x = 100$  is marked with dashed lines. The lower plots show the  $x$ -,  $y$ - and  $z$ -components (in blue, green, and red, respectively) of the displacement vectors of all vertices as a function of the  $x$ -positions. (a) Composite structure of kirigami II and III, both of which have polarization  $(0,0)$ . The lowest eigenmode has eigenvalue  $\omega^2 = 1.82 \times 10^{-9}$  and resembles a bulk bending mode. (b) Composite structure of kirigami I (polarization  $(1,0)$ ) and II (polarization  $(0,0)$ ). The lowest eigenmode has eigenvalue  $\omega^2 = 1.42 \times 10^{-16}$  and is highly localized near the domain wall at  $x = 100$ .



# Reflection and Refraction of Flexural Waves at Geometric Boundaries

Arthur A. Evans<sup>1</sup> and Alex J. Levine<sup>1,2,3</sup>

<sup>1</sup>*Department of Chemistry and Biochemistry, UCLA, Los Angeles, California 90095-1596, USA*

<sup>2</sup>*Department of Physics and Astronomy, UCLA, Los Angeles, California 90095-1596, USA*

<sup>3</sup>*Department of Biomathematics, UCLA, Los Angeles, California 90095-1596, USA*

(Received 18 March 2013; published 16 July 2013)

We present a theory of flexural wave propagation on elastic shells having nontrivial geometry and develop an analogy to geometric optics. The transport of momentum within the shell itself is anisotropic due to the curvature, and as such complex classical effects such as birefringence are generically found. We determine the equations of reflection and refraction of such waves at boundaries between different local geometries, showing that waves are totally internally reflected, especially at boundaries between regions of positive and negative Gaussian curvature. We verify these effects by using finite element simulations and discuss the ramifications of these effects for the statistical mechanics of thin curved materials.

DOI: [10.1103/PhysRevLett.111.038101](https://doi.org/10.1103/PhysRevLett.111.038101)

PACS numbers: 87.10.Pq, 46.40.Cd, 46.70.De, 87.16.D–

Curved shells appear in nature over a vast range of length scales from carbon nanotubes [1] to continental plates [2]. Understanding their mechanics and, in some cases, equilibrium fluctuations plays a key role in a variety of systems of interest in biological physics and material science such as viral capsids [3,4], cellular membranes [5–7], plant morphogenesis [8], and self-assembled origami [9–11]. In spite of the large range of length scales and material properties, the mechanics of these shells are unified by the constraints imposed by the coupling of elasticity and geometry in materials whose lateral extent is much larger than their thickness.

This geometric property leads to a dramatic separation of the energy scales associated with bending and stretching. Generically, thin sheets and filaments are significantly softer to bending, allowing a unified treatment of wrinkling, crumpling, and a host of other morphological transitions under external forces or confinement [12–18]. Shells having a more complex geometry in their unstrained state, however, develop an inherent resistance to bending from the geometric coupling of the soft bending mode to the stiffer stretching one [19,20], as a consequence of Gauss's *theorem egregium*, which relates changes in Gaussian curvature to stretching of the surface. Recently, an analysis of curved shell indentation by Vaziri and Mahadevan [21] of the response to static locally imposed forces has shown that the linear response of the deformation field depends qualitatively on the sign of the Gaussian curvature.

Motivated by this analysis, we examine in this Letter the propagation of flexural waves in shallow shells of constant curvature. We show that there is a useful analogy between this problem and the more familiar analysis of the propagation of light with the local curvature playing the role of the index of refraction. We derive an analog of Snell's law for refraction between two interfaces with differing optical properties; in our case, the material is identical across the

interface, but only the local geometry changes. We find that curved shells are generically birefringent and may exhibit total internal reflection. Additionally, waves within regions of negative curvature propagate primarily along certain directions, and interfaces separating positive and negative Gaussian curvature regions lead generically to a range of incident angles that exhibit total internal reflection. The combination of these two effects indicates that curved elastic manifolds may act as barriers causally disconnecting regions of differing Gaussian curvature, leading to anomalously slow phonon equilibration, with potential implications for the statistical mechanics of such surfaces.

Even with a linear constitutive relation for the material's elasticity, the equations governing elasticity of thin surfaces are nonlinear due to geometry. For certain cases, however, they may be linearized and useful expressions coaxed from the more general ones. The energy functional that describes a thin, elastic shell is given by  $\mathcal{F} = \int_S (N^{\alpha\beta} E_{\alpha\beta} + M^{\alpha\beta} K_{\alpha\beta})$ , where  $E_{\alpha\beta}$  and  $K_{\alpha\beta}$  are the deformation tensors associated with strain and bending of a surface, respectively. A linearly elastic material allows us to write the local stress tensor as  $N^{\alpha\beta} = Yh[(1-\nu)E_{\alpha\beta} + \nu E_{\gamma}^{\gamma}]$  and the bending moment tensor as  $M^{\alpha\beta} = \kappa[(1-\nu)K^{\alpha\beta} + \nu K_{\gamma}^{\gamma}]$ ; these linear functionals of the curvature and deformation tensors of the surface introduce Young's  $Y$  and bending  $\kappa$  moduli, the shell thickness  $h$ , and Poisson ratio  $\nu$ . The details are standard and can be found in Refs. [22,23].

The Euler-Lagrange equations that result from this expression are nonlinear in both geometry and deformation. In only a few situations are there known analytic solutions that take into account the nonlinearities of geometric origin [24,25]. Conversely, by considering a flat shell but retaining the nonlinearities in the deformation state, one arrives at the Föppl–von Kármán equations, which are notoriously difficult to solve [26]. We will consider the intermediate asymptotic limit of the

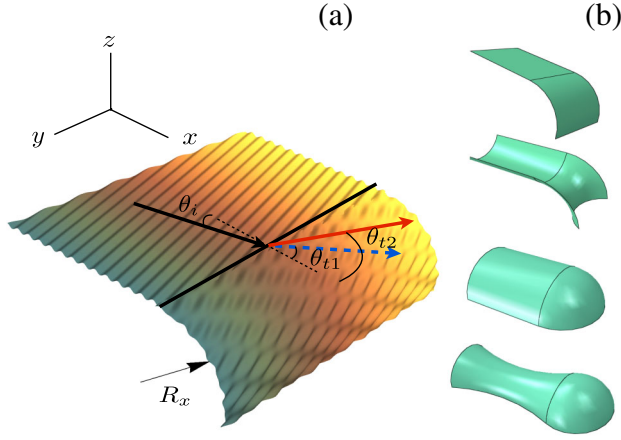


FIG. 1 (color online). (a) Schematic of flexural waves refracting upon passage from one region of curvature to another, separated by the black line. Two refracted waves are produced in the birefringent (cylindrical) region on the right. (b) Prototypical interface types for traveling flexural waves on curved surfaces. Along the interface, kinematic constraints require the curvature to be continuous, leaving only a small number of possible choices.

Donnell-Mushtari-Vlasov equations [21,22], where nonlinearities in the deformation field are neglected but stresses introduced by leading order curvature terms are retained. In this case the deformation tensors may be written in terms of the in-plane displacements  $v_\alpha$ , the normal displacement  $\zeta$ , and the curvature tensor of the undeformed shell  $d_{\alpha\beta}$  as

$$K_{\alpha\beta} \approx D_\alpha D_\beta \zeta, \quad (1)$$

$$E_{\alpha\beta} \approx \frac{1}{2}(D_\alpha v_\beta + D_\beta v_\alpha) - d_{\alpha\beta} \zeta, \quad (2)$$

with  $D_\alpha$  the covariant derivative on the surface. These approximations neglect terms higher order than  $O(d_{\alpha\beta})$  in the stress. This results in neglecting terms of the form  $d_{\alpha\gamma} d_\beta^\gamma M^{\alpha\beta}$  and  $D_\alpha (d_\beta^\beta M^{\gamma\alpha})$  in the force balance, substantially simplifying the analysis. In the absence of  $d_{\alpha\beta}$ , these deformation tensors reduce to the flat case and the equations of plate elasticity are recovered. In anticipation of examining a “shallow” shell, we assume that the spatial extent of the deformations is small compared to the shell’s radii of curvature, so we may replace covariant derivatives by partial derivatives:  $D_\alpha \rightarrow \partial_\alpha$ . In the same limit we may simplify the in-plane stresses by introducing the Airy stress function  $\chi$ , defined by  $N^{\alpha\beta} = \epsilon^{\alpha\eta} \epsilon^{\beta\xi} \partial_\eta \partial_\xi \chi$  ( $\epsilon^{\alpha\beta}$  is the 2D alternating tensor). We are immediately led to the following equations of undulatory dynamics (in vacuum) and compatibility of the surface [22]:

$$\kappa \nabla^4 \zeta - \mathcal{L}[\chi] = -\rho h \frac{\partial^2 \zeta}{\partial t^2}, \quad (3)$$

$$\frac{1}{Yh} \nabla^4 \chi + \mathcal{L}[\zeta] = 0, \quad (4)$$

where  $\rho$  is the shell’s mass density. The linear operator  $\mathcal{L} = \epsilon^{\alpha\eta} \epsilon^{\beta\xi} d_{\alpha\beta} \partial_\eta \partial_\xi$  is a measure of the incompatibility of the surface with the flat space solution [27] and couples bending and stretching through the local curvature.

In analogy to the standard development of Snell’s law, in which one considers the propagation of light across an interface separating two regions with differing but spatially uniform dielectric constants, we consider flexural waves propagating from one region of constant curvature to another—see Fig. 1(a). A continuously varying local geometry may later be accounted for by a succession of such interfaces between regions of constant curvature. A flexural wave propagates through one region, with a given (possibly anisotropic) dispersion relation, impinges upon a region of differing geometry, and must conserve momentum at the interface due to translational invariance; hence, momentum conservation requires refraction [28]. Unlike in classical optics, where any two dielectric constants may, in principle, be in contact, the continuity of the surface and its local slopes forces the principal curvature along the interface to remain constant. Consequently, there are only four possible combinations of curvature mismatch allowed at an interface—see Fig. 1(b). In all cases, we choose a coordinate system aligned with the principal axes of curvature; it will be useful to further parameterize their geometry by defining  $\beta = R_x/R_y$  to be the ratio of these principal curvatures.

To examine the dispersion relation for traveling plane waves in regions of constant geometry, we look for solutions of Eqs. (3) and (4) of the form  $\zeta(\mathbf{x}, t) = e^{i\mathbf{q} \cdot \mathbf{x} - i\omega t} \hat{\zeta}(\mathbf{q}, \omega)$ ,  $\chi(\mathbf{x}, t) = e^{i\mathbf{q} \cdot \mathbf{x} - i\omega t} \hat{\chi}(\mathbf{q}, \omega)$ , obtaining a dispersion relation  $\omega(\mathbf{q})$  as the solution to [29,30]

$$\rho h \omega^2 = \kappa q^4 + \frac{Yh}{q^4} \mathcal{L}_q^2, \quad (5)$$

$$\mathcal{L}_q = \frac{q_y^2}{R_x} + \frac{q_x^2}{R_y}, \quad (6)$$

From this solution we determine the group velocity  $\mathbf{v}_g = \partial \omega / \partial \mathbf{q}$  of flexural waves to be

$$\omega(\mathbf{q}) \frac{\partial \omega}{\partial \mathbf{q}} = 2q^3 \hat{\mathbf{q}} + \frac{(1-\beta) \sin 2\theta}{q} (\sin^2 \theta + \beta \cos^2 \theta) \hat{\mathbf{q}}^\perp, \quad (7)$$

where  $\theta$  is the angle between  $\mathbf{q}$  and the  $x$  axis, and we have nondimensionalized times and lengths by  $\omega \rightarrow \omega/\omega_R$  and  $q \rightarrow q\ell$ , where  $\omega_R^2 = Y/(R_x^2 \rho)$  is the radial “ringing frequency” of a cylinder of radius  $R_x$ , and  $\ell^4 = \kappa R_x^2 / Yh$ . For  $q\ell \ll 1$  the shell can be considered in the “membrane” limit, where bending terms can be completely neglected. For  $q\ell \gg 1$  the shell is essentially flat. Our analysis focuses on  $q\ell \sim 1$ . The first term in Eq. (7) reproduces the usual flexural wave dispersion relation for thin plates

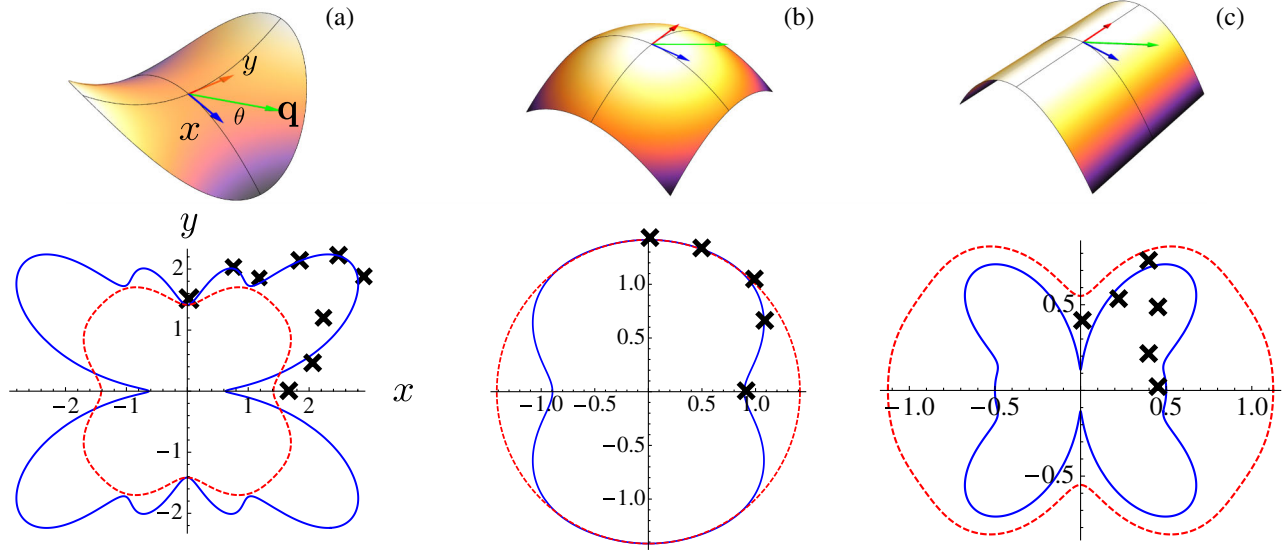


FIG. 2 (color online). Examples of anisotropic flexural wave group velocities for different values of  $\beta$ . Figures show group velocities on a polar plot, with  $\theta$  measured from the positive  $x$  axis. Black symbols show group velocity measurements from finite element simulations—see Supplemental Material—[33] to be compared to the (solid blue line) predictions of the linearized theory. (a) For saddles  $\beta < 0$ , the velocity has at least four lobes of maximum speed (compare to the static deformation characteristics in Ref. [21]) as seen for  $\beta = -1, -3$  [solid (blue) and dashed (red) lines, respectively], with  $q = 1$ . (b) Group velocities at  $q = 1$  for ellipsoidal surfaces for  $\beta = 1$  (solid blue line), a sphere, and  $\beta = 2$  (dashed red line) show smaller variations with direction. (c) Cylinders are more pathological because  $\beta = 0$  and the Gaussian curvature is zero. As a result, the anisotropy depends solely on the wave number:  $q = 0.5, 0.75$  [solid (blue) and dashed (red) lines, respectively]. This pathology is seen most clearly in the magnitude of disagreement between the linearized theory and the finite element simulations; see Supplemental Material [33] for more details.

$\rho h \omega^2 = \kappa q^4$ , while the second term carries momentum perpendicular to the wave vector and depends on curvature. The magnitude of the group velocity is also anisotropic as shown in Fig. 2 for saddle, ellipsoidal, and cylindrical surfaces.

For a generic anisotropic surface, a flexural ray will bend with respect to the principal axes. In order to address this, consider the anisotropic term in Eq. (7):  $(1 - \beta) \sin(2\theta)(\sin^2\theta + \beta \cos^2\theta)$ . Except for a sphere ( $\beta = 1$ ), this term is generally nonvanishing, so that the group and phase velocities are not collinear, unless the waves propagate along the principal curvature directions  $\theta^* = 0, \pi/2$ . When not along one of these special directions where they do not bend, rays bend towards the direction of smallest curvature for  $\beta > 0$  [31]. For  $\beta < 0$ , there is a new special direction  $\theta^* = \tan^{-1}\sqrt{-\beta}$ : If  $\theta < \theta^*$ , the rays bend towards the  $x$  axis; otherwise, they bend towards the  $y$  axis. These results can be understood in terms of Fermat's principle [29,31,32].

We now turn to the refraction and reflection at the boundary between two different geometries. A ray with wave vector  $\mathbf{q}$  making an angle of  $\theta_i$  with respect to the  $x$  axis is injected into a region with principal curvature ratio  $\beta_i$  and encounters a boundary along the  $y$  axis (see Fig. 1) with a different geometry, parameterized by  $\beta_r$ , and wave number  $\mathbf{k}$ . Matching the undeformed surface at the boundary requires  $R_y$  to be continuous through the interface, resulting in four allowed configurations—see Fig. 1(b).

We calculate the transmitted angle  $\theta_t$  with respect to the boundary normal—see Fig. 1—in terms of the incident angle  $\theta_i$  by imposing conservation of the momentum tangent to the interface, i.e.,  $|\mathbf{q}| \sin\theta_i = |\mathbf{k}| \sin\theta_t$ , resulting in the Snell's law analog

$$[\omega^2 - \mathcal{A}(\beta_i, \theta_i)]^{1/4} \sin\theta_i = [\omega^2 - \mathcal{A}(\beta_r, \theta_t)]^{1/4} \sin\theta_t, \quad (8)$$

where  $\mathcal{A}(\beta, \theta) = (\beta \cos^2\theta + \sin^2\theta)^2$  contains the geometric information. The simplest forms of these results are for a plate, cylinder, sphere, and saddle, where  $\mathcal{A} = 0, \sin^4\theta, 1$ , and  $\cos^2(2\theta)$ , respectively.

Several representative curves of  $\theta_t$  as a function of  $\theta_i$  are shown in Fig. 3(a) (for simplicity, we use only  $\beta = 0, \pm 1$ ). The dashed and solid curves show the transmitted ray angles—two solutions are possible in birefringent cases. There are no solutions in the gray regions indicating total internal reflection (TIR). We do not show results for the sphere-cylinder interface, since we wish to highlight the effects of anisotropy on birefringence and TIR; these effects are far more pronounced in the other prototypical interfaces. Consider as an example the plate-cylinder interface (see Supplemental Material [33] for numerical tests of this case), where the incident region has  $\mathcal{A} = 0$ , while the cylindrical region has  $\mathcal{A}(0, \theta_t) = \sin^4\theta_t$ . Because the cylindrical region has an anisotropic dispersion relation, the phase velocity can be multivalued, and, in order to



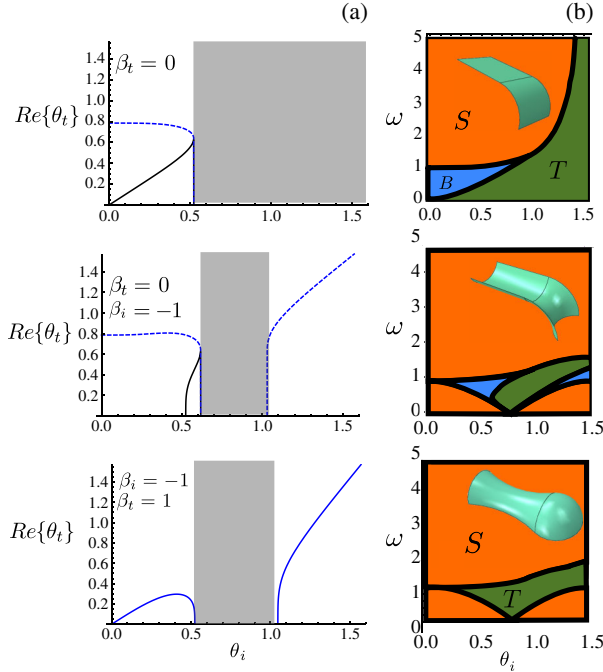


FIG. 3 (color online). Transmitted angle as a function of the incident angle, for  $\omega = 0.5$ . (a) Representative curves for  $Re\{\theta_t\}$  as a function of  $\theta_i$ . Gray regions represent areas where  $Im\{\theta_t\} \neq 0$ , indicating total internal reflection. (b) Single mode transmission (S), birefringence (B), and total internal reflection (T) at different frequencies for different geometries (displayed as insets).

conserve momentum, it is possible that two rays are transmitted. This birefringence occurs in anisotropic dielectric media as well and results from the multivaluedness of the phase velocity in the medium [34]. Interfaces that include regions of negative Gaussian curvature include bands of TIR, as opposed to a critical angle above which all the incident rays are reflected. The solutions of Eq. (8) depend on both frequency and incident angle. Scanning over the input parameters, we arrive at the plots shown in Fig. 3(b), in which regions of single transmitted ray propagation (S), dual ray propagation (B), and total internal reflection (T) are shown. For large  $\omega$ , the curvature effects disappear, as the interface becomes transparent to sufficiently short wavelengths, except at grazing incidence. It is of particular interest that in saddle regions most of the energy propagates at particular angles that depend on  $\beta$ ; this point taken in tandem with Snell's law results indicates that for the right value of  $\beta$  and  $\omega$  flexural waves will be trapped within the negative Gauss curvature regions.

To test these analytic results, we performed finite element simulations using ABAQUS (Dassault Systèmes) on a closed shell having boundaries between regions of constant geometry; see Supplemental Material [33] for simulation details. The most dramatic results are obtained at boundaries between positive and negative Gaussian curvature. Consequently, we examine the “peanut” shell in Fig. 4

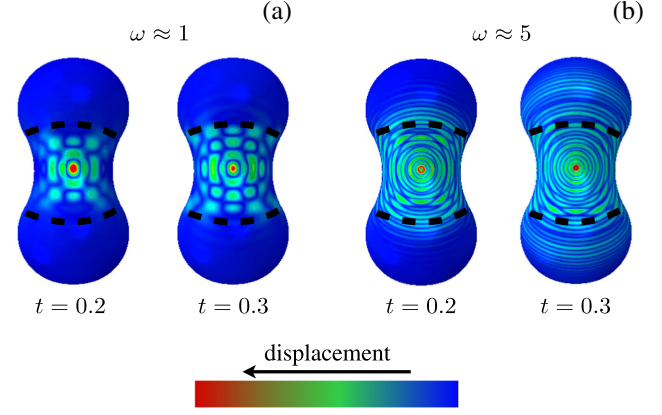


FIG. 4 (color online). Finite element simulations showing total internal reflection at the boundary of negative and positive Gaussian curvatures, denoted by the dashed line. (a) For  $\omega \approx 1$ , the linear theory predicts a range of incident angles for which rays exhibit TIR. For this shell, with  $\beta \approx -0.5$ , the rays propagate preferentially at  $\theta^* \sim \tan^{-1}(\sqrt{-\beta}) \approx 35^\circ$ , which falls within the predicted band of incident angles for TIR. The shell does not have a constant curvature, and we use a point force instead of a plane wave so the wave trapping is temporary. Over longer times, they leak into the positive Gaussian curvature region. (b) For  $\omega \approx 5$ , the shell is predicted to be essentially transparent. This too is supported by the simulation.

formed from a catenoidlike region (negative Gauss curvature) with  $\beta \approx -0.5$  bounded at the top and bottom by spherical caps  $\beta = 1$ . The boundaries are shown by (black) dashed lines. At time  $t = 0$ , we apply an oscillatory point force at the equator of the shell with  $\omega \approx 1$  (left) or  $\omega \approx 5$  (right). For  $\omega \sim 1$  the analytic theory predicts a wide range of incident angles leading to TIR—see Figs. 3(a) and 3(b), bottom panel; we see that for short times waves are confined to the saddle region reflected off the top and bottom boundaries—see Fig. 4(a). Over time, they leak into the spherical caps due primarily to transmission occurring at normal incidence, as expected from the theory—see Fig. 3(b), bottom panel. For  $\omega \approx 5$ , the interface is predicted to be essentially transparent; indeed, the simulation shows that waves propagate freely across the boundary—see Fig. 4(b).

We have shown the utility of an analogy to geometric optics for understanding the dynamics of flexural waves on surfaces of nontrivial geometry. Curvature acts as the local index of refraction, and interfaces between positive and negative Gaussian curvature, in particular, lead to total internal reflection of waves propagating from the negative curvature side. This suggests that such boundaries generate causally disconnected regions on the manifold such that flexural waves in the two sectors cannot equilibrate, at least within our linear analysis. The implications for the statistical mechanics of such waves on manifolds of complex geometry have not been explored. More generally, one may inquire about the role of localization and enhanced back-scattering from randomly curved surfaces even without the

singular limit of crumpling [35–37]. In addition to such random shapes, one may be able to use prescribed geometries to redirect flexural waves with a purely geometric waveguide to “cloak” regions of the membrane, as has been explored by using anisotropic metamaterials [38]. Nonlinearities ignored here are known, in some cases, to lead to anomalous elasticity [7,27] and result in dynamical equations reminiscent of weak turbulence [39]; the role of geometry in such cases remains to be fully explored.

A.J.L. thanks L. Mahadevan for enjoyable conversations. The authors acknowledge NSF Grant No. DMR-1006162.

- 
- [1] C. Bower, R. Rosen, L. Jin, J. Han, and O. Zhou, *Appl. Phys. Lett.* **74**, 3317 (1999).
  - [2] P. Kearey, K. A. Klepeis, and F. J. Vine, *Global Tectonics* (Wiley-Blackwell, New York, 2009).
  - [3] J. Lidmar, L. Mirny, and D. R. Nelson, *Phys. Rev. E* **68**, 051910 (2003).
  - [4] T. Kuriabova and A. J. Levine, *Phys. Rev. E* **77**, 031921 (2008).
  - [5] Y. K. Park, C. A. Best, K. Badizadegan, R. R. Dasari, M. S. Feld, T. Kuriabova, M. L. Henle, A. J. Levine, and G. Popescu, *Proc. Natl. Acad. Sci. U.S.A.* **107**, 6731 (2010).
  - [6] Y. K. Park, C. A. Best, T. Kuriabova, M. L. Henle, M. S. Feld, A. J. Levine, and G. Popescu, *Phys. Rev. E* **83**, 051925 (2011).
  - [7] J. Paulose, G. A. Vliedenthart, G. Gompper, and D. R. Nelson, *Proc. Natl. Acad. Sci. U.S.A.* **109**, 19551 (2012).
  - [8] J. Dervaux and M. Ben Amar, *Phys. Rev. Lett.* **101**, 068101 (2008).
  - [9] C. Py, P. Reverdy, L. Doppler, J. Bico, B. Roman, and C. N. Baroud, *Phys. Rev. Lett.* **98**, 156103 (2007).
  - [10] J. Kim, J. A. Hanna, M. Byun, C. D. Santangelo, and R. C. Hayward, *Science* **335**, 1201 (2012).
  - [11] Y. Klein, E. Efrati, and E. Sharon, *Science* **315**, 1116 (2007).
  - [12] L. Pocivavsek, R. Dellsy, A. Kern, S. Johnson, B. Lin, K. Y. C. Lee, and E. Cerda, *Science* **320**, 912 (2008).
  - [13] B. Roman and J. Bico, *J. Phys. Condens. Matter* **22**, 493101 (2010).
  - [14] A. A. Evans and E. Lauga, *Phys. Rev. E* **79**, 066116 (2009).
  - [15] H. King, R. D. Schroll, B. Davidovitch, and N. Menon, *Proc. Natl. Acad. Sci. U.S.A.* **109**, 9716 (2012).
  - [16] B. Davidovitch, R. D. Schroll, D. Vella, M. Adda-Bedia, and E. A. Cerda, *Proc. Natl. Acad. Sci. U.S.A.* **108**, 18227 (2011).
  - [17] A. Vaziri, *Thin-Walled Struct.* **47**, 692 (2009).
  - [18] A. A. Evans, S. E. Spagnolie, D. Bartolo, and E. Lauga, *Soft Matter* **9**, 1711 (2013).
  - [19] D. Vella, A. Ajdari, A. Vaziri, and A. Boudaoud, *Phys. Rev. Lett.* **109**, 144302 (2012).
  - [20] A. Lazarus, H. C. B. Florijn, and P. M. Reis, *Phys. Rev. Lett.* **109**, 144301 (2012).
  - [21] A. Vaziri and L. Mahadevan, *Proc. Natl. Acad. Sci. U.S.A.* **105**, 7913 (2008).
  - [22] F. I. Niordson, *Shell Theory* (North-Holland, Amsterdam, 1985).
  - [23] T. R. Powers, *Rev. Mod. Phys.* **82**, 1607 (2010).
  - [24] E. Cerda and L. Mahadevan, *Proc. R. Soc. A* **461**, 671 (2005).
  - [25] E. Cerda and L. Mahadevan, *Phys. Rev. Lett.* **80**, 2358 (1998).
  - [26] L. D. Landau and E. M. Lifshitz, *Theory of Elasticity* (Pergamon, Oxford, 1986), 3rd ed.
  - [27] D. R. Nelson, *Defects and Geometry in Condensed Matter Physics* (Cambridge University Press, Cambridge, England, 2002).
  - [28] H. Goldstein, *Classical Mechanics* (Addison-Wesley, New York, 1980).
  - [29] O. A. Germogenova, *J. Acoust. Soc. Am.* **53**, 535 (1973).
  - [30] A. N. Norris, *Wave Motion* **21**, 127 (1995).
  - [31] A. N. Norris and D. A. Rebinsky, *J. Vib. Acoust.* **116**, 457 (1994).
  - [32] A. A. Evans and A. J. Levine (to be published).
  - [33] See Supplemental Material at <http://link.aps.org/supplemental/10.1103/PhysRevLett.111.038101> for a brief discussion of the numerical methods and tests of reflection and refraction.
  - [34] M. Born and E. Wolf, *Principles of Optics: Electromagnetic Theory of Propagation, Interference and Diffraction of Light* (Cambridge University Press, Cambridge, England, 1999).
  - [35] T. A. Witten, *Rev. Mod. Phys.* **79**, 643 (2007).
  - [36] A. Gopinathan, T. A. Witten, and S. C. Venkataramani, *Phys. Rev. E* **65**, 036613 (2002).
  - [37] G. Seizilles, E. Bayart, M. Adda-Bedia, and A. Boudaoud, *Phys. Rev. E* **84**, 065602 (2011).
  - [38] N. Stenger, M. Wilhelm, and M. Wegener, *Phys. Rev. Lett.* **108**, 014301 (2012).
  - [39] G. Düring, C. Josserand, and S. Rica, *Phys. Rev. Lett.* **97**, 025503 (2006).

# Reflection and Refraction of Flexural Waves by Geometric Boundaries: Supplementary information

Arthur A. Evans<sup>1</sup> and Alex J. Levine<sup>1,2</sup>

*<sup>1</sup>Department of Chemistry & Biochemistry  
UCLA, Los Angeles, CA 90095-1596*

*<sup>2</sup>Department of Physics & Astronomy,  
UCLA, Los Angeles, CA 90095-1596*

(Dated: June 3, 2013)

PACS numbers:

## I. SIMULATION DETAILS

We use the commercial finite element software package ABAQUS to simulate the dynamics of flexural wave propagation in thin elastic shells. Within this package, the shells' material properties are defined by specifying its three-dimensional Young's modulus  $Y$ , Poisson's ratio  $\nu$ , and thickness  $h$ . The bending rigidity  $\kappa$  is then derived from these quantities yielding  $\kappa = Yh^3/(12\sqrt{1-\nu^2})$ . Further details can be found in [1, 2]. In addition, one must specify the mass density of the shell material, but this simply sets the frequency scale for the oscillatory dynamics and is of little consequence for our analysis. For completeness, however, the numerical values used are listed below. The numerical solution for the dynamics of the shell proceeds using a finite element method that is well known. We use quadrilateral shell elements that span the entire thickness, with 5 integration points across the thickness using a Simpson quadrature method. Mesh sensitivity tests were performed to ensure that the results are independent of the element size.

In all of our measurements we apply an oscillatory point force to a single node on the shell, directed perpendicular to the surface. The magnitude of the force is sufficiently small that the linear response regime is appropriate for describing the displacement of the shell. This point is examined numerically by varying the amplitude of the applied force. Velocity measurements are then taken from sample points defined on nodes away from the point of force application, and the normal displacement is measured as a function of time.

## II. GROUP VELOCITY

We can verify Eq. 7 in the main text by examining the propagation of waves numerically. To do so, we construct shells of revolution in the form of a cylinder, an ellipsoid, and a catenoid (see Fig. 1). Locally, each of these surfaces will behave as a shell with  $\beta = 0, \beta > 0$ , and  $\beta < 0$ , respectively. The material properties and the frequency of oscillation for the point force is then chosen to be such that the reduced frequency matches the example group velocity plots in Fig. 2 of the main text. Since ABAQUS has no intrinsic dimensional units, we choose the material parameters of the shell in order to select an  $O(10)$  ringing frequency, which also depends on the global geometry. For example, in the cylindrical case we allow the shell to extend very far in the y-direction ( $L_y = 20$ ), while setting the radius of curvature in

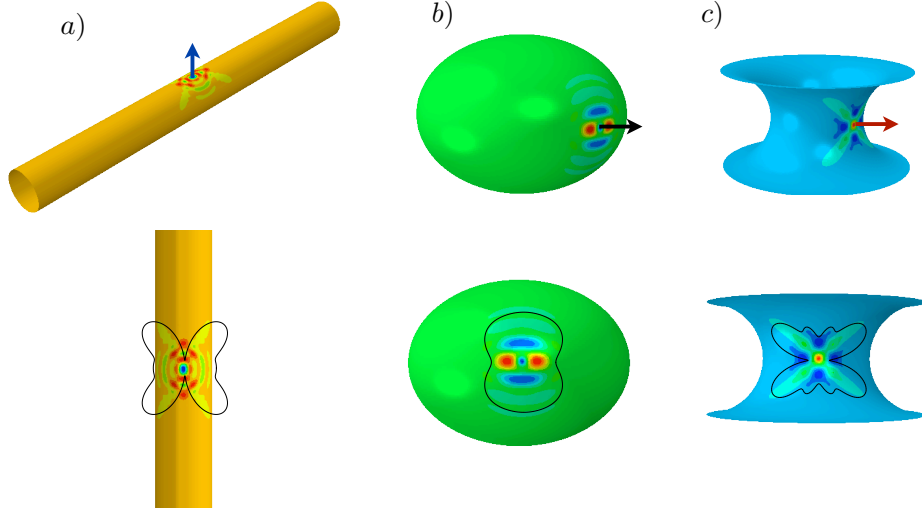


FIG. 1: Examples of the deformation patterns of various shapes used to compute group velocities. a) Top panel: Orthographic view of a cylindrical shell with a point force directed normal to the surface. Bottom panel: Top view of cylindrical shell with deformation pattern used to measure group velocity (group velocity profile from linearized analysis overlaid for comparison). b) Ellipsoid with normally directed point force and curvature mismatch  $\beta \approx 2$ . c) Saddle-shaped shell with normally directed point force and curvature mismatch  $\beta \approx -3$ . This example cannot be a closed shell since a surface with globally negative Gaussian curvature cannot be embedded in three dimensions without self-intersection. In all the cases the color-coding corresponds to the magnitude of the normal displacement. The measurements of the group velocity are collected from a quarter-circle arc (i.e.  $\theta \in \{0, \pi/4\}$ ) at shell nodes approximately equidistant from the point of force application.

the x-direction  $R_x = 1$ . Then by setting  $Y = 10^6$ ,  $\rho = 10^3$ ,  $\nu = 0.3$ , and  $h = 0.1$ , we obtain a ringing frequency of  $\omega_R \approx 31.6$ . To compare with the group velocity plot in the main text we then require the dimensionless wave vector  $q = 0.5$ , which sets  $\omega \approx 1/4$ . The length and frequency scales are all approximate since in our scaling analysis in the main text we assumed that the curvature is constant, while in a general shell the principal curvatures will vary in space.

Choosing several representative points on the shells, we measure the group velocity of wave packets traveling through these sample points and identify the angle of propagation with respect to the point where the force is applied. Example time series are shown in Fig. 2. The left trace is for  $\theta = 0$  on the cylindrical shell, while the right is for  $\theta = \pi/2$ . For a



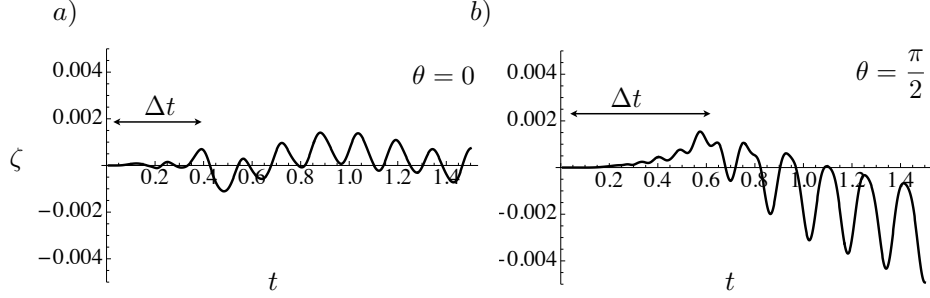


FIG. 2: Plot of several time series for displacement of test nodes. Wave packets travel at the speed of the group velocity, so that, by making time of flight measurements for the packets, one can extract the group velocity. The extracted group velocity is, in actuality, averaged over the path the traveled by the packet during the measurement time  $\Delta t$ .

point a distance  $L$  from the point of force application, we measure a time delay  $\Delta t$  between the beginning of force application and the arrival of the resulting wave packet at the point of interest. This allows us to measure an approximate group velocity  $v_G \approx L/\Delta t$  for waves at each point on the shell. In Fig. 2, we show representative examples of wave packets passing a fixed point on the shell. Comparing the measurements for the group velocity to our analytical predictions in Fig. 2 of the main text, we see that the numerical results are quantitatively consistent with our predictions. We find the least degree of quantitative agreement for the case of the cylindrical shell. This can be understood by recalling the approximations inherent in the shallow shell theory. This theory neglects terms of order  $O(1/R^2)$  in the stress tensor, and the inclusion of terms of this order introduce a regularizing “mass” term into the dispersion relation. The neglect of such higher order terms in the curvature is one of the simplifications of shallow shell theory, and for surfaces with non-zero Gaussian curvature its neglect leads to sub dominant corrections. For the special case of cylindrical shells, which have vanishing Gaussian curvature, this neglected term becomes significant, leading to observable differences between our theory, based on the shallow shell assumptions, and the numerical results.

### III. BIREFRINGENCE AND TOTAL INTERNAL REFLECTION

As with the group velocity, we measure the propagation of waves as they pass geometric boundaries. For this we generate the shapes shown schematically in Fig. 1 and Fig. 3a in the

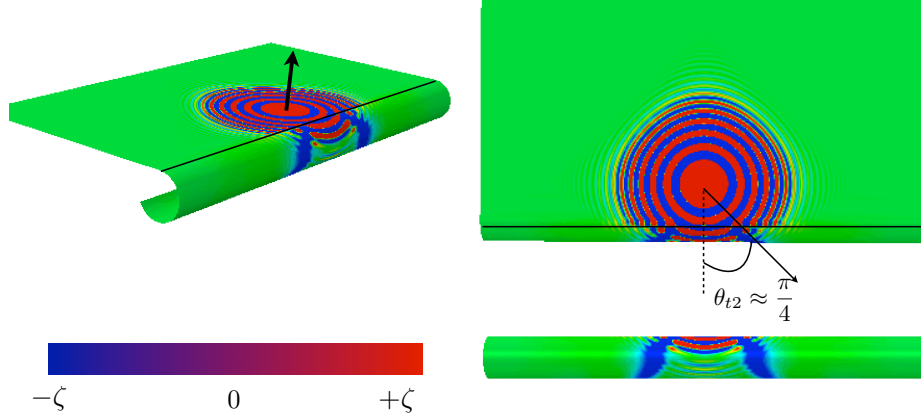


FIG. 3: Simulated wave propagation in the plate/cylinder interface model. We apply a small oscillatory point force denoted by the black arrow, and clamp the boundaries of the shell. The boundaries are far enough from most of the action for this to be a reasonable set of conditions. We set the reduced frequency  $\omega = 1/2$  to observe the same birefringence and total internal reflection predicted in the main text. Upper left: orthographic view of normal displacement  $\zeta$  for dimensionless time  $t=1.25$ . Upper right: top view of same snapshot in time. The waves propagating into the cylinder are clearly truncated at a specific angle, denoted here as  $\theta_{t2}$ , and measurement of this angle yields a value of  $\pi/4$ , the exact angle predicted for one of the birefringent modes (see figure 3a of main text).

main text (i.e. the plate/cylinder interface), and then apply an oscillatory point force normal to the shell in order to examine the presence of birefringence and total internal reflection. As before, sample points are placed at representative points of the shell to measure the dominant propagation angle.

For this case we verify that at the appropriate reduced frequency  $\omega$  and the approximate values of  $\beta$ , birefringence and total internal reflection occur in the same parameter range as predicted by the theory. An example is found in the deformation pattern shown in Fig. 3. Here we choose  $Y = 10^6, \rho = 10^3, h = 0.1$  and the radius of curvature of the cylindrical section is  $R_x = 1$ . We then simulate the dynamics of the deformation, and the angle of the transmitted ray is clearly determined from the above figure; the presence of total internal reflection is demonstrated by the lack of any propagation at shallower angles. These results are both in agreement with the linearized theory presented in the main text showing that the predictions of refraction and total internal reflection describe well the full dynamics of

waves impinging on a boundary between differing curvatures.

We verify the predicted behavior for the other shapes shown in Fig. 3 in the main text as well. These data are not shown. In Fig. 4 of the main text, we demonstrate more generally the applicability of these results to more complex curved shells where the constant curvature assumption is not strictly satisfied.

- 
- [1] L. D. Landau and E. M. Lifshitz, *Theory of elasticity* (Pergamon Press, Oxford, 1986), 3rd ed.  
[2] F. I. Niordson, *Shell Theory* (North-Holland, 1985).



# Emergence and design of extrinsic properties in mechanical metamaterials

Nan Yang,<sup>1,2,3\*</sup> Chun-Wei Chen,<sup>3</sup> Jinkyu Yang,<sup>3</sup>  
Jesse L. Silverberg,<sup>4,5,6\*</sup>

<sup>1</sup>Tianjin Key Laboratory of the Design and Intelligent Control  
of Advanced Mechatronical Systems, Tianjin University of Technology  
Xiqing District Tianjin 300384, China

<sup>2</sup>College of Engineering, Shantou University  
Shantou University, Shantou 515063, China

<sup>3</sup>Department of Aeronautics and Astronautics, University of Washington,  
Seattle WA 98195, USA

<sup>4</sup>Wyss Institute for Biologically Inspired Engineering, Harvard University,  
Boston MA 02115, USA

<sup>5</sup>Department of Systems Biology, Harvard Medical School,  
Boston MA 02115, USA

<sup>6</sup>Division for Advanced Sciences and Data Research, Multiscale Systems, Inc.  
Worcester MA 01609, USA

\*To whom correspondence should be addressed;  
E-mail: yn@tjut.edu.cn and js@mss.science

*One Sentence Summary:* We introduce, study, and demonstrate a new form of reprogrammable metamaterial by turning a design obstacle into a design opportunity.

**Metamaterials are a class of engineered materials routinely violating basic assumptions of ordinary matter. While metamaterials are typically assembled from carefully designed mesoscale units, the intended bulk-scale functionality can be obscured by unintended emergent effects driven by non-additive unit-unit interactions. These**



interactions are often sensitive to the number of units and their overall arrangement, making them extrinsic to the unit-scale design. Such extrinsic effects lead to unusual circumstances where two very similar bulk metamaterial structures fabricated from the same mesoscale unit can have very different properties, which in turn complicates the development of general-purpose metamaterial technologies. Here, we reconceptualize bulk-scale extrinsic properties as a design opportunity, and repurpose them to construct a new class of exponentially reconfigurable origami- and kirigami-inspired metamaterials. We illustrate the use of extrinsic properties to design a variety of passive mechanical devices including a reconfigurable frequency filter, as well as a single structure that transforms between a waveguide, a wave lens, and a wave cloak. Bench-top experiments validate the core concepts of this framework and show how extrinsic effects can be useful even when they arise unintentionally.

Mechanical metamaterials are a class of materials designed with a wide range of exotic responses to external forces (1–19). They are often lighter, have fewer moving parts than an equivalent simple machine, and can exhibit functionality through passive power consumption. Typically, metamaterials are built by modularly assembling smaller mesoscale units with the use of geometry to control mechanical function. Whether through origami-like folding sheets (1, 3, 4, 14, 15, 18–22) or selective removal of material (4, 6, 8, 23–25), the geometry of each module is the principle driver of exotic bulk-scale mechanical phenomena. This aspect of metamaterial design is attractive because it encodes bulk-scale response functions into properties that are *intrinsic* to individual modules. However, unintended factors *extrinsic* to individual units, such as unit-unit interactions, can arise and obscure the intended unit-scale design. These extrinsic effects are often structure-specific, driven by self-interactions, and can depend on shape, size, orientation, dimensionality,

and topology of the bulk material (2, 4–7, 14, 18, 19, 25). This sensitivity to bulk-scale details makes extrinsic properties difficult to predict, prescribe, or plan when designing mesoscale units, and therefore they present a critical obstacle to general-purpose metamaterial technologies. We therefore need a strategy that short-circuits the challenges of these unintended effects while still allowing for a wide range of useful mechanical behavior.

To this end, we introduce a general-purpose platform for constructing metamaterial devices. In essence, we replace the infinite design space of continuous geometric parameters (18, 26–30) with a finite design space of  $N$  tessellated units that have  $\sim 4^N$  discrete configurations (6, 17, 31). This design strategy allows us to choose metamaterial properties by selecting a specific configuration while holding the bulk material’s shape, size, orientation, dimensionality, and topology constant. Thus, rather than eliminating extrinsic phenomena, their contributions are incorporated into an exponentially large menu of possibilities that can be selectively chosen from when configuring the metamaterial.

Our approach is best explained by first introducing a mesoscale unit, which is comprised of a thin foldable material bonded at the edges (Fig. 1A-C) (SM). The unit’s design was created using origami and kirigami techniques previously developed for modular metamaterial construction (22). To the best of our knowledge, it has not been previously studied. This unit has two symmetric flanges that actuate using weakly-coupled degrees of freedom (Fig. 1C,  $\theta_1$  and  $\theta_2$ ;  $\theta_1$  is the dihedral angle of facets BCFG and BCF’G’;  $\theta_2$  defined similarly) (SM). Each flange has two extreme states resulting in four configurations: both flanges up (Fig. 1C, configuration [1,1], black square), both down (Fig. 1C, configuration [0,0], black triangle), and a symmetric pair of configurations with one up and one down (Fig. 1C, [0,1] and [1,0], black diamond and circle). Following convention, we model folding creases as linear torsional hinges and computed the energetics of geometrically-allowed configurations assuming ideal rigid facets (Fig. 1D, black diagonal lines  $\theta_2 = \theta_1$  and  $\theta_2 = 360^\circ - \theta_1$ ). These crease-only deformations are embedded in a larger energetic landscape where the facet material elastically bends (Fig. 1D, color plots elastic potential

energy from folding and bending) (see derivations in SM) (*3, 14, 15, 18, 20, 21*). Whether or not bending is permitted, an isolated unit is intrinsically tristable with a strong energetic minimum for the  $[1,1]$  configuration, weak energetic minima for the  $[0,1]$  and  $[1,0]$  configurations, and no minimum corresponding to the  $[0,0]$  configuration (Fig. 1E). However, when the unit is embedded in a  $3 \times 3$  tessellation, we find an altered energetic landscape where all four configurations now have local energetic minima (Fig. 1F and G, perimeter units held in  $[1,1]$  while central unit configuration varies). Thus, extrinsic unit-unit interactions lead to a new stable state with popping transitions between its various configurations (SM). Moreover, a vibrational analysis using Finite Element Method (FEM) simulations shows the band structure resulting from this extrinsic multistability has a gap around 2.9 kHz in the  $\Gamma X$  direction that can be reversibly opened or closed depending on whether the unit is in  $[1,1]$  or  $[0,0]$  (Fig. 1H, red and blue lines; band gap highlighted by gray rectangle) (see SM for details on FEM of paper-like materials in this geometry with different moduli) (*10–12, 16, 17, 32*). Integrating the band structure shows the Density of States (DOS) exhibits a high degree of sensitivity to the module’s configuration (Fig. 1I, red and blue lines). Because these vibrational properties are so strongly configuration-specific, the extrinsic interactions of Popping and Emergently-Reprogrammable Meta-material TEssellations (PERMuTE) provide an avenue to exponentially reconfigurable functionality.

Examining the properties of a  $1 \times 3$  PERMuTE material helps illuminate its potential as a platform for general-purpose reconfigurable metamaterials. Again using FEM, we input a time-dependent force generated by 11 equally-spaced frequencies,  $F(t) = F_0 \sum_{\kappa=5}^{15} \sin[2\pi(\kappa \cdot 100)t]$  (Fig. 2A) (SM). When the PERMuTE material is in the  $[0,0][0,0][0,0]$  configuration (Fig. 2B, top), we find it functionally behaves as a vibrational filter (Fig. 2C, top) that suppresses 10 of the 11 input frequencies (Fig. 2D, top). We then reconfigure the PERMuTE material to  $[0,0][1,1][0,0]$  (Fig. 2B, middle) by popping its middle unit, and find it now transmits a more complex waveform (Fig. 2C, middle) with two well-pronounced

frequencies mixed with low-amplitude side-band contributions (Fig. 2D, middle). Popping another unit (Fig. 2B, bottom) of the same PERMuTE structure to generate the  $[1,1][1,1][0,0]$  configuration then leads to another new output waveform (Fig. 2C, bottom) that again consists of two well-pronounced frequencies (Fig. 2D, bottom). However, in this third configuration, the output frequency composition has substantially changed relative to the previous two settings. With only 3 of the  $4^3 = 64$  configurations examined (SM), these results already illustrate how extrinsic factors producing the PERMuTE material’s band structure and multistability lead to configuration- and frequency-specific filtering. Noting extrinsic properties are sensitive to the number of modules and their macroscopic assembly, we recognize the specific band structure for this  $1 \times 3$  tessellation is distinct from that of an isolated unit or another size structure. We therefore expect a 2D PERMuTE material to have similar functional properties, but with a new degree of design freedom.

Using similar methods, we analyzed vibrational properties of a  $9 \times 9$  PERMuTE material to determine what types of devices reside within the configurations of this structure. Of the  $4^{81}$  possibilities available (SM), we focus here on three. For the first device, we popped a “+” shape of units to  $[1,1]$  and set the remainder to  $[0,0]$  (Fig. 3A, top). This pattern was chosen to produce a 1-input/3-output waveguide that we tested by oscillating the input edge unit at various frequencies  $f$  (Fig. 3A, bottom; orange unit) while measuring the response amplitude throughout the structure (Fig. 3A, bottom; red heatmap). Defining the response signal efficiency  $\eta(f)$  as the average output amplitude (Fig. 3A, bottom; green units) divided by the average perimeter amplitude (Fig. 3A, bottom; black units), we find  $\eta(f)$  can be quite large (Fig. 3A, bottom;  $\eta(1,007 \text{ Hz}) \approx 14$ ). These large efficiencies arise when input oscillations excite the specific configuration’s band structure resonances. For the second device, we reset all units to  $[0,0]$  and then popped a triangular shaped region into  $[1,1]$  (Fig. 3B, top). This reconfiguration programmed the PERMuTE material to function as a vibrational wave lens that focuses a distributed line of input oscillation (Fig. 3B, bottom; orange units) onto a single output unit (Fig. 3B, bottom;

green unit). Again sweeping frequency while measuring the response signal efficiency, we found a range of functional values where  $\eta(f) > 1$  (Fig. 3B, bottom;  $\eta(658 \text{ Hz}) \approx 4$ ). For the third device, we reset the configuration to an annulus of  $[0,0]$  units with the goal of creating an interior wave cloaking region isolated from vibrations (Fig. 3C, top; central region is targeted for vibration isolation). Measuring  $\eta(f)$ , we found values generally  $< 1$  with the best performance leading to  $\approx 80\%$  vibration suppression (Fig. 3C, bottom;  $\eta(89.9 \text{ Hz}) \approx 0.2$ ). In this type of cloaking device, resonant modes are confined to the edge and prevented from propagating through the annulus. While the functional range of frequencies for these three devices vary, the basic unit's geometry remains the same. In real-world applications, the fabrication material can be tailored to optimally prescribe the resonances affecting  $\eta(f)$  (SM). As such, the demonstration of a waveguide, wave lens, and wave cloak all reversibly programmed from a single PERMuTE material highlight its potential as a general-purpose metamaterial platform.

In light of the insights gained by FEM studies (Figs. 1-3), we fabricated PERMuTE devices from lasercut cardstock and tested the mechanical properties in bench-top experiments. We first verified an isolated unit is intrinsically tristable (Movie S1), whereas units in a  $3 \times 3$  tessellation are quadstable (Movie S2). We then verified the mechanical properties were dependent on extrinsic interactions with a longitudinal force-displacement measurement of the central unit (Fig. 4A, photos) that showed sensitivity to the configuration of adjacent units (Fig. 4A, dark and light green data). We also found the extrinsic multistability separating  $[0,0]$  from  $[1,1]$  vanished from this force-displacement experiment when testing an isolated unit (Fig. 4A, gray data). Additional transverse compression measurements of a single unit in the  $[0,0]$ ,  $[0,1]$ ,  $[1,0]$ , and  $[1,1]$  configurations verified the predicted symmetry between  $[0,1]$  and  $[1,0]$  (Figs. 1E and 4B). The same transverse compression on a  $3 \times 3$  tessellation with varying number of units in the  $[0,0]$  configuration (Fig. 4C) (SM) showed the zero-frequency mechanical properties could be easily and reversibly programmed due to extrinsic multistability.



Moving to finite-frequency measurements, we tested a  $3 \times 3$  PERMuTE structure to verify the anticipated functionality of extrinsic properties. Performing a frequency sweep on the tessellation in five distinct configurations showed resonant peaks that shifted up-and-down while maintaining a near-constant central frequency (Fig. 4D, peaks marked  $P_1$ ,  $P_2$ , and  $P_3$ ) (SM). These measurements demonstrate a range of extrinsic behavior depending on how many units were set to  $[0,0]$ , with  $P_3$  vanishing in one configuration, while  $P_2$  jumped 5-fold between its extremes. At higher frequencies, we also found that varying configurations caused resonance peaks to discretely shift by  $\Delta f_1 = (9 \pm 1)$  Hz and  $\Delta f_2 = -(9 \pm 1)$  Hz (Fig. 4E). Interestingly, this shift groups configurations so that 0, 1, and 3 units in  $[0,0]$  have indistinguishable resonance peaks (Fig. 4E, gray, orange, tan lines), while configurations with 7 and 9 units in  $[0,0]$  are almost identically shifted (Fig. 4E, purple, black lines). On one hand, these configuration-specific shifts experimentally realize a frequency-filtering metamaterial (Fig. 2D). On the other hand, the reversible generation, enhancement, and alteration of resonance peaks (combined results of Fig. 4D and E) are the critical ingredients necessary for constructing the waveguide, wave lens, and wave cloak devices (Fig. 3). Even though these physical experiments only explored 5 of the  $4^9 = 262,144$  possible configurations over a limited frequency range, the experimental evidence validates the existence of extrinsic properties and demonstrates how their realization is practically implemented with PERMuTE.

The design strategy underlying PERMuTE metamaterials neither eliminates unintended extrinsic effects nor predicts their emergence. Instead, we repurpose them into a menu of properties for device functionality. In real-world scenarios, this involves (i) choosing a bulk macroscopic assemblage of units, (ii) pre-computing the response functions over a range of frequencies, then (iii) selecting and optimizing the configuration for a given application. These steps contrast with current methodology for metamaterial design, which involves fixing gradients in unit geometry to statically program bulk-scale properties (5, 6, 8, 14, 15, 18). These steps underscore the fact that band structure will

generally be unique to the tessellation and its configuration; a partial 2.9 kHz gap in an infinite tessellation (Fig. 1H) may not necessarily appear in a  $1 \times 3$  or  $9 \times 9$  tessellation (Figs. 2 and 3), making structure-specific response both the reality and challenge of extrinsic metamaterial properties. Nevertheless, whether designing a multipurpose platform or a single-use structure, the extrinsic design strategy used here further accelerates the predictability, flexibility, and programmability of metamaterial technology toward high-impact commercial applications.

## References

1. J. L. Silverberg, A. A. Evans, L. McLeod, R. C. Hayward, T. Hull, C. D. Santangelo, I. Cohen, *Science* **345**, 647 (2014).
2. J. Christensen, M. Kadic, O. Kraft, M. Wegener, *MRS Communications* **5**, 453 (2015).
3. J. L. Silverberg, J.-H. Na, A. A. Evans, B. Liu, T. C. Hull, C. D. Santangelo, R. J. Lang, R. C. Hayward, I. Cohen, *Nature Materials* **14**, 389 (2015).
4. P. M. Reis, H. M. Jaeger, M. Van Hecke, *Extreme Mechanics Letters* **5**, 25 (2015).
5. B. G.-g. Chen, B. Liu, A. A. Evans, J. Paulose, I. Cohen, V. Vitelli, C. Santangelo, *Physical Review Letters* **116**, 135501 (2016).
6. C. Coulais, E. Teomy, K. de Reus, Y. Shokef, M. van Hecke, *Nature* **535**, 529 (2016).
7. J. T. Overvelde, T. A. De Jong, Y. Shevchenko, S. A. Bercera, G. M. Whitesides, J. C. Weaver, C. Hoberman, K. Bertoldi, *Nature Communications* **7**, 10929 (2016).
8. C. Coulais, D. Sounas, A. Alù, *Nature* **542**, 461 (2017).
9. K. Bertoldi, V. Vitelli, J. Christensen, M. van Hecke, *Nature Reviews Materials* **2**, 17066 (2017).
10. A. Nanda, M. A. Karami, *Journal of Sound and Vibration* **424**, 120 (2018).

11. H. Yasuda, C. Chong, E. G. Charalampidis, P. G. Kevrekidis, J. Yang, *Physical Review E* **93**, 043004 (2016).
12. M. Thota, S. Li, K. Wang, *Physical Review B* **95**, 064307 (2017).
13. T. Frenzel, M. Kadic, M. Wegener, *Science* **358**, 1072 (2017).
14. H. Fang, K. Wang, S. Li, *Extreme Mechanics Letters* **17**, 7 (2017).
15. P. P. Pratapa, P. Suryanarayana, G. H. Paulino, *ASME 2017 International Design Engineering Technical Conferences and Computers and Information in Engineering Conference* (American Society of Mechanical Engineers, 2017), pp. V05BT08A038–V05BT08A038.
16. O. R. Bilal, A. Foehr, C. Daraio, *Proceedings of the National Academy of Sciences* **114**, 4603 (2017).
17. O. R. Bilal, A. Foehr, C. Daraio, *Advanced Materials* **29** (2017).
18. Z. Zhai, Y. Wang, H. Jiang, *Proceedings of the National Academy of Sciences* **115**, 2032 (2018).
19. B. Liu, J. L. Silverberg, A. A. Evans, C. D. Santangelo, R. J. Lang, T. C. Hull, I. Cohen, *Nature Physics* **14**, 811 (2018).
20. A. A. Evans, J. L. Silverberg, C. D. Santangelo, *Physical Review E* **92**, 013205 (2015).
21. V. Brunck, F. Lechenault, A. Reid, M. Adda-Bedia, *Physical Review E* **93**, 033005 (2016).
22. N. Yang, J. L. Silverberg, *Proceedings of the National Academy of Sciences* **114**, 3590 (2017).

23. Y. Cho, J.-H. Shin, A. Costa, T. A. Kim, V. Kunin, J. Li, S. Y. Lee, S. Yang, H. N. Han, I.-S. Choi, *et al.*, *Proceedings of the National Academy of Sciences* **111**, 17390 (2014).
24. R. Zhu, H. Yasuda, G. Huang, J. Yang, *Scientific Reports* **8**, 483 (2018).
25. C. Coulais, C. Kettenis, M. van Hecke, *Nature Physics* **14**, 40 (2018).
26. Z. Wang, L. Jing, K. Yao, Y. Yang, B. Zheng, C. M. Soukoulis, H. Chen, Y. Liu, *Advanced Materials* **29**, 1700412 (2017).
27. D.-G. Hwang, M. D. Bartlett, *Scientific reports* **8**, 3378 (2018).
28. Y. Chen, T. Li, F. Scarpa, L. Wang, *Physical Review Applied* **7**, 024012 (2017).
29. D. Z. Rocklin, S. Zhou, K. Sun, X. Mao, *Nature communications* **8**, 14201 (2017).
30. S. Babae, J. T. Overvelde, E. R. Chen, V. Tournat, K. Bertoldi, *Science advances* **2**, e1601019 (2016).
31. H. Fang, S.-C. A. Chu, Y. Xia, K.-W. Wang, *Advanced Materials* **30**, 1706311 (2018).
32. P. P. Pratapa, P. Suryanarayana, G. H. Paulino, *Journal of the Mechanics and Physics of Solids* **118**, 115 (2018).

## Acknowledgments

We thank X.T. Shi, H. Yasuda, H. Kim, R. Chaunsali and J. E. O’Neil for discussion about this topic and assistance with experiments.

## Funding

N.Y. was supported by the China Postdoctoral Foundation Grant No.2012M520572, Tianjin Municipal Education Commission Grant No.20120401, Tianjin Natural Science Foundation Grant 14JCZDJC39500, and the National Natural Science Foundation of China

Grants 11872046, 11772197, 11672208, and 11402171. J.Y. and C.-W. C. acknowledge the financial support from the NSF (CAREER-1553202) and the Washington Research Foundation. J.L.S. was independently funded.

## **Author contributions**

N.Y. and J.L.S. designed research; N.Y. and C.C. performed research; N.Y., J.K., and J.L.S. analyzed data; N.Y. and J.L.S. wrote the paper; J.K. and J.L.S. supervised the research. The authors declare no conflict of interest. N.Y. and J.L.S. contributed equally to this work.

## **Competing interests**

The authors have no competing interests to declare.

## **Data and materials availability**

All data, code, and materials used in this work are freely available upon request.

## **List of Supplementary Materials**

- Detailed derivations and additional results
- Fig. S1 - S10
- Movies S1 and S2



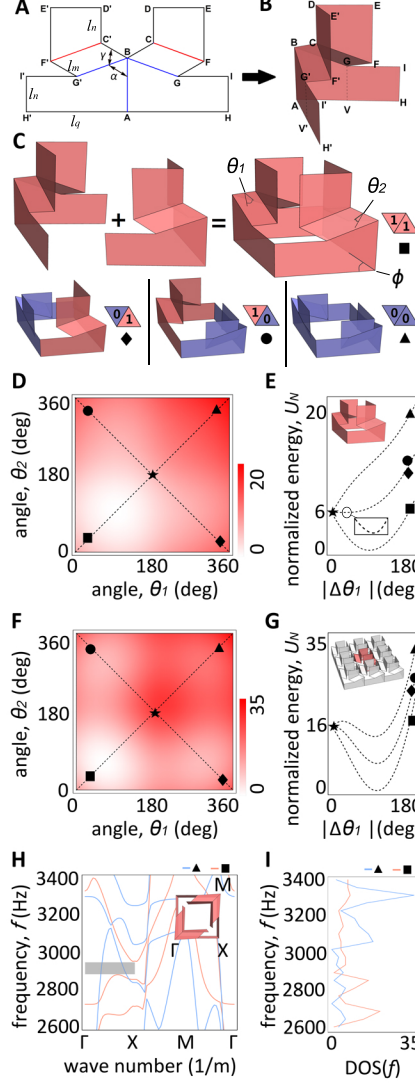


Figure 1: Design of a mechanical metamaterial unit with extrinsic properties. **(A)** Geometry and folding pattern of a half-unit. Red and blue lines denote mountain and valley folding creases, respectively. Edge  $CD$  joins with  $C'D'$ . **(B)** Half-unit assembled. **(C)** Two half-units join along edges  $HI$  and  $H'I'$  to create a full unit. Two DOFs ( $\theta_1$  and  $\theta_2$ ) quantify whether flanges are up (pink) or down (purple). Four distinct configurations are denoted by  $[0,0]$  ( $\blacktriangle$ ),  $[0,1]$  ( $\blacklozenge$ ),  $[1,0]$  ( $\bullet$ ), and  $[1,1]$  ( $\blacksquare$ ). Dihedral angle  $\phi$  along  $VA V'$  is used for measuring transverse compression. **(D)** Energetics of deformation in the  $(\theta_1, \theta_2)$  configuration space. Diagonal lines are accessible strictly by crease deformations. Off-diagonal region is accessible by bending along  $GV$  and  $G'V'$ . **(E)** Energetics of crease deformation (diagonal lines from **(D)**) show the basic unit (inset) is tristable with the  $[1,0]$  and  $[0,1]$  configurations being identical curves.  $|\Delta\theta_1| = |\theta_1 - 180^\circ|$  measures deformations away from the degenerate point ( $\star$ ). **(F)** Energetics of the same unit embedded in a  $3 \times 3$  tessellation are rather different. **(G)** On inspection, the embedded unit (inset) is now quadstable due to extrinsic unit-unit interactions. **(H)** Frequency-dependent band structure is sensitive to the unit's configuration. A band gap in the  $[1,1]$  configuration (highlighted gray) vanishes in the  $[0,0]$  configuration. **(I)** DOS shows configuration-specific vibration transmission properties.

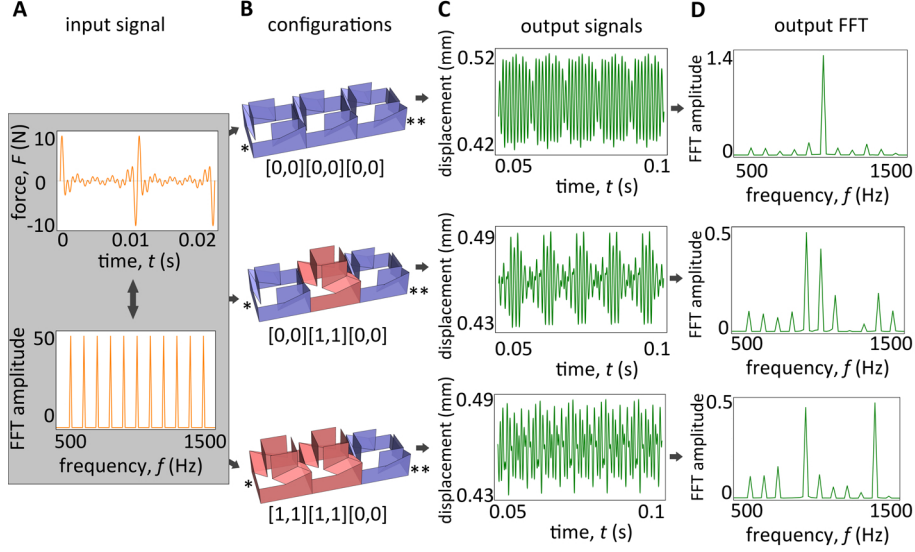


Figure 2: Combining units into a  $1 \times 3$  PERMuTE material produces a frequency filter with dynamically reprogrammable transmission properties. (A) Input force  $F(t)$  (upper plot; time-domain) generated by a 11-component frequency comb (lower plot; frequency-domain). (B) Three metamaterial devices are sequentially programmed into the structure by popping individual mesoscale units into the  $[0,0]$  or  $[1,1]$  configurations. Input force was applied at  $*$  and output was measured at  $**$ . (C) Time-domain output signal during steady oscillation shows all three devices function as frequency filters with distinct transmission properties. The ratio of output amplitude to input amplitude is about  $0.11 \text{ mm} / 0.14 \text{ mm} \approx 0.79$ . (D) Frequency-domain output signal shows transmission profile for each device.

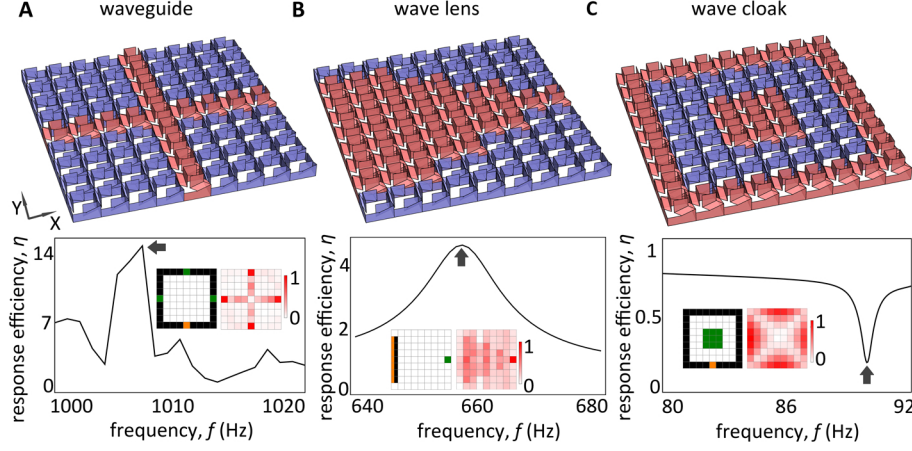


Figure 3: Combining units into a  $9 \times 9$  PERMuTE material produces a general-purpose platform for designing mechanical metamaterial devices. **(A)** Waveguide device transmits input oscillations along the “+” shaped channel (pink  $[1,1]$  units), but nowhere else (purple  $[0,0]$  units). **(B)** Wave lens device transmits input oscillations along a line of input units (left-most triangular edge of pink  $[1,1]$  units), and focuses oscillations to a single point on the opposite side of the device (right-most tip of triangle). **(C)** Wave cloak device insulates central  $3 \times 3$  region (pink  $[1,1]$  units) from input oscillations on the outer edge (pink  $[1,1]$  units) with a doughnut of non-transmitting units (purple  $[0,0]$  units). Upper: 3D renderings of each device. Lower: frequency-dependent response efficiency  $\eta(f)$  for each device. Arrows point to optimal frequency,  $f^*$ . Left inset: schematic showing where signal was input (orange), target output was measured (green), and reference output for calculating  $\eta$  was measured (black);  $\eta$  is average maximum-amplitude at green divided by average maximum-amplitude at black. Right inset: heatmap of normalized oscillation amplitudes at  $f = f^*$ .

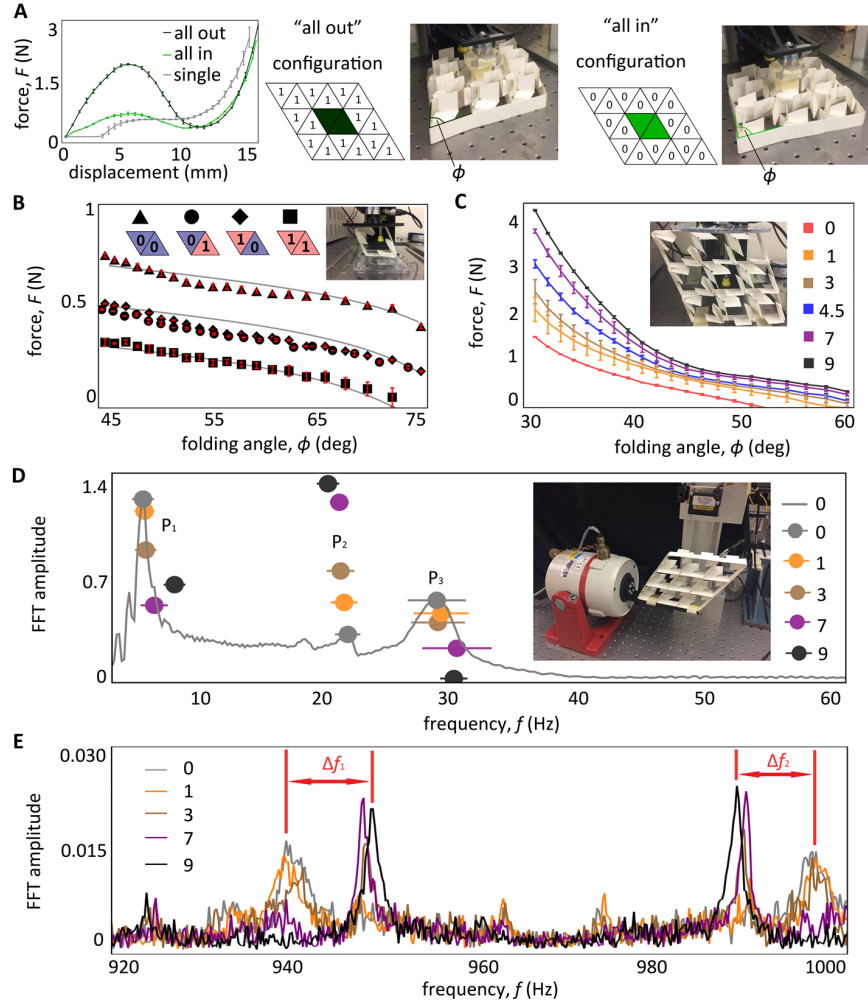


Figure 4: Experiments validate PERMuTE as a general-purpose design platform for meta-material technology. **(A)** Comparing longitudinal force-displacement measurements of a  $3 \times 3$  PERMuTE material with the central unit popped from [1,1] (dark green line) to [0,0] (light green line) shows sensitivity to the configuration of adjacent units. Comparison with a single isolated PERMuTE unit (gray line) shows no bistability. This data is direct evidence of extrinsic behavior. Schematic shows configuration of each flange; photos show loading orientation and differences in the equilibrium folding angle  $\phi$  that result from the programmed PERMuTE configuration. **(B)** Transverse compression measurements of a single unit verifies symmetry with respect to the [0,1] and [1,0] configurations. Solid lines are theoretical fits. **(C)** Transverse compression measurements of a  $3 \times 3$  PERMuTE material demonstrates the force response  $F(\phi)$  can be dynamically reprogrammed by changing configuration of individual units. Data ranges between 0 (red) and 9 (black) units popped in the [0,0] configuration. Data for 4.5 units corresponds to 9 popped flanges. **(D)** Frequency-domain response of a  $3 \times 3$  PERMuTE material with zero units in [0,0] (gray line) has two resonance peaks  $P_1$  and  $P_3$ , and a plateau at  $P_2$  (gray points). Additional points show how peaks at  $P_1$ ,  $P_2$ , and  $P_3$  rise-and-fall when between 1 (orange) and 9 (black) units are popped into the [0,0] configuration. Horizontal lines indicate full-width-at-half-height for each peak. **(E)** Frequency-domain response of the same structure also show resonance peaks shift in a configuration-dependent manner.

# Supplementary Materials

## Supplementary Movies

- Movie S1 - Intrinsic tristability of a single PERMuTE unit
- Movie S2 - Extrinsic quadstability of a  $3 \times 3$  PERMuTE bulk material

## PERMuTE unit design and geometry

The basic PERMuTE unit (Fig. 1A-C) is a planar geometric shape cut from a thin foldable material and assembled according to the crease pattern with edge  $CD$  joined to  $C'D'$ . As designed, this modular unit has five parameters consisting of three lengths  $\ell_m \equiv \overline{BC} = \overline{BC'} = \overline{GF} = \overline{GF'}$ ,  $\ell_n \equiv \overline{CD} = \overline{C'D'} = \overline{HI} = \overline{H'I'}$ ,  $\ell_q \equiv \overline{AH} = \overline{AH'}$ , and two angles  $\alpha, \gamma$  (Fig. 1A). Throughout all of our modeling and experiments, we set

$$\{\ell_m, \ell_n, \ell_q, \alpha, \gamma\} = \{15 \text{ mm}, 17.5 \text{ mm}, 50 \text{ mm}, 70^\circ, 50^\circ\}. \quad (\text{S1})$$

Additionally, we utilize  $(\theta_1, \theta_2)$  as the two “weakly-coupled Degrees of Freedom (DOF)” to describe each unit’s configuration. To be precise, the PERMuTE geometry has two uncoupled linearly-independent DOF:

$$\begin{aligned} \Theta_1 &= (\theta_1 - \theta_2)/\sqrt{2}, \quad \text{and} \\ \Theta_2 &= (\theta_1 + \theta_2)/\sqrt{2}. \end{aligned} \quad (\text{S2})$$

The easiest way to show these relations is to perform a coordinate transformation on  $(\theta_1, \theta_2)$  and rotate the plane by  $45^\circ$ . Practically, the convenience offered by  $(\theta_1, \theta_2)$  is to express a formulation that matches our hands-on intuition for the PERMuTE unit’s physical behavior, especially regarding the motion of the flanges. Mathematically, this convenience means we use variables that are linearly coupled to one another according to Eqs. S2. If we insert the contours defined by  $\theta_1 = \theta_2$  and  $\theta_2 = 360^\circ - \theta_1$  into the expressions for  $\Theta_1$  and  $\Theta_2$  we indeed confirm  $(\Theta_1, \Theta_2)$  forms an orthogonal basis. Of course, these geometric relations for the DOF become more complicated when material

bending is introduced. This complication leads to a situation where the practical benefits and conceptual conveniences of  $(\theta_1, \theta_2)$  ultimately outweigh the geometric idealization of  $(\Theta_1, \Theta_2)$ .

## PERMuTE unit mechanics

The PERMuTE geometry was introduced by first discussing a one DOF half-unit (Fig. 1A-B), then combining two identical half-units to create the basic 2 DOF unit (Fig. 1C). To understand the mechanical properties of this structure, we first consider the crease energy of a half-unit  $U_{\text{half}}(\theta)$ , where  $\theta$  is the angular DOF for the crease  $\overline{BC}$ . Noting the half-unit has one crease with length  $\overline{BC} = \ell_m$ , one crease with length  $\overline{CD} = \ell_n$ , one crease with length  $\overline{AB} = \ell_n + (\ell_q/2) \cot \alpha$ , and four creases with length  $\overline{BG} = \overline{CF} = \overline{BG'} = \overline{C'F'} = \ell_q/(2 \sin \alpha)$ , we express the crease energy as

$$U_{\text{half}}(\theta) = \frac{k_c}{2} \left[ \left( 2\ell_n + \frac{\ell_q}{2} \cot \alpha \right) (\phi(\theta) - \phi_0)^2 + \left( \frac{2\ell_q}{\sin \alpha} (\zeta(\theta) - \zeta_0)^2 \right) \right], \quad (\text{S3})$$

where linear torsional elasticity with crease constant  $k_c$  is assumed,  $\phi(\theta)$  measures the angle of the PERMuTE's base (Fig. 1C),  $\zeta(\theta)$  measures the angle between facets  $BCGF$  and  $ABGV$ , and energy minima for each term is set by the constant angles  $\phi_0$  and  $\zeta_0$ . Based on observations with experimental prototypes, we fixed the equilibrium angle constants such that  $\phi_0 = 60^\circ$  and  $\zeta_0 = 120^\circ$  for a simple crease without constraints. In addition, we define  $\phi(\theta)$  and  $\zeta(\theta)$  according to

$$\sin \frac{\phi(\theta)}{2} = \left[ \frac{\sin \gamma}{\sin \alpha} \right] \sin \frac{\theta}{2}, \quad (\text{S4})$$

and

$$\cos \zeta(\theta) = \frac{\cos \xi(\theta) - \cos \alpha \cos \gamma}{\sin \alpha \sin \gamma}, \quad (\text{S5})$$

where

$$\xi(\theta) = \begin{cases} \arcsin \left[ \frac{\sin \alpha \cos(\phi/2)}{\sqrt{\cos^2 \alpha + \sin^2 \alpha \cos^2(\phi/2)}} \right] + \arcsin \left[ \frac{\sin \gamma \cos(\theta/2)}{\cos^2 \gamma + \sin^2 \gamma \cos^2(\theta/2)} \right], & \frac{\pi}{2} \geq \alpha > \gamma, \\ \pi - \arcsin \left[ \frac{\sin \alpha \cos(\phi/2)}{\sqrt{\cos^2 \alpha + \sin^2 \alpha \cos^2(\phi/2)}} \right] + \arcsin \left[ \frac{\sin \gamma \cos(\theta/2)}{\cos^2 \gamma + \sin^2 \gamma \cos^2(\theta/2)} \right], & \alpha > \frac{\pi}{2} > \gamma. \end{cases} \quad (\text{S6})$$



Here,  $\xi$  is the angle between  $\overline{BC}$  and  $\overline{CD}$ .

Combining two half-units creates a single unit described by a 2 DOF energy function that incorporates the additional crease energy from the edges where the two half-units are joined

$$U(\theta_1, \theta_2) = U_{\text{half}}(\theta_1) + U_{\text{half}}(\theta_2) + k_c \ell_n ((\pi - \phi) - (\pi - \phi_0))^2. \quad (\text{S7})$$

The third term in Eq. (S7) couples the two DOF by requiring  $\phi(\theta_1) = \phi(\theta_2)$ . This constraint permits two solutions consistent with the definition in Eq. (S4); either  $\theta_2 = \theta_1$  or  $\theta_2 = 360^\circ - \theta_1$ . Therefore, a crease-only energy model for the basic PERMuTE unit has an accessible configuration space with four branches (Fig. 1D, black lines; Fig. 1E, energy curves) radiating from one degenerate point at  $(\theta_1, \theta_2) = (180^\circ, 180^\circ)$ , which is where the solutions of  $\phi(\theta_1) = \phi(\theta_2)$  cross. Once assembled, the PERMuTE geometry imposes constraints that drive the angles  $\phi$  and  $\zeta$  away from their rest values. In the absence of external loads, these pre-stresses leave a residual energy in the system  $\approx 0.29k_c$  at its lowest value (Fig. 1E, lowest point on [1,1] branch (■)). Geometrically, this energetic minima corresponds to  $\phi = 75.3^\circ$  and  $\zeta = 129^\circ$ , which produces a symmetric configuration  $(\theta_1, \theta_2) = (97.0^\circ, 97.0^\circ)$ . For the tessellated  $3 \times 3$  PERMuTE structure (Fig. 1G, lowest point on [1,1] branch (■)), the residual energy is  $\approx 0.56k_c$  with  $\phi = 64.0^\circ$ ,  $\zeta = 139^\circ$ , and  $(\theta_1, \theta_2) = (81.1^\circ, 81.1^\circ)$ .

The idealized energetic model considered thus far is based on linearly elastic mechanics of creases and geometric constraints of the PERMuTE design. Real materials, however, tend to have bending of material in the planar facets, and physical prototypes suggest the vast majority of this bending occurs along  $\overline{GV}$  and  $\overline{G'V'}$  (Fig. 1B), significantly complicating the coupling between two half-units. The total energy of a single unit with bending is given by

$$U_{\text{full}}(\theta_1, \theta_2) = U_{\text{half}}(\theta_1) + U_{\text{half}}(\theta_2) + U_{\text{bend}}(\theta_1, \theta_2), \quad (\text{S8})$$

where

$$\begin{aligned} U_{\text{bend}}(\theta_1, \theta_2) &= k_b \ell_n (\phi_{\nu_1} - \pi)^2 + k_b \ell_n (\phi_{\nu_2} - \pi)^2 + k_c \ell_n (\psi(\theta_1, \theta_2) - (\pi - \phi_0))^2, \quad \text{and} \\ \psi(\theta_1, \theta_2) &= 3\pi - \frac{\phi_1(\theta_1) + \phi_2(\theta_2)}{2} - \phi_{\nu_1} - \phi_{\nu_2}. \end{aligned} \quad (\text{S9})$$

Here, the angle variables  $\phi_{\nu_1}$  and  $\phi_{\nu_2}$  quantify bending at the base of the PERMuTE unit (Fig. S1),  $\psi(\theta_1, \theta_2)$  is a useful auxiliary variable, and the bending energy is modeled as a linear torsional spring with bending constant  $k_b$ . When  $\phi_1$  and  $\phi_2$  are fixed by  $\theta_1$  and  $\theta_2$ , the bending energy is minimized such that  $\partial_{\phi_{\nu_1}} U_{\text{bend}} = 0$  and  $\partial_{\phi_{\nu_2}} U_{\text{bend}} = 0$ . We therefore have

$$\begin{aligned} \phi_{\nu_1} &= -\frac{-2k_c\phi_0 + k_c\phi_1 + k_c\phi_2 - 2\pi k_b - 4\pi k_c}{2(k_b + 2k_c)}, \\ \phi_{\nu_2} &= -\frac{-2k_c\phi_0 + k_c\phi_1 + k_c\phi_2 - 2\pi k_b - 4\pi k_c}{2(k_b + 2k_c)}, \end{aligned} \quad (\text{S10})$$

demonstrating that at the energetic minimum  $\phi_{\nu_1} = \phi_{\nu_2}$ , as expected by symmetry and equipartition. Moreover, we note  $\lim_{k_b/k_c \rightarrow \infty} \phi_{\nu_1} = \lim_{k_b/k_c \rightarrow \infty} \phi_{\nu_2} = \pi$ , which is consistent with the expectation that an infinitely rigid material would exhibit no bending. Substituting into the expression for  $U_{\text{bend}}$  and simplifying shows

$$U_{\text{bend}}(\theta_1, \theta_2)/k_c = 2\ell_n \left( \frac{k_b}{k_c} \right) \left[ \frac{2\phi_0 - \phi_1(\theta_1) - \phi_2(\theta_2)}{2(2 + k_b/k_c)} \right]^2 + \ell_n (\psi(\theta_1, \theta_2) - (\pi - \phi_0))^2. \quad (\text{S11})$$

Bending on the additional two sides of the PERMuTE base are computed analogously to Eq. (S11) (Fig. S1, mirror-symmetric geometry across the  $AOA'$  line). Moreover, when PERMuTE units are assembled into a larger lattice with  $N$  total units, both the bending energy in Eq. (S11) and the second term in Eq. (S3) cause adjacent units sharing common  $\phi_1, \phi_2, \phi_{\nu_1}$ , or  $\phi_{\nu_2}$  to couple their two  $(\theta_1, \theta_2)$  DOF. These overlapping variables between units directly couple the local configuration of each unit's flanges to the global configuration of the bulk tessellation. As such, unit-unit coupling at the base of each PERMuTE unit directly leads to the extrinsic properties of the bulk material. Calculations illustrating this principle shown in the main text use  $k_b/k_c = 1,000$  (Fig. 1D-G).

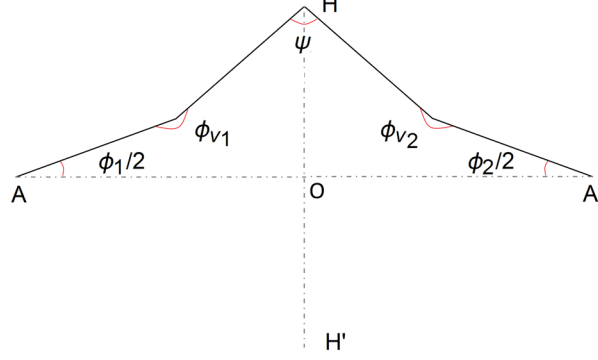


Figure S1: Schematic of a PERMuTE unit's base illustrating key variables when two half-units are combined. A half-unit consists of the vertices  $HAH'$  or  $HA'H'$  (see also Fig. 1A-B). Observations with hand-fabricated prototypes suggest bending is localized to the region modeled by the bending angles  $\phi_{v1}$  and  $\phi_{v2}$ .

For the  $3 \times 3$  PERMuTE material, we computed the energetic landscape of  $(\theta_1, \theta_2)$  for the central unit while all other units were held in the  $[1, 1]$  configuration. We repeated this calculation for different values of  $k_b/k_c$  and found the overall landscape was unchanged due to the constraints in Eqs. (S10), and the solutions along  $\theta_2 = \theta_1$  or  $\theta_2 = 360^\circ - \theta_1$  were similarly constant. As such, the isolated unit is always tristable while the embedded unit is quadstable, for sufficiently large  $k_b/k_c$ . This result is expected because the values of  $(\theta_1, \theta_2)$  along the lines  $\theta_2 = \theta_1$  and  $\theta_2 = 360^\circ - \theta_1$  do not require bending and are therefore only determined by the mechanics of creasing.

Band structure calculations (Fig. 1H) were performed in COMSOL 5.1 using the Parametric Sweep / Eigenfrequency module applied to a Normal-size free tetrahedral mesh with the geometry of the PERMuTE unit in the  $[0, 0]$  and  $[1, 1]$  configurations. We set  $\phi = 90^\circ$ , chose periodic boundary conditions in the  $xy$  directions to mimic the effect of a tessellation, and fixed material properties to mimic card stock paper. Specifically, we set the Poisson's ratio  $\nu = 0.3$ , Young's modulus  $Y = 3.64$  GPa, mass density  $\rho = 871$  kg/m<sup>3</sup>, sheet thickness to 2 mm,  $\ell_m = 15$  mm,  $\ell_n = 17.5$  mm, and  $\ell_q = 50$  mm. From these numerical simulations, we computed the frequency-dependent density of states,  $\text{DOS}(f)$  (Fig. 1I). Functionally,  $\text{DOS}(f)$  is a histogram over  $k$ -space; this calculation was performed by binning the number of modes on the dispersion curves with a bin width of

50 Hz (Fig. 1I, bins centered on  $f$  count number of modes in the interval of  $f \pm 25$  Hz). Regarding the combined efforts of analytic calculations, FEM simulations, and experiments, we additionally note the energetics of PERMuTE units were calculated with  $\phi_0 = 60^\circ$ , which in combination with the overall crease pattern, drives the equilibrium value of  $\phi = 64^\circ$ . These angles closely mimic experimental structures (Fig. 4), where gravitationally-induced self-compression shifts  $\phi$  to  $\approx 60^\circ$ . FEM simulations (Figs. 1-3) were performed with  $\phi = 90^\circ$  to ensure simple boundary conditions and well-defined normal directions for input and output oscillatory forcing.

Our main findings in the band structure calculations are (i) the existence of band gaps, (ii) a band structure that varies with the PERMuTE unit's configuration, and (iii) a band gap that opens/closes as the configuration varies. To expand on these results and verify that they are insensitive to specific parameters, we changed the value of the Young's modulus from  $Y = 3.64$  GPa to 1.0 GPa and reran the simulations (Fig. S2). In these new data we again found configuration-sensitive band gaps and band structure. In fact, across each frequency range we examined, we found at least one band gap that opened/closed as the structure went between the  $[0,0]$  and  $[1,1]$  configurations. This finding suggests the existence of switchable band gaps are quite common in the kHz band, and ultimately that this phenomenon may be a generic feature of the metamaterial's design.

## PERMuTE bulk configuration counting

A PERMuTE unit has 4 possible configurations denoted  $[0,0]$ ,  $[0,1]$ ,  $[1,0]$ , and  $[1,1]$  (Fig. 1C). A PERMuTE material consisting of  $N$  units then has  $4^N = 2^{2N}$  possible configurations. A nuance of this counting is that we retain configurations exhibiting symmetries with other configurations. For example, a configuration  $\mathcal{C}_i$  may be identical to another structure  $\mathcal{C}_j$  when rotated by  $180^\circ$ . We count these structures as being distinct entities despite this symmetry because in real-world applications, PERMuTE materials are presumably attached or anchored to other components. This anchoring breaks rotational symmetry and as a result, the rotational equivalence may no longer hold.

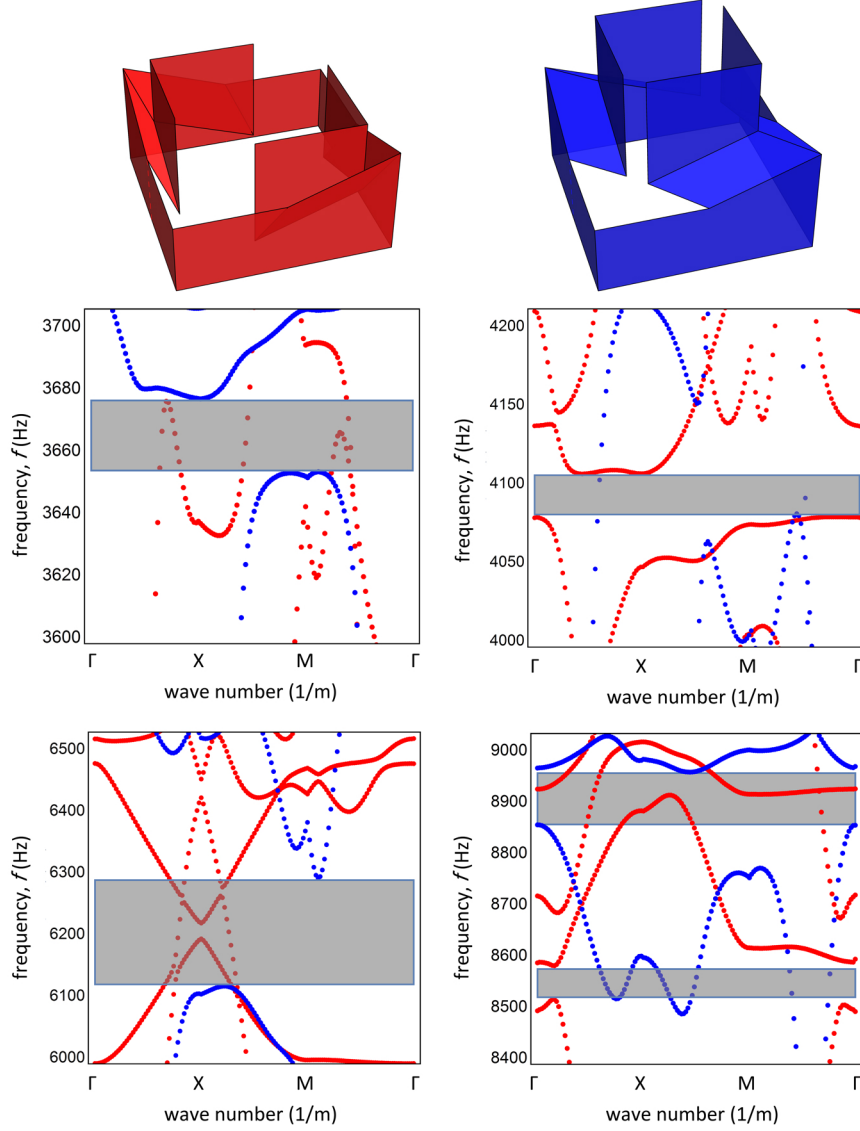


Figure S2: Additional band structure calculations demonstrate the generic nature of programmable band gaps in PERMuTE materials. Each of the four plots show dispersion relations across various frequency ranges in the kHz band for a unit in the  $[0, 0]$  configuration (red) and the  $[1, 1]$  configuration (blue). Orientation of modes is same as in main text (Fig. 1H, inset).

## PERMuTE frequency filter mechanics

Vibrational dynamics for the  $1 \times 3$  PERMuTE material (Figs. 2 and S3) were calculated in COMSOL 5.1 using a Normal-size free tetrahedral mesh with the geometry of each PERMuTE unit in variable configurations. We set  $\phi = 90^\circ$ , chose free boundary conditions to mimic the effect an applied force to an unconstrained structure, and fixed material properties to mimic card stock paper. Specifically, we set the Poisson’s ratio  $\nu = 0.3$ , Young’s modulus  $Y = 3.64$  GPa, mass density  $\rho = 871$  kg/m<sup>3</sup>, sheet thickness to 2 mm,  $\ell_m = 15$  mm,  $\ell_n = 17.5$  mm, and  $\ell_q = 50$  mm. Mass dampening was introduced and set to 100 to avoid unphysical exponentially-growing strains at resonant frequencies. The initial displacement field and velocity field were all zero. The boundary loading type for the input was set to “face excitation” (Figs. 2 and S3, input force applied at \*). We use a time-dependent solver in COMSOL from 0 to 0.1 s, with a step size of  $5 \times 10^{-4}$  s. The resulting amplitude is obtained from the “total displacement” value (Figs. 2 and S3, output measured at \*\*). While time-dependent transient oscillations appear early on, they are damped out by  $t = 0.05$  s, and FEM computations produce steady oscillations for the remainder of the simulation. Thus, in plots we show results from  $0.05 \leq t \leq 0.10$ .

## PERMuTE $9 \times 9$ bulk mechanics

The PERMuTE  $9 \times 9$  material (Figs. 3 and S4) was analyzed in COMSOL 5.1 using the same setup as the  $1 \times 3$  PERMuTE frequency filter. However, the model was computed in the frequency domain with vibration deformations incorporated.

## Experimental prototype fabrication

Prototype PERMuTE structures were fabricated using Strathmore 500 Series 3-ply Bristol card stock that was laser cut using a PERMuTE design pattern generated in Mathematica 10.2. To join edges for each unit’s assembly, additional card stock was glued to the facets so that the crease mechanics were identical to folds elsewhere in the structure. To



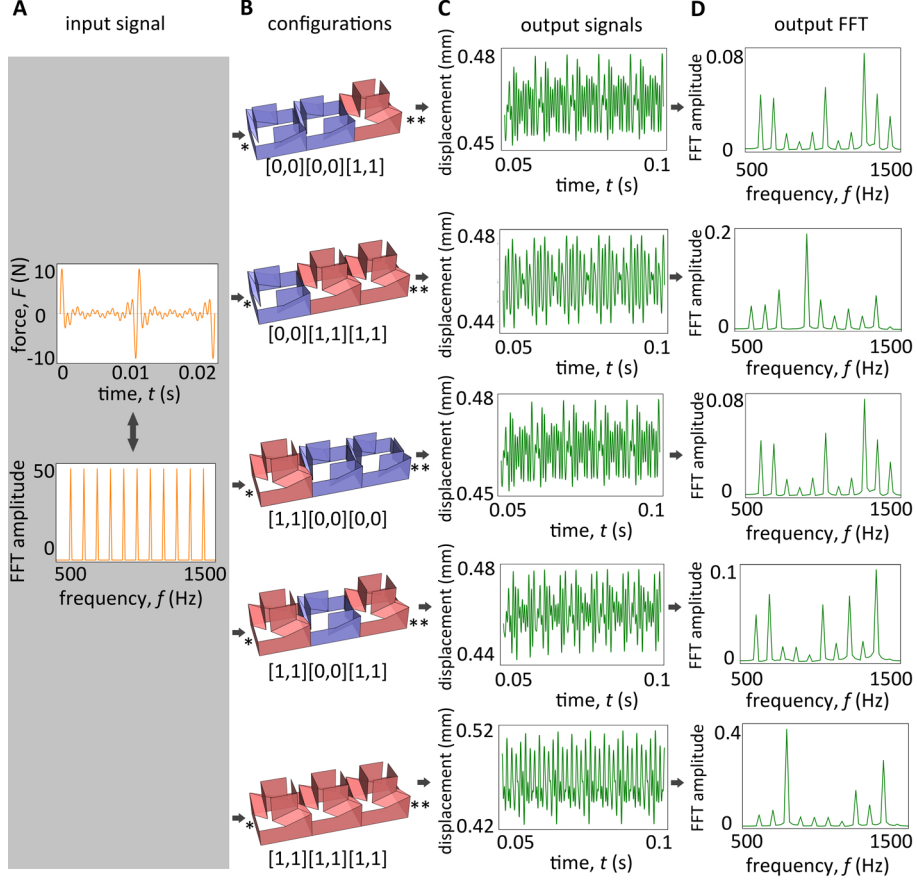


Figure S3: Combining units into a  $1 \times 3$  PERMuTE material produces a frequency filter with dynamically reprogrammable transmission properties. **(A)** An input time-dependent force  $F(t)$  consisting of an 11-component frequency comb can be converted into a range of output responses. **(B)** In addition to the three metamaterial devices shown in the main text, we show five more devices here that are sequentially programmed into the structure by popping mesoscale units into  $[0,0]$  or  $[1,1]$  configurations. **(C)** Time-domain output signal during steady oscillation shows all five devices function as frequency filters with distinct transmission properties. **(D)** Frequency-domain output signal shows transmission profile for each device.

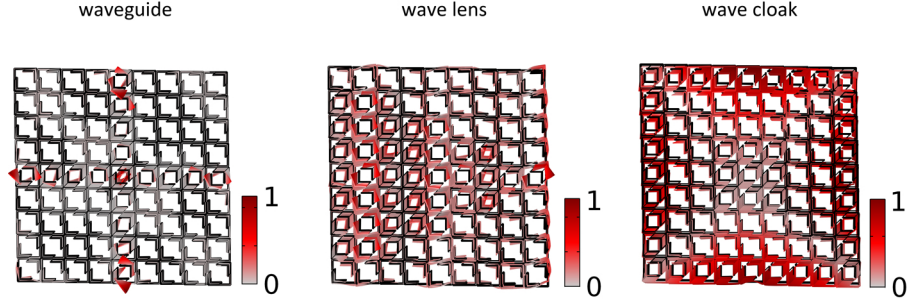


Figure S4: 3D renderings from a top-down view of the  $9 \times 9$  PERMuTE material color-coded by normalized deformation amplitude. From left-to-right, these deformations arise at driving frequencies of 1,007 Hz, 658.0 Hz, and 89.90 Hz, corresponding to the natural resonances of the desired functionalities.

join units into a  $3 \times 3$  tessellation, a long card stock strip was used along the perimeter (Fig. S5). The intersection of creases at vertices are often found to be mechanically complex due to the presence of material stretching. We therefore removed a small circular domain at each vertex to avoid such effects and allow for a simpler creasing- and bending-driven set of material properties. Our overall approach is useful for rapidly designing and fabricating prototypes to perform bench-top experiments examining extrinsic metamaterial properties. However, this approach carries with it draw-backs associated with the heterogeneous effects from gluing panels and imperfect alignment during assembly. In addition, these fabrication materials have poor long-term durability. As such, the hand-made approach is likely insufficient for industrial-scale manufacturing.

## Experimental compression measurements

In compression measurements, force was applied to various PERMuTE structures at a constant loading speed of 0.5 mm/s. Longitudinal force-displacement measurements were performed with the force applied only to the central PERMuTE unit in a  $3 \times 3$  tessellation (Fig. 4A). Transverse force-displacement measurements were performed on an isolated PERMuTE unit (Fig. 4B) as well as a  $3 \times 3$  structure (Fig. 4C). In transverse-compression of an isolated PERMuTE unit, the stress-free size of the unit was 49 mm across and



Figure S5: Photographs of the  $3 \times 3$  PERMuTE material provide a top-down view (left) and a three-quarters perspective view (right). Notice that material has been removed at vertices to avoid the effects of material stretching.

compression was increased until the unit was 34 mm. In all cases, experiments were repeated three consecutive times for each configuration and averaged. Error estimates reported in the main text (Fig. 4A, B, and C) are the minimum and maximum values across all repeated measurements, demonstrating a high degree of reproducibility in hand-folded bench-top PERMuTE prototypes. The experimentally accessible range for the folding angle  $\phi$  was different between an isolated unit ( $45^\circ \leq \phi \leq 75^\circ$ ) and the  $3 \times 3$  tessellation ( $30^\circ \leq \phi \leq 60^\circ$ ). When units are combined and inserted into the testing apparatus,  $\phi$  decreases under compression from the structure's own weight. Nevertheless, in both cases, we were still able to probe  $\approx 30^\circ$  in compression.

To supplement measurements reported in the main text, we performed a variety of additional transverse compression tests to experimentally determine how the number and pattern of *flanges* in either the [0] or [1] state affects static compression measurements (Fig. S6). This notational shift from the full PERMuTE unit to a half-PERMuTE unit allows us to compactly illustrate and compare a wide variety of patterns by labeling which flanges are in the [0] configuration and classifying patterns by the number of flanges in that state. We observed that the number of flanges in a given configuration has up to a 2-fold effect on the force-displacement measurement, while the specific pattern of flanges seems to have little effect when the number of flanges in the [0] and [1] states is held constant.

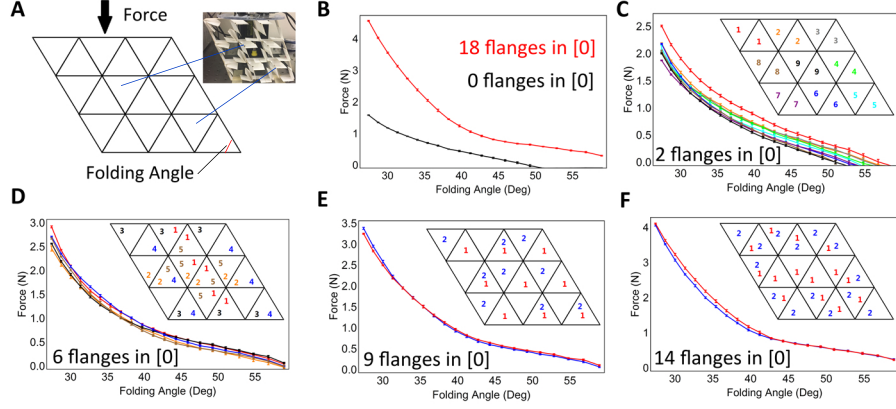


Figure S6: Supplemental compression experiments examining a  $3 \times 3$  PERMuTE meta-material in greater detail. (A) Schematic distinguishing the flanges of each PERMuTE module's half-unit (Fig. 1A) illustrated here as triangles. Photograph inset maps triangles to individual flanges in the larger structure. Transverse loading is applied by a force  $F$  exerted with a constant load speed. (B) Comparing force-displacement curves when a structure has all 18 flanges in the  $[0]$  configuration to its response with none of the flanges are in the  $[0]$  configuration shows a nearly 2-fold increase in the force required to maintain a given compression. (C) We systematically measure the force-displacement relationship when two flanges are in the  $[0]$  configuration (e.g., a PERMuTE unit set to  $[0,0]$ ), while all other flanges are in the  $[1]$  configuration (e.g., all other PERMuTE units set to  $[1,1]$ ). Each of the nine colored force-displacement curves correspond to the same-color flanges numbered in the inset set to  $[0]$ . For example, the red curve corresponds to the flanges marked with a red '1' set to the  $[0]$  configuration; the orange curve corresponds to the flanges marked with an orange '2' set to the  $[0]$  configuration; etc. (D) We examine five patterns of six flanges set to  $[0]$ . Even though these patterns vary substantially, each results in a nearly-identical force-displacement curve. Along similar lines, we examined (E) nine flanges in the  $[0]$  configuration and (F) 14 flanges in the  $[0]$  configuration. As before, the specific pattern has little effect on the static force-displacement relationship.

Therefore, these data demonstrate that for static compression the *number* of flanges in a given configuration matters far more than the specific *pattern*. As a consequence, we can maintain nearly-constant mechanical properties with respect to static loading by keeping the number of flanges in a given configuration constant, while selectively choosing a variety of frequency-dependent metamaterial response by varying their spatial pattern. This finding offers significant new design possibilities for materials that need to maintain constant moduli but dynamically reprogrammable vibrational response.

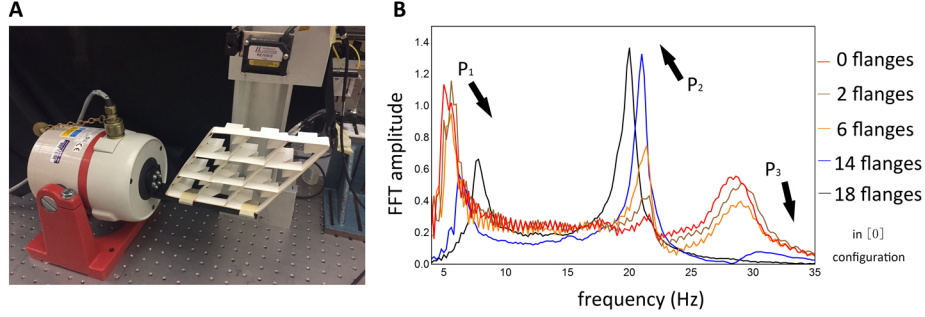


Figure S7: Frequency-dependent experiments validate the existence and utility of extrinsic metamaterial properties. (A) Photograph showing experimental setup. (B) Measured displacements are Fourier transformed to demonstrate that resonance peaks  $P_1$ ,  $P_2$ , and  $P_3$  can be turned “on,” “off,” or shifted depending on the configuration of the PERMuTE structure. This data is direct evidence in support of the simulation results described in the main text and shows in an experimental prototype the necessary ingredients for constructing PERMuTE metamaterial devices.

## Experimental frequency-sweep measurements

Frequency-dependent mechanical experiments were performed with an Arbitrary Waveform Generator (20 MHz function / Agilent 33220A) and vibrator used to apply transverse oscillations to a  $3 \times 3$  PERMuTE structure in various configurations (Fig. 4D and S7). Displacement responses were measured with an IL-065 laser displacement detector (Fig. S7A, detector measured oscillatory displacements of the “top” transverse surface by viewing from above). Frequency sweeps from 1 to 100 Hz were performed within 5 s for an input wave with an amplitude of 0.5 mm so that the full range of displacement was 1 mm. Displacement measurements were Fourier transformed and the resulting frequency-space representation demonstrates the reversible removal and generation of resonance peaks that are determined by the PERMuTE structure’s configuration (Fig. S7B,  $P_1$ ,  $P_2$ , and  $P_3$ ).

Expanding on these results, we examined how the number of flanges in the [0] configuration and their spatial pattern affect the measurable frequency range in this bench-top setup (Fig. S8). Similar to the static transverse compression measurements, these data showed the *number* of flanges in [0] has a stronger effect than their specific *pattern*. These

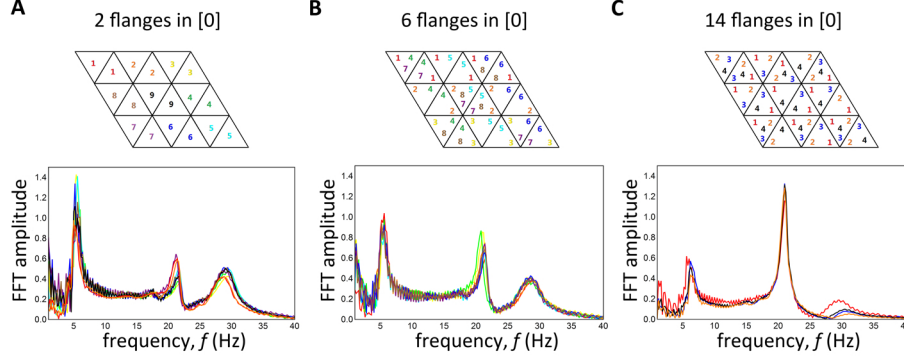


Figure S8: Frequency-dependent experiments studying effects of spatial configuration on mechanical metamaterial properties in a  $3 \times 3$  PERMuTE material. Frequency-space results on structures with (A) two flanges in the [0] configuration, (B) six flanges in the [0] configuration, and (C) 14 flanges in the [0] configuration show the number of flanges in [0] affect the overall response curves, but shows little variation when the number of flanges in [0] is held constant. Legend convention relating the flange pattern to the colored curves in each plot is identical to Fig. S6.

experiments were generally limited to configurations with a high degree of symmetry, at relatively modest frequencies where  $f \leq 100$  Hz, and the input amplitude was  $\mathcal{O}(10^{-2})$  smaller than the structure's overall size. While these restrictions on the input oscillations were required to prevent any irreversible structural damage, the experiments suggest either non-linear responses at these low frequencies or higher-frequency input oscillations are required to detect configuration-specific response.

## Model fitting for experimental force-compression data

As a method to test and validate our understanding of the PERMuTE unit's mechanical properties, we developed a simple elastic model to compare against the experimental data. In this model, we take a top-down view of zero-frequency transverse compression at force  $F$  and simplify the structure to a schematic of its base (Fig. S9). We reduce the full complexity of an isolated PERMuTE unit to three linearly elastic springs that are a function of the angle  $\phi$ . The three spring terms correspond to the two flanges and the unit's base. If a flange is popped up into the [1] configuration, then its equivalent spring has a spring constant  $k_1^*$  and equilibrium angle  $\phi_1^*$ . If the flange is popped down into



the [0] configuration, then its equivalent spring has a spring constant  $k_2^*$  and equilibrium angle  $\phi_2^*$ . The base is then accounted for by an equivalent spring with constant  $k_3^*$  and equilibrium angle  $\phi_3^*$ . For small compressions, the initial height of the in-plane geometry goes from  $h_0 = \ell_q \sin \phi$  to  $\ell_q \sin(\phi + \delta\phi)$  so that the work done is

$$F \cdot (h_0 - h) = F \cdot (\ell_q \sin \phi - \ell_q \sin(\phi + \delta\phi)) \approx -F \ell_q \cos \phi \cdot \delta\phi. \quad (\text{S12})$$

For a PERMuTE unit in the [0,0] configuration at mechanical equilibrium, Eq.(S12) must be balanced by an equal and opposite force so that

$$F_{[0,0]} = -\frac{2k_2^*(\phi - \phi_2^*) + 2k_3^*(\phi + \phi_3^* - \pi)}{\ell_q \cos \phi}. \quad (\text{S13})$$

Likewise, in the [0,1] and [1,0] configurations, force balance leads to

$$F_{[0,1]} = F_{[1,0]} = -\frac{k_1^*(\phi - \phi_1^*) + k_2^*(\phi - \phi_2^*) + 2k_3^*(\phi + \phi_3^* - \pi)}{\ell_q \cos \phi}, \quad (\text{S14})$$

while the [1,1] configuration has

$$F_{[1,1]} = -\frac{2k_1^*(\phi - \phi_1^*) + 2k_3^*(\phi + \phi_3^* - \pi)}{\ell_q \cos \phi}. \quad (\text{S15})$$

With these expressions, we performed a simultaneous fit of all data in all four experimental force-displacement measurements (Fig. 4B, points) to all four predicted equations by minimizing the six-parameter error function

$$\begin{aligned} \epsilon(k_1^*, k_2^*, k_3^*, \phi_1^*, \phi_2^*, \phi_3^*) &= \sum_{i=1}^n (F_{[0,0]}(\phi_i) - F_{[0,0]}^{\text{exp}}(\phi_i))^2 + \sum_{i=1}^n (F_{[0,1]}(\phi_i) - F_{[0,1]}^{\text{exp}}(\phi_i))^2 + \\ &\quad \sum_{i=1}^n (F_{[1,0]}(\phi_i) - F_{[1,0]}^{\text{exp}}(\phi_i))^2 + \sum_{i=1}^n (F_{[1,1]}(\phi_i) - F_{[1,1]}^{\text{exp}}(\phi_i))^2. \end{aligned} \quad (\text{S16})$$

In this expression, we sample the model's predicted force at each of the  $4n$  measured angles  $\phi_i$ ,  $i = 1 \dots n$  and compute the squared difference with the experimentally measured force  $F^{\text{exp}}(\phi_i)$  at the corresponding configuration. This six-way fit was simultaneously optimized for 1,948 data points and we found  $k_1^* = (6.55 \pm 0.47) \text{ N}\cdot\text{mm}$ ,  $k_2^* = (14.77 \pm 0.34)$

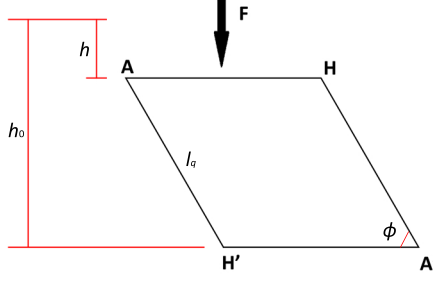


Figure S9: Top-down view of a PERMuTE unit can be schematized as a parallelogram. Force-compression experiments apply a force  $F$  as shown that deform the unit from  $h_0$  by an amount  $h$ . The vertices are identically labeled as in the main text (Fig. 1A,B).

N·mm,  $k_3^* = (4.22 \pm 0.13)$  N·mm,  $\phi_1^* = (0.0058 \pm 0.075)^\circ$ ,  $\phi_2^* = (55.44 \pm 0.033)^\circ$ ,  $\phi_3^* = (0.0073 \pm 0.013)^\circ$ , where all error estimates are the 95% confidence interval of the fit. These values were used to generate plots shown in the main text (Fig. 4B, black lines).

### 3D PERMuTE Materials

While the main text focused on 1D and 2D PERMuTE structures, an obvious question is whether there exists a 3D analog. In fact, it is quite easy to construct such structures by joining two PERMuTE units together: one unit is as-shown in the main text (Fig. 1C), while the other unit is flipped upside-down. Taking two PERMuTE units in these orientations and joining them at the flanges gives a 3D dumb-bell like shape that is similarly a 2 DOF structure with four possible configurations. While we do not perform a full mechanical analysis to determine whether this unit is tristable or quadstable, we simply show that a 3D volume of these double-PERMuTE units gives rise to a metamaterial whose surface can be dynamically and reversibly reconfigured (Fig. S10). Obviously, many of the ideas regarding the band structure, band gaps, and PERMuTE device construction can be extended to the 3D context, though the resulting complexity is a non-trivial jump beyond what has been considered here.

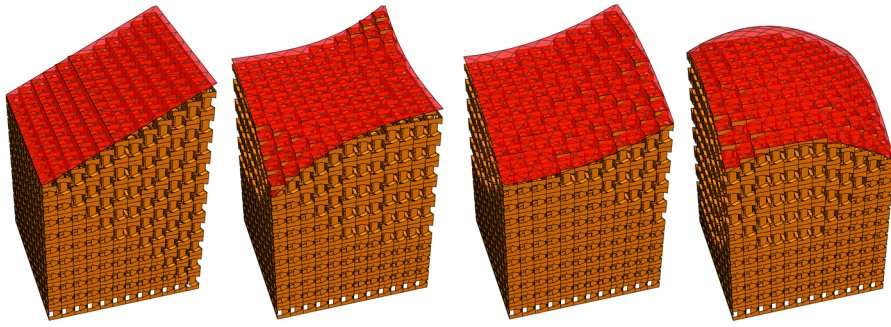


Figure S10: A 3D PERMuTE structure has all the same ingredients that give the 1D and 2D PERMuTE structures their interesting metamaterial properties. In addition, it has the ability to take multiple different surface profiles. This gallery of images shows a single  $12 \times 12 \times 10$  PERMuTE structure in four configurations with four different “metasurfaces.”